Some crystal field effects in Nd(_x)Gd(_1-x)Co(_2)

G.J. Primavesi

SOME CRYSTAL FIELD EFFECTS IN $Nd_xGd_{1-x}Co_2$

by

G.J. Primavesi, B.Sc.

Presented in candidature for the degree of

Doctor of Philosophy

February 1972

ABSTRACT

This work describes the design and construction of a self-balancing vibrating sample magnetometer. The instrument was used to study some of the magnetic properties of the pseudobinary compounds, $(Nd_xGd_{1-x})Co_2$. The structural and magnetic data for certain compositions within the series show deviations from the behaviour expected from a simple ferrimagnetic system. In particular one composition exhibits three apparent compensation points in its remenance versus temperature curve, a unique phenomenon. These anomalies are shown to arise from the effects of the crystal field and internal magnetic field upon the tripositive neodymium ion. A consistent semi-quantitative picture of the process is presented which accounts for the observations provided that the easy axis in the compounds is the 111 direction.

CONTENTS

Page

NOMENCLATURE

A	atomic weight
B_4, B_6	crystal field coefficients
B_J	Brillouin function
e	electronic charge
g	Landé g-factor
G	de Gennes function
H_{app}	applied magnetic field
H_c	crystal field Hamiltonian
H_D	demagnetising field
H_{int}	internal magnetic field
H_z	Zeeman contribution to total Hamiltonian
i_σ	current in magnetometer D.C. coil
J_{eff}	effective exchange constant
J_{int}	interband mixing exchange contribution
J_{sf}	s-f exchange interaction
k	Boltzmann's constant
k_f	wave vector of electron at Fermi level
N	Avogadro's number
O_n^m	Stevens Operator equivalents
S	Magnetometer calibration factor
s_e	conduction electron spin
χ	magnetic susceptibility
μ_B	Bohr magneton
σ	magnetisation

LIST OF FIGURES

Figure

Figure

CHAPTER 4

Figure

CHAPTER 5

Figure

CHAPTER 5 (continued)

CHAPTER 6

LIST OF TABLES

ACKNOWLEDGEMENTS

I would like to extend my sincere thanks to my supervisor, Dr. K. N. R. Taylor, for the constant help and inspiration he has provided throughout this work. My thanks are due to Dr. I. R. Harris of the University of Birmingham who provided many of the specimens and some helpful discussions. I am indebted to the Science Research Council for the award of a research studentship. My appreciation must go to the entire Physics Department, particularly to its head, Professor G. D. Rochester, the staffs of the workshops for their forebearance and, of course, to my immediate colleagues in the solid state group. Finally these acknowledgements would be incomplete without the inclusion of the non-technical staff and particularly Mrs. J. Moore who so ably typed the manuscript.

CHAPTER 1

INTRODUCTION

Since relatively pure rare earths became readily available some fifteen years ago interest in their properties and those of their compounds has burgeoned. The chemically similar rare earths are interesting magnetically by virtue of the buried 4f shell that is progressively filled across the Lanthanide series. This shell results in magnetic properties of the ion in a host lattice that are almost the same as those of the free ion and a truly localised magnetic moment arises. The behaviour of the rare earths is fairly well understood whereas the transition metal magnetic processes still pose unsolved problems, and it is in the hope that the relative simplicity of the rare earths may assist in solving the complexities of the transition metals that many workers have turned their attention to rare earth-transition metal compounds. Apart from this academic interest, the extensive range of possible rare earth intermetallic compounds promises and has realised technologically useful properties.

The study reported in this thesis is part of the programme of research at the Rare Earth solid state group of Durham University into the magnetic and structural properties of the pseudobinary Laves phase rare earth (R) 3d transition series (B) intermetallic compounds of type RB_2. In chapter 2 a review of the reported magnetic and structural studies on these compounds is given.

Chapter 3 is confined to some basic theory of ferrimagnetic materials and the foundations for crystal field calculations. The more commonly known theories such as molecular field theory of ferromagnetism have merely been

referred to in order to conserve space.

In the fourth chapter the apparatus designed and constructed by the author is described in some detail and in chapter five the experimental results are presented in tables and graphs and a description of the specimen preparation and examination is included.

Finally in chapter six the results are discussed and accounted for. Two appendices follow the last chapter containing electronic circuits and the computer programmes utilised in the work.

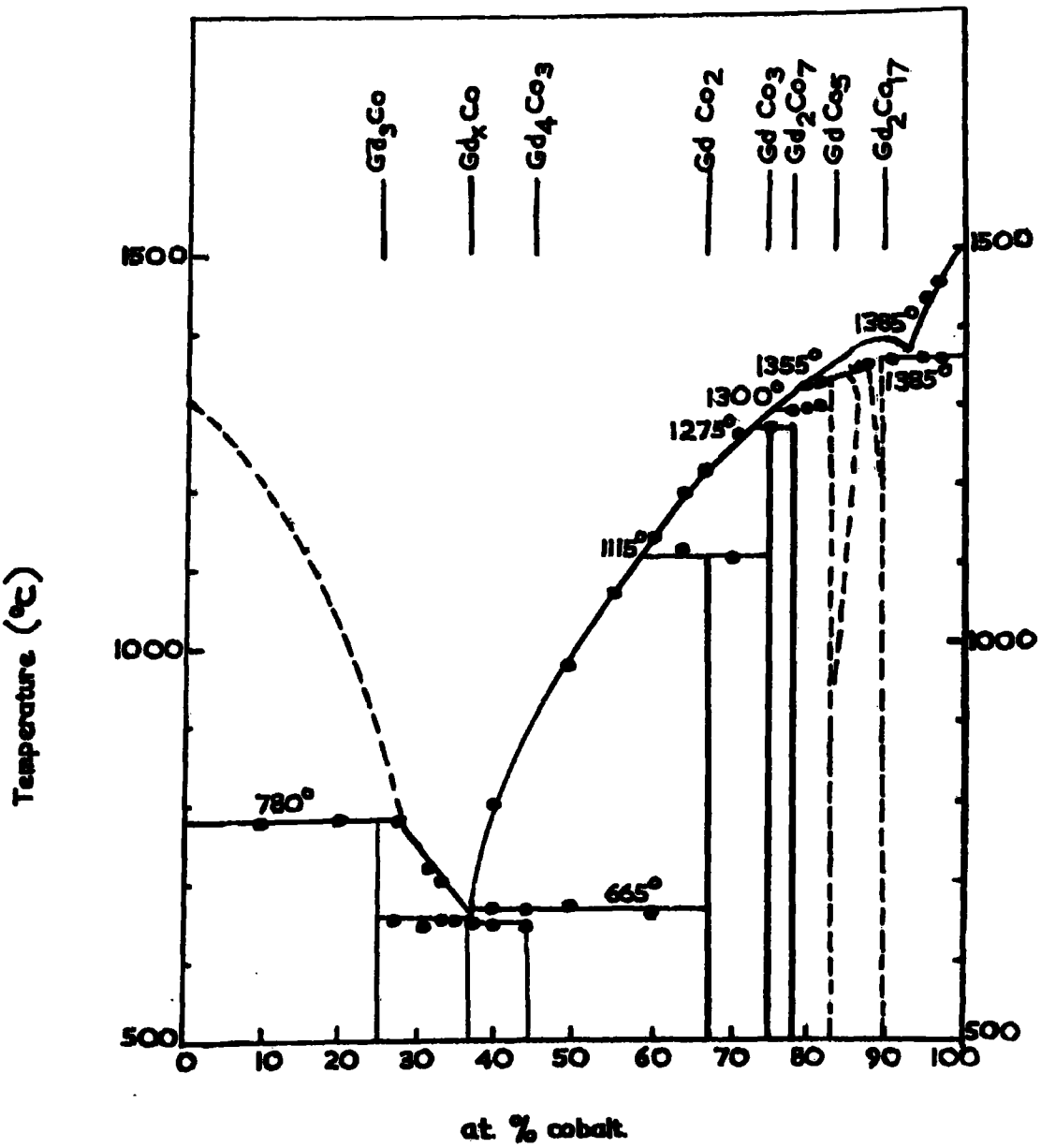

FIG. 2.1 GADOLINIUM – COBALT PHASE DIAGRAM.

CHAPTER 2

THE RARE EARTH-TRANSITION METAL LAVES PHASE COMPOUNDS

2.1 Introduction

The fourteen rare earth elements may be combined with metals of the 3d, 4d and 5d transition series to form a prolific number of compounds. The study of the magnetic properties of these compounds began initially in d.1960, when pure rare earth metals became more readily available, in the hope that suitable alloying might yield materials with the high Curie temperatures of the iron group elements and also the large atomic magnetic moments associated with the rare earths. The phase diagrams for the systems are rich in compounds for the four 3d elements to the right of chromium in the periodic table (i.e. Mn, Fe, Co, and Ni). However, there is only one stoichiometry common to all four elements and that is the RB_2 compound, in which R is the rare earth and B the transition metal. The RB_3 and R_2B_{17} are the next largest family of compounds since they form with Fe, Co and Ni only. The largest overlapping group of compounds are formed with Co and Ni and among these the structures of the AB_5 and A_2B_7 stoichiometries are related through plane displacement and atomic substitution.

In fig. 2.1 is shown the phase diagram for the Gd-Co system and the large number of compounds that form can be seen. The early measurements (refs. 2.1 - 2.4) of the variation of magnetisation with composition for the iron and cobalt compounds revealed deep minima in the vicinity of, for example, $\sim$ 25% Gd concentration for the Gd - Co system (see fig. 2.2 after ref. 2.5). The indication of these studies was that the two types of magnetic moments were coupled antiparallel in the heavy rare earth (HRE) compounds giving

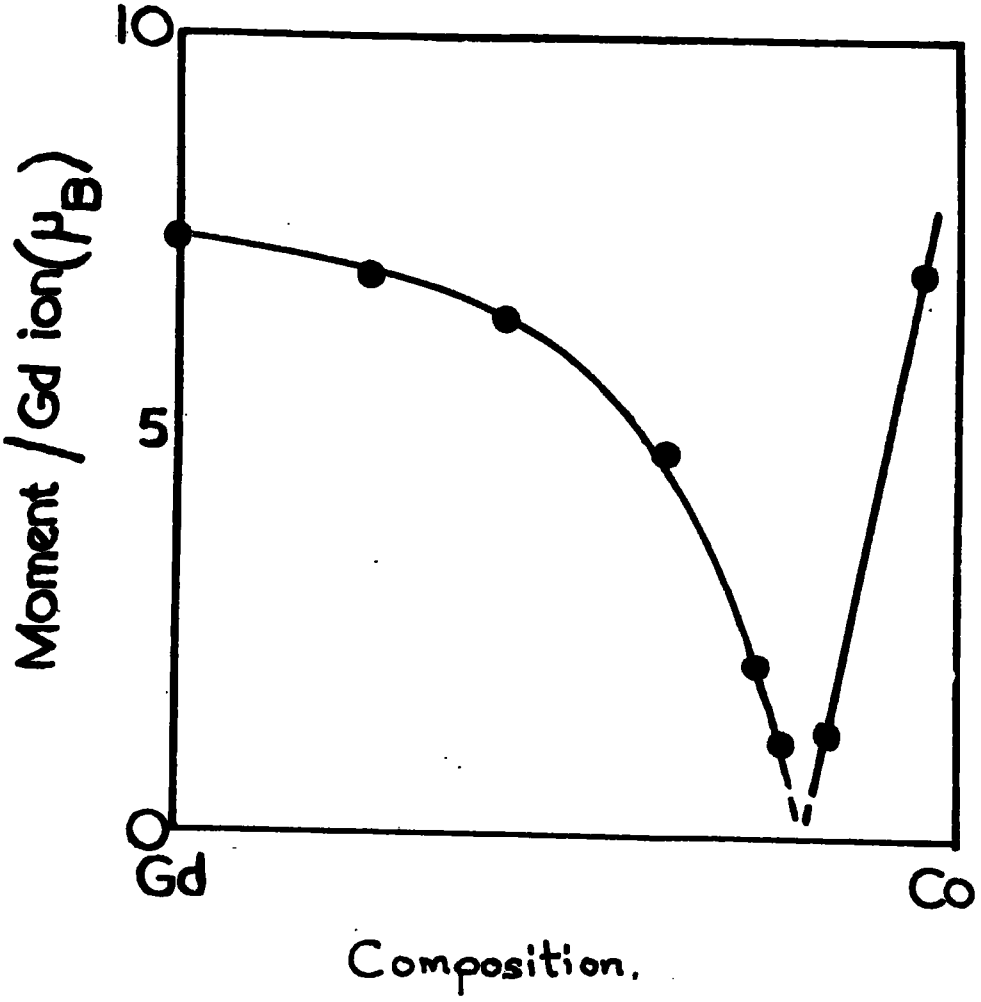

FIG. 2.2. MAGNETIC MOMENT OF THE COMPOUNDS IN THE Gd–Co SYSTEM.

ferrimagnetism, and with the light rare earth (LRE) compounds the moments are parallel giving ferromagnetism (refs. 2.3, 2.6). The search for technologically useful materials has been successful despite this set back with the $SmCo_5$ type compounds which have very high anisotropy giving enormous coercivity and also large energy product (as much as $\sim$ 30 M gaussoersted), however the magnetic moment is derived almost entirely from the transition metal and the possible advantage of the high moments of the HREs has been forfeited. Of all the possible stoichiometries, the RB_2 structure is the simplest, crystallizing in one of the Laves phases which are either cubic or hexagonal, and the structure of compounds on either side of the RB_2s becomes progressively more complex. It is the relative simplicity of the RB_2 structure together with the vast number of related compounds (including the 4d, 5d series and dialuminides etc.) which form in Laves phases, that make the system ideal for extensive theoretical and experimental studies, and indeed the majority of the work on the rare earth intermetallics has been directed at the RB_2s. The factors relating to the formation of the Laves phases and a review of some of the magnetic properties of the dialuminide and 3d transition metal Laves phases are given in the remainder of this chapter. A comprehensive review of the rare earth-intermetallic compounds is given in ref. 2.7.

2.2 Formation and Stability of Laves Phases (RB_2)

The Laves phases denote a large group of related intermetallic compounds, RB_2, having one of the following structure types (i) $MgCu_2$ (C15, cubic), (ii) $MgZn_2$ (C14, hexagonal), or (iii) $MgNi_2$ (C36, hexagonal). The cubic

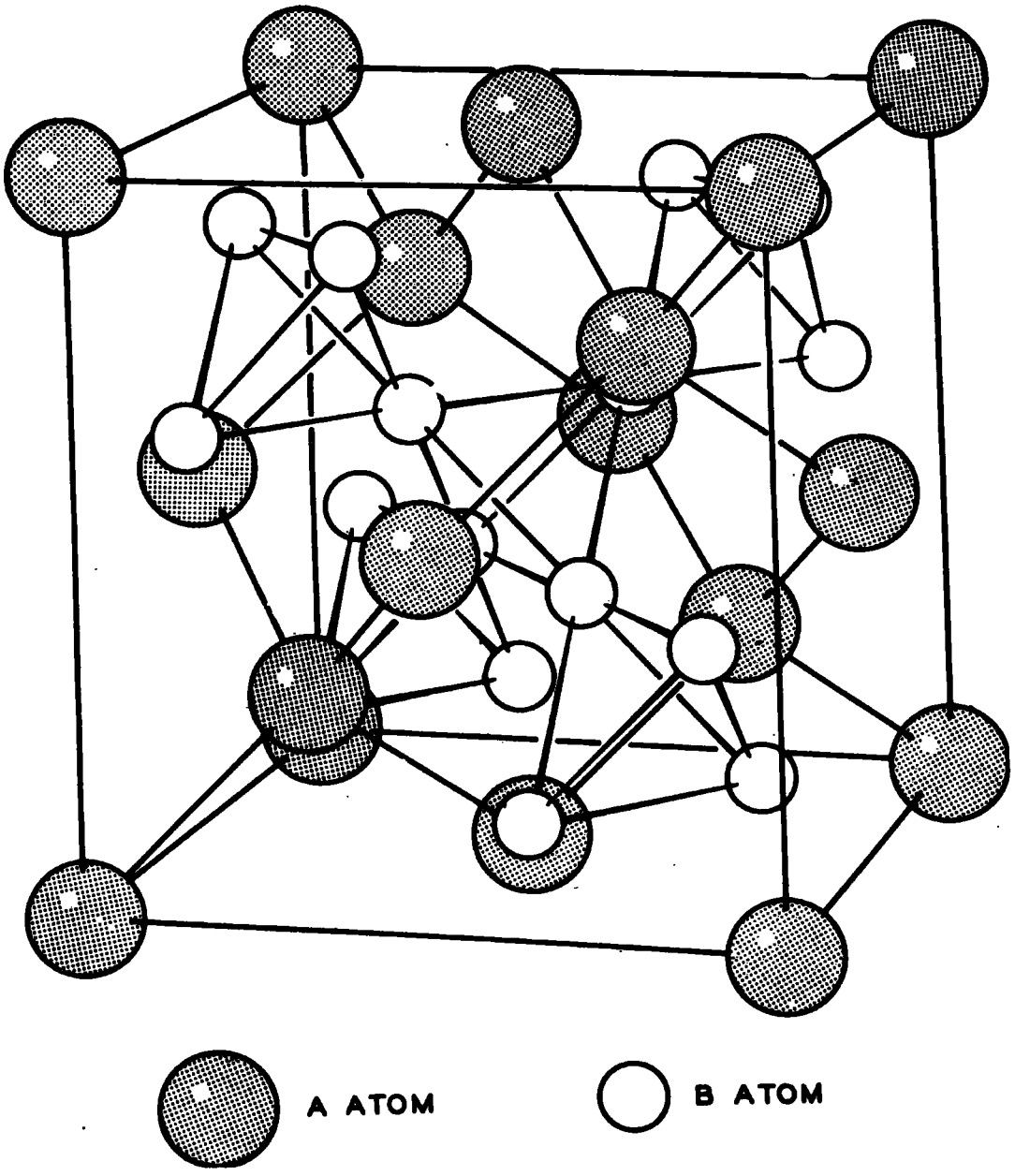

FIG. 2.3 C15 Laves Phase Structure

phase is represented in fig. 2.3 and can be regarded as two interpenetrating lattices of R and B atoms. The B atoms lie at the corners of tetrahedra joined at the points, the spaces in between the matrix of tetrahedra are filled with the larger R atoms in a diamond array. There are 8 formula units (24 atoms) per unit cell in the cubic phase. The C14 hexagonal ($MgZn_2$) phase contains 4 formula units per unit cell and the C36 hexagonal ($MgNi_2$) phase contains 8 formula units per cell. The three structures are closely related; the R atom structures can be considered in terms of the stacking of three double layers (A, B, and C) of hexagonally arranged R atoms. The stacking sequences for the $MgZn_2$, $MgCu_2$ and $MgNi_2$ structures are then ABAB..., ABCABC..., and ABACABAC... respectively, the last structure may be considered as an intermediate state between the other two.

The Laves phases are very close packed structures and clearly one of the main considerations for the formation of the phases will be the size ratio between the R and B atoms (ions). The pioneer work on these structures was performed by Laves (refs. 2.8, 2.9), who extended the ideas of Goldschmidt (ref. 2.10) on the importance of radius ratios. On the basis of a hard sphere model with A atoms in mutual contact, the ideal size ratio (ion ratio) is $r_a/r_b = 1.225$ for all three Laves phases (demonstrating their similarity). In existing compounds the ratio of the Goldschmidt radii of the pure elements varies from 1.05 - 1.68 but the effective radius ratio is nearly always within the range 1.1 - 1.3 by size adjustment of the elemental radii. It is generally thought (ref. 2.11) that the radius ratio is not effective in determining which of the phases will preferentially form, but rather that it is the electron

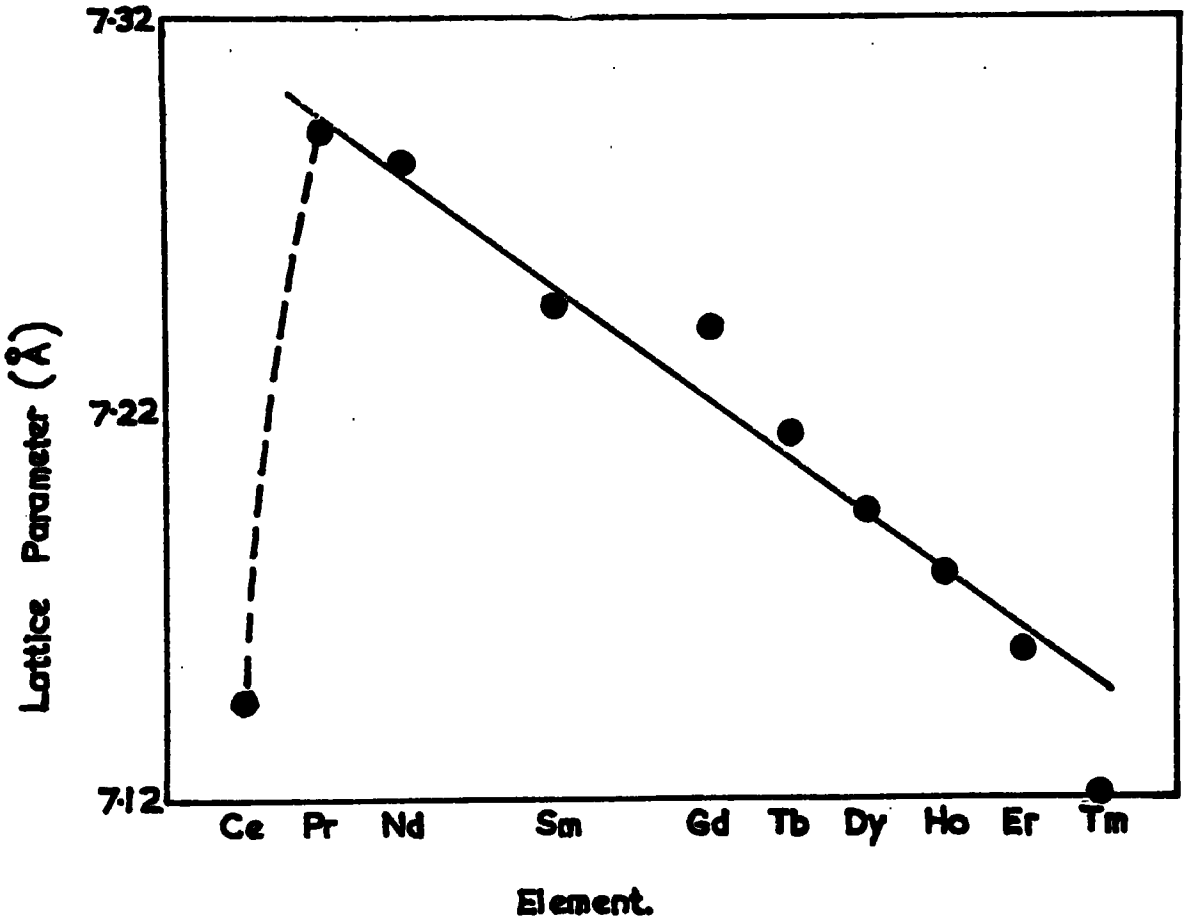

FIG. 2.4 LATTICE PARAMETERS OF THE RCo_2 COMPOUNDS.

per atom ratio which is the dominant factor in this respect. This ratio is known better perhaps as the valence electron concentration (vec) and refers to the average number of valence electrons per atom in the structure. Hume-Rothery (ref. 2.12) first demonstrated the importance of vec in relation to structure stability in the phase diagrams of Cu, Ag and Au alloyed with Sn, Zn, and Cd. The basis of this process lies in the differing bandstructure (ref. 2.13) associated with each phase since the most stable configuration will be that for which the Fermi energy (E_f) is lowest. This consideration requires that there be a large density of states (at the given vec considered) at the E_f. It appears from the work of Laves and Witte (ref. 2.14) on the prototype phases that the cubic (C15) phase is stable for a vec in the range 1.33 - 1.75, however for a vec above this range the density of states falls for this structure and the C36 hexagonal phase is favoured for a vec range of 1.8 - 1.95. The C14 structure is stable for a small range of vec at $\sim$ 2.00 and above this range in general reverts to the cubic phase. At vec values intermediate to these ranges two phase materials are formed. It should be stressed, however, that even a correct size ratio and vec do not guarantee the formation of a Laves phase, for example although the conditions are apparently favourable for the RCu_2 compounds these do not form Laves phases. The implication is that there are further factors to be assessed in deciding the possibility of formation of a stable phase. One further aspect of the RB_2 phases is their very high coordination, for example in the $MgCu_2$ phase the R atoms are coordinated to four more equidistant A atoms and twelve B atoms at a slightly smaller distance giving an effective coordination of 16. The overall average coordination for the phases is $13\frac{1}{3}$.

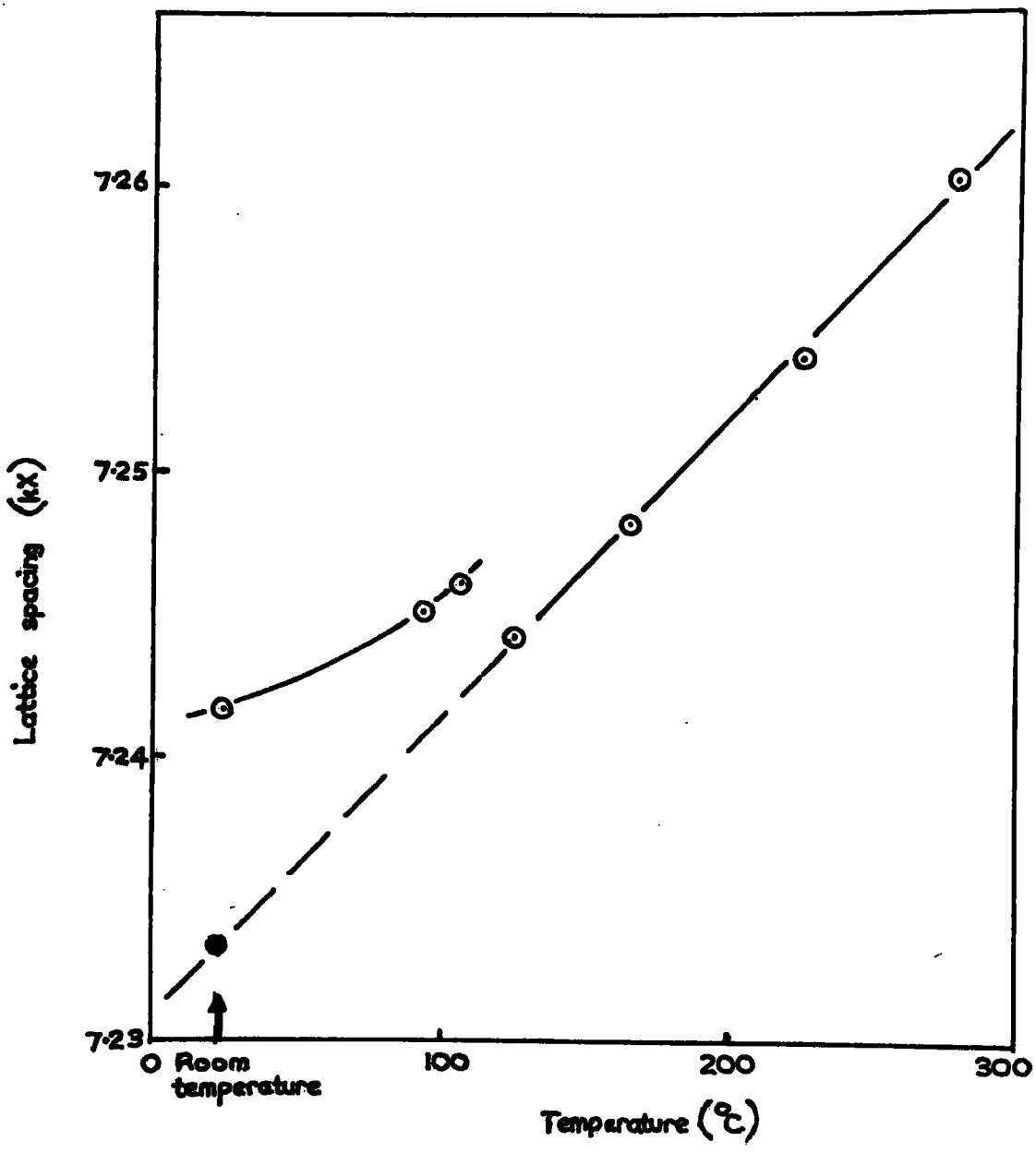

FIG. 2.5. LATTICE EXPANSION OF $GdCo_2$.

2.3 Structural Properties of the RB_2's with 3d transition metals

Reference to the Gd-Co phase diagram of fig. 2.1, shows that the RB_2's form peritectically and this has resulted in some diversity in the reported results of both structural and magnetic studies, due to the presence of second phases in the compounds. It is possible to achieve better specimens by careful annealing but it is very difficult to eliminate all traces of second phases.

The lattice parameters of the RB_2's (with Fe, Co or Ni) show the usual Lanthanide contraction as is seen in fig. 2.4 for the cobalt series. The Cerium compound shows a large negative deviation from the expected value and this is associated with the loss of the one 4f electron of Cerium to the conduction band leaving the ion quadripositive (ref. 2.15a). The generally peculiar properties of intermetallic compounds containing Cerium arise from the ease with which Cerium can lose its 4f electron leaving the average Cerium ion with a charge between 3+ and 4+. The anomaly associated with $GdCo_2$ is associated with magnetostrictive expansion caused by the material being ordered at the measuring temperature. Fig. 2.5 shows the expansion vs temperature curve for $GdCo_2$ (ref. 2.15b) and the discontinuity at the Curie temperature (412K) is clearly seen. The extrapolation of the high temperature spacing to room temperature gives a 'nonmagnetic' spacing for $GdCo_2$ in much closer agreement with the Lanthanide contraction prediction. Further evidence for a 'nonmagnetic' spacing at room temperature in agreement with the expected results comes from Pseudobinary studies of systems like (GdY) Co_2 (ref. 2.16). Chatterjee and Taylor (ref. 2.17) have observed a general expansion of the

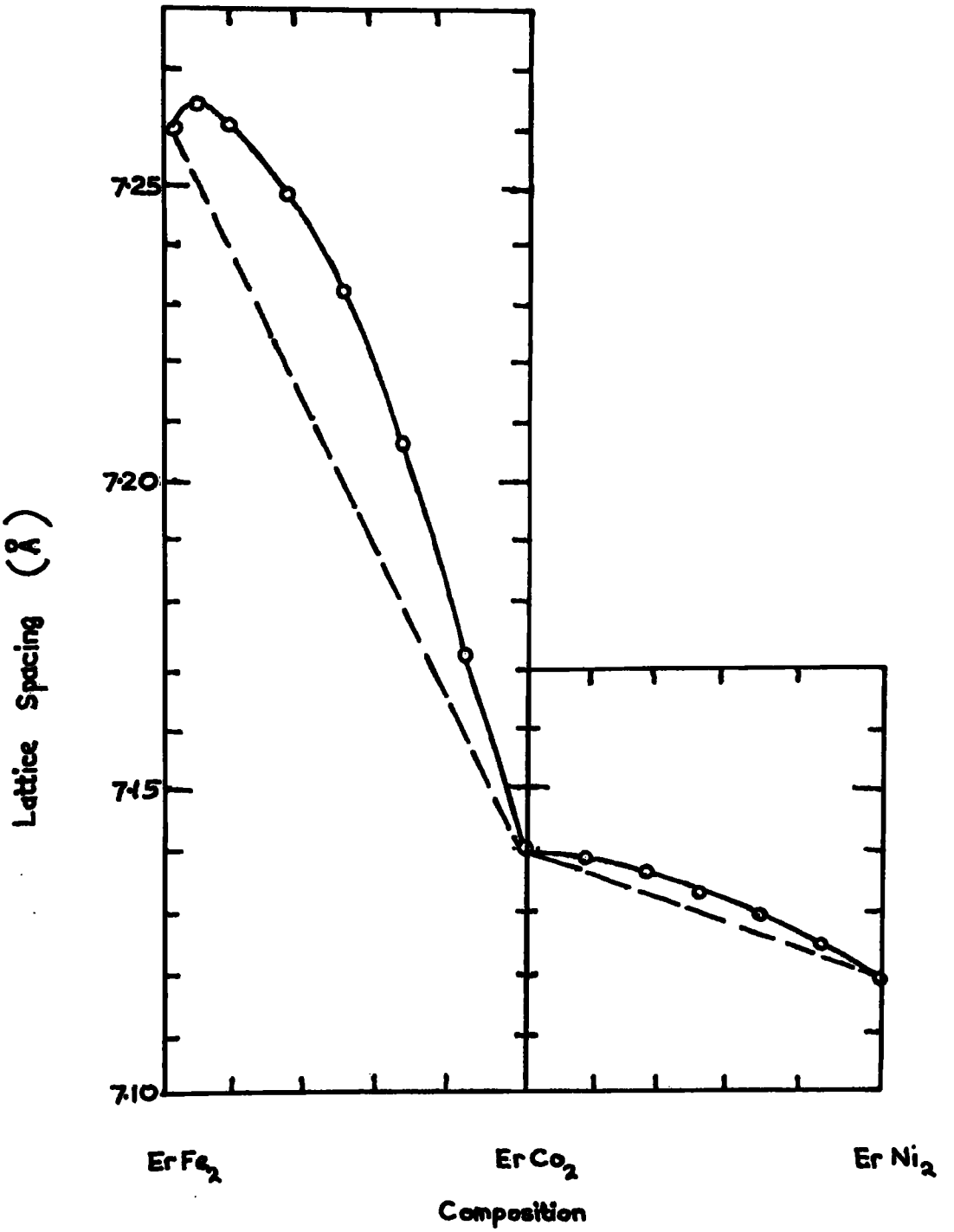

FIG. 2.6. LATTICE PARAMETERS FOR THE ErB_2 COMPOUNDS

lattice upon magnetic ordering with the HRE RCo_2 compounds.

The lattice spacings of the pseudobinary and terminal compounds of the series Er Fe_2 - Er Co_2 - $ErNi_2$ are given in fig. 2.6 and these results show that the iron compounds have larger lattice spacings than the cobalt or nickel compounds by approx. 2%, and that the nickel compounds are slightly smaller than those with cobalt by approx. 0.3%. The pseudobinary series in general show positive deviations from Vegards Law (linear interpolation between the terminal compounds) with the exception of some of the gadolinium compounds where the anomalous behaviour is simply associated with the ordering effects mentioned above. Attempts at making pseudobinary systems between nickel and iron $R(Fe-Ni)_2$) (ref. 2.15, 2.16) have resulted in two phase specimens in part of the intermediate region, the second phase being the hexagonal C36 type. Since the type of Laves phase is not determined by size effects but rather by the vec, and in the case of the $R(Fe-Ni)_2$ compounds the change in vec is similar to that in going via the RCo_2 compound, reason for the formation of the C36 phase is obscure. Oesterreicher and Wallace(ref. 2.18) in studies on the systems $Gd(Fe,Al)_2$ and $Gd(Co,Al)_2$ and $(Er(Co,Al)_2$ showed the effect of the changing vec on the structure, where they observed the presence of the C14 hexagonal phase in the intermediate ranges. Their magnetic results are discussed in the next section.

The RMn_2 compounds have received the least attention of the 3d compounds with most of the work limited to studies with the heavy rare earths (ref. 2.19). The preparation of the manganese compounds appears to be more affected by second phases in the usual methods of manufacture (arcmelting, induction melting etc.) and the compounds have successfully been prepared using a complicated

amalgam process.

The RAl_2 compounds also crystallize in the Laves phases with lattice parameters closely comparable with the RNi_2's and as such are useful in studying the RB_2's with a nonmagnetic partner. These compounds are discussed in the next section. A complete table of lattice parameter data may be found in ref. 2.7.

2.4 Magnetic Properties

2.4.1 Rare Earth-dialuminides (RAl_2)

Before discussing the 3d transition metal Laves phases it is useful to consider the RAl_2's in which the rare earth ion alone carries a magnetic moment, since the properties of these compounds may be used in relation to the more complex 3d compounds.

The rare earth dialuminides all show ordered behaviour (ref. 2.20) with the exceptions of $LaAl_2$, $LuAl_2$ and $YbAl_2$, not surprisingly in this last compound the Yb is divalent and hence its 4f shell is full. $CeAl_2$ has been shown to be antiferromagnetic with a Néel temperature below 4K (ref. 2.21). Magnetostatic measurements on the other compounds indicate a ferromagnetic rare earth spin structure but with the ordered magnetic moments as much as 20% below the free ion value (gJ). The behaviour in the paramagnetic region gives an effective moment in accordance with the theoretical value of $g\,(J(J+1))^{\frac{1}{2}}$. The usual RKKY theory, (see e.g. ref. 2.7), as applied to the indirect coupling in the rare earth metals, predicts that the ordering temperatures should be proportional to the de Gennes function

$(g-1)^2 J(J+1)$ provided that the exchange is via polarisation of the conduction electrons. The Curie temperatures of the heavy rare earths show reasonable agreement, the light rare earths are only fair and these results are taken to imply that the exchange interaction is fundamentally of the RKKY type. Prior to the magnetostatic results, Jaccarino et al. (ref. 2.22 and 2.23) were able to determine both the magnitude and sign of the conduction electron polarisation at the Al site using the Knight shift of the Al^{27} nmr and at the rare earth site using the g-shift in e.p.r. studies. The results of these studies showed that there is a negative interaction between the rare earth spin (S) and that of the conduction electrons (s_e). It should be pointed out that the effectiveness of the parallel coupling of the rare earth spins via polarisation of the conduction electrons is independent of the actual sign of this polarisation. Further evidence for the ferromagnetic coupling of the rare earth spin angular momenta arises from work on the (Gd,Nd) Al_2 system (ref. 2.20) in which ferrimagnetism is observed. The light rare earths have J = L-S and hence if ferromagnetic coupling of the spins (S) occurs the net Nd moment ($\propto$ J) will be antiparallel to that of the Gd ion.

The reduced moment values have been attributed to the effect of the crystal field on the (2J+1) degenerate multiplet of the rare earth ion. This phenomenon was first treated by Bleaney (ref. 2.24) to account for the similar behaviour observed in the RNi_2's but may be applied directly to the RAl_2's because of the similarity in lattice parameter. The crystal field lowers the degeneracy of the ionic state and together with the exchange field

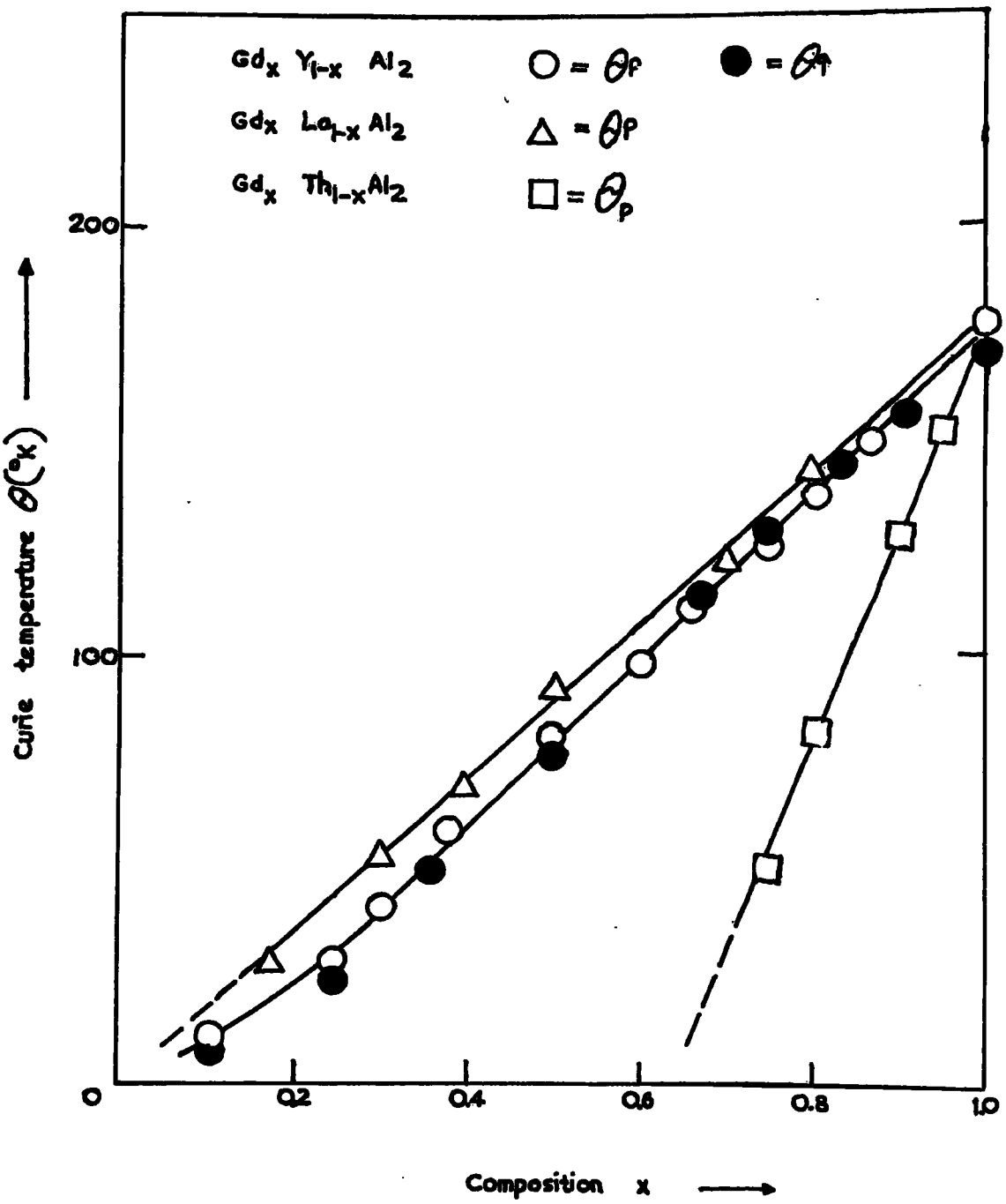

FIG 2.7. CURIE TEMPERATURES FOR THE Y, La, & Th, SUBSTITUTED $GdAl_2$ COMPOUNDS.

causes mixing of the nondegenerate states to produce a quenched magnetic moment. This process is treated in detail in chapter 3, section 3.3 The original calculations were crude insofar as they included the exchange field as a perturbation whereas this field is often comparable to,or larger than,the crystal field. Furthermore, only the 4th degree crystal field terms were used together with the assumption that the easy axis of magnetisation is the 100 direction. This assumption is certainly not justified in the case of the RFe_2 compounds (see next section). Support for the presence of fairly large crystal field effects has come from low temperature specific heat measurements (ref. 2.25). The results of neutron diffraction studies on $DyAl_2$, $NdAl_2$ and $PrAl_2$ (refs. 2.26, 2.27) have indicated rare earth moments that are considerably greater than those obtained from the magnetostatic work implying that the crystal field effects are not as large as was thought. Furthermore, the $DyAl_2$ spectra were best fitted by some weak helical antiferromagnetic ordering over and above the existing ferromagnetic spin structures.

Pseudobinary work (ref. 2.28) on the compounds $GdAl_2$, $TbAl_2$ and $ErAl_2$ with the rare earth partially substituted by Y, La or Th have shown that the interactibn in the RAl_2's is of the RKKY type. Fig. 2.7 shows the results for the three substitutions in $GdAl_2$. The Curie temperature shows a linear decrease to zero with increasing Y or La content as may be predicted on simple dilution of the rare earth sublattice. The effect of substituting quadripositive thorium is to increase the number of conduction electrons and hence the Fermi energy E_f and Fermi momentum k_f leading to a

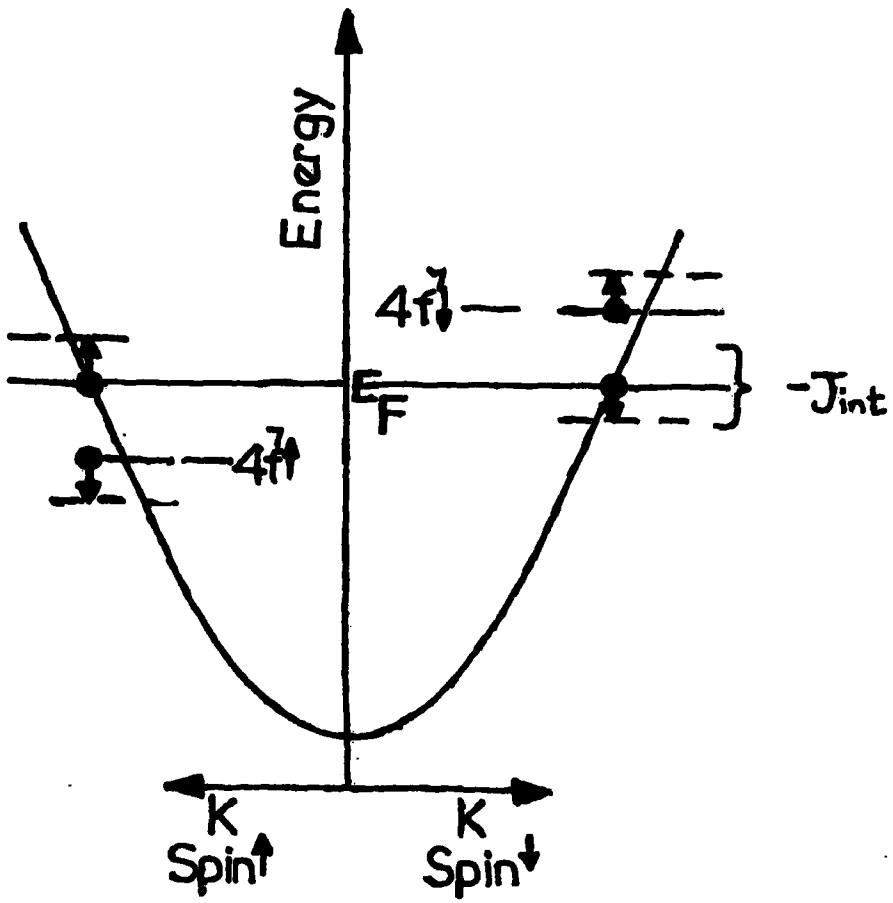

FIG 2.8. INTERBAND MIXING EFFECT FOR GADOLINIUM.

decrease in the Curie temperature from which both k_f and J_{sf}, the rare earth conduction electron exchange interaction, can be estimated. The negative exchange interaction J_{sf} found in this way compares favourably with the results from the Knight shift and e.p.r. studies (refs. 2.22, 2.23) although the former technique relates to the conduction electron polarisation seen by the Al^{27} nucleus. (Work on $GdAl_2$ has given very similar results for the J_{sf} obtained by each technique). Further evidence for the relative magnitudes of J_{sf} arises from the results of spin disorder resistivity (refs. 2.29, 2.30) and the reduction of the superconducting transition temperature in $LaAl_2$ by addition of the magnetic rare earth elements (ref. 2.31). Recently (ref. 2.32) a positive g-shift has been reported for e.p.r. in Gd doped $LaAl_2$ implying that J_{sf} is positive.

Although the magnetic results have shown that an RKKY type of interaction is responsible for the observed properties, it should be pointed out that a negative value for J_{sf}, the exchange integral, is incompatible with simple RKKY theory since this integral is of its nature positive. This dilemma has been qualitatively resolved (and possibly quantitatively if the theoretical values used in estimation and also the experimental analysis can be improved) by Watson et al. (refs. 2.32, 2.33) using an effective exchange constant, J_{eff}, comprising the J_{sf} of the RKKY interaction and a further interaction, J_{int}, arising from the effects of interband mixing. This process may be qualitatively understood by referring to fig. 2.8 which applies to Gd with a half filled 4f shell. It depicts a simple unmagnetised conduction band with the Fermi level E_f, with a highly localised 4f spin↑band lying well below

this level. The unoccupied 4f↓ orbitals are represented by the narrow band above E_f. A conduction electron state of spin ↑ just above E_f will, in general, have a non-zero matrix element $\langle \phi 4f | h | \psi_K \rangle$ with an occupied 4f ↑ wave function, causing mixing of the two states. The result of this interaction is to raise the energy of the state at the Fermi surface and cause the 4f ↑ to acquire a certain amount of conduction electron character - this is called an Emission process. The reverse process (absorption) occurs for the unoccupied 4f ↓ states which mix with the occupied conduction electron spin ↓ states giving them a 4f character and lowering their energy. The net result of this interband mixing is to upset the conduction electron spin populations giving an increase in the number of spin ↓ electrons at the expense of the spin ↑ electrons. The polarisation so produced is in opposition to that produced by the RKKY interaction which affects the spin ↑ electrons alone, by decreasing their energy, and hence polarising them towards the spin ↑ state. As a result the effective exchange, J_{eff}, may be of either sign depending upon which interaction is dominant. Recent studies of the Knight shift and magnetic susceptibility on the rare earth copper compounds (RCu) (ref. 2.34) have clearly shown that an RKKY interaction plus interband mixing are consistent with the experimental results. The interband mixing causes a decrease in the observed moment in magnetostatic measurements and it may be that the reduced moments in the RAl_2's, originally attributed to crystal field effects, are entirely due to this process. It is more likely however, that the two effects both play an important part in determining the observed moment in these compounds.

2.4.2 Rare earth-3d Transition metal AB_2's

The replacement of the aluminium ions by one of the magnetic iron group transition metals (Mn, Fe, Co, or Ni) will complicate the magnetic interactions and also, depending upon the particular 3d-element, vary the valence electron concentration. We shall consider the RNi_2, RCo_2 and RFe_2 compounds (and RMn_2) finally discussing the various pseudobinary systems.

In the paramagnetic state, the nickel compounds exhibit Curie-Weiss behaviour except for the compounds $CeNi_2$, $LuNi_2$ and $SmNi_2$ (ref. 2.35). The first two of these three compounds are Pauli paramagnets the Cerium being quadripositive in the latter having lost its 4f electron to the conduction band. The anomalous behaviour of $SmNi_2$ may be attributed to excitation into the next $J = {}^7/2$ multiplet of the Sm ion (g.s.$J = {}^5/2$) since the multiplet separation in this particular case is approximately equal to kT for T about room temperature. The fact that $LuNi_2$ and $Y Ni_2$ exhibit temperature independent susceptibility implies that the Ni ions carry zero magnetic moment since in Lu the 4f shell is full and Y has no 4f electrons. The saturation magnetic moment of $GdNi_2$ further supports the idea of zero nickel moment since the measured moment is very close to the Gd free ion value (gJ). Neutron diffraction studies (ref. 2.36) on the $TbNi_2$ have been unable to detect any nickel moments so that it is generally assumed that the nickel is in the nonmagnetic $3d^{10}$ state by electron transfer from the conduction band. (The fact that this process requires 4 electrons, 2/atom of Ni, makes it hard to justify, see later). The saturation moments of the rest of the RNi_2's may then be associated purely with the rare earth component (including the induced conduction electron polarisation, of course) and on this basis it is

found that the moments are reduced to a similar extent as was found in the RAl_2 compounds. As before, Bleaney (ref. 2.24) attributed this reduction to the affect of the crystal field on the rare earth ion assuming that the easy axis of magnetisation is the 111 axis. On the simple model Bleaney put forward, the maximum and minimum moments of the rare earth ion were estimated by including the exchange field as a perturbation which causes mixing of the already crystal field split levels. This procedure is not very satisfactory since the exchange field is often too large to consider as a perturbation (see Ch. 3), however, the predicted quenching of the rare earth orbital angular momentum gives a range of magnetic moments which are of the correct magnitude, showing that crystal field effects are most likely to be an important factor in these compounds.

The Curie temperatures of the RNi_2's when plotted against the de Gennes function follow two straight lines, one for the heavy and the other for the light rare earths. As in the RAl_2 series this is taken to indicate that the magnetic interaction is RKKY in origin.

The saturation moments of the cobalt and iron compounds with gadolinium have values of $5.09\mu_B$ (author's results) and $3.35\mu_B$ respectively and since the gadolinium moment must be of order $7\mu_B$ (it is an S-state ion and its magnetic moment is unaffected by the crystal field) then the transition metals must have antiparallel moments of order $1\mu_B$ for Cobalt and $1.8\mu_B$ for Fe. The rest of the heavy rare earths show results consistent with this picture of ferrimagnetic structures, the light rare earths however are interpreted in terms of ferromagnetic coupling of the moments. Wallace (ref. 2.37) gives a

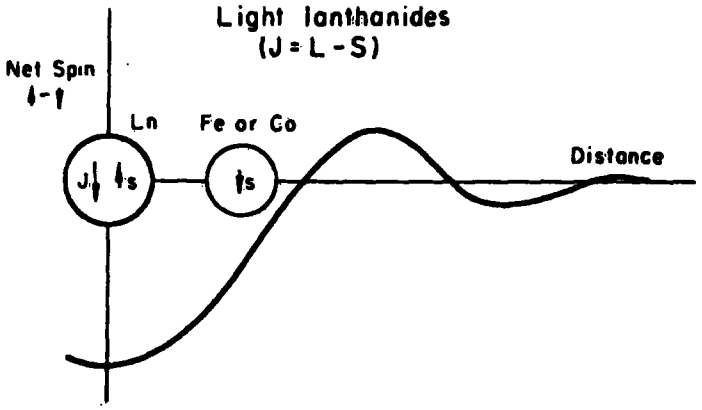

Schematic representation of the pairwise interaction of a light rare earth with Fe or Co through the polarization of the conduction electrons. The coupling aligns the spin vectors antiparallel but since J and S are opposed for light rare earths the magnetic coupling is ferromagnetic.

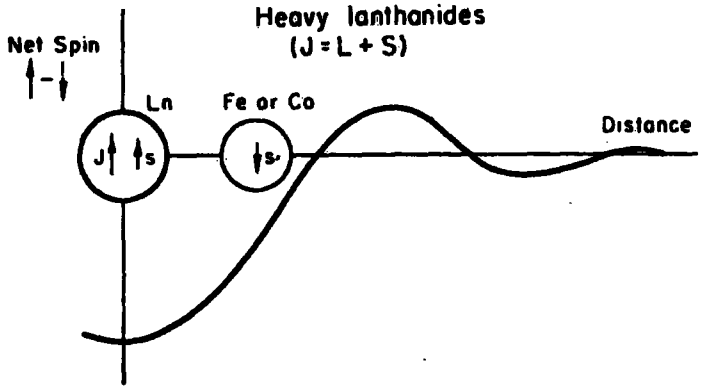

Schematic representation of the interaction of a heavy rare earth ion with Fe or Co. Since J and S in this case are parallel, the interaction produces antiferromagnetic coupling.

FIG 2.9. WALLACE'S COUPLING THEORY FOR THE RFe_2 AND RCo_2 COMPOUNDS

reasonable account of the process and it is reproduced here. The results of the g-shifts on RAl_2 compounds show that the spin polarisation wave has a negative value at the rare earth site. The work of Stevens (ref. 2.38) has shown by Mössbauer studies, that Fe interacts with the conduction electrons to give a polarisation parallel to the iron moment and the situation for Co is presumably similar. The shape of the spin polarisation wave is given by the RKKY theory and the amplitude at the rare earth centre is known, however the first cycle wavelength has to be determined. Information comes immediately from the nmr results cited earlier for the RAl_2 series. These show that the negative polarisation extends, or possibly is negative again, out to the Al site. It is reasonable however to assume that the polarisation wave is still on its firstchalf cycle since the R-Al distance is only $\sim$ 10% greater than the R-R distance. With these assumptions in mind it is possible to construct the picture shown in fig. 2.9., after Wallace, for the light and heavy rare earths. As before the effectiveness of the coupling does not depend on the sign of the polarisation which could just as well be positive as it is in the rare earth metals (it is, of course, necessary that the first cycle wavelength be of the same value). The resultant structures arrive immediately from the fact that the net J in the light rare earths is given by J = L-S, whereas in the heavies J = L+S.

Bearing this structure in mind and assuming constant Co and Fe moments (see neutron diffraction results later in this section) it is possible to estimate the rare earth moments from the saturation moment data. The conduction electron polarisation is ignored in these estimations but is not

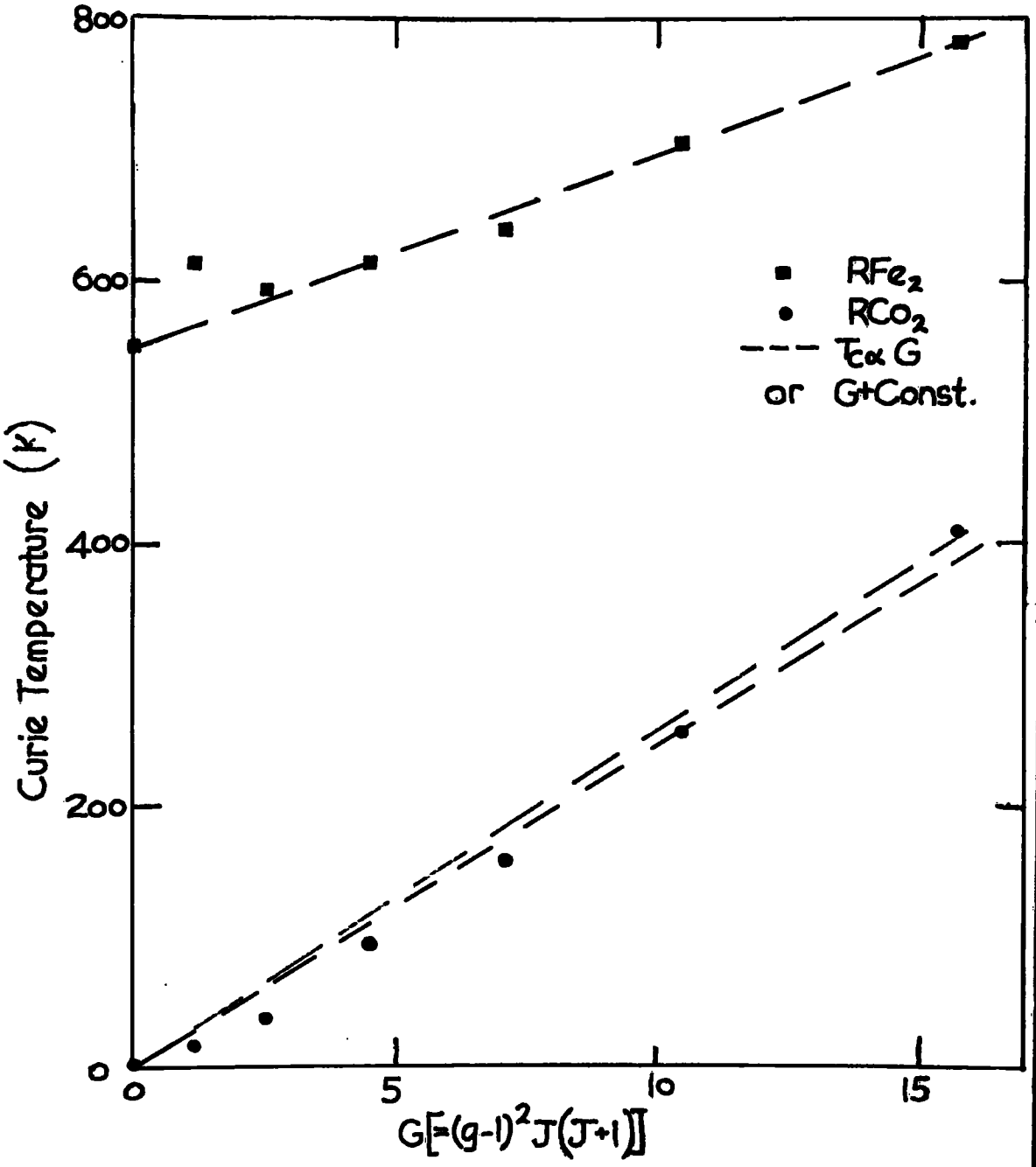

FIG. 2.10. CURIE TEMPERATURE Vs DE GENNES FUNCTION

expected to be much greater than $\sim$ a few tenths of a Bohr Magneton. For the cobalt series the rare earth moments are reduced from the free ion values and are taken to be crystal field quenched. The crystal field effects are smaller in the cobalt compounds for two reasons. Firstly, the cobalt is probably more charged than the nickel thereby reducing the B_4 and B_6 crystal field coefficients (see chapter 3 section 3.4) and secondly, the lattice parameters of the cobalt series are larger than those of the nickel compounts causing a further reduction of the crystal field coefficients in which the lattice parameter appears as a $\frac{1}{a^5}$ term in B_4, $\frac{1}{a^7}$ for B_6 . The spacing difference between the iron and cobalt compounds is a factor of $\sim$ 10 greater than the difference between the cobalt and nickel series. This, together with the smaller degree of electron transfer in the iron compounds, results in almost negligible crystal field effects for these compounds, so that the rare earth moments are in general taken as the free ion values. The moment associated with the iron varies quite considerably - from 2.2 μ_B in $DyFe_2$ through 1.45μ_B in YFe_2 to 0.55μ_B in UFe_2 (which is a C15 Laves phase compound).

The Curie temperatures of the Cobalt and Iron series are shown plotted against the de Gennes function in fig. 2.10, where the fit for the Cobalt series can be seen to be fairly good. A reasonable fit is obtained for the iron compounds provided that a constant is added onto the equation, this constant representing the Fe - Fe interaction given by the intercept on the T axis at G = 0. The Curie temperature of YFe_2 which corresponds to G = 0 is 550K in excellent agreement with the predicted value. The similar compound for the cobalt series has zero as the intercept and indeed the prevailing evidence is that YCo_2 is non magnetic although it was thought to be anti-

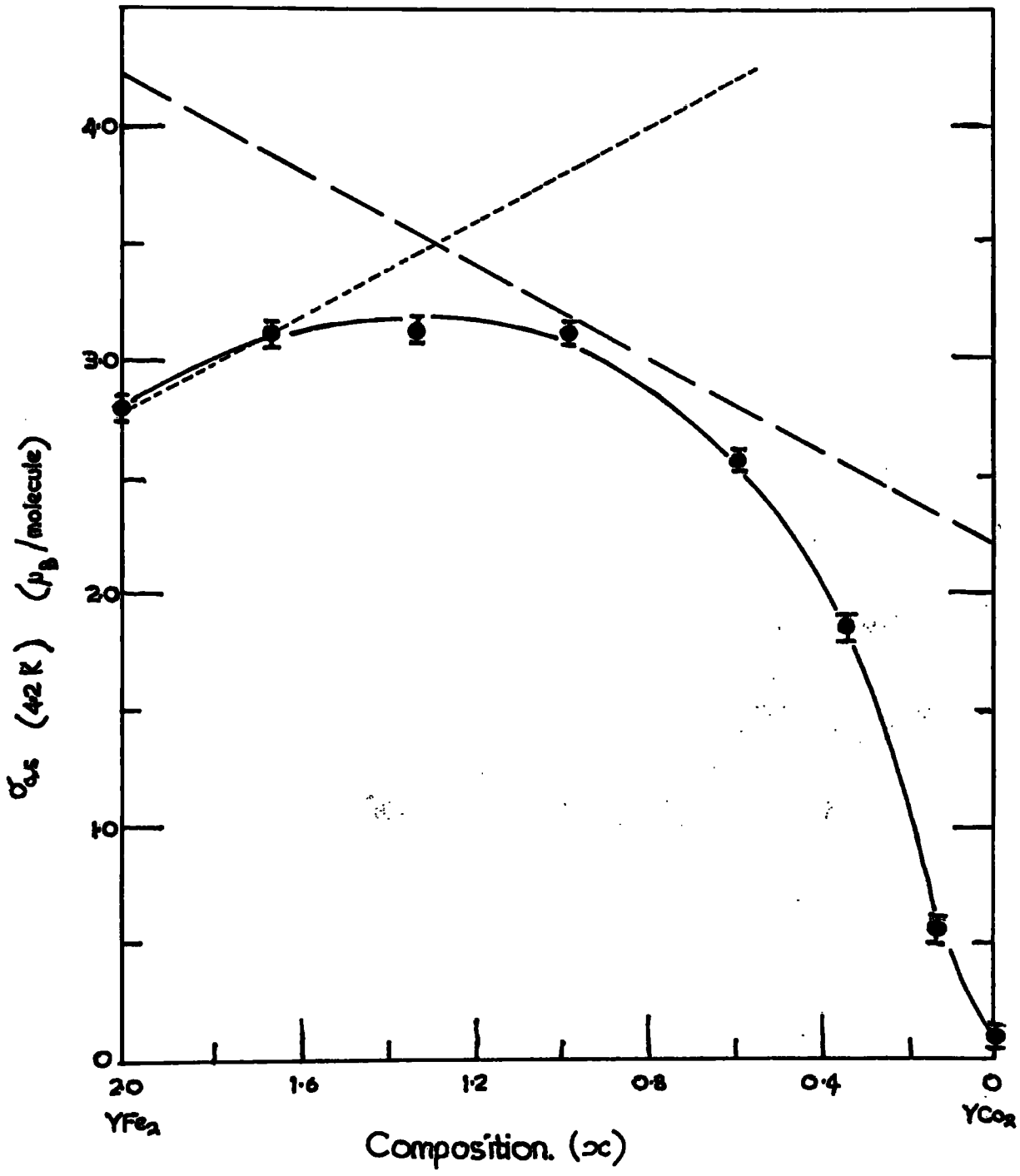

FIG. 2.11. SATURATION MAGNETISATION FOR Y $Fe_{2x}Co_{2-x}$.

ferromagnetic (see refs. 2.39, 2.40) at one time.

The nature of the transition moment has for some time been a matter for contention, arguments being proposed in favour of both a localised moment and an itinerant electron moment. Pseudobinary studies on the systems $(DyY)Fe_2$ and $Gd(CoNi)_2$ (refs. 2.41, 2.42) have favoured the latter model. These compounds show a nonlinear variation of the transition metal moment (μ_T) with composition and, further the moment changes appreciably over quite small ranges of composition, a fact that is incompatible with the simple electron transfer effects to be associated with the variation. The observed behaviour was explained on a model in which the 3d electrons form a band giving rise to an itinerant electron moment. These studies have been extended to include the system $Y(Fe,Co)_2$ (ref. 2.43, 2.44) and also $Zr(Fe,Co)_2$ (ref. 2.45). The magnetic results of the $Y(FeCo)_2$ series are shown in fig. 2.11. The rapid collapse of the moment at $\sim$ 20% Fe concentration is similar to the collapse of the transition metal moment observed in the middle of the $Gd(CoNi)_2$ system. This phenomenon is attributed to the reduction and subsequent collapse of the splitting of the 3d-subbands in association with the increased 3d-electron concentration and the inter-transition metal exchange interaction, both of which are linked directly with actual value of the moment of the transition metal. Further pseudobinary work (ref. 2.46, 2.47) has further supported the itinerant moment model, and in fig. 2.12 are shown the saturation moment and Curie temperatures plotted against composition for the series $(Ho(Fe-Co)_2$ and $Ho(Co-Ni)_2$. In this diagram the reduction in total moment in the vicinity of $HoCo_2$ is seen to accompany a

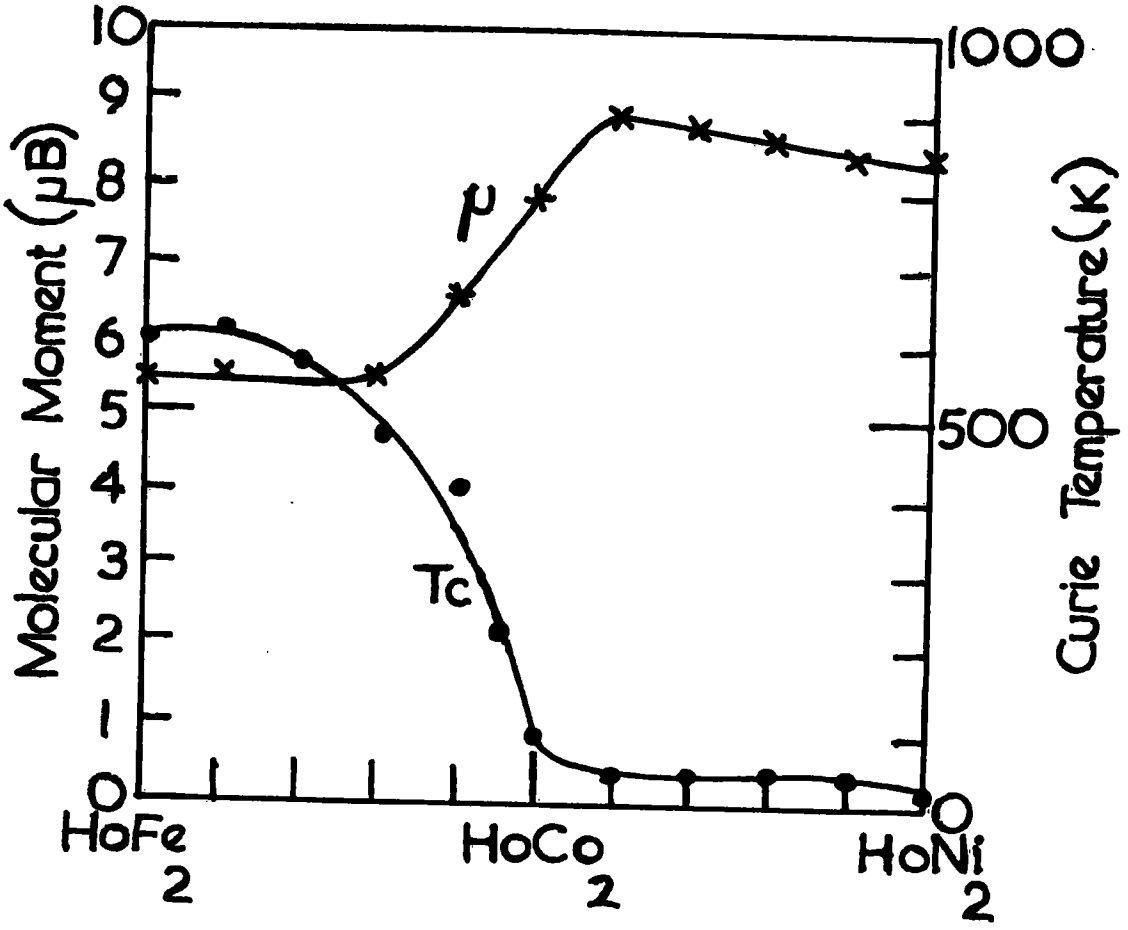

FIG. 2.12. MAGNETIC RESULTS FOR HoB_2

sharp rise in the Curie temperature. This behaviour is understood in terms of the development of a transition metal moment due to the changing 3d-electron concentration, the detailed band structure, and the effect of the increasing exchange upon the rare earth. This increase in exchange field will cause the rare earth ion moment to further approach the free ion value as the crystal field splitting is overcome by the exchange field, and calculation of the effect of the two fields can account for the observed behaviour (ref. 2.48). Fig. 2.13 shows the results of this calculation for the similarly behaved Er compounds. Crystal field effects are clearly important in these compounds, although actual calculations of the magnitude of the effect require a prior knowledge of the easy direction. No single crystal studies of these compounds have yet been reported, however hyperfine field studies using the Mössbauer technique have given the easy axis in the poly-crystalline RFe_2 compounds (ref. 2.49 - 51). The hyperfine field at the transition metal has contributions from the magnetic moment of the compound and these contributions are not necessarily identical for each transition metal. For example, if the easy axis is along the 111 direction then the three transition metals that are "off-axis" (see fig. 2.3) are indistinguishable from each other but inequivalent to the ion that is situated on the axis. In this case two Mössbauer spectra result with an intensity ratio of 3:1. The 100 direction may be the easy axis in which case all sites are equivalent and one spectrum alone results, similarly in the 101 (or 110) direction there are two pairs of inequivalent sites giving rise to a double spectrum with an intensity ratio of 1:1. The results

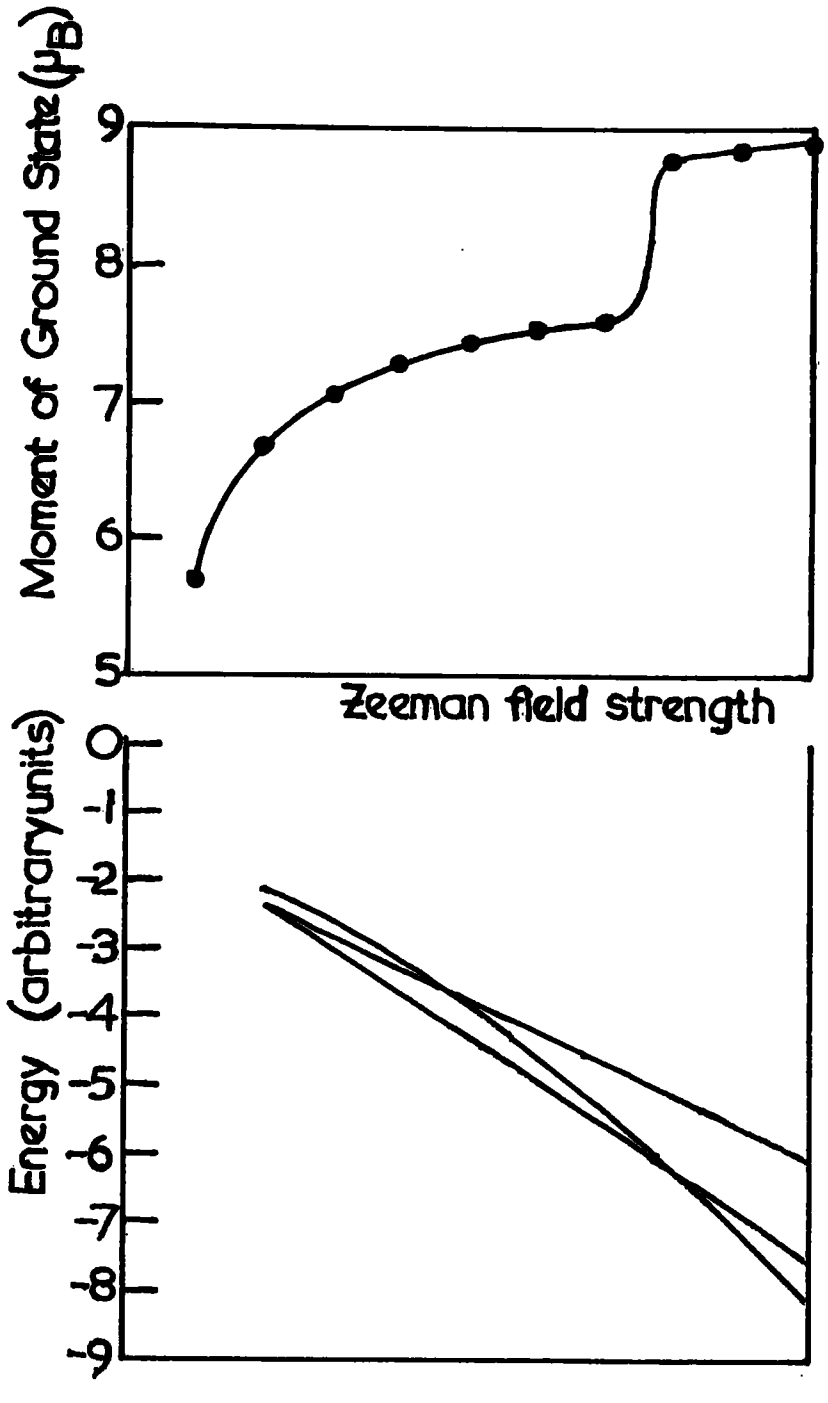

FIG. 2.13. EFFECT OF THE ZEEMAN FIELD UPON THE MOMENT & ENERGY DIAGRAM OF Er^{3+}

for the iron compounds showed that all three directions occurred in the series although Bowden (ref. 2.50) was able to predict, upon a simple crystal field model using the signs of the crystal field coefficients, which of the 111 or 100 directions would occur, giving excellent agreement with those compounds that did not show the 101 easy axis. These results will be referred to later in chapter 6.

The interactions within the iron and cobalt compounds are more complex than for those of the Nickel (and Aluminium) compounds, since the transition metal has a moment. The possible interactions are (i) the R-R which is RKKY in origin, (ii) the R-B which also goes via the conduction electrons and (iii) the B-B interaction (direct) which is most likely the strongest of the three (certainly true of the iron compounds). The B-B interaction is clearly linked to the other two since the magnetic moment of YCo_2 is probably zero and its Curie temperature, if it exists, is less than 2K (ref. 2.40). The interactions probably arise from some bootstrap process which in turn depends upon the 3d band structure.

The magnetisation versus temperature behaviour for the heavy rare earths Cobalt and iron compounds is typical of the ferrimagnetic structures of these compounds, - the curves showing the dips and compensation points associated with ferrimagnetism (see chapter 3). As mentioned previously in relation to the lattice parameters there has been some diversity in reported magnetic properties the earlier measurements suffering severely from second phases in the materials. Indeed the cobalt and iron compounds consistently show high temperature "tails" arising from small amounts of second phases.

Some evidence for these may be seen in the results for the compounds studied in this work in chapters 5 and 6.

The work of Oesterreicher et al. on the $R(Al,Co)_2$ series cited earlier (ref. 2.18) gave magnetic results that were consistent with the idea that the 3d-band was progressively filled as Al ions were added resulting in a reduction of the transition metal moment to zero. This work has been extended to include similar studies with RMn_2 compounds (ref. 2.52). The electron transfer theory of the 1967 study (ref. 2.18) is now thought to be only a partial transfer since the transfer necessary to account for the reduction of the magnetic moment to zero in the $Gd(Fe,Al)_2$ series (and in general) requires too large a charge separation to be sustained. The $R(Mn,Al)_2$ series, where it is expected that the v.e.c. will be very low since Mn can accept 4 electrons/atom to fill its 3d band, shows no moment associated with the Mn ion and further, in the $Gd(Mn,Al)_2$ series the C15 structure persists throughout. This finding implies that the v.e.c. remains reasonably constant in the above compounds although, in the $Er(Mn,Al)_2$, a very small range of the C14 phase is detected - these results are at variance with the electron transfer theory. The conclusion must be that transfer undoubtedly does occur but to an extent that is difficult to assess and certainly not to the previously envisaged levels.

Neutron diffraction studies have been carried out on some of the RCo_2 compounds by Moon et al. (ref. 2.53) and more recently on some of the $Er(Co,Al)_2$ and $Tb(Co,Al)_2$ compounds (ref. 2.54). The earlier results showed slightly higher moments associated with the rare earth ions and cobalt

moments of 0.8 μ_B/ion in the LRE compounds and 1.0 μ_B/ion in the HRE compounds, these moment values are further discussed in chapter 6. The neutron diffraction spectra revealed some extra temperature dependent peaks which were then attributed tothe possible presence of second phase effects. The results of the $R(Co,Al)_2$ studies show a tendency towards antiferromagnetic ordering with the exhibition of Néel points at low applied field strengths. The neutron diffraction results are interpreted in terms of a partially ordered state under these conditions, with some evidence of a helical spin structure. It should be pointed out, however, that the above structure was observed in low moment compounds in which the ordering temperatures are also very low, thus it is likely that the small exchange forces are affected by second order effects causing the helical structure and partial disorder to be present.

Recent studies of the pseudobinary system $Dy(CoNi)_2$ have shown a further interesting aspect of the RB_2 compounds, since this series shows an extensive time dependence of its magnetisation at low temperatures (refs. 2.55, 2.56). This behaviour has been interpreted in terms of the formation of narrow domain walls and the intrinsic pinning inherent in such a system (ref. 2.57).

In conclusion, it may be said that the rare earth-3d transition metal compounds of type RB_2, exhibit a wide variety of magnetic effects, the detailed explanation of which has yet to be perfected. The magnetic moments of the rare earths are dependent on the exchange interactions which have been shown to be of the RKKY type leading to polarisation of the conduction electrons. These moments are quenched to a degree depending upon the crystal field which in turn depends upon the transition metal. Accurate specification

of the moments to be associated with either component of the RB_2 is made difficult by the conduction electron polarisation which as shown above can either be positive or negative (or zero, presumably). The dominant exchange interactions in the Fe or Co compounds are the R-B and B-B interactions both of which are severely influenced by the B moment itself. The transition metal moment has been best understood on an itinerant electron model dependent upon band filling effects (via electron transfer) and variation in the exchange together with the detailed structure of the bands. This last term is purely speculative at the present with no theoretical calculations of the structure in these compounds.

The current work presents the results of magnetic studies on the pseudo-binary compounds $(Gd,Nd)Co_2$ in which it was intended to study the affect of the rare earth total sublattice upon the cobalt moment. In this system the gadolinium and neodymium moments ($\propto J$) are antiparallel resulting in a compensated rare earth sublattice at some composition value. Gadolinium is, as always, the obvious choice for the heavy rare earth since it is an S-state ion and as such it is essentially unaffected by the crystal field. The light rare earths all have sizeable crystal field effects but in Sm and Pr the multiplet separation of the spin orbit coupling is small enough to endanger the fidelity of J as a good quantum member, leaving Nd as the other choice. Some rather unusual magnetisation behaviour was found and this has been interpreted in terms of crystal field effects on the Nd ion.

CHAPTER 2 - REFERENCES

2.1 Vickery, R.C., Sexton, W.C., Novy, V., and Kleber, E.V. — J. Appl. Phys., 31, 366S, (1960)

2.2 Nesbitt, E.A., Wernick, J.H., and Corenzwit, E., — J. Appl. Phys., 30, 365, (1959)

2.3 Nesbitt, E.A., Williams, H.J., Wernick, J.H., and Sherwood, R.C., — J. Appl. Phys., 33, 1674, (1962)

2.4 Hubbard, W.M., Adams, E., and Gilfrich, J.V., — J. Appl. Phys., 31, 368S, (1960)

2.5 Lemaire, R., — Cobalt 32, 132, (1966)

Cobalt 33, 201, (1966)

2.6 Nesbitt, E.A., Williams, H.J., Wernick, J.H., and Sherwood, R.C., — J. Appl. Phys., 32, 342S, (1961)

2.7 Taylor, K.N.R., — Advances in Physics (to be published) (1971)

2.8 Laves, F., and Witte, H., — Metallwirtschaft 14, 645, (1935)

2.9 Laves, F., — Naturwiss, 27, 65, (1939)

2.10 Goldschmidt, V.M., — Z. Metallk, 13, 449, (1921)

2.11 Dwight, A.E., — Trans. ASM, 53, 479, (1961)

2.12 Hume-Rothery, W., — J. Inst. Metals 35, 307, (1926)

2.13 Jones, H., — Proc. Roy. Soc., A144, 225, (1934)

Proc. Roy. Soc., A147, 396, (1934)

2.14 Laves, F., and Witte, H., — Metallwirtschaft, 15, 840, (1936)

2.15a Mansey, R.C., Raynor, G.V., and Harris, I.R., — J. Less Comm. Metals, 14, 329, (1968)

2.15b Mansey, R.C., Raynor, G.V., and Harris, I.R., — J. Less Comm. Metals, 14, 337, (1968)

2.16 Christopher, J.T., Piercy, A.R., and Taylor, K.N.R., — J. Less Comm. Metals, 17, 59, (1969)

2.17	Chatterjee, D., and Taylor, K.N.R.,	J. Less Comm. Metals, 25, 431, (1971)
2.18	Oesterreicher, H., and Wallace, W.E.	J. Less Comm. Metals, 13, 91, (1967)
2.19	Kirchmayer, H.R.,	I.E.E.E. Trans. Mag., Mag 2, 493,(1966)
2.20	Williams, H.J., Wernick, J.H., Nesbitt, E.A., and Sherwood, R.C.,	J. Phys. Soc. Jap., 17, B1,91,(1962)
2.21	Swift, W.M., and Wallace, W.E.,	J. Phys. Chem. Solids, 29, 2053,(1968)
2.22	Jaccarino, V., Matthias, B.T., Peter, M., Suhl, H., and Wernick, J.H.,	Phys. Rev. Letters 5, 251, (1960)
2.23	Jaccarino, V.,	J. Appl. Phys., 32, 1028, (1961)
2.24	Bleaney, B.,	Proc. Roy. Soc., A176, 28, (1963)
2.25	McDermott, M.J., and Marklund, K.K.,	J. Appl. Phys., 40, 1007, (1969)
2.26	Nereson, N., Olsen, C.E., and Arnold, G.,	J. Appl. Phys., 37, 4525, (1966)
2.27	Olsen, C.E., Nereson, N., and Arnold, G.,	J. Appl. Phys., 38, 1395, (1967)
2.28	Buschow, K.H.J., Fast, J.F., van Diepen, A.M., and de Wijn, H.W.,	Phys. Stat. Sol., 24, 715, (1967)
2.29	Van Daal, H.J., and Buschow, K.H.J.,	Sol. Stat. Comm., 7, 217, (1969)
2.30	Van Daal, H.J., and Buschow, K.H.J.,	Phys. Rev. Letts., 23, 408, (1969)
2.31	Maple, M.B.,	Sol. Stat. Comm., 8, 1915, (1970)
2.32	Watson, R.E., Koide, S., Peter, M., and Freeman, A.J.,	Phys. Rev., 139, A167, (1965)
2.33	Watson, R.E., Freeman, A.J., and Kiode, S.,	Phys. Rev., 186, 625, (1969)

2.34	de Wijn, H.W., Buschow, K.H.J., van Diepen, A.M.,	Phys. Stat. Sol., 30, 759, (1968)
2.35	Farrel, J., and Wallace, W.E.,	J. Inorg. Chem., 5, 105, (1966)
2.36	Felcher, G.P., Corliss, L.M., and Hastings, J.M.,	J. Appl. Phys., 36, 1001, (1965)
2.37	Wallace, W.E.,	Prog. Sci. Tech. of Rare Earths, ed. Vol. III, p.1, (1968)
2.38	Stearns, M.B.,	J. Appl., Phys., 36, 913, (1965)
2.39	Taylor, K.N.R., Ellis, M.D., and Darby, M.I.,	Phys. Letts., 20, 327, (1966)
2.40	Lemaire, R., and Schweizer, J.,	Phys. Letts., 21, 366, (1966)
2.41	Piercy, A.R., and Taylor, K.N.R.,	J. Appl. Phys., 39, 1096, (1968)
2.42	Taylor, K.N.R.,	Phys. Letts., 29A, 372, (1969)
2.43	Piercy, A.R., and Taylor, K.N.R.,	J. Phys., C., 2, 1112, (1968)
2.44	Abel, A.W., and Craig, R.S.,	J. Less Comm. Metals, 16, 77, (1968)
2.45	Kanematsu, K.,	J. Appl. Phys., 39, 465,(1968)
2.46	Buschow, K.H.J., and van Stapele, R.P.,	J. Appl. Phys., 41, 4066, (1970)
2.47	Slanicka, M., Primavesi, G.J., and Taylor, K.N.R.,	J. Phys., F, 1, 5, (1971)
2.48	Taylor, K.N.R.,	(1971) Unpublished work.
2.49	Wertheim, G.K., Jaccarino, V., and Wernick, J. H.,	Phys. Rev., A135, 151, (1964)
2.50	Bowden, G.J.,	Ph.D. Thesis, Manchester, (1967)
2.51	Bowden, G.J., Bunbury, D. St.J., Guimareas, A.P., and Snyder, R.E.,	J. Phys. C. 1, 1376, (1968)
2.52	Oesterreicher, H., Corliss, L.M., and Hastings, J.M.,	J. Appl. Phys., 41, 2326, (1970)

2.53 Moon, R.M., Koehler, W.C., and Farrel, J., — J. Appl. Phys., 36, 978, (1965)

2.54 Oesterreicher, H., — J. de Phys., 32, C1 - 1141, (1971)

2.55 Taylor, K.N.R., — Phys. Letts., 35A, 153, (1971)

2.56 Taylor, K.N.R., Melville, D., and Primavesi, G.J., — J. Phys. F (to be published) (1971)

2.57 Zijlstra, H., — I.E.E.E. Trans. Mag., Mag.6,179,(1970)

CHAPTER 3

THEORETICAL BASIS

3.1 Introduction

The well known Weiss Molecular Field theory of ferromagnetism (see e.g. ref. 3.1) has been used to explain the behaviour of the spontaneous magnetisation below the Curie temperature, the Curie point itself and the paramagnetic region. There have been improvements to the original theory but these do not greatly affect the present work (for a review see ref. 3.2).

If Russel-Saunders coupling of the orbital (L) and spin (S) angular momenta may be applied to the material, to give a total angular momentum quantum number (J) and associated Landé factor (g), then the theory predicts that the magnetisation per unit mass ($\sigma_{H,T}$), at a field (H) and temperature (T) is given by the expression

$$\sigma_{H,T} = g.\ J.\ \mu_B.\ B_J(y).\ \frac{N}{A}\ .$$

In this equation, N, is Avogadro's number, A, the atomic or molecular weight, μ_B, the Bohr magneton and $B_J(y)$ the standard Brillouin function*. It is possible to find from the magnetisation $\sigma_{H,T}$, a useful quantity known as the Bohr magneton number given by

$$P = \sigma_{H,T}.\ \frac{A}{N} \qquad \text{.....(3.1)}$$

which represents the magnetic moment associated with the atom, or molecule, in units of the μ_B. Within a domain, the magnetisation with no applied field, $\sigma_{0,T}$, is termed the spontaneous magnetisation and at absolute zero, $\sigma_{0,0}$, is called the absolute saturation magnetisation. Under these conditions

* $B_J = \frac{2J+1}{2J}\ \text{Coth}\left(\frac{2J+1}{2J}\right)y - \frac{1}{2J}\ \text{Coth}\ \frac{y}{2J}$

$$\sigma_{0,0} = g.\ J.\ \mu_B.\ \frac{N}{A} \ ,$$

corresponding to complete alignment of the atomic (molecular) moments. This state can also be attained by the application of a sufficiently large field and the $\sigma_{S,0}$ representing the condition is called the saturation magnetisation. Although $\sigma_{S,0}$ and $\sigma_{S,T}$ are not the same as $\sigma_{0,0}$ and $\sigma_{0,T}$, they are almost numerically equivalent, and generally in this work it is $\sigma_{S,T}$ that is measured (see section 4.3.6).

3.2 Ferrimagnetism

A ferrimagnetic material may be defined as one which, below a certain temperature, possesses a spontaneous magnetisation arising from a non-parallel arrangement of the strongly coupled atomic moments. This may be caused by unequal moments oppositely aligned, or equal (or unequal) moments in some canted structure. The simplest arrangement, that of two antiparallel sublattices A and B, was treated originally by Néel (ref. 3.3). Even in this case there are several possibilities: (a) equal moments at the sites of each sublattice but more A sites than B sites (and vice-versa), (b) unequal moments on the A and B sublattice sites with equal number of sites, and (c) unequal moments and unequal numbers of sites. When systems with more than two sublattices are considered the situation becomes more complicated and is discussed later in this section.

Néel's molecular field approach to the two sublattice system was as

follows. The molecular fields for the sublattices, A and B, are written

$$H_{mA} = -N_{AA}\sigma_A - N_{AB}\sigma_B$$
$$H_{mB} = -N_{AB}\sigma_A - N_{BB}\sigma_B \qquad \ldots\ldots\ldots(3.2)$$

where $N_{AB} > 0$ for ferrimagnetism and $N_{AA} \neq N_{BB}$ (or else the system is simply antiferromagnetic) are the molecular field constants for the AB, AA and BB interactions respectively. It is usual to express the smaller interactions N_{AA} and N_{BB} in terms of the (usually) dominant N_{AB} interaction by the equations:

$$\alpha = \frac{N_{AA}}{N_{AB}}$$

$$\beta = \frac{N_{BB}}{N_{AB}}$$

The individual sublattice magnetisations can then be found by the usual molecular field calculations to give

$$\sigma_A(0,T) = \sigma_A(0,0)\ B_{J_A}(X_A)$$

$$\sigma_B(0,T) = \sigma_B(0,0)\ B_{J_B}(X_B)$$

where $X_A = \frac{J_A g_A \mu_B H_{mA}}{kT}$ and $B_{J_A}(X_A)$ is the Brillouin function (similarly for the B sublattice). If it is assumed that the sublattice magnetisation vectors are antiparallel then the magnitude of the resulting total spontaneous magnetisation $\sigma_R\,0,T$ is

$$\sigma_R 0,T = |\sigma_A 0,T - \sigma_B 0,T|$$

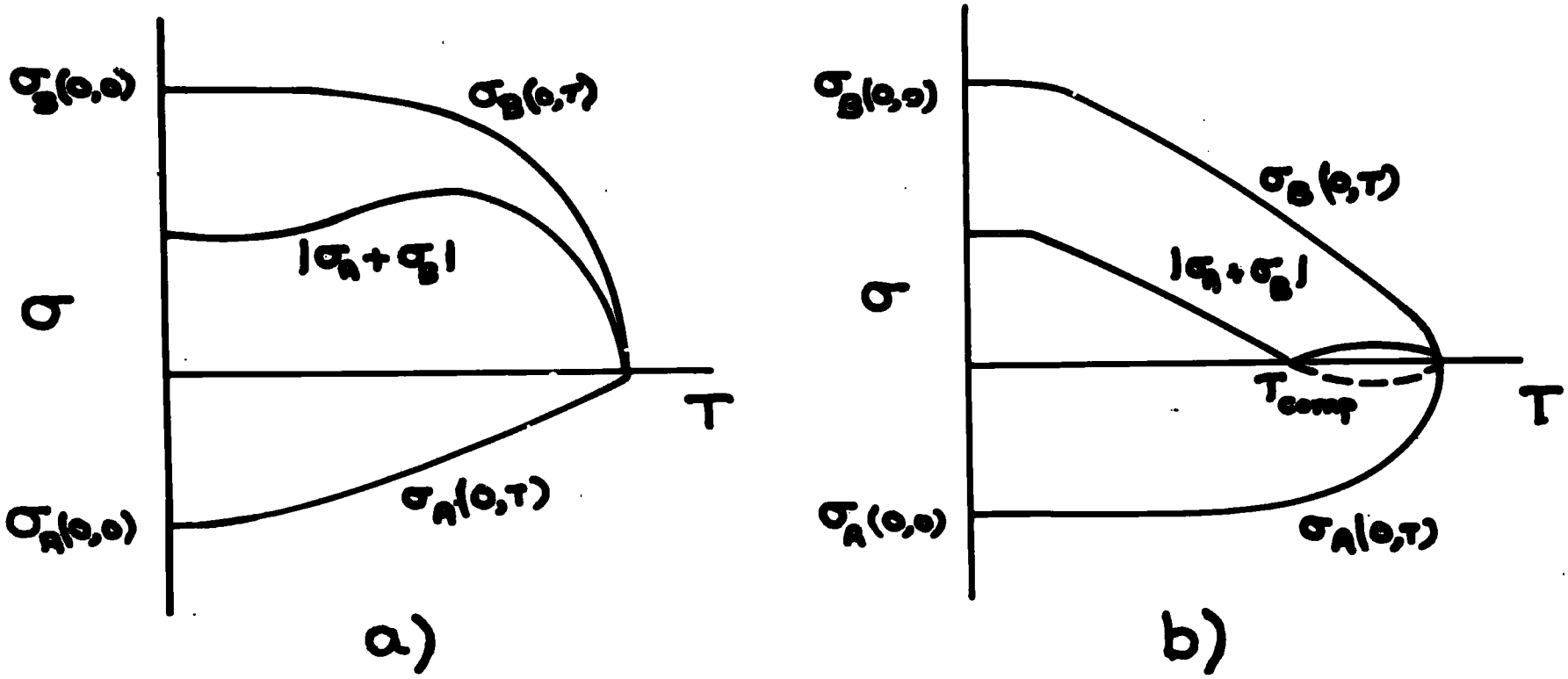
$\sigma_B(0,0)$
$\sigma_B(0,T)$
$|\sigma_A+\sigma_B|$
σ
T
$\sigma_A(0,0)$
$\sigma_A(0,T)$
a)
$\sigma_B(0,0)$
$\sigma_B(0,T)$
$|\sigma_A+\sigma_B|$
σ
T_{comp}
T
$\sigma_A(0,0)$
$\sigma_A(0,T)$
b)

FIG. 3.2.1

The variation of the magnetisation with temperature will depend on the quantities $\frac{\sigma_A 0,T}{\sigma_B 0,T}$, α and β, but the actual sublattice magnetisations decrease monotonically with increasing temperature until the Curie temperature is reached where they both become zero. However, some unusual σ vs T curves may result because of the difference between the variation of the magnetisations of the two sublattices with temperature, and these curves may be studied as a function of α and β with constant $\sigma_A 0,T / \sigma_B 0,T$ or vice versa. Figures 3.2.1 and 3.2.2 illustrate some possible curves. The first figures show the situation for $\sigma_A 0,0 < \sigma_B 0,0$ and in (a) the net molecular field on the A sites is less than that on the B sites causing the A sublattice magnetisation to fall with increase in temperature more rapidly than that of the B sublattice. This, in effect, means that the AA interaction must be antiferromagnetic and the BB interaction less so, or even ferromagnetic (i.e. $\alpha > \beta$). The second part of the diagram represents the reverse situation ($\beta > \alpha$), and in this case the spontaneous magnetisation reverses its direction passing through zero at a temperature known as the compensation temperature (T_{comp}). (Note - the dotted curve represents the spontaneous magnetisation, but when observations are made a field has to be applied causing the spin system as a whole to 'flip' when the compensation point is reached and it is the solid curve that is detected as a consequence of this). The series of curves shown in fig. 3.2.2 represent the effect of varying the ratio $\sigma_A 0,T / \sigma_B 0,T$ (by, for example, varying the chemical composition) for constant values of α and β, on the behaviour of σ against reduced temperature T/T_c (in order to have a common temperature). In the curve, labelled 4, the quantities $\sigma_A 0,0$ and $\sigma_B 0,0$ are equal and opposite

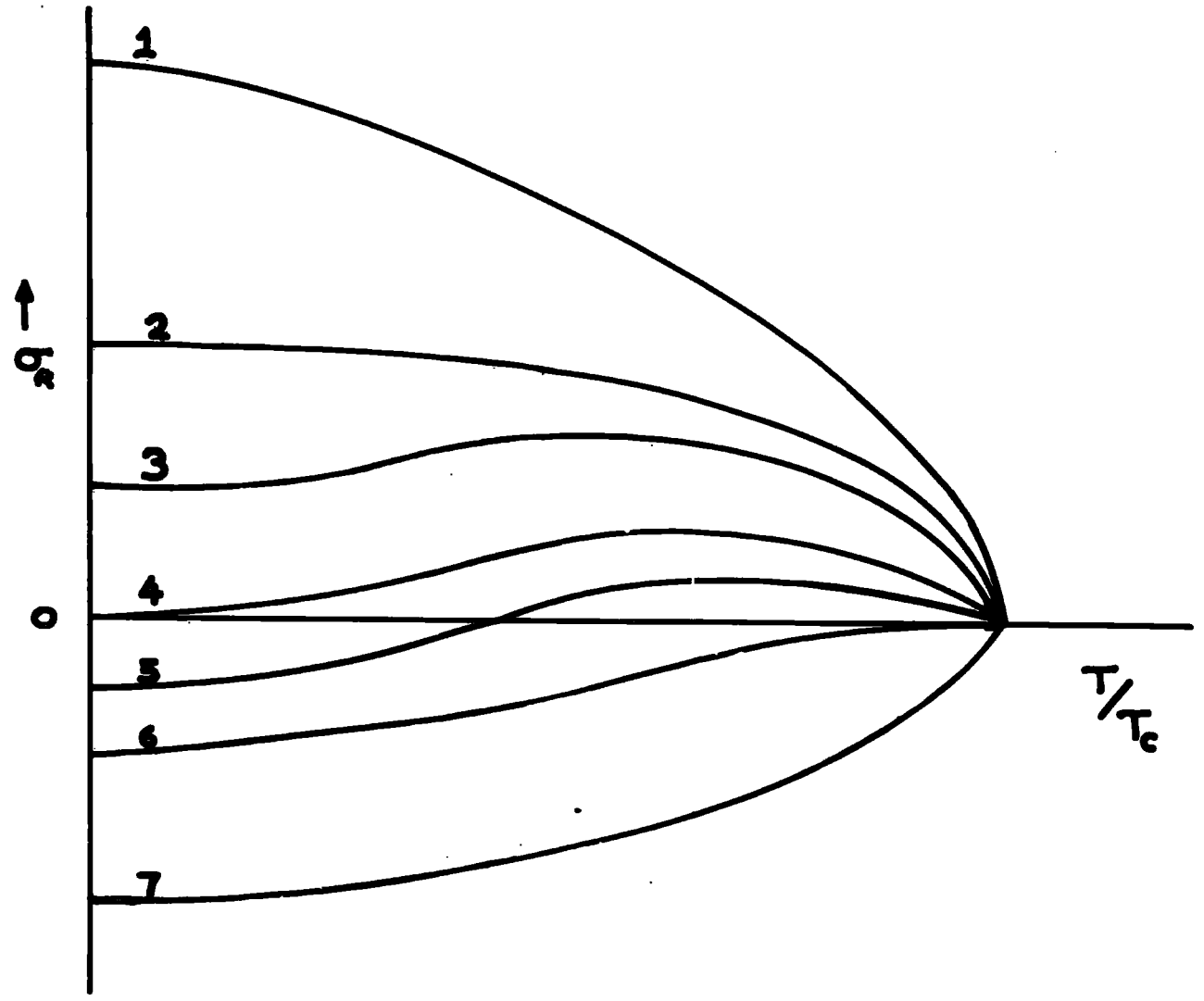

Fig. 3.2.2

giving a resultant $\sigma_R 0,0 = 0$, however, since $H_{mA} \neq H_{mB}$ $(\alpha \neq \beta)$, above absolute zero and below the Curie temperature $\sigma_R 0,T \neq 0$. Curve 2 represents the transition point between curves of the 'Brillouin-type' (eg 1) and those similar to curve 3 (also fig. 3.2.1a). For curves 1 to 3, the ratio $\sigma_A 0,0/\sigma_B 0,0 < 1$; for curves 5 to 7 the ratio $\sigma_A 0,0/\sigma_B 0,0 > 1$. The 6th curve represents the transition between curves which exhibit the compensation point phenomenon (eg fig. 3.2.1b) and those of type 7. It can be seen from the foregoing that with a simple two sublattice system a rich variety of σ vs T curves is possible.

Yafet and Kittel (ref. 3.4) extended the Néel theory to include the case where the antiferromagnetic AB interaction is comparable in size to the antiferromagnetic AA and BB interactions. In this situation, the A sublattice itself may split into two antiparallel sub-sublattices, A_1 and A_2, similarly for the B sublattice with the result that various overall configurations are possible:- (a) antiparallel A and B total sublattices (↑↓), (b) some triangular configuration (◁ or ▷), or (c) antiferromagnetism within the two A and B sublattices independently of each other (↕↕). Another interesting feature of this extended theory is the possibility of transitions between the various spin configurations with change in composition and temperature.

Lotgering (ref. 3.5) applied the Yafet and Kittel theory to the spinel structure $A[B_2]X_4$, where A and B are magnetic ions and the AB interaction is comparable to the AA and BB interactions. The configuration in this type of structure is such that there are two A - sublattices, and four B - sublattices, represented by $A_1A_2\ [B_1 - B_4]\ X_8$. By a consideration of the magnitudes of the

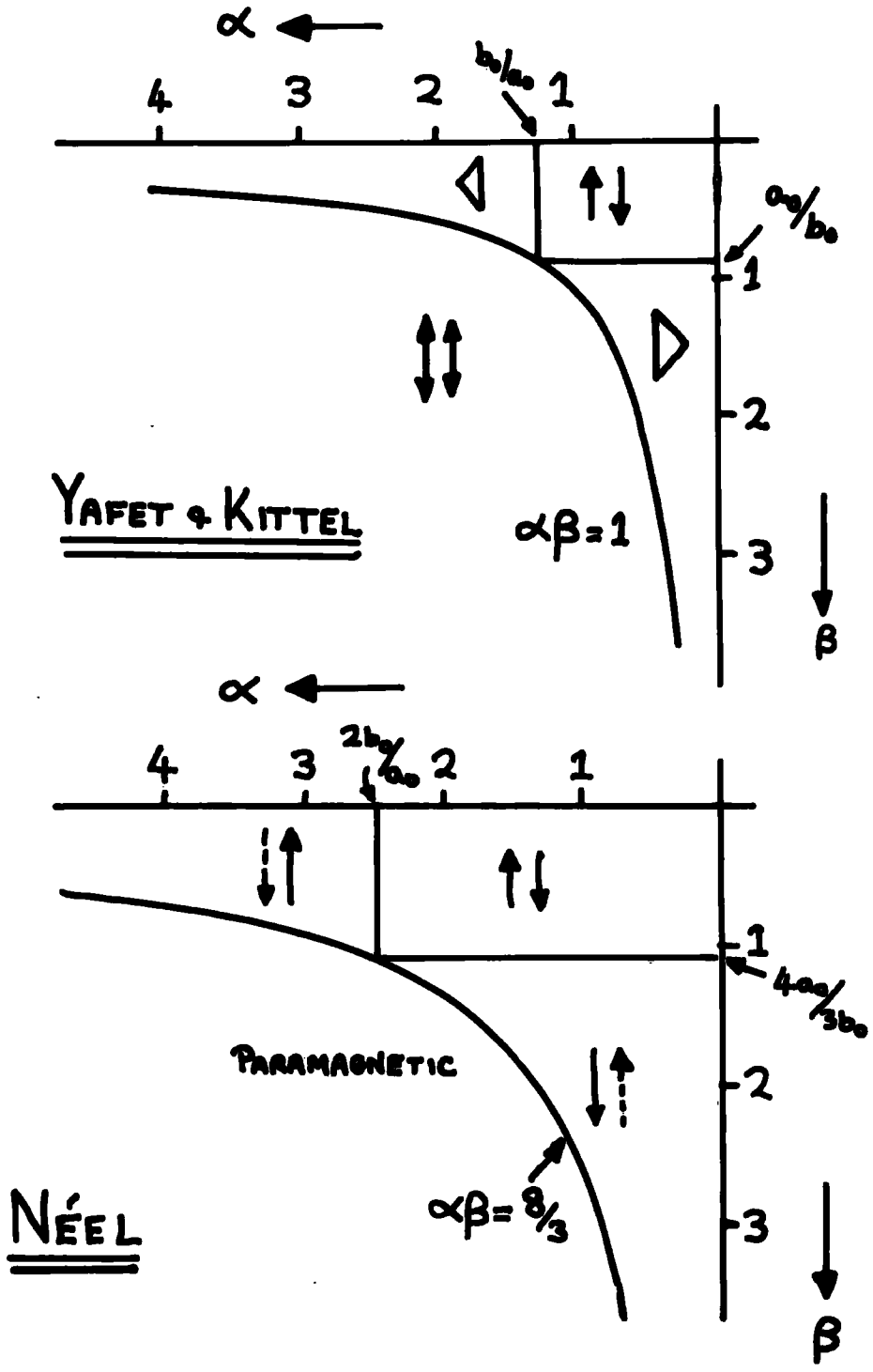
α
4
3
2
b_0/a_0
1
a_0/b_0
1
2
3
β
YAFET & KITTEL
αβ=1
α
4
3
$2b_0/a_0$
2
1
1
$4a_0/3b_0$
PARAMAGNETIC
2
3
β
NÉEL
αβ= 8/3

FIG. 3.2.3

superexchange interactions within the system, it is possible to simplify the calculations and deduce the stable configurations of the spin system at absolute zero relative to the dominant Weiss molecular field constants, α and β, for the A and B sublattices respectively. Fig. 3.2.3 (after ref. 3.5) illustrates the $\alpha - \beta$ diagrams for the two theories (note: these diagrams apply also to the more simple two sublattice ferrimagnetic systems since they express the results in terms of the dominant interactions). The terms ao and bo represent the net sublattice magnetisation vectors at OK and the ratio bo/ao (= 1.25) is the same in each of the diagrams. The Néel theory allows only antiparallel arrangement of the sublattice magnetisations with the result that in the two regions X and Y one of the sublattices has to have a reduced magnetisation although there is no reasonable mechanism whereby this can be achieved, and furthermore, because one of the sublattice moments is not saturated the requirement by the Third Law of thermodynamics that $\left[\frac{\partial M}{\partial T}\right]_H = 0$ at absolute zero is violated. The Yafet and Kittel theory overcomes this problem by allowing canting of the saturated sub-sublattice moments.

The three major interactions AB, AA and BB may be represented by three Curie temperatures, T_C, T_A and T_B respectively since the interactions are independent of one another and, further, are of differing magnitudes. In the ferrites where the AB interaction dominates, the observed ferrimagnetic Curie point depends only on T_C, however, in the spinels the observed collapse of magnetic ordering will take place at the temperature T_L corresponding to the Curie temperature of the largest of the interactions. The intermediate behaviour, $0 < T < T_L$, will be governed by the other two temperatures and, as

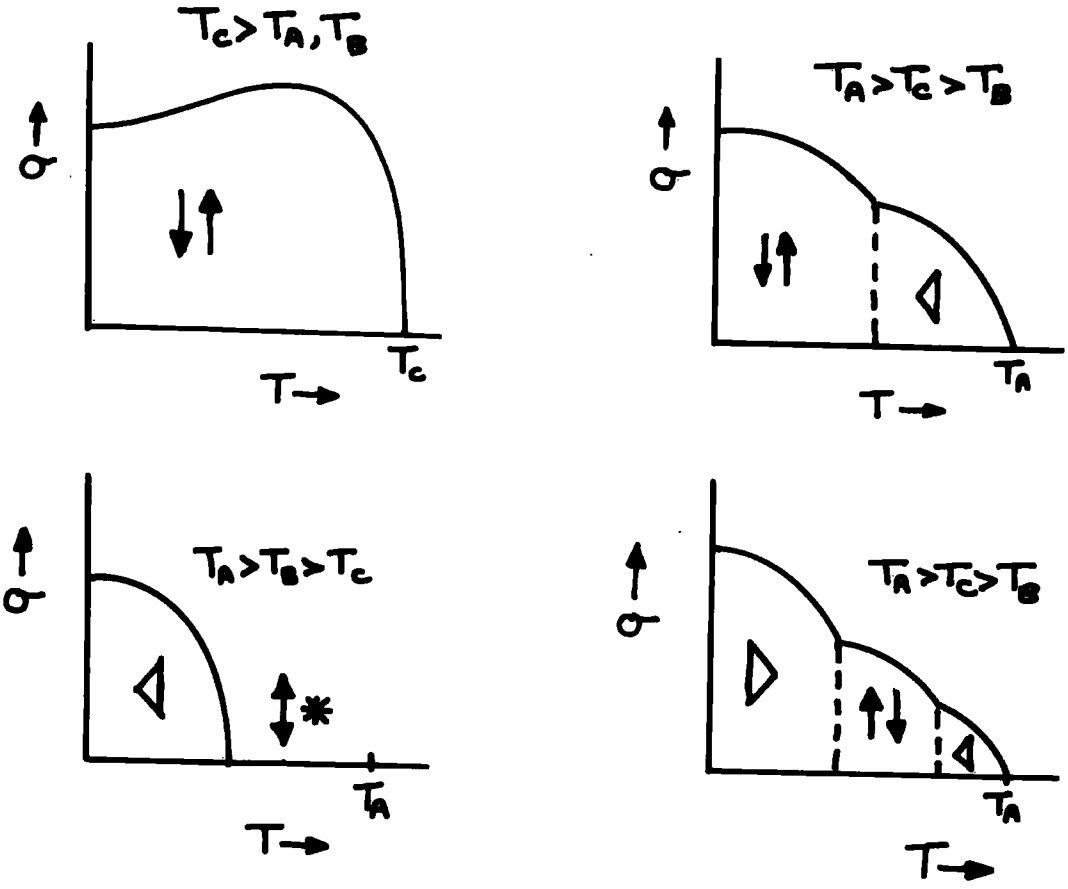

FIG 3.2.4

a result, transitions in the spin configuration can occur, as is illustrated for some cases in fig. 3.2.4. The direct evidence for triangular spin configurations is only attainable by neutron diffraction experiments and it is thought that some of the chromium spinels may have this arrangement although there is little evidence from σ vs T data (ref. 3.6).

The situation for metallic ferrimagnetic materials, such as are investigated in this work, differs from that of the spinels and normal ferrites since in this case, the exchange interactions are not superexchange (although some are indirect) and therefore can be ferromagnetic within a sublattice. This ferromagnetic coupling within the sublattice tends to simplify the resulting total spin structure favouring a parallel or antiparallel arrangement of the magnetisation vectors. However, the interactions may still have differing critical temperatures resulting in the probability of anomalous σ vs T behaviour. The compounds studied in this work are further discussed in this light in Chapter 6.

3.3 Crystal Field Calculations

3.3.1 Introduction

A particular ion in a lattice is situated in an electrostatic field due to the influence of the surrounding charged atoms. This field is called the crystal field and will possess a degree of symmetry relating directly to the structure of the lattice.

Consider a rare earth ion situated in the lattice. The ground state of this ion is a $2(J+1)$-fold degenerate multiplet ($J = L \pm S$ according to Hund's Rules and Russel-Saunders coupling). If the ion is placed at coordinates

(r,θ,ϕ) near the origin and is under the influence of ions i at $\underline{R}_i$ then the field in polar coordinates is

$$V_c(r,\theta,\phi) = \sum_i \frac{q_i}{|\underline{r} - \underline{R}_i|} \qquad \ldots\ldots\ldots (3.3)$$

on a simple point charge basis. The effect of this field on the ion is to lower the $2(J+1)$-fold degeneracy to an extent depending on the symmetry of the field and the value of J. The exact nature of the levels can be specified using group theory, but two useful rules can be employed and these are defined below:-

(i) KRAMERS THEOREM. This states that in the absence of any magnetic fields (applied or exchange) the levels of an ion with an odd number of electrons can at most be split into doubly degenerate levels by the crystal field. Thus rare earth ions with half integral values of J (eg Nd^{3+}, $J = \frac{9}{2}$, $L = 6$, $S = \frac{3}{2}$) when situated in a crystal field will have Kramers degeneracy.

(ii) JAHN-TELLER EFFECT. The crystal structure of a system containing a degenerate ground state will spontaneously distort in such a way as to remove this degeneracy, unless the ground state is a Kramers doublet. That is ions with an even number of electrons will always have a singlet ground state (eg Pr^{3+}, $J = 4$).

The original crystal field work was carried out at Oxford to account for the results of e.p.r. measurements on the rare earth ethyl sulphates, which are cubic in structure. The susceptibility results show that the crystal field splittings are smaller than the multiplet separation (next J state in Russel-

TABLE 3.1

	IRON GROUP TRANSITION METALS	RARE EARTHS
COULOMB ENERGY	$10 - 40 \times 10^3 cm^{-1}$ $15 - 60 \times 10^3 °K$	$5-40 \times 10^3 cm^{-1}$ $8-60 \times 10^3 K$
SPIN-ORBIT COUPLING (L+S) = J	$100 - 800\ cm^{-1}$ $150 - 1200\ K$	$600 - 3000\ cm^{-1}$ $900 - 4500\ K$
CRYSTAL FIELD SPLITTING	$10 - 20 \times 10^3 cm^{-1}$ $15 - 30 \times 10^3 K$	$0 - 700\ cm^{-1}$ ($300\ cm^{-1}$) $0 - 1000\ K$

Saunders coupling) implying that J remains a good quantum number in these salts. This result may be expected from the fact that the 4f electrons in general are in relatively deeply buried orbitals, unlike the 3d electrons in the iron group transition metals in which the crystal field splitting greatly exceeds the multiplet separation. Some indication of the comparison of the magnitudes of these effects in the two types of ion is given in table 3.1.

3.3.2 The Crystal Field

In the case of cubic symmetry the field given by equation 3.3 may be expanded in Cartesian coordinates to give

$$V^{100}(x,y,z) = C + C_4\left[x^4+y^4+z^4 - \frac{3}{5}r^4\right] + D_6\left[(x^6+y^6+z^6) + \frac{15}{4}\left(x^2y^4 + x^2z^4 + y^2x^4 + y^2z^4 + z^2x^4 + z^2y^4\right) - \frac{15}{4}r^6\right] \quad \ldots\ldots (3.4)$$

in which the z-axis is a fourfold axis of symmetry (100 axis). The constant C may (in general) be ignored since it is independent of x, y, or z. The constants C_4 and D_6 depend upon the coordination of the neighbouring ions relative to the central ion calculated on the simple point charge model. The potential must obey Laplaces equation and therefore may be expanded into spherical harmonics in which case the number of terms in the expansion is greatly reduced by the symmetry of the crystal. For example a centre of inversion renders all harmonics $Y_\ell^m = 0$ when ℓ is an odd integer. Further simplification arises when the matrix elements of the hamiltonian between the 4f electron wave functions are considered; these have the form

$$\int \phi^*_{4f}\ q\ V_c(r,\theta,\phi)\ \phi_{4f}\ d\tau$$

The 4f wave functions contain spherical harmonics up to $\ell = 3$ i.e. Y_3^{μ} so the angular integrals involved are

$$\int Y_3^{\mu} \quad Y_{\ell}^{m} \quad Y_3^{\mu} \sin\theta \, d\theta d\phi$$

which can be shown to vanish unless $\ell < 6$. The situation with the 3d transition metals is simpler requiring terms up to the 4th degree ($\ell < 4$) only, since d electrons have an orbital quantum number of two.

The cubic crystalline field may be expressed in polar coordinates as

$$V_C^{100}(r,\theta,\phi) = C + D_4' \left\{ Y_4^0(\theta,\phi) + \left(\frac{5}{14}\right)^{\frac{1}{2}} \left[Y_4^4(\theta,\phi) + Y_4^{-4}(\theta,\phi) \right] \right\}$$
$$+ D_6' \left\{ Y_6^0(\theta,\phi) - \left(\frac{7}{2}\right)^{\frac{1}{2}} \left[Y_6^4(\theta,\phi) + Y_6^{-4}(\theta,\phi) \right] \right\} \qquad \ldots\ldots(3.5)$$

where, again, D_4' and D_6' depend on the coordination.

If the magnetic ion has a charge q_i then the crystalline potential energy will be

$$H_c = \sum_j q_i V_j \qquad \ldots\ldots(3.6)$$

where the $\sum_j$ is over the electrons in the unfilled shells.

3.3.3 Evaluation of the Matrix elements

There are two common methods for finding the matrix elements of H_c between the coupled wavefunctions.

(a) Direct Integration:

This method is the more fundamental of the two. The free ion wavefunctions are expanded into a product involving the individual electron wavefunctions ϕ_i

on which the terms $V(x_i y_i z_i)$ in H_c act. In polar coordinates the elements are formed from sums of integrals such as

$$\int \phi^* \quad (r_i \theta_i \phi_i)\ r^n\ Y_n^m(r_i \theta_i \phi_i)\ \phi\ (r_i \theta_i \phi_i)\ d\tau$$

The radial part of this integral $\langle r^n \rangle$ is not accurately known and is used as a parameter, alternatively, a theoretically calculated value is used (ref. 3.7). The angular part of the integral can now be evaluated using the rules discussed by Bleaney and Stevens (p. 128 and 130 of ref. 3.8). The direct integration method is complicated and seldom used, the second method being preferred.

(b) Stevens Operator Equivalents Method.

This method can be used to evaluate matrix elements between coupled wavefunctions that are specified by an angular momentum quantum number J (or L). The procedure eliminates the need to return to the single electron wavefunction by using, instead, an 'operator equivalent' to H_c, comprising angular momentum operators which act on the angular part of the wavefunctions of the coupled system while isolating the ignorance of the detailed properties of the states in a common factor. (This process is an application of the Wigner-Eichart theorem see e.g. ref. 3.9.)

The cartesian function f(x,y,z) of a given degree converts to operator equivalent form by the replacement of x, y and z by J_x, J_y and J_z respectively, allowing for non-commutation of J_x, J_y and J_z in products of x, y and z by using all the possible combinations of J_x etc. and dividing by the number of these combinations. A few examples are

$$\sum_i (3z_i^2 - r_i^2) \equiv \alpha_j \langle r^2 \rangle \left[3J_z^2 - J(J+1)\right] = \alpha_j \langle r^2 \rangle O_2^0$$

$$\sum_i (x_i^2 - y_i^2) \equiv \alpha_j \langle r^2 \rangle \left[J_x^2 - J_y^2 \right] = \alpha_j \langle r^2 \rangle O_2^2$$

$$\sum_i (x_i^4 - 6x_i^2 y_i^2 + y_i^4) = \sum_i \left\{ \left[(x_i + iy_i)^4 + (x_i - iy_i)^4 \right] \div 2 \right\}$$

$$\equiv \beta_J \langle r^4 \rangle \tfrac{1}{2} \left[J_+^4 + J_-^4 \right] = \beta_J \langle r^4 \rangle O_4^4$$

(Note:- $J_\pm = Jx \pm iJy$ are the step up/down operators).

Thus matrix elements from the expression

$$\sum_i (3z_i^2 - r_i^2)$$

between coupled states $|LSJ\ J_z\rangle$ (or $|J_z\rangle$ for brevity) are equal to those of $\alpha_J \langle r^2 \rangle \theta_2^0$ between the angular part of the coupled wavefunctions i.e.

$$\langle J_z' | \sum_i (3z_i^2 - r_i^2) | J_z \rangle \equiv \alpha_J \langle r^2 \rangle \langle J_z' | \left[3J_z^2 - J(J+1) \right] | J_z \rangle$$

In the latter part of the equality, $\langle r^2 \rangle$ is the radial part of the integral, α_J are multiplicative constants depending upon ℓ (the orbital quantum number of the electrons in the unfilled shell) and n' (the number of electrons in that shell and also J (or L & S). The multiplicative constants for the fourth and sixth degree expressions are β_J and γ_J respectively.

Equation 3.4 for the cubic crystalline field may be transformed into operator equivalents and yields for the crystal field Hamiltonian

$$H_c^{100} = \frac{C_4}{20} \beta_J \langle r^4 \rangle \left[O_4^0 + 5O_4^4 \right] - \frac{D_6}{224} \gamma_J \langle r^6 \rangle \left[O_6^0 - 21O_6^4 \right] \quad \ldots.(3.7)$$

$$H_c^{100} = B_4^0 \left[O_4^0 + 5O_4^4 \right] + B_6^0 \left[O_6^0 - 21O_6^4 \right] \quad \ldots.(3.8)$$

where the terms B_n^0 comprise the coordination constants (C_n) the multiplicative

factors (α,β, & γ) and the radial part of the integral ($\langle r^n \rangle$). This Hamiltonian is expressed relative to the 100 axis but may be changed into that for the 111 axis by writing the cartesian expressions for the O_n^m and using the transformation matrix

$$\begin{bmatrix} x_i \\ y_i \\ z_i \end{bmatrix} = \begin{bmatrix} 1/\sqrt{6} & -1/\sqrt{2} & 1/\sqrt{3} \\ 1/\sqrt{6} & 1/\sqrt{2} & 1/\sqrt{3} \\ -\sqrt{2/3} & 0 & 1/\sqrt{3} \end{bmatrix} \begin{bmatrix} X_i \\ Y_i \\ Z_i \end{bmatrix}$$

(ref. 3.10.), and reconverting the result into operator equivalents, from which process the 111 axis Hamiltonian is

$$H_c^{111} = \left(-\frac{2}{3}\right) B_4 \left[O_4^0 + 20\sqrt{2}\, O_4^3\right] + \left(\frac{16}{9}\right) B_6 \left[O_6^0 - \frac{35}{\sqrt{8}} O_6^3 + \frac{77}{8} O_6^6\right] \quad \ldots.(3.9)$$

where the B_4 and B_6 are the same constants as for the H_c^{100} case.

To set up the matrix, the elements may be found by operating with the O_n^m using the normal rules, or, recourse may be had to the published results of this process in for example Hutchings (ref. 3.11). By suitable matrix operations the original matrix may be simplified to form submatrices, the number of such submatrices being dependent upon the symmetry of the crystal field. The submatrices may be solved in the usual way, by the subtraction of eigenvalues (λ) from the diagonal elements and finding the solution of the resulting secular equation by equating its determinant to zero. Alternatively, standard computer programmes may be used and in the present work diagonalisation was accomplished with a Jacobi reduction programme (see appendix II).

3.3.4 The Crystal Field Hamiltonian

A number of ways have been followed by various authors in the setting up of the crystal field Hamiltonian and as a check on the computer programmes, the results of Lea, Leask and Wolf (ref. 3.12) were recalculated for J = 9/2. Their Hamiltonian takes the form

$$H = W\left[x\left(\frac{O_4}{F_{(4)}}\right) + (1 - |x|)\left(\frac{O_6}{F_{(6)}}\right)\right] \qquad \ldots\ldots(3.10)$$

in which $$W\,x = B_4 . F(4) \text{ and } W(1-|x|) = B_6 . F(6) \ldots\ldots(3.11)$$

In these equations B_4 & B_6, have their usual meaning, and O_4 and O_6 represent the fourth and sixth degree operator equivalent expressions. The factors $F_{(4)}$ and $F_{(6)}$ are merely numerical multipliers extracted from the matrix elements to make the results for a span of J-values similar in magnitude. It can be seen from equations 3.11 that W is a parameter which slides the energy scale and that x specifies the ratio of the fourth degree to sixth degree crystal field effects. This process may appear to be somewhat arbitrary but arises from the fact that B_4 and B_6 contain coordination factors based on the point charge model and also the radial integrals $\langle r^n \rangle$ which are difficult to calculate with any degree of accuracy. Hence the terms B_4 and B_6 are used as parameters by employing the relations in equ. 3.11 and varied to suit the experimental conditions.

A slightly simpler form for the Hamiltonian of equation 3.10 was used in this work

$$H = SF\left[x\left[B_4O_4\right] + (1-|x|)\left[B_4O_6\right]\right] \qquad \ldots\ldots(3.12)$$

in which B_4 is used as the energy term for 4th and 6th degree terms, x represents

directly the ratio of the 4th/6th degree crystal field energy, and SF is an adjustable scaling factor.

3.3.5 The Effect of Magnetic Interactions

When calculations of the effect of the crystal field are made on materials in which there are magnetic fields due to, for example, exchange interactions, the total Hamiltonian must include the Zeeman term, unless this term is small enough to be introduced as a perturbation. In normal ferromagnetic materials with Curie temperatures of some hundreds of degrees Kelvin, the internal (exchange) fields can be as high as several megaoersteds ($\sim 10^3$ KA.mm^{-1}) and in these cases the Zeeman splitting of the multiplet is often many times larger than the crystal field splitting. The Zeeman term in the total Hamiltonian may be written

$$H_z = -g.\mu_B H_{int} J \qquad .....(3.13)$$

where H_{int} is the internal magnetic field (comprising the exchange and any applied fields). This term only contributes diagonal matrix elements since all the off-diagonal elements are zero

$$(g \mu_B H_{int} \langle m_J' | J | m_j \rangle = 0 \quad \text{unless } m_j' = m_j).$$

Thus the total Hamiltonian may be written

$$H_T^{hk\ell} = SF \left[x \left[B_4 O_4\right] + (1 - 1x1) \left[B_4 O_6\right] \right] - g\mu_B . H_{int} . J \ldots (3.14)$$

The solution of the energy matrix set up in this way yields the eigenvalues and eigenvectors of the (2J+1) energy levels, which may, of course, be degenerate. The eigenvectors then led immediately to the observable

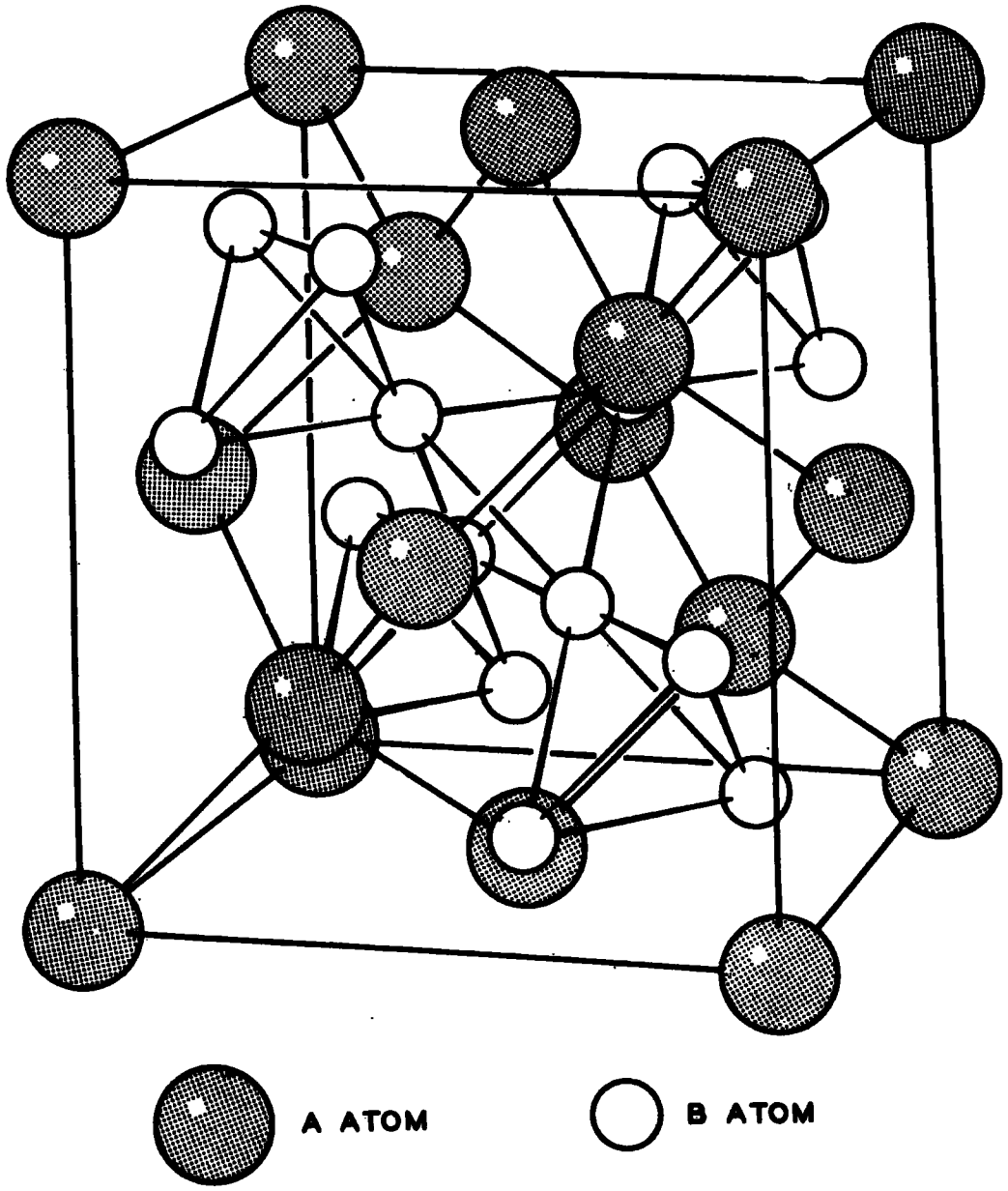

Fig. 3.4.1a

magnetic moment associated with the ion in a particular state from the equation -

$$\mu_J = g \mu_B \sum_j a_j^2 m_j \qquad \ldots\ldots\ldots(3.15)$$

where a_j is the coefficient of the $|m_j>$ term of the eigenvector, since the eigenvectors are linear combinations of the free ion states. The magnetic moment associated with the ion at a temperature T may be found from the addition of μ_J (the moment of each state) multiplied by the relevant Boltzmann factor, hence,

$$\mu_T = \frac{\sum_j \mu_J e^{-\frac{\Delta E_J}{kT}}}{\sum_j e^{-\frac{\Delta E_J}{kT}}} \qquad \ldots\ldots\ldots(3.16)$$

where μ_J is the moment associated with the jth energy level and ΔE_J is the difference in energy between the jth level and the ground state, and the summation extends over all levels within the (2J+1)-multiplet split by the exchange and crystal fields.

3.4 Application of Crystal Field Calculations to the RE-TM Cubic Laves Phase Compounds

The problem in applying crystal field calculations to any particular material is merely one of finding an expression for the crystal field potential and finding the correct combination of Steven's operator equivalents. This procedure is simplest in the case of cubic fields since these have been studied in the past and are well represented in the literature.

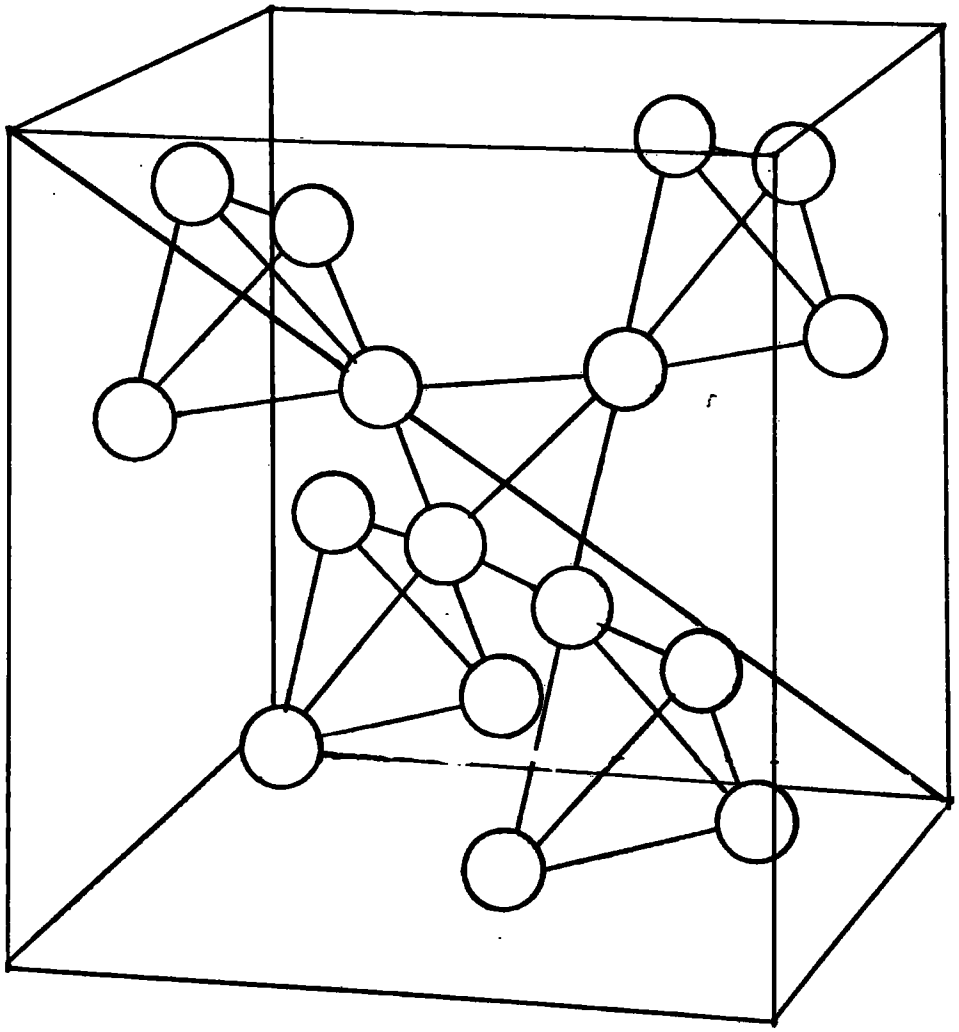

Fig. 3.4.1 b.

The Cubic Laves phases contain 8 molecules/unit cell(formula AB_2) that is 8A and 16B ions. It is the crystal field at the A site (rare earth site) that is required. The cubic Laves phase structure is shown in fig. 3.4.1a, the second part of the diagram (3.4.1b) shows the B ions only. The nearest neighbours to the A ions are twelve B ions at

$$R_1 = \sqrt{\frac{11}{8}}\, a_o = 0.415\, a_o$$

where a_o is the lattice parameter. It is not immediately clear that these B ions are in any way cubically arranged but they do have a 3-fold symmetry axis along the 111-direction of the unit cell (see fig. 4.3.1b) with 6 ions at $\cos\theta = (\frac{3}{11})^{\frac{1}{2}}$, ϕ = 30, 90, 150, 210, 270 and 330°;

3 ions at $\cos\theta = -(\frac{1}{33})^{\frac{1}{2}}$ ϕ = 0, 120, 240;

and 3 ions at $\cos\theta = -(\frac{25}{33})^{\frac{1}{2}}$ ϕ = 0, 120, 240.

The next nearest neighbours are four A ions arranged in a regular tetrahedron at

$$R_2 = \frac{\sqrt{3}}{4}\, a_o = 0.433\, a_o \left(= (\tfrac{12}{11})^{\frac{1}{2}}\, R_1\right) \qquad \ldots\ldots (3.17)$$

and in the same polar coordinates

one ion at $\cos\theta = 1$

and three ions at $\cos\theta = -\frac{1}{3}$ ϕ = 60, 180, 300.

The next shell of neighbours comprises B ions at 0.65 a_o and these are appreciably further away and hence neglected. The crystal field has been calculated (ref. 3.13) for the nearest and next nearest neighbour ions and the potential does show cubic symmetry. The coordination constants within

the crystal field coefficients B_4 and B_6, may be found on the point charge model and hence

$$B_4 = \frac{7}{36} \frac{e^2}{R_2^5} \left\{ Z_2 - 1.20\, Z_1 \right\} \langle r^4 \rangle \beta_J$$

$$B_6 = \frac{1}{18} \frac{e^2}{R_2^7} \left\{ Z_2 + 0.303\, Z_1 \right\} \langle r^6 \rangle \gamma_J \qquad \text{.....(3.18)}$$

These coefficients may then be numerically evaluated to gauge their order of magnitude and substituted into the expression for the total Hamiltonian (equ. 3.14).

CHAPTER 3 - REFERENCES

3.1	Morrish, A.H.	Physical Principles of Magnetism (Wiley 1966)
3.2	Phillips, T.G., and Rosenberg, H.M.	Repts. Prog. Phys., 24, 285, (1966)
3.3	Néel, O.L.,	Ann. Phys. (Paris) 3, 137 (1948)
3.4	Yafet, Y., amd Kittel, C.	Phys. Rev. 87, 290 (1952)
3.5	Lotgering, F.K.,	Philips Res. Rept., 11, 190 (1956)
3.6	Kasper, J.S.,	Bull Am. Phys. Soc., 4, 178 (1959)
3.7	Freeman, A.J., and Watson, R.E.	Phys. Rev., 127, 2058 (1962)
3.8	Bleaney, B., and Stevens, K.W.H.,	Rept. Prog. Phys., 16, 108, (1953)
3.9	Merzbacher, E.,	Quantum Mec hanics, Wiley 1961 (p.515)
3.10	Ebina, Y., and Tsuya, N.,	Sci. Rep. Ritu., B-(Elect. Comm.), 15 (Suppl.) 1, (1963)
3.11	Hutchings, M.T.,	Solid State Physics Vol. 16, 227, (1964)
3.12	Lea, K.R., Leask, M.J.M., and Wolf, W.P.,	J. Phys. Chem. Sol., 23, 1381, (1962)
3.13	Bleaney, B.,	Proc. Roy. Soc., A276, 28, (1963)

CHAPTER 4

EXPERIMENTAL APPARATUS

4.1 Introduction: Principal Methods of Magnetisation Measurements

There are three major classes of methods for measuring magnetic moments; the Faraday method, which involves measuring the force on a sample placed in a non-uniform magnetic field; the indirect method of observing some phenomenon dependent upon the magnetic properties of the material; and finally, the detection of the magnetic flux density in the vicinity of the specimen.

The force method of magnetic moment determination has been used to great advantage to develop sensitive devices such as the Sucksmith ring balance (Ref.4.1) and a susceptibility balance employing the force principle is described in the next Section (4.2). There are several drawbacks to this method of measurement, the main one being that the magnetic moment is not observed in a uniform field, since a field gradient is essential to produce the force. Furthermore, this method is not readily adaptable to measurement of magnetisation versus applied field or crystallographic orientation. Objections have also been raised on theoretical grounds by Wolf (Ref. 4.2) to the use of the force method on highly anisotropic materials.

Numerous indirect ways of measuring magnetic moments via associated properties include the Faraday effect, galvano-magnetic effects, such as the ferromagnetic Hall effect, and microwave ferromagnetic resonance observations (see e.g. Ref. 4.3 page 228). The advantages and disadvantages of the indirect techniques are typified by ferromagnetic resonance measurements in which the magnetisation can be found provided that the detailed shape of the specimen is known. It is also clear that these methods are limited in that the particular

phenomenon is observed only in a narrow class of materials, and even then considerable prior knowledge about the specimen is required. In spite of these disadvantages, the indirect method can yield extremely sensitive results.

The third method relies on the detection of the induced voltage in a pick-up coil when the flux associated with the specimen changes, owing to a change in applied magnetising force or pick-up coil position in relation to the sample. An example of the first type is the Pulsed Magnetometer, in which a high field is applied to the specimen for a time of the order of milliseconds and the resultant flux change in the specimen is detected by pick-up coils situated round the specimen. The disadvantage of this method is that the pick-up coils detect the effect of the changing magnetising force upon free space as well as on the specimen. Consequently, the method is used only in pulsed field work where the required high fields (200 Koe) are achieved for times of the order of a few milliseconds and in which no other detection system is possible.

Vibrating coil magnetometers have been successfully made (Ref. 4.4) in which the coil system is vibrated parallel to the applied field. The disadvantage of this method lies in the fact that the magnetic field needs to be very uniform, otherwise complicated corrections are necessary to account for the spurious e.m.f's induced in the pick-up system. Furthermore, for small magnetic moments, the magnetic effects of materials surrounding the specimen become appreciable and added corrections are necessary.

The vibrating sample magnetometer (VSM) was developed mainly by Foner (Refs. 4.5, 4.6) and his particular system has the advantage, when using iron-cored magnets, of specimen vibration perpendicular to the magnetic field direction, thereby saving the destructive magnet redesign necessary for parallel vibration.

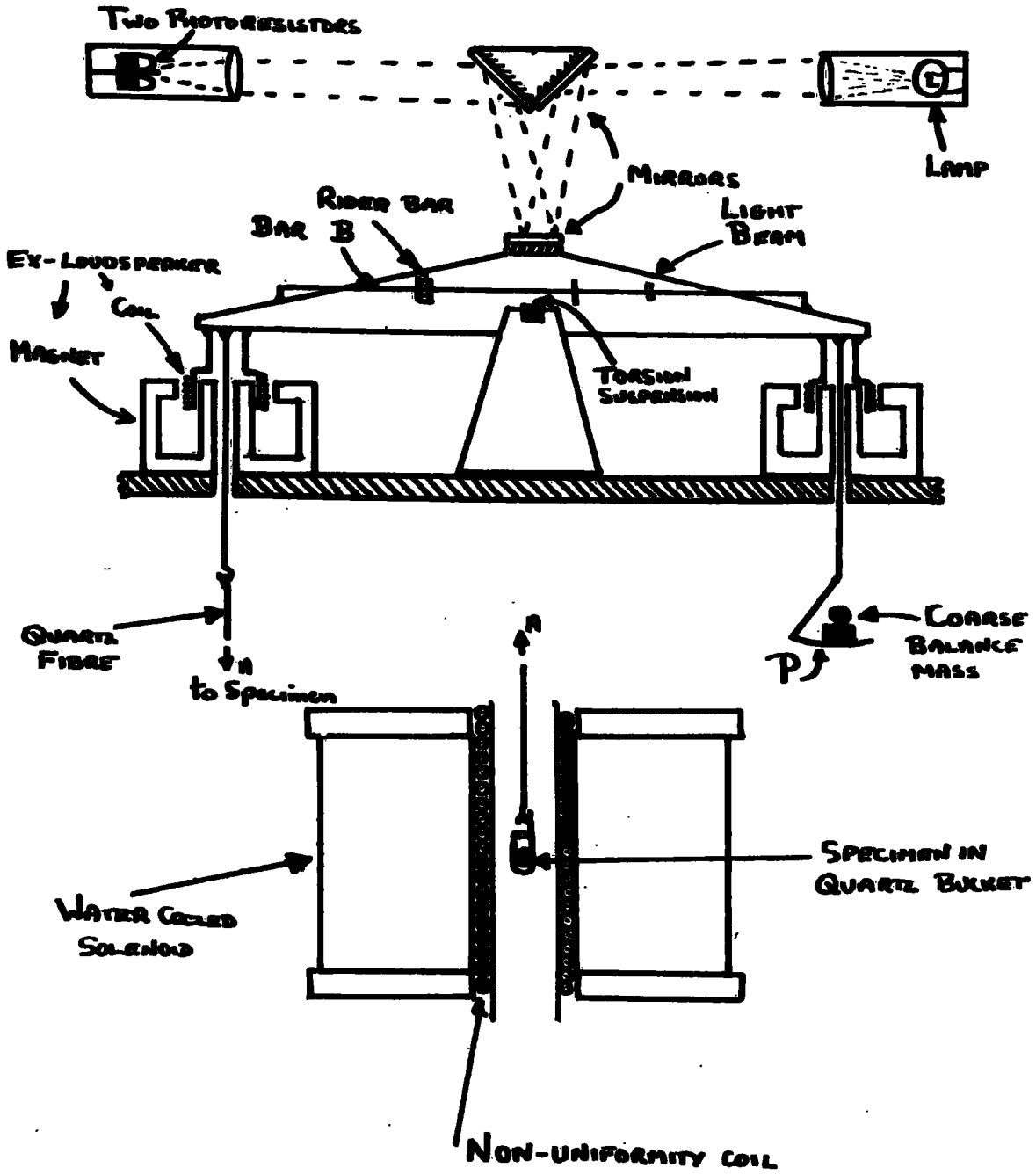

FIG. 4.2.1. SUSCEPTIBILITY BALANCE

The magnetometer developed by the author in the present work, following Ellis (Ref. 4.7), is basically similar to the Foner instrument except that an air-cored solenoid is used to provide the magnetic field and therefore a simpler pick-up coil system is possible in conjunction with vibration parallel to the field direction.

The advantages of the VSM over other types of magnetometer are that it can be made insensitive to small magnetic field instabilities, magnetic field non-uniformity, and yet be very sensitive to magnetic moment.

4.2 The Susceptibility Balance

4.2.1 The instrument used for susceptibility measurements has been described previously (Ref. 4.8) and only a brief account is given below. In the present work the apparatus was improved by the addition of a continuously variable rider system for initial balancing, and by using transitorised circuitry in place of the original valve electronics. The diagram, Fig. 4.2.1, shows the basic balance construction. The light beam has a torsion suspension at its centre, this suspension also carrying the current to the two coils situated at the ends of the beam. The coils are situated in the loudspeaker type magnets shown in the diagram. The balance condition is electronically detected by means of the optical system and the two photoresistors. Very coarse balancing is attained by addition of weights to the pan, P, less coarse and fine balance are achieved using the three riders of largely differing mass on the bar B. The ultimate balance is maintained by an electronic servosystem which acts in such a way as to keep equal illumination on the photoresistors, by adjusting the current in the two coils and hence the torque on the balance beam. When the specimen, located in a quartz bucket, is situated

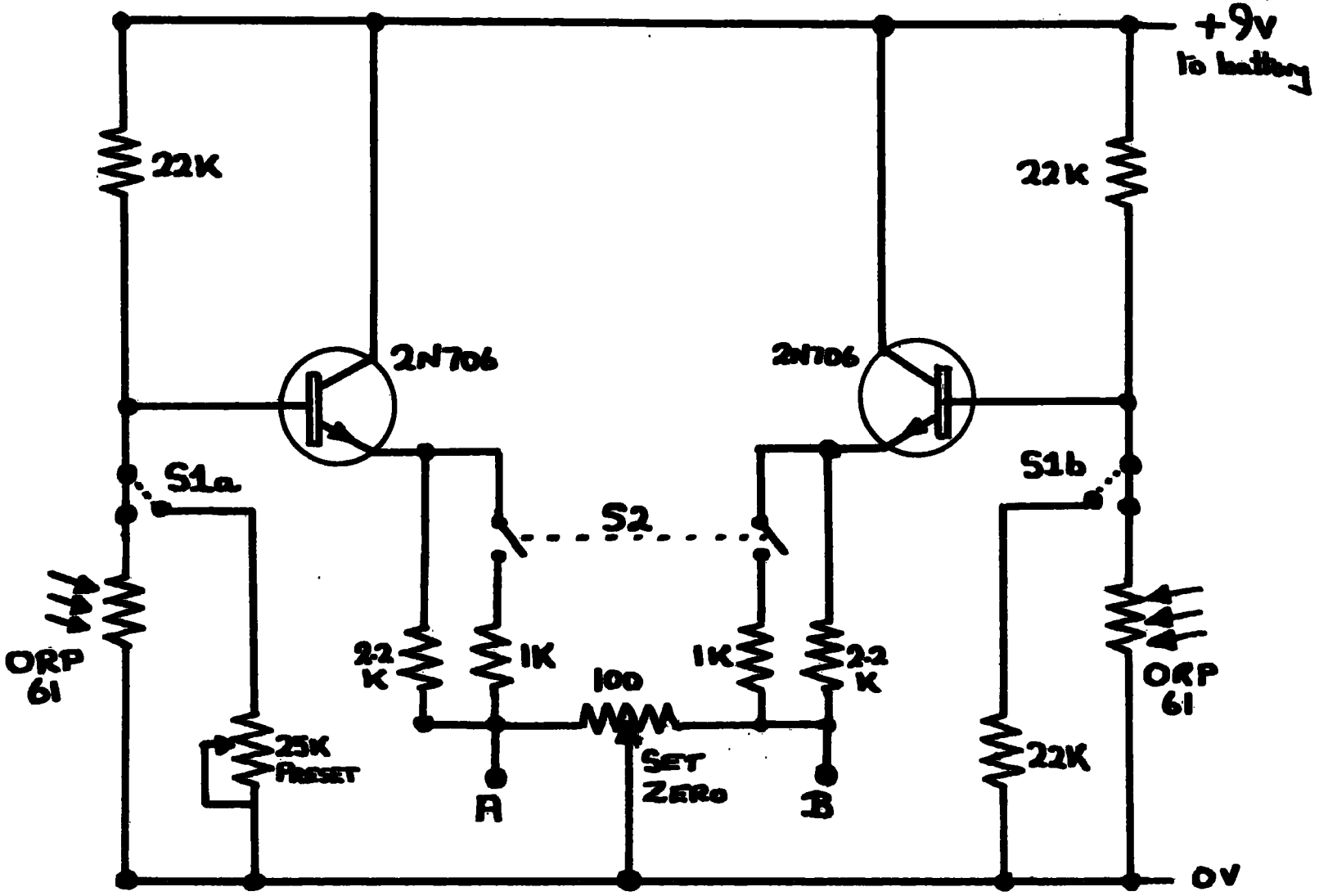

FIG 4.2.2. SUSCEPTIBILITY BALANCE SERVO-SYSTEM.

in a non-uniform magnetic field, the resultant force is detected by the momentary deflection of the beam, causing irregular illumination of the photoresistors, this in turn giving rise to a restoring torque. This torque is sufficient to return the beam to its original position minus the slight deflections inherent in any servo - system. The magnetic field is applied using a water-cooled solenoid (Ref. 4.9), the additional field gradient, or non-uniformity, being derived from the inserted coil shown in the figure.

Fig. 4.2.2 gives the circuit of the servosystem. The photoresistors are Mullard's (type ORP 61), the resistance of which decreases with increase in illumination. The output is taken to the balance coils from the points A and B. A scalamp galvanometer, connected in parallel with the coils, monitors the output voltage and gives a direct indication of the current. In setting up the balance system prior to measurement, the photoresistors are switched out (S1) and the two parallel resistors enable electronic balancing to be carried out using the set zero control. It is possible to increase the output current available by switching (S2) in the parallel emitter resistors, this, however, decreases the stability.

4.2.2. Interpretation of Measurement

For a specimen magnetised with a field H_z and situated in a field non-uniformity $\frac{dH_z}{dz}$, the force on the specimen, F_z is given by

$$F_z = Q_z \cdot \frac{dH_z}{dz} ,$$

where Q_z is the dipole moment in the z direction (Ref. 4.10).

Now,

$$Q_z = m \cdot \chi \cdot H_z$$

where m is the mass of the specimen and χ is the susceptibility per unit mass.

Therefore $$F_z = m.\chi.H_z.\frac{dH_z}{dz} .$$

The field H_z may be replaced by $C_1 h$ where h is the reading on the field control helipotentiometer and C_1 is a constant. Further, the force, F_z, is measured in terms of a change of scalamp galvanometer scale reading, ΔI. Thus $F_z = C_2 . \Delta I$ where C_2 is a constant.

We can therefore write

$$\chi = \frac{\Delta I}{m.h}\left[\frac{C_2}{C_1 \frac{dH_z}{dz}}\right] \qquad .....(4.1)$$

where the bracketed term is a constant, if $\frac{dH_z}{dz}$ is constant. The other quantities are directly measurable. By using a suitable calibration specimen the constant

$$C = \frac{C_2}{C_1 \frac{dH_3}{dz}} ,$$

may be measured. The maximum sensitivity of the balance was such that it could detect 0.25×10^{-5} emu / gm with a sample of 100 mgm. However, field instabilities caused by the water cooling (current shunting) of the magnet reduced the sensitivity by a factor of ten giving a practical limit of 2.5×10^{-5} emu/ gm.

4.3 The Vibrating Specimen Magnetometer

4.3.1 Principles of Operation

The basic principle of the magnetometer is that a magnetised specimen is equivalent to a small current carrying coil insofar as both produce a dipole magnetic field, and therefore it is possible to compare the two dipole fields by detecting the flux in their vicinity with pick-up coils.

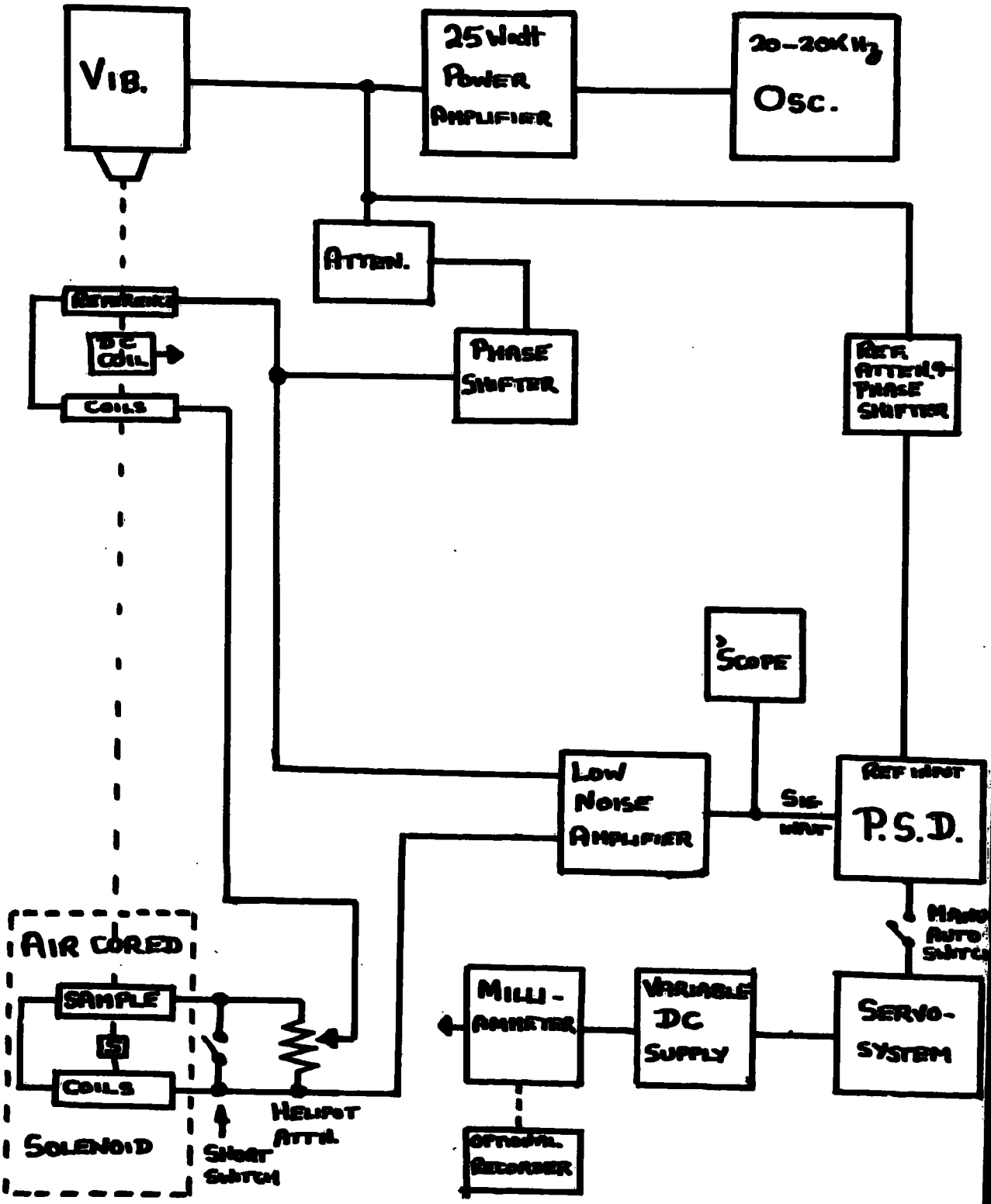
VIB.
25 Watt Power Amplifier
20-20K Hz Osc.
ATTEN.
PHASE SHIFTER
REF. ATTEN. & PHASE SHIFTER
DC COIL
COILS
SCOPE
LOW NOISE AMPLIFIER
SIG. INPUT
REF INPUT
P.S.D.
AIR CORED
SAMPLE
COILS
SOLENOID
SHORT SWITCH
HELIPOT ATTN.
MILLI-AMMETER
VARIABLE DC SUPPLY
SERVO-SYSTEM
OPTIONAL RECORDER

FIG. 4.3.1.

Figure 4.3.1 is a block diagram of the VSM built by the author. The vibrator is driven by the power amplifier and variable frequency oscillator. The vibrator is mechanically connected, via a rod, to the reference dc coil and the sample, the sample being some distance from the vibrator and reference coil, and situated in a variable magnetic field parallel to the axis of the rod. The specimen, when magnetised, acts as a small oscillating dipole, and induces an alternating emf in the sample pick-up coils. This emf may be electrically shorted by means of the "Short Switch', or reduced by using the helical potentiometer attennuator (helipot). The reference coil carries a small variable dc and consequently also appears as an oscillating dipole to the reference pick-up coils. The resultant emf in these coils depends on the magnitude and direction of the dc, and therefore this emf may be adjusted to balance that from the sample pick-up coils. Alternatively, the helipot can be adjusted to give amplitude balancing of the signals. Both pick-up coil systems comprise pairs of coils wound in series opposition, this procedure drastically reducing unwanted pick-up from the external magnetic field in the one case and synchronous vibrator derived pick-up in the other case. The dipole signals however, are added in the two coils giving twice the signal obtained using one coil. The upper coil of the pair of reference coils is in closer proximity to the vibrator than the lower coil, and in order to reduce the synchronous pick-up further, the upper coil is wound with fewer turns thereby compensating for the asymmetry of the pick-up. In spite of this, the coherent pick-up is still at an unacceptable level necessitating the use of the attenuator and phase shift network to obtain a coherent signal of equal amplitude and opposite phase to that of the coherent pick-up thereby eliminating this unwanted signal. This

process is carried out with no current in the dc reference coil and the short switch on.

Since all these signals are very small (ranging from 10μV to a few mV) it is necessary to amplify the net signal using a low noise amplifier (LNA). This has a maximum gain of 10^5 and its output is fed to an oscilloscope to provide a visible display of the signal; the oscilloscope also serves as a check on the oscillator amplitude and frequency, and the power amplifier output. The production of a null input to the LNA is further assisted by the use of a phase sensitive detector (PSD) which, apart from rejecting off frequency signals gives a coherent signal gain of a further 3dB. The PSD reference signal is derived from the power amplifier output and the necessary phase (and amplitude)is obtained with the reference phase shifter shown in the diagram.

Therefore, with this system, the specimen signal can be matched with the reference dc coil signal by adjustment of the variable DC supply. Since the specimen signal relates directly to its magnetic moment and magnetisation (see section 4.3.6(c)), these properties can be found in terms of a current in the dc coil. The instrument may be calibrated by using a sample of known magnetisation and mass (see section 4.3.6(d)), and hence the magnetometer can be used to measure the magnetisation of any specimen provided that it is large enough to be detectable (see section 4.3.6(d)).

The magnetometer is further equipped with a servo mechanism linked to the PSD balanced output which adjusts the variable dc supply in such a way as to maintain a null input to the LNA when the specimen signal alters. This system enables automatic output onto an XY recorder for magnetisation versus field, or temperature, measurements, alternatively for magnetisation variation with

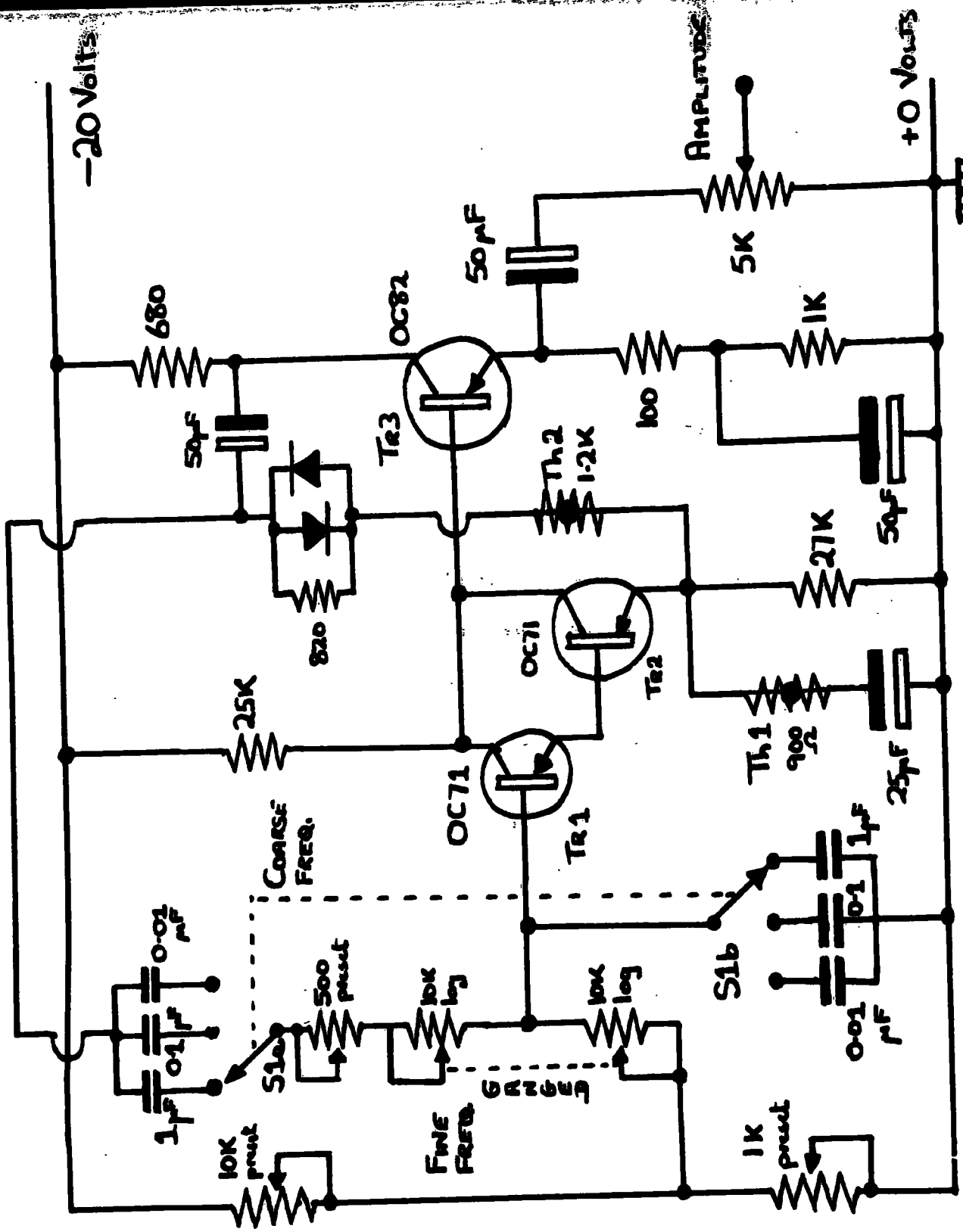

FIG. 4.3.2. WIEN BRIDGE OSCILLATOR CIRCUIT

time a normal chart recorder may be employed.

4.3.2 Electronic Details

In this sub-section details of each part of the magnetometer are given.

(a) Oscillator, Preamplifier and their Power Supply.

The oscillator is a transistor adaptation of the well known Wien Bridge oscillator and has the advantage, apart from compactness over valve circuits, that direct coupling is possible eliminating undesirable phase shifts and large high voltage capacitors.

Figure 4.3.2 shows the oscillator circuit. A frequency span of 20Hz - 20KHz is covered by three overlapping ranges switched by the 3-way 2-pole switch, fine control being afforded by the twin gang 10 K logarithmic potentiometer. The advantages of being able to vary the frequency are further discussed in section 4.3.2(c). The bias current of transistor (tr 1), is small due to its high input impedance, consequently the effect of bias resistance change in frequency alteration is minimised. The amplifier (tr3) is used to further reduce the effects of changes in the resistive arms of the bridge, the amplifier output impedance being very low. Amplitude control is exercised by the thermistor (th2 - STC type A) which is in the negative feed back element. Variation in ambient temperature also effects this control element necessitating the use of the compensating thermistor (th1, also STC type A). The impedance of this thermistor depends on ambient temperature, rather than signal level, and when the temperature rises the negative feed-back signal is reduced by the shunting effect of the thermistor. By suitable choice of the capacitor in series with thermistor 1, the reduced resistance of thermistor 2, for a rise

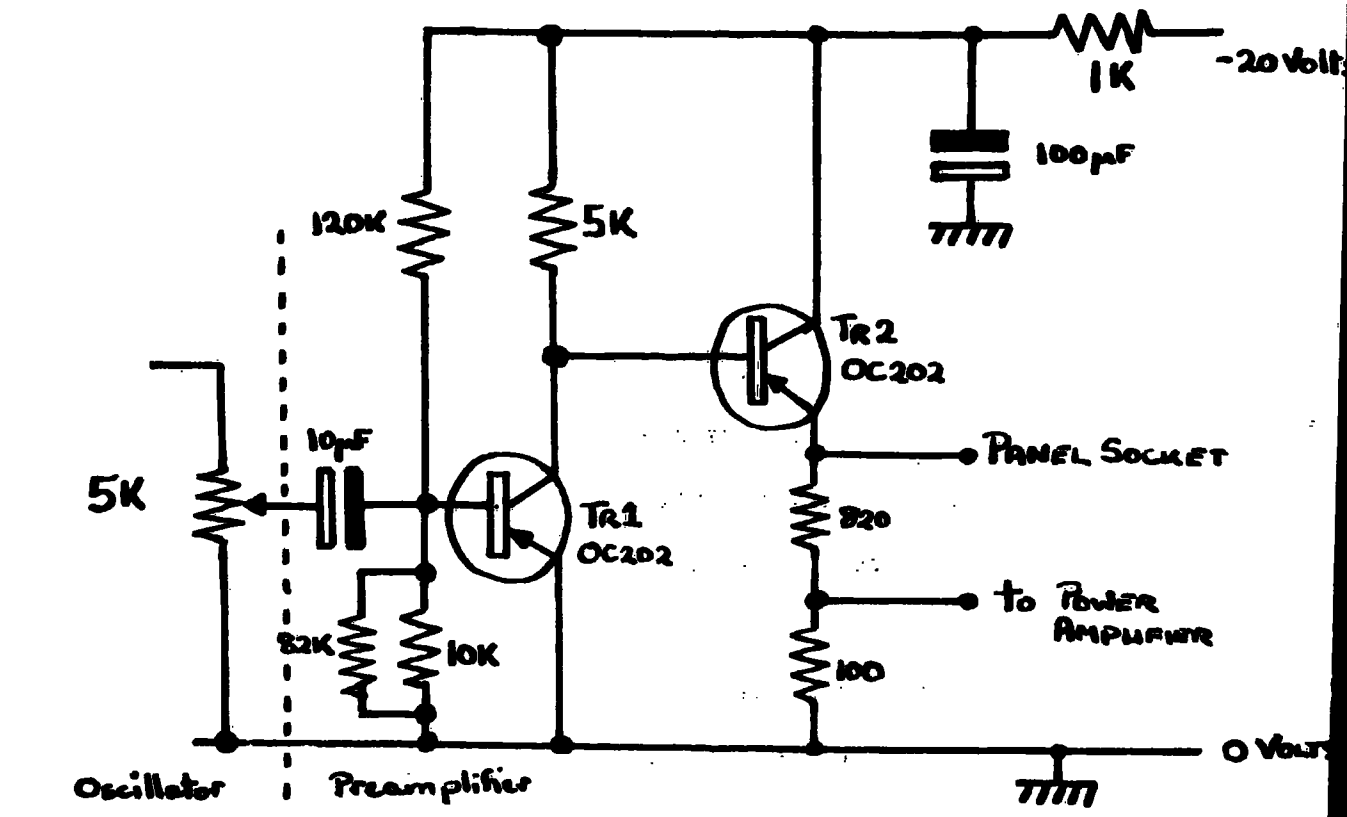

FIG. 4.3.3 PREAMPLIFIER.

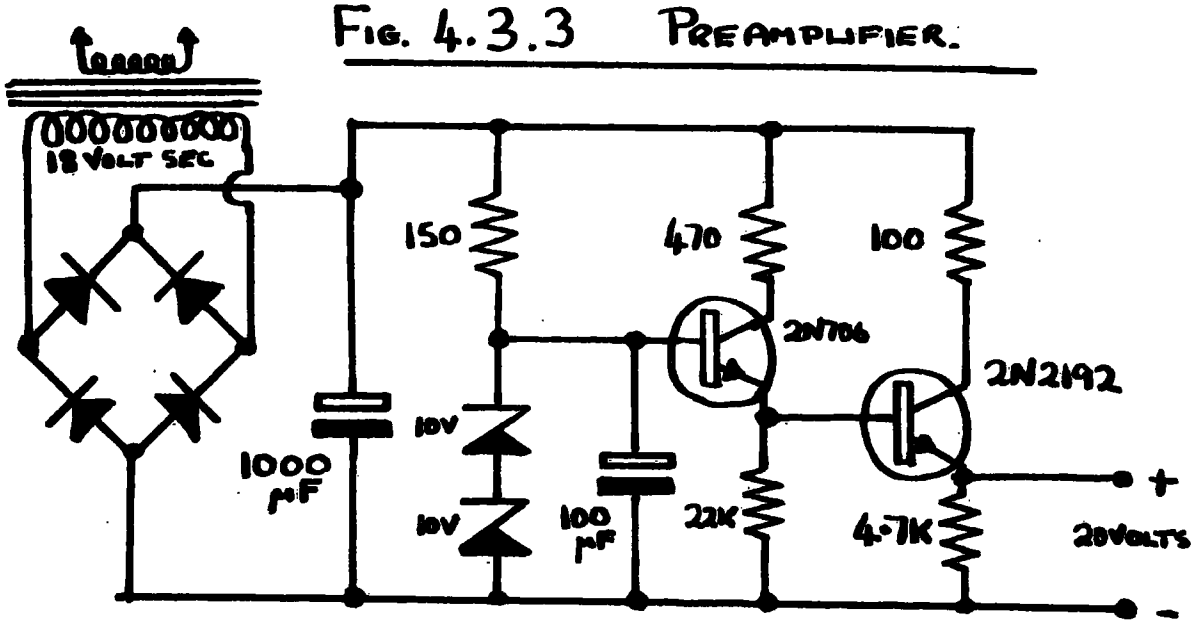

FIG. 4.3.4 20 VOLT POWER SUPPLY.

in temperature, can be exactly compensated giving the oscillator a temperature independent output. The diode network in the feedback circuit ensures reliable oscillation by virtue of the diodes' nonlinearity, a signal of some 100 mV being required to lower the effective resistance from infinity to a few hundred ohms. The critical components in the circuit are the biassing resistors of tr1, consequently preset potentiometers are used in this part of the circuit.

In order to drive the power amplifier without loading the oscillator, a preamplifier is used. The circuit is given in Fig. 4.3.3. The emitter resistance of tr2 is tapped to provide the 100 mV drive to the power amplifier, the full emitter output voltage is taken to an output on the oscillator/power amplifier chassis for monitoring the oscillator output.

The 20 volt stabilised power supply is fairly conventional and its circuit is shown in Fig. 4.3.4.

(b) The Power Amplifier.

Since the magnitudes of signals induced by the vibrating sample (and dc coil) are directly proportional to the amplitude of oscillation, it is desirable that this be as large as is feasible, allowing for mechanical limits in the rigidity of the rod and specimen tube. This requirement necessitates high input power to the vibrator, and so a 25 watt Henrys Radio amplifier was used for the purpose. This commercial unit required some modification and the circuit is shown in Fig. 4.3.5. Under heavy load conditions, the current in the earthed positive supply line is of order 1 amp, resulting in coherent ohmic signals on the supply line of up to a few millivolts. These signals were eliminated by using a separate thick positive lead from the power supply to the high current

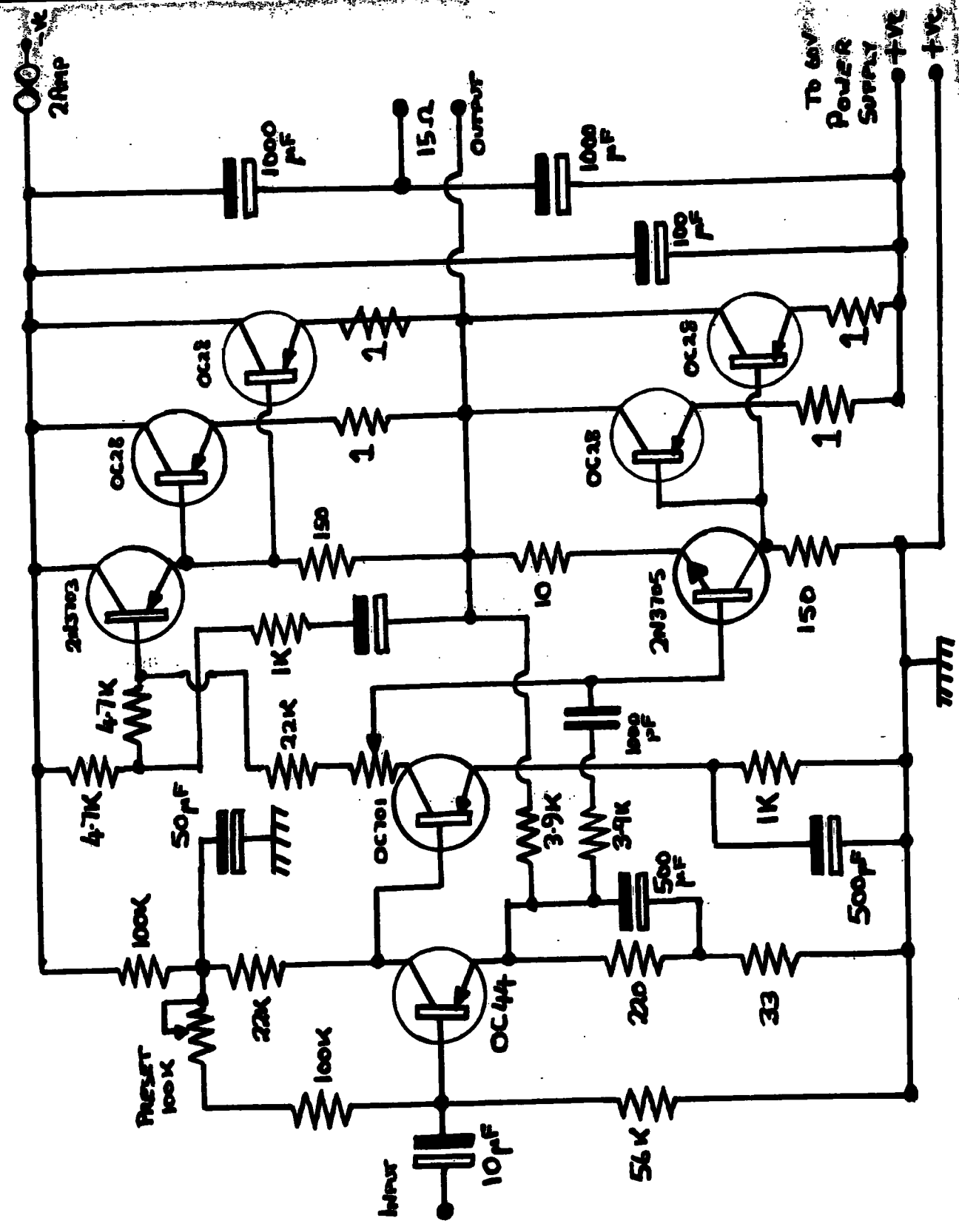

FIG. 4.3.5. 25 WATT POWER AMPLIFIER.

output transistors and decoupling further both the amplifier positive supplies (capacitors C1 and C2). The amplifier itself is of the directly coupled type giving an excellent frequency response, with less than 0.1% distortion at full output power. Under continuous high output working, it was necessary to cool the power transistors with a suitable blower, otherwise the output transistors (OC28's) tended to fail carrying the two driver transistors with them. The 8Ω output of the amplifier was matched to the 3Ω impedance of the vibrator with a suitable transformer, this affects, somewhat, the frequency response but as mentioned below is perfectly satisfactory at the operating frequency. The 60 volt power supply is a Henrys Radio MRU60 type.

The layout of the power amplifier/oscillator chassis is shown in Fig. 4.3.6. The second Fig. 4.3.7 gives the electrical interconnections for this chassis.

(c) The Vibrator and Reasons for Choice of Vibration Frequency.

The vibrator is a commercial unit (Ling Altec Shaker model 201) working on the same principle as that of the moving coil loudspeaker. It is designed for large amplitude high acceleration vibration and under working conditions gives an amplitude of about 2mm at 70 H_z. The mechanical mounting of the vibrator is treated later, in section 4.3.3.

The frequency of 70 Hz chosen as the normal operation frequency achieves the best solution to several opposing conditions. The vibration amplitude, theoretically, is inversely proportional to the frequency at a given input vibrator power, the signal induced in the pick-up coils by the oscillating dipoles is proportional to the amplitude and to the rate of change of motion, given by ν the frequency of oscillation. However, it was found that the largest

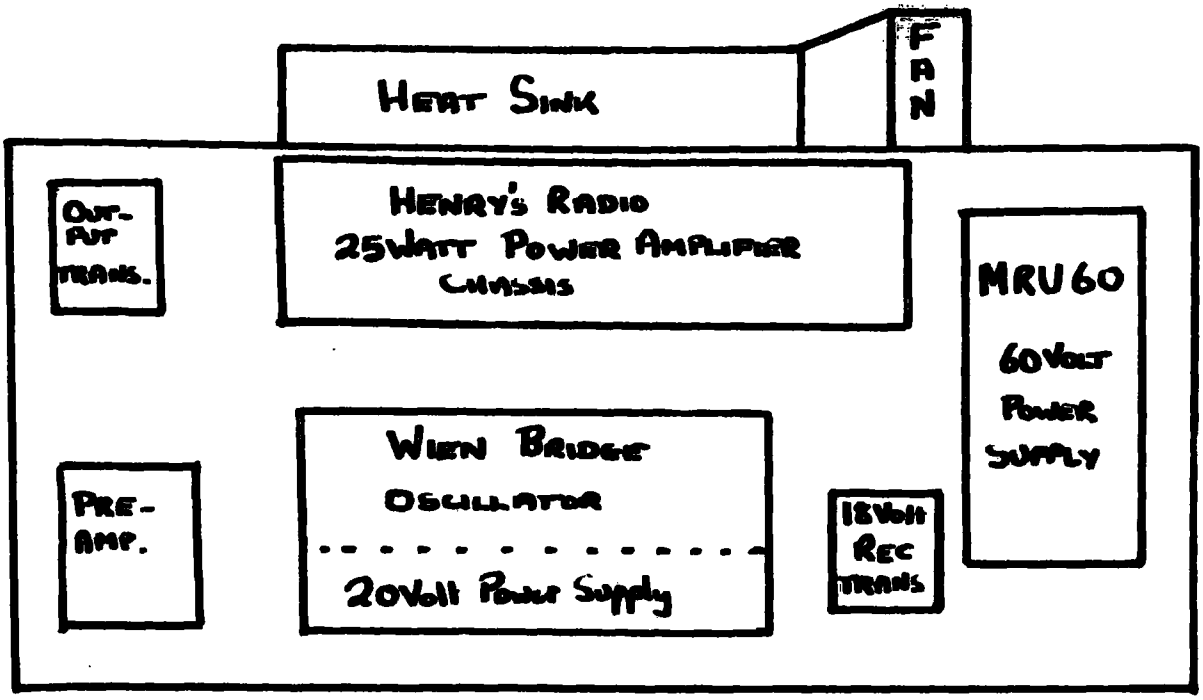

FIG. 4.3.6. OSC/POWER AMPLIFIER CHASSIS LAYOUT

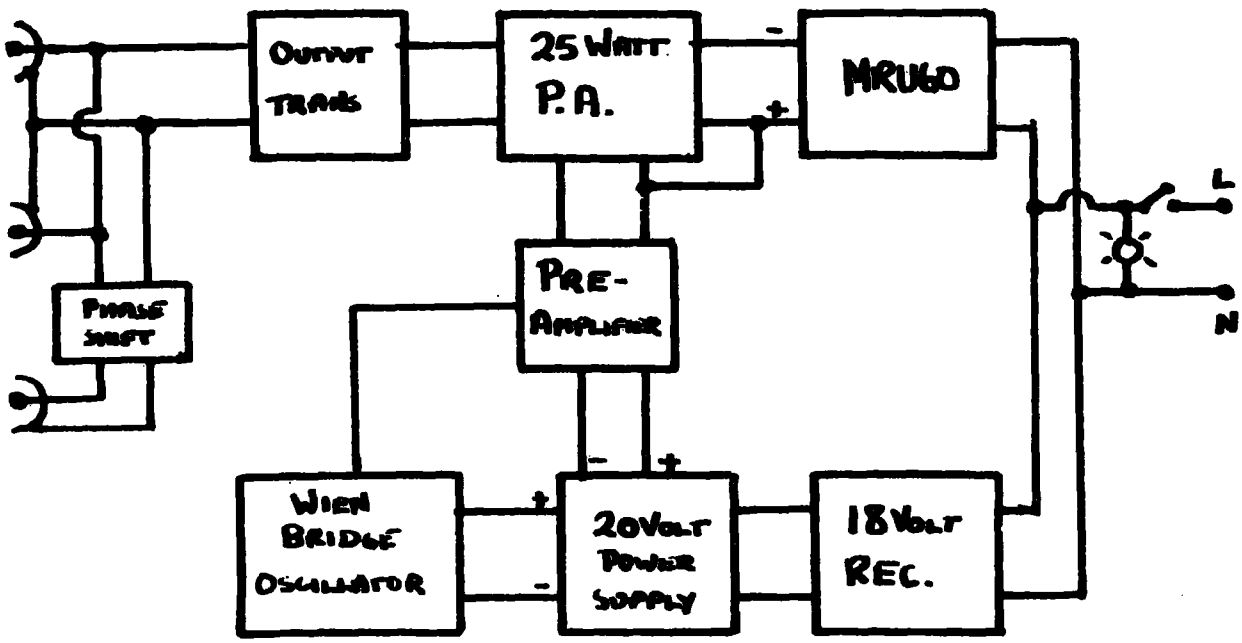

FIG. 4.3.7. WIRING DIAGRAM OF ABOVE CHASSIS

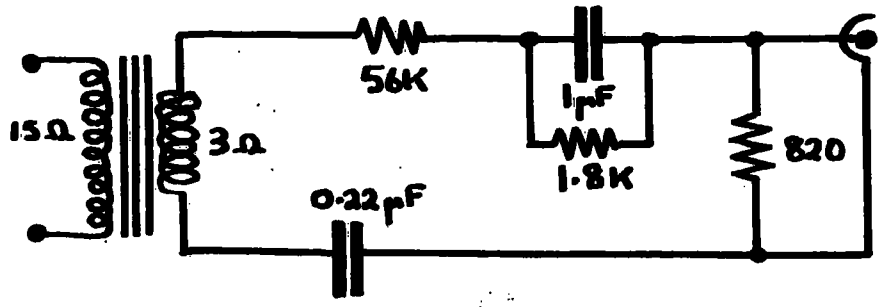

FIG. 4.3.8. PHASE SHIFT NETWORK.

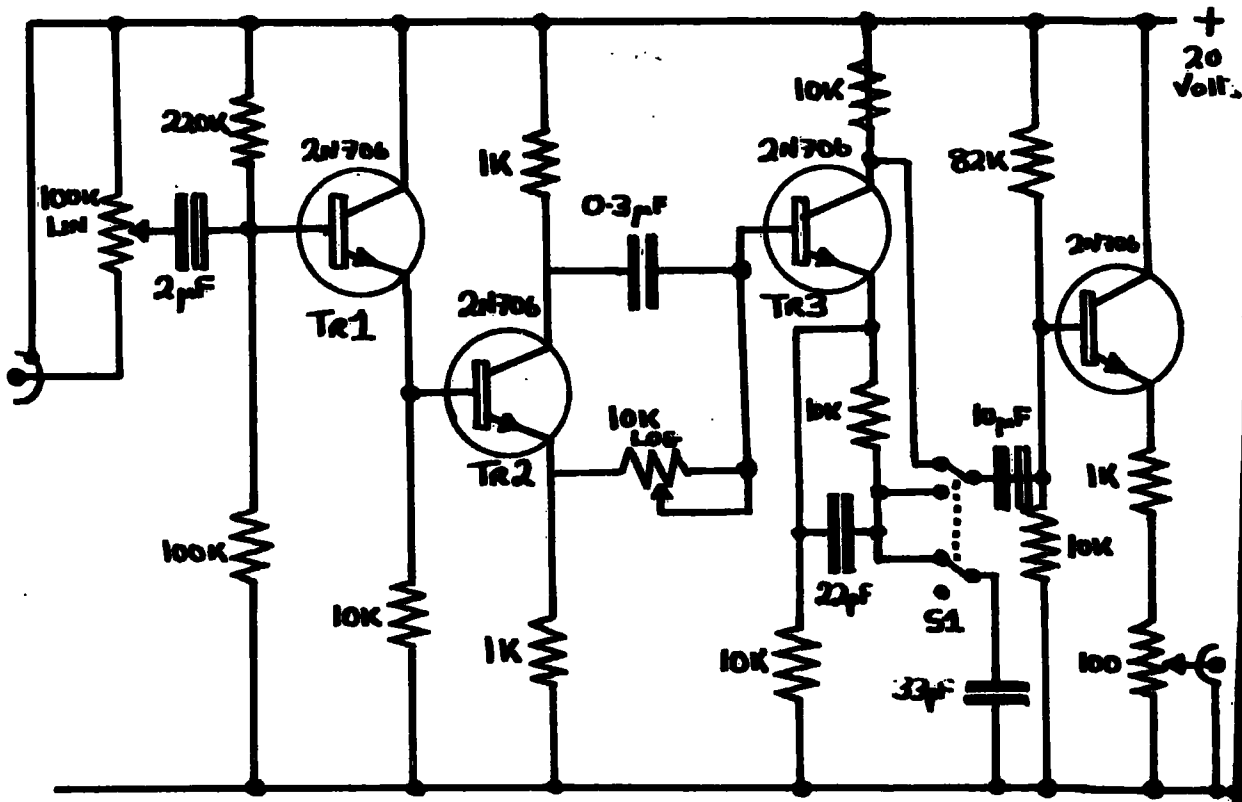

FIG. 4.3.9. VARIABLE PHASE SHIFT CIRCUIT

signal is obtained at large amplitudes and low frequency, as opposed to remaining constant at a given vibrator power. The reason for this behaviour is that the vibrator has a non-linear response of frequency vs amplitude at a given power input. The choice of a low frequency has the further conditions that it should be as far as possible from mains frequency and its harmonics. A frequency below 50 Hz suffers from beat frequency effects with mains pick-up, leaving the range 50 - 100 Hz from which 70 Hz was selected as the most reasonable operating frequency.

It should be noted that the ability to vary the frequency gives the possibility of using the electronics in a vibrating reed magnetometer. This type of magnetometer employs very much smaller specimens (< 1 mgm) mounted on a high-frequency vibrating reed and in order to ensure high amplitude, the reed is made to resonate. The normal pick-up systems and magnetometer circuitry can then be used to detect and measure the magnetisation.

(d) Attenuator and Phase Shift Network for Synchronous Pick-up Elimination.

The signal for this network is derived from the main power amplifier output transformers, and its amplitude and phase are adjusted with the preliminary circuit (Fig. 4.3.8). The adjusted signal is the input to the attenuator and phase shift circuit in Fig. 4.3.9. An emitter follower (Tr1) supplies the phase splitting stage (Tr2) which has equal amplitude but opposite phase signals on its emitter and collector. The phase of the signal that appears on the base of Tr3 varies with the setting of RV1, further, the output from this transistor can be switched with S1 giving a 180° phase shift of the input to the final emitter follower stage. The variable resistor RV2 reduces the output signal to the very small signal required to balance the synchronous pick-up. In this manner

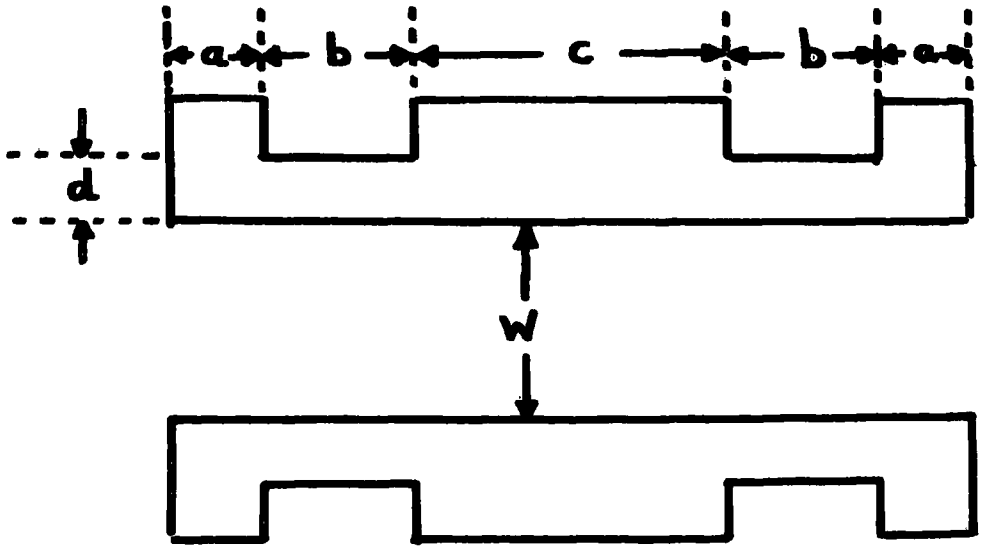

	a (mm)	b(mm)	c(mm)	d(mm)	W(mm)
LOW TEMPERATURE COIL	5	7	5	1·5	7
HIGH TEMPERATURE COIL	5	10	8	2·5	19·6

FIG. 4.3.10. COIL FORMERS

the synchronous pick-up may be eliminated, whatever its phase. The circuit is powered by a stabilised power supply similar to that shown in Fig. 4.3.4.

(e) Pick-up Coil Systems and DC Reference Coil.

The dc coil and magnetised specimen both act like small magnetic dipoles, and the usual dipole field formulae may therefore be applied to obtain the magnitude and direction of the field at any point. Since two pick-up coils are used in series opposition these must be placed on either side of the dipole in such a way that the flux change is a maximum for a given vibration amplitude. This position arises when the flux at the coil circumference is at right angles to the axis of oscillation (and the dipole) and the locus of such positions is along a cone of angle 55° with the axis. Therefore, for a given average coil radius, the average separation for maximum signal pick-up can be determined.

The reference coils, using 34 swg enamelled copper wire on a perspex former, were wound asymmetrically, as mentioned previously with 1,650 turns on the upper coil and 2,520 turns on the lower one, this asymmetry considerably reducing synchronous pick-up. The former dimensions are given in the mechanical construction diagram, Fig. 4.3.15.

Two pairs of specimen pick-up coils were devised, one for low temperature work (0 - 400K) and the other for high temperature work (300 - 1000K). The low temperature coils were wound with 650 turns each of 44 swg enamelled copper wire on a pyrophyllite former, this material being better adapted to withstanding the temperature cycling than, for example, PTFE. The high temperature coils, apart from the larger dimensions, are similar to the low temperature coils, and both coil formers are shown in Fig. 4.3.10. The high temperature system is further discussed in section 4.3.4(d).

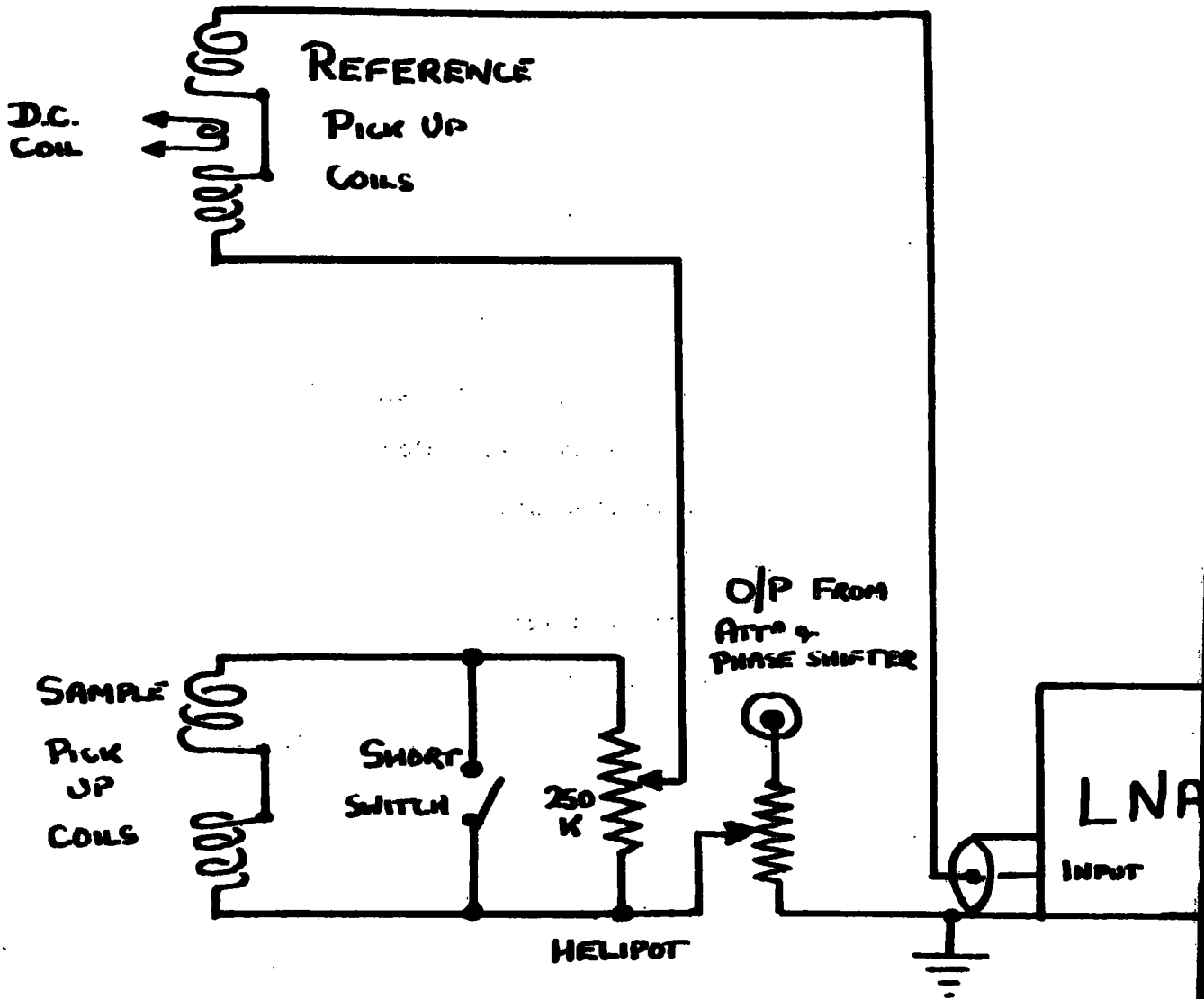

FIG. 4.3.11. L.N.A. INPUT CIRCUIT.

The dc reference coil was wound on a perspex former carried on the vibrator rod and is shown in Fig. 4.3.15. Enamelled copper wire of 34 swg was used for this coil which had 750 turns, and a resultant magnetic moment of 3.3×10^{-10} tesla m^3/mA (3.3 gauss cm^3/mA). It is perhaps worth noting that the moment of a 100 mgm specimen (of typical molecular weight = 250) with $1\mu_B$ per formula unit gives a moment of 2×10^{-9} tesla m^3. The dc coil is capable of carrying the full 50 mA output of the variable dc supply without any appreciable heating effects.

The input circuit to the LNA, showing the pick-up coils, short switch, helipot attenuator and synchronous pick-up elimination feed, is given in Fig. 4.3.11. Owing to the presence of high impedance, (LNA 80 KΩ input impedance, helipot 250 KΩ) the circuit required screening.

(f) Low Noise Amplifier (LNA).

This unit is a commercial transistor amplifier made by Brookdeal Electronics (type LA 350) and its circuits are included in Appendix 1. The amplifier has a variable band width (3dB points) and for normal 70 Hz operation the 3dB points are set at 30 Hz and 100 Hz. The maximum gain of 100 dB ($\times 10^5$, voltage gain) is adjustable in steps of 5dB down to 45 dB (200, voltage gain). The input impedance of the LNA can be switched to 80 KΩ or 2 MΩ; in the high impedance position the amplifier becomes unstable, with a high frequency oscillation, at high gain settings, so in normal use the low impedance input is used.

(g) Phase Sensitive Detector (PSD).

The PSD is also from Brookdeal Electronics (type PM322) and designed for use in conjunction with the LNA. The PSD circuits are given in Appendix 1. A

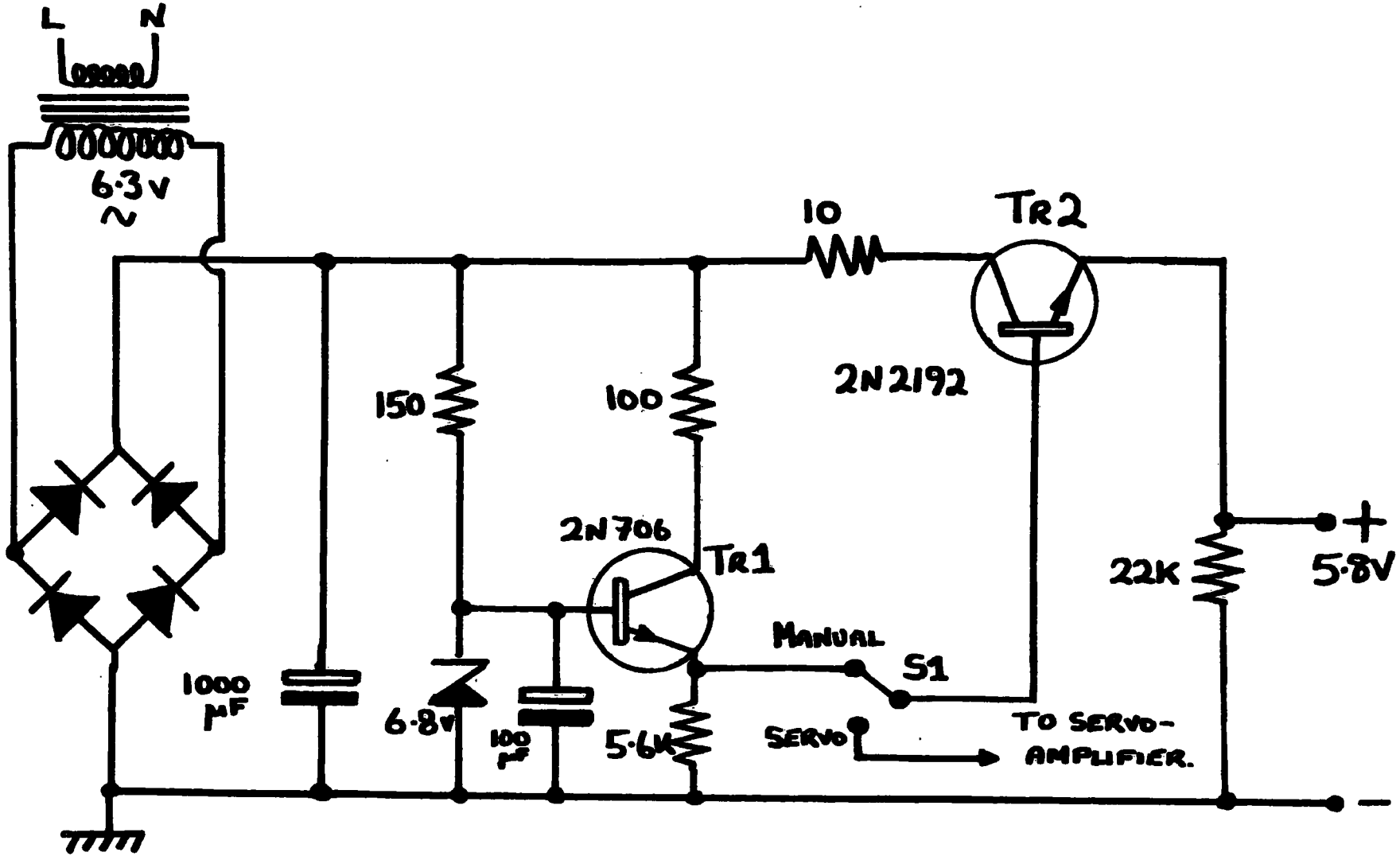

FIG. 4.3.12. VARIABLE D.C. SUPPLY.

sufficient reference signal is indicated by a neon lamp on the front panel, a similar lamp being used in the signal channel to indicate overloading. A normal PSD balanced output is supplied and this facility is used to operate the servomechanism described later (k). The balanced output is also linked to a panel meter giving a visual indication of the phase of the input signal, and it is this meter which indicates the presence of a null input (at 70 Hz) to the LNA.

(h) Oscilloscope.

The oscilloscope is a Heathkit Model OS-2 and its circuits are given in Appendix 1. The oscilloscope is used to monitor the LNA output, oscillator frequency, power amplifier output, and the LNA input, by means of a switch on the magnetometer console. Its most important role is the monitoring of the LNA output when the synchronous pick-up is being eliminated using the phase shift and attenuator circuits, since it is possible to obtain a zero on the PSD with an input signal that is $\pi/2$ out of phase with the reference. If the latter was the case then the LNA would not be usable at high gain because this out of phase signal would cause overloading.

(i) Reference Phase Shifter (PSD).

The circuit for this unit is almost identical to that of Fig. 4.3.9. except that it has preset controls and a modified output stage. The reference signal phase can be set with the preset controls by using a double beam oscilloscope to observe both it and the LNA output signal (when there is a 70 Hz input). This circuit is required mainly after the magnetometer frequency is changed when the inherent phase shift in the signal circuit changes requiring a corresponding alteration of the reference phase.

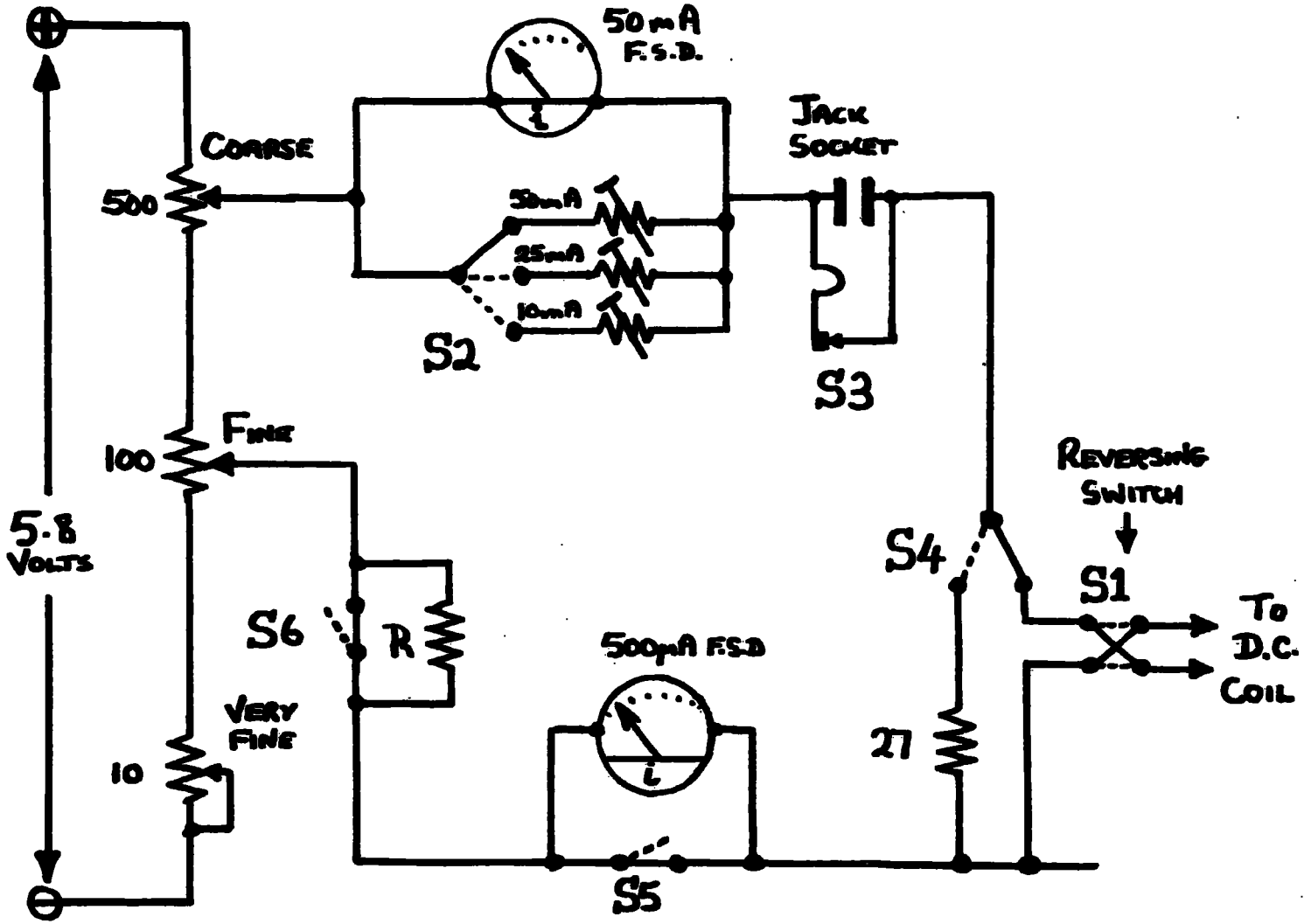

FIG 4.3.13. CURRENT CONTROL & METER CIRCUITS.

(j) Variable DC Supply and Meter Circuit.

The dc supply is a 6 volt zener stabilised type, the circuit of which is given in Fig. 4.3.12. Stabilisation is achieved by holding the base of tr1 at the zener voltage of 6.8 volts. The less than unity voltage gain of the two emitter follower configurations results in an output voltage, across the 22 K , of 5.8 volts. The supply will deliver up to 50 mA with no detectable ripple effects in the magnetometer circuits. The console auto/manual switch links the base of the output transistor to either the servo-system (next section) or the emitter of tr1.

The power supply output is connected across a potential divider which embodies the manual current controls; in the automatic mode these current controls are set at maximum. Fig. 4.3.13 gives the circuit of the meter section. A reversing switch S1, provides for the advent of reversed magnetisation in the sample, or, more commonly, reversal of the specimen pick-up coil leads or magnet current. The dc coil current is measured using the main console mounted milliammeter, this meter having three switched ranges (S2, - 10 mA, 25 mA and 50 mA f.s.d.). More sensitive measurements are made on the 500 μA f.s.d. meter, switched into the circuit by S5, or alternatively an Avometer may be plugged into the Jack socket (S3). For small currents (< 1 mA) the degree of current change for a given manual adjustment is too coarse, and in this case a normally shorted series resistor, R, may be switched (S6) into the circuit reducing the maximum current to less than 10 mA, hence giving finer current control. As mentioned previously, it is periodically necessary to check that the synchronous pick-up signal is still balanced out (i.e. no specimen signal) and in this test the dc coil current must be zero. Rather than reduce it to zero using the controls,

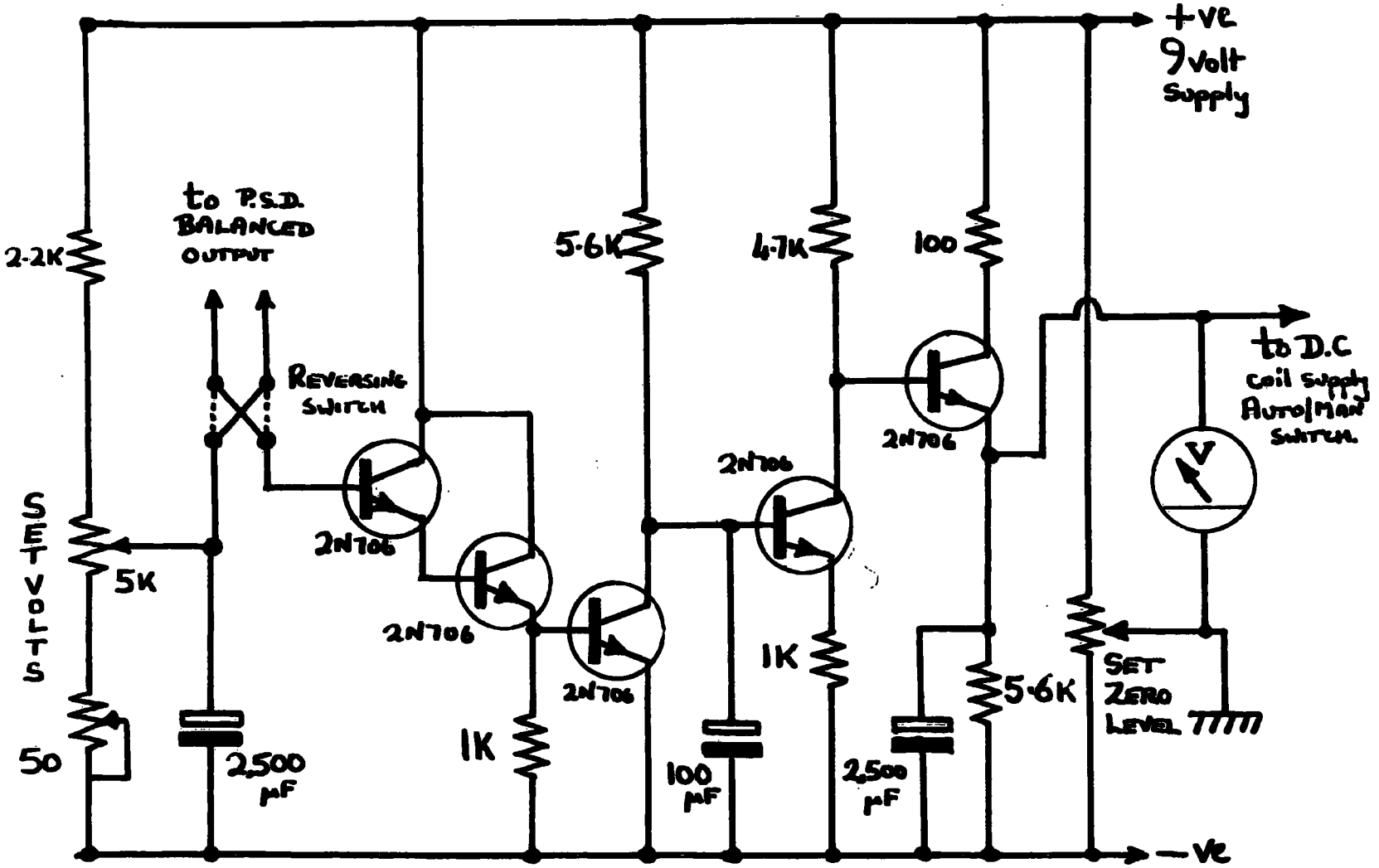

FIG. 4.3.14. SERVOAMPLIFIER CIRCUIT.

or even switching it off, the current is switched, S4, through a 27Ω resistor instead of the dc coil. This process eliminates the drift that results from intermittent use of a power supply.

(k) Servosystem and Auto/Manual Switch.

The output voltage of the dc coil power supply may be varied by changing the base voltage of its output transistor. A range of at least 0 - 6.5 volts is required for the output range 0 - 5.8 volts. The balanced output of the PSD varies by ± 10 mV (on maximum PSD output meter sensitivity) and this voltage requires amplification in order to drive the power supply output stage. The servo-amplifier circuit is given in Fig. 4.3.14. A high input impedance is obtained using the super-alpha pair (tr1 and tr2) therefore giving a minimal effect on the PSD output. The next two stages achieve the necessary gain (350) giving an output variation of 0 - 7 volts at the emitter of the final stage transistor, and in the Automatic mode this voltage is applied to the output transistor of the variable dc power supply. The PSD balanced output is smoothed internally giving a time constant of 0.3 seconds and the three large capacitors in the servo-amplifier circuit make the response time of this large enough to prevent hunting (or severe self-oscillation). The output of the servo-amplifier is very sensitive to the initial biassing of tr1 because the amplifier is directly coupled, and this biassing is achieved by means of a fine and coarse "set volts" potentiometers. In order that the dc coil current may be reduced to zero automatically, the voltage applied to the base of the power supply output transistor must be slightly negative (- 0.5 volts), and this requirement is met by floating the 9 volt servo-amplifier power supply, relative to the general magnetometer earth, using the set zero potentiometer. This

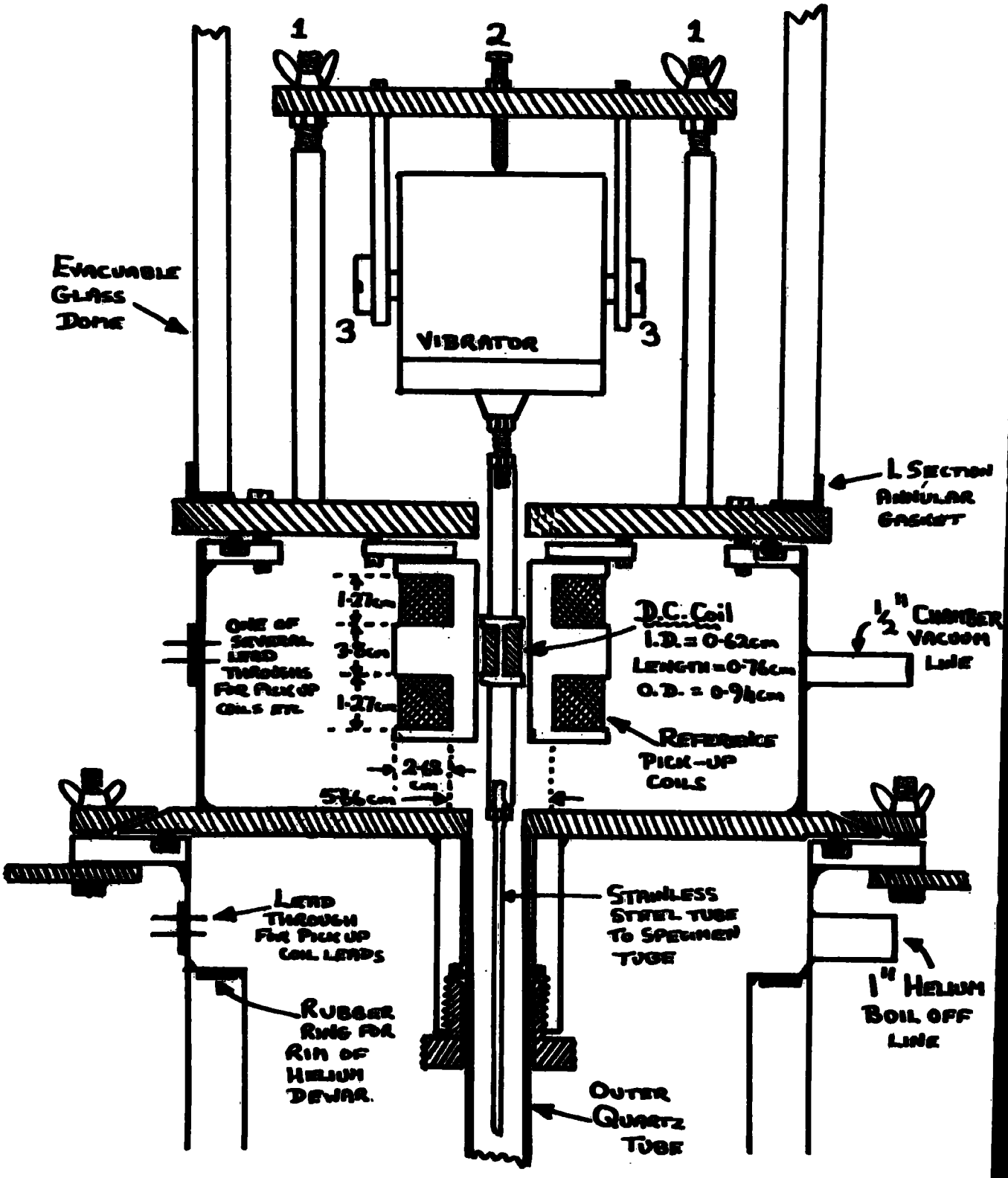

FIG. 4.3.15. MECHANICAL CONSTRUCTION.

ensures that the available drive can be set to vary from - 0.5 volts to 6.5 volts.

The magnetometer can be made to self balance by choosing the correct polarity for the servo-amplifier input using the reversing switch, this allowing for the reverse current situations mentioned in the previous sub-section. All servomechanisms require some degree of off-balance in order to operate, the extent of this being inversely proportional to the servoloop gain. In the present system, the off balance can be improved in two ways: first, the output of the servo-amplifier can be set nearer to the required value using the fine set volts control (this is not servoaction of course !); secondly, the LNA gain can be increased, until oscillation sets in, thus reducing the dc coil current error caused by the given off balance.

Automatic recording of the balance current (i_σ) against temperature (or field) can be attained by monitoring the voltage across a standard resistor plugged in series with i_σ (jack socket see Fig. 4.3.13), with an X-Y recorder. Thermocouple leads (or Hall Probe leads) are attached to the X axis input, and the Y axis input is connected to the standard resistor terminals.

4.3.3. Mechanical Details

Fig. 4.3.15 shows the mechanical construction and essential dimensions of the vibrator and reference coil assembly. The rod is attached to the vibrator by means of a 2BA stud with lock nuts at each end; the quartz sample tube which is a close fit inside the outer quartz tube (which bears the sample pick-up coils) forms the lower bearing of the vibrating system. By adjustment of the

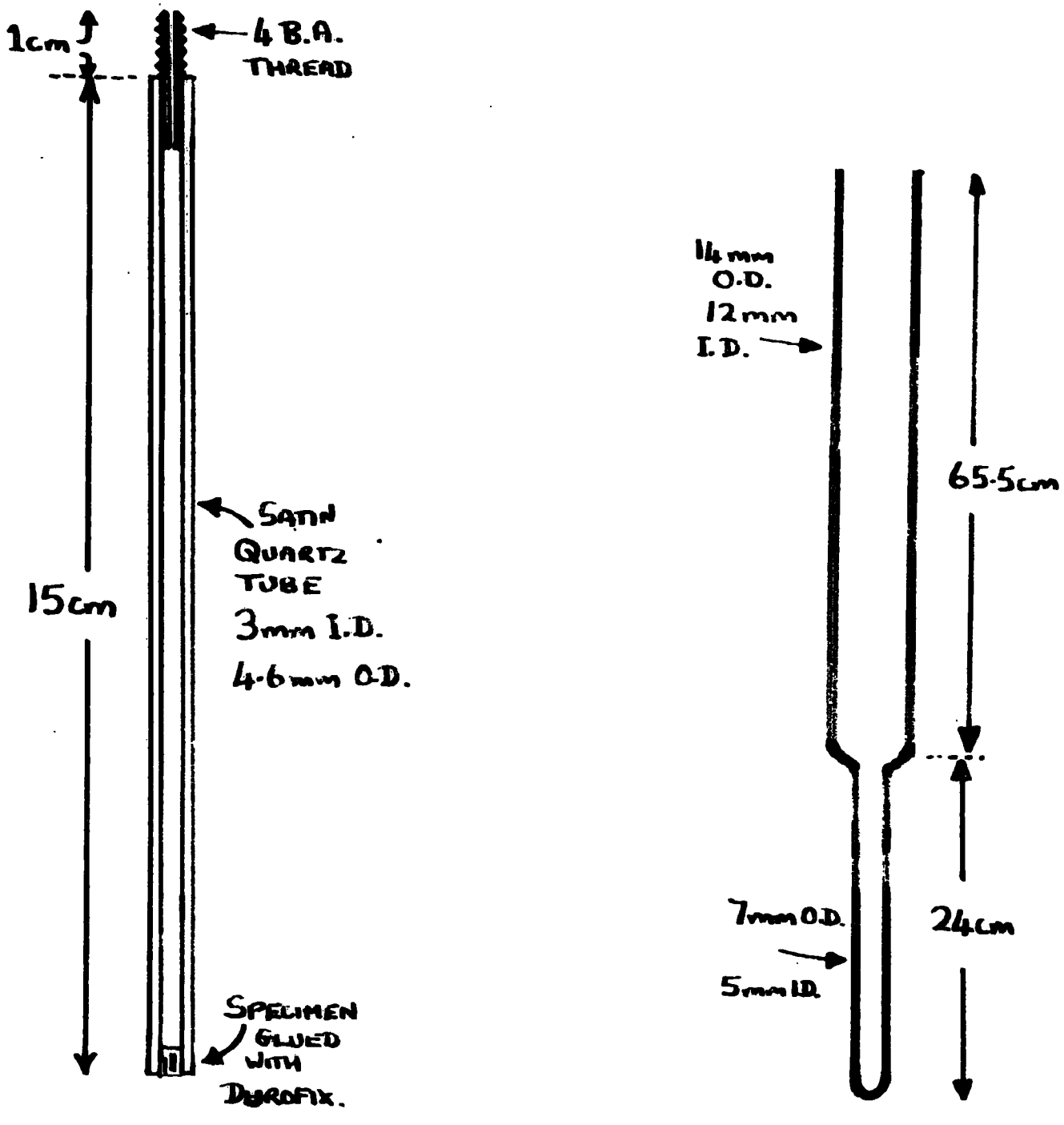
1cm
4 B.A. THREAD
15cm
SATIN QUARTZ TUBE
3mm I.D.
4·6mm O.D.
SPECIMEN GLUED WITH DUROFIX.
SAMPLE TUBE
14mm O.D.
12mm I.D.
65·5cm
7mm O.D.
5mm I.D.
24cm
OUTER QUARTZ TUBE

FIG 4.3.16.

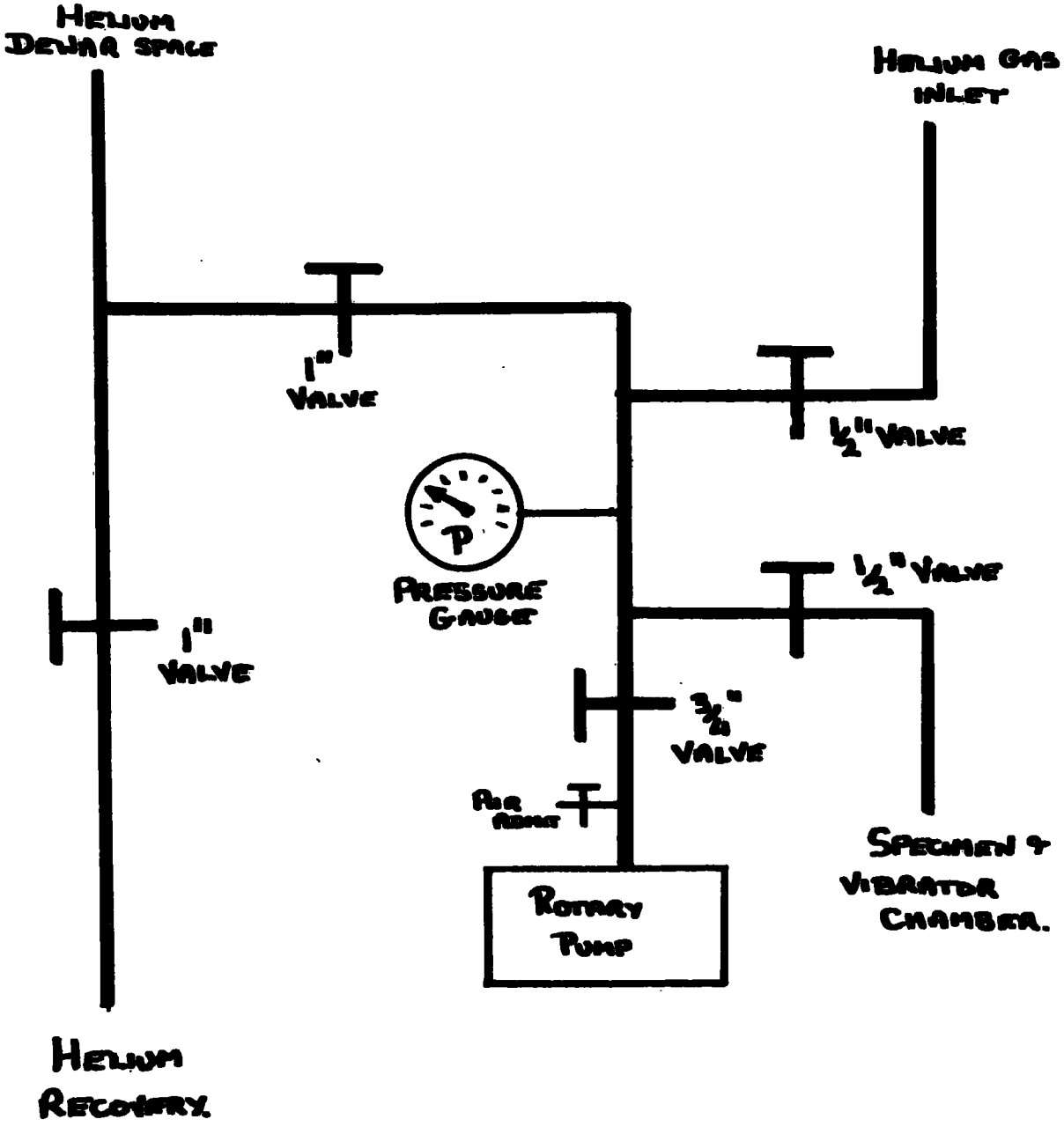

FIG. 4.3.17. VACUUM SYSTEM.

screws, labelled 1, 2 and 3 in the figure, it is possible to vary the vibrator position thereby ensuring there is no contact between the vibrating rod and the surrounding reference coil former.

During measurements the specimen tube and vibrator assembly were filled with helium gas to act as a heat exchanger and also prevent condensation or solidification of other gases at liquid helium temperature. Specimens can be changed at liquid helium temperatures simply by removing the vibrator and withdrawing the rod with the specimen tube attached, this operation being performed with a flow of helium into the reference coil chamber, to prevent any replacement of helium with air.

The dimensions of the quartz tubes used in the magnetometer are given in Fig. 4.3.16.

A photograph of the completed magnetometer appears in the frontispiece.

4.3.4 Sattelite Systems

(a) Vacuum systems.

Fig. 4.3.17 gives a schematic representation of the system. The purposes of the system are as follows:-

(i) to enable filling of the inner chamber (specimen and vibrator space) with helium gas, as mentioned above,

(ii) to allow flushing of the helium dewar with helium gas and collection of any boiled off helium gas,

(iii) to flush and evacuate the helium dewar wall space, and

(iv) to allow pumping over liquid gases (nitrogen and helium).

TABLE 4.1

Paraffin as a cooling agent in relation to Water

	Water	Paraffin
Specific heat	1	0.51
Viscosity ($20^{\circ}C$)	1	0.5
Conductivity	1	0.2
Density	1	0.8
Latent Heat of Vapourisation	1	0.065

(b) Solenoid and Power Supply.

The solenoid has been described previously (ref. 4.8) and during the present work was modified and rewound. Eddy current effects were reduced by inserting an inner core made of nylon in place of the original brass tube. The main improvement, however, was the change to forced paraffin cooling in place of water cooling, this having the effects of (i) eliminating current shunting by the water, and (ii) preventing rapid corrosion of the internal connections of the magnet by electrolysis. The disadvantages of this type of cooling lies in the far lower efficiency (~ 10 times less) of paraffin when compared to water, table 4.1 illustrates the point. This problem was overcome, in part, by the installation of three water cooled heat exchangers in the paraffin return pipe, even so, when operating the magnets at fields in excess of 10 Koe it is necessary to do so for short periods of time (< 5 minutes), or excessive heating occurs.

The magnet power supply is a Brentford 75 Kwatt (250 v and 300 A) stabilised unit, with a stability better than 1 in 10^4. The supply is coarsely controlled by a motor driven 3-phase variac, fine control being exercised by 120 parallel power transistors, in series with the current. This system in conjunction with the solenoid allows field rises to 10 Koe in as little as 10 seconds. Slower speeds are obtained with a remote control unit, which also has a continuously variable helipotentiometer for manual adjustment of the field. Two sources of stabilisation may be selected, voltage or current and it is current stabilisation that is used for the solenoid to overcome the resistance change resulting from the heating of the solenoid.

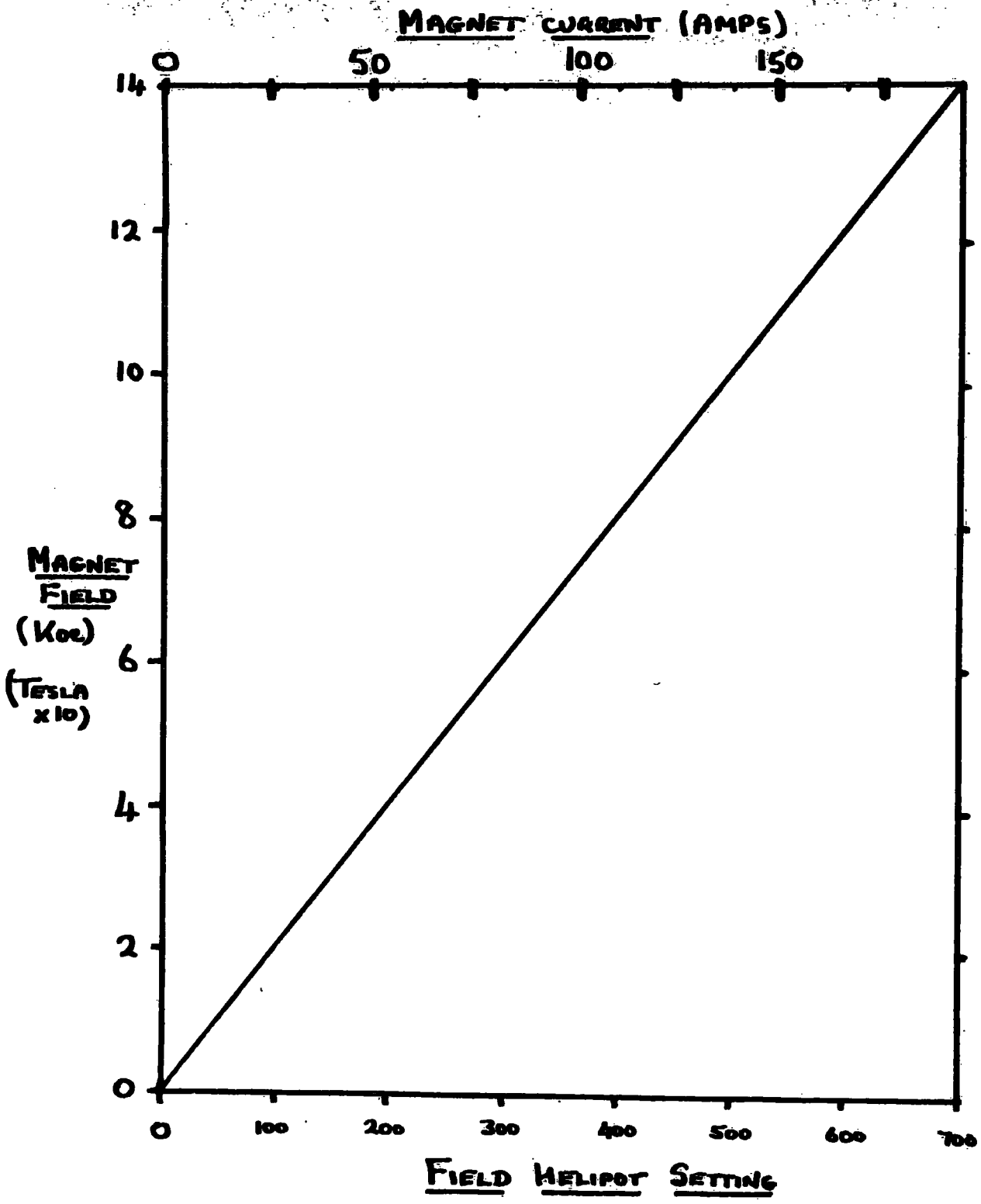

FIG. 4.3.18. MAGNET CALIBRATION.

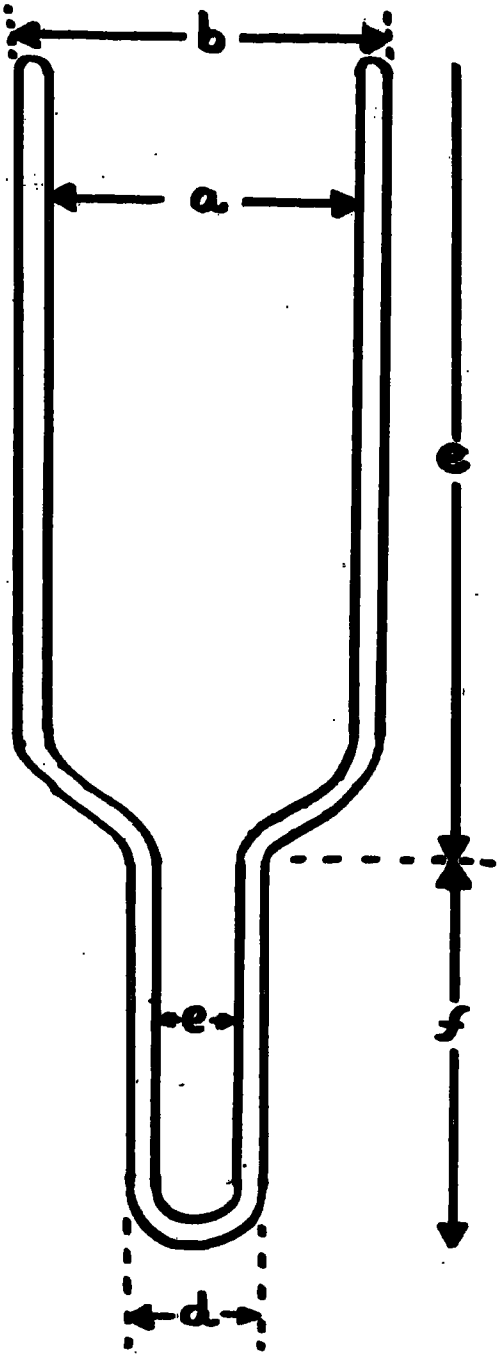

Dewar	Dimensions (in cm)					
	a	b	c	d	e	f
Helium	9·3	11·3	57	3·0	1·6	29·5
Nitrogen	13·4	15	42	4·8	3·3	30

Fig. 4.3.19. Dewar vessels

The magnet was calibrated using an Axial Hall Probe, the electronics of which are included in appendix 1. The Hall Probe was itself calibrated against the NMR of protons in water up to 5.5 K gauss (0.55 Tesla). The magnet calibration is given in Fig. 4.3.18, as a field against helipot reading or current in the solenoid, and is linear since, with paraffin cooling, all the current passes through the solenoid windings.

(c) Dewar Systems.

The dewars are made of Pyrex glass and are tailed as shown with dimensions, in the diagram, Fig. 4.3.19. The nitrogen dewar was evacuated and sealed permanently, but the inner helium dewar is flushed and pumped on each occasion of use to remove any helium gas, which can diffuse through the inner wall. Removal and replacement of the dewars is assisted by lowering the solenoid on a hydraulic mounting. Temperatures between liquid helium and room were obtained in the usual manner with the system.

(d) High Temperature Coil System.

High temperature measurements (> 400 k) using a VSM normally require a modified sample pick-up coil system so that the wires can withstand the high temperature environments. This requirement is met usually by the use of glass fibre insulation or a helically grooved former, the first method limited by the melting point of glass and the latter by the very much reduced number of turns possible for the pick-up coils. The system derived, for use up to 1000°C, is shown in Fig. 4.3.20. The furnace is wound non-inductively of Kanthal wire insulated with Refrosil quartz sleeving and held in place by the quartz nipples drawn from the inner tube. The multiturn pick-up coils are isolated from the furnace by the quartz dewar, and cooled by a continuous and variable flow of

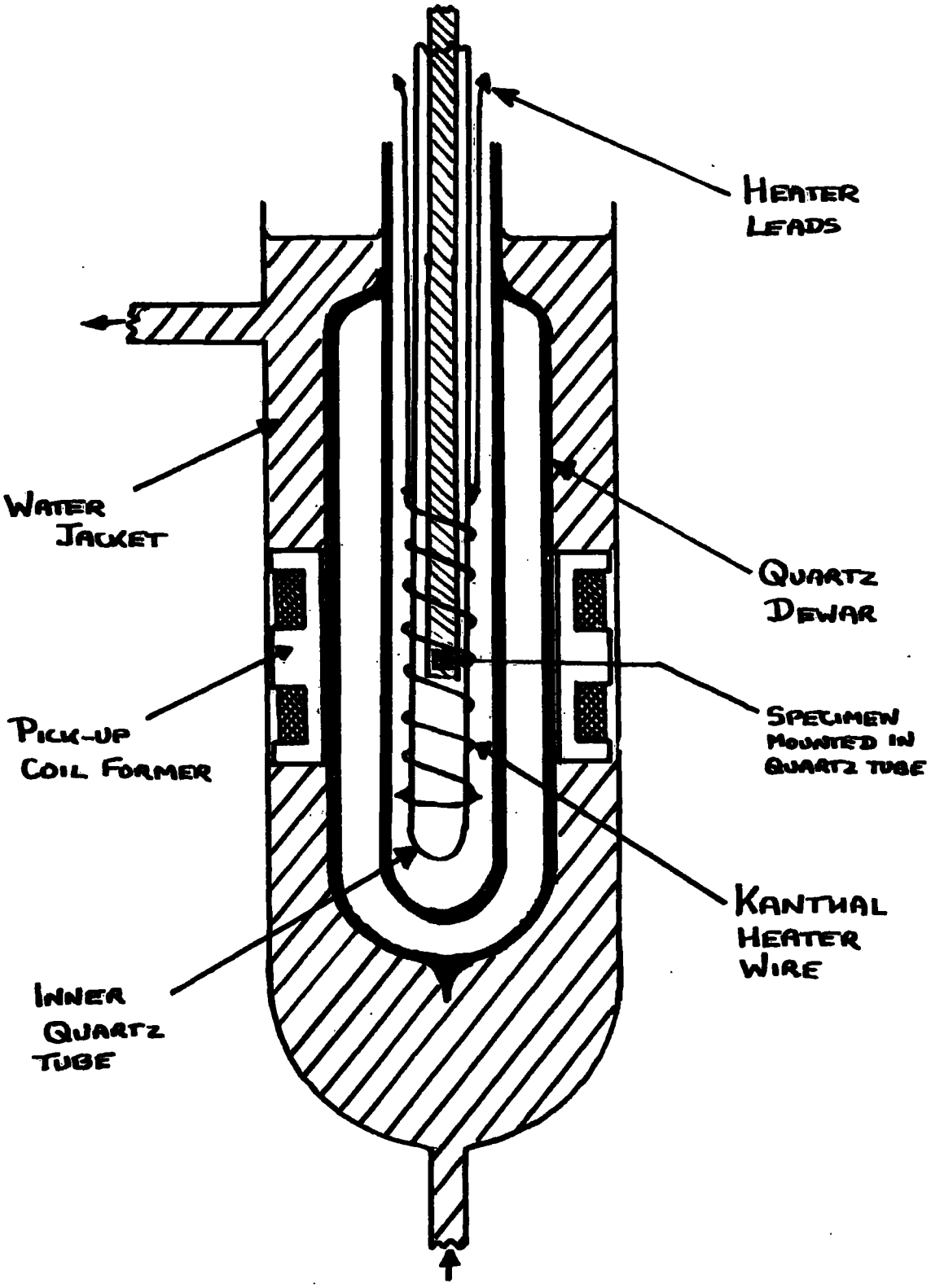

FIG. 4.3.20. HIGH TEMPERATURE SYSTEM

water down grooves on the coil former. Using this system it is possible to attain temperatures up to 1000°C with a stability governed by the control of the current and water flow, of a few degrees C.

4.3.5 Temperature Measurement

Throughout the main part of this work, temperatures were measured using a copper-constantan thermocouple in contact with the specimen. Standard thermocouple quality copper and constantan wires were used, insulated with PTFE sleeving, and the juctions made in a normal bunsen flame. The thermoelectric emf's are measured using a Pye Portable Potentiometer built into the magnetometer console, and a Scalamp Galvanometer to detect the potentiometer balance point. The thermocouple calibration was checked periodically at several fixed points and compared with the standard reference tables (ref.4.11).

More recently, for temperatures below nitrogen (77K) a gold vs copper thermocouple has been added to the system. The gold wire, available from Oxford Instruments Cryospares Division, has a small (0.2%) Iron addition, giving a thermoelectric power of about 10 μV per degree at liquid helium temperature, compared with the 1 μV per degree of a copper-constantan thermocouple. There are no standard tables available for this type of couple, so it was necessary to calibrate at liquid nitrogen (77K), pumped nitrogen (3mm pressure, 54.5°K), liquid neon (27K) and liquid helium (4.2K). A computer programme was written to fit the observed calibration points to a third degree polynomial and from the results the emf vs temperature data were calculated. The programme and data appear in appendix 2. The thermoelectric power falls

off rapidly above 100K so that its use is restricted to the range 4.2K to 77K.

It should be noted that although constantan at 4K has a fairly high susceptibility the amount of wire in the specimen area is small and only in extreme sensitivity measurements is any correction necessary. Another point is that although Gold, with iron impurity, is normally used with Chromel, giving a thermoelectric power of 16 μV per degree, Chromel is ferromagnetic at low temperature giving a signal sufficiently large to swamp any specimen requiring high sensitivity, hence the use of copper as the other junction material.

The potentiometer is designed for accumulator operation, however a small power supply was built instead and its circuit is given in appendix 1.

4.3.6 Physical Considerations

In this section, some factors such as the size of specimen and demagnetising effects are discussed, the physical methods for finding the magnetic moment and Curie point from the measurements, and finally the calibration and accuracy are considered.

(a) Effect of Variation of Specimen Size on Measured Signal.

It was thought that the size of the specimen may affect the measured signal thereby causing a varying calibration factor, dependent on the specimen dimensions. The following calculations for a spherical specimen was performed to account for the experimental fact that the calibration factor is independent of the size of the specimen.

Consider a magnetised spherical specimen of radius, r, situated at the centre of a one turn pick-up coil of radius, R, where $r < R$. The flux density

in the specimen is given by

$$B = \frac{M}{V} - D.\frac{M}{V} + \mu_o H \text{ app}$$

where M is the magnetic moment of the sphere, V its volume, D the demagnetising factor assocuated with specimen shape (see next section (b)), and H app the applied magnetising force. For a sphere D = 1/3 giving

$$B = \frac{2}{3}\frac{M}{V} + \mu_o \text{Happ}.$$

In the vsm the latter term, μ_oHapp in the equation does not contribute to the signal in the pick-up coils since it is a constant and a property of the free space the specimen occupies. Further, the signal from the vibrating sample depends on that part of the varying flux which threads the coil. This quantity, ϕ_m, is given by the equation

$$\phi_m = B.\,\Pi r^2 - \phi_L \qquad \ldots\ldots(4.2)$$

where ϕ_L represents the lost flux in the space between the specimen surface and the coil.

Now $\phi_L = \int_r^R B_{r',\theta} dA$ where $B_{r',\theta}$ is the flux density external to the specimen at distance r' and angle θ with the axis of the coil. A magnetised sphere appears externally as a dipole at its centre so that the usual dipole equations for the tangential component, B_θ, and radial component, Br, may be applied. In this case $\theta = 90^\circ$ and Br is zero giving

$$B_\theta = \frac{M}{4\pi r^3}$$

and hence

$$\phi_L = \int_r^R \frac{M}{4\pi r^3}\, dA.$$

The area element δA can be expressed radially as

$$\delta A = 2\pi r.\ \delta r.$$

hence

$$\phi_L = \int_r^R \frac{M}{2r^2}\, dr = \frac{M}{2}\left[\frac{1}{r} - \frac{1}{R}\right].$$

Therefore, from equation 4.2

$$\phi_m = \frac{2}{3}\,\frac{M}{V}.\ \pi r^2 - \frac{M}{2r} + \frac{M}{2R}$$

but

$$V = \frac{4}{3}\pi r^3$$

so

$$\phi_m = \frac{M}{2R} \qquad \ldots\ldots(4.3)$$

Equation 4.3 thus proves that the specimen signal is independent of its size and dependent only on its magnetic moment and the radius of the pick-up coils. Further calculation reveals that for a system of two separated pick-up coils the detected signal is reduced by virtue of the increased lost flux, but remains independent of the specimen size (limited, of course, by the condition $r < R$).

(b) The Demagnetising Field.

Since in magnetisation (σ) measurements it is often desired to plot σ vs field, the effect of the demagnetising field produced by the induced poles on the specimen itself must be taken into account. This demagnetising field depends on the shape of the specimen and its intensity of magnetisation (magnetic moment, or pole strength, per unit volume) thus the internal field

may be written

$$H_{int} = H_{app} + H_D$$

where H_D is the demagnetising field strength. For a flat specimen magnetised perpendicular to its main surface, the entire demagnetising field, produced by the surface poles, traverses the sample giving a maximum reverse field effect. However, in a long thin specimen magnetised along its axis, the poles at its ends produce a reverse field that is predominantly external to the specimen, resulting in a small demagnetising field effect in the specimen. The size of the demagnetising field has been calculated for ellipsoids, in which the field is uniform, and in the case of, for example, a saturated Gadolinium sphere amounts to more than 1 Koe. In the present work, with maximum fields of order 10^4 oersted, the demagnetising fields can give up to a 10% reduction in the internal field, a serious effect when extrapolating field plots (see next section (c)). Consequently the specimens were selected as needles and several of them glued in the specimen tube, to give the required sample mass, such that the field vector was along the needle axis. An alternative procedure would have been to fashion spherical specimens and use the known demagnetising factor for a sphere to find the internal field. However, the specimens are fairly reactive particularly when freshly exposed, as they would be in a "Race Track" grinder, and the use of needle like specimens reduces the field to less than 2% which is an acceptable level. The demagnetising effects were studied particularly with the calibration (iron) specimens (section 4.3.6d) and the above justifications for ignoring the effects proven within experimental error.

(c) Molecular Moment and Curie Point.

The molecular moment can be related directly to the absolute saturation moment, $\sigma_{o,o}$ (see section 3.1). Unfortunately to measure this quantity requires either an infinite field or zero temperature, so that, in practice, extrapolation from large fields at low temperature is necessary. Normal ferromagnetic materials are composed of domains, each of which has $\sigma_{0,T}$ associated with itself, but the domains may have a variety of orientations. An experimental empirical relationship has been found to apply at low temperatures for fields of 10^3 to 3×10^4 oersteds (ref. 4.3 p.265), of the form

$$\sigma_{H,T} = \sigma_{S,T} \left(1 - \frac{a}{H} - \frac{b}{H^2}\right) + cH \qquad \ldots\ldots(4.4)$$

where $\sigma_{S,T}$ is termed the saturation magnetisation, and $a > b >> c$ are constants. The terms $\frac{a}{H}$ and $\frac{b}{H^2}$ are thought to arise from domain and imperfection effects. The final factor, cH, is relatively small at fields of 30 Koe but becomes significant at higher values of H (as in pulsed magnetometry), and is thought to arise from a redistribution of spin states, resulting in an increase in the domain magnetisation above the spontaneous value ($\sigma_{0,T}$). The saturation magnetisation, $\sigma_{S,T}$, is not the same as $\sigma_{0,T}$ but at fields of $\sim 10^4$ oe it is sufficiently close for the difference to be negligible. Since in the present work it was not possible to obtain σ vs H data at low fixed temperatures, apart from 4.2K, the saturation magnetisation was obtained by extrapolating a σ vs $\frac{1}{H}$ plot to $\frac{1}{H} = 0$ at 4.2K. This point represents the application of infinite field, and at low temperature, $\sigma_{S,T}$ can be taken to mean absolute alignment of the molecular moments (i.e. $\sigma_{S,T} = \sigma_{0,0}$). From this result the molecular moment is calculated using equation 3.1.

There are many methods commonly used to determine Curie temperatures, a few examples being from the maximum in the variation with temperature of the coefficient of resistance, from the vanishing of initial permeability, or from the disappearance of the spontaneous magnetisation ($\sigma_{0,T}$). In the present work, an adaptation of the last method is used. Belov (ref. 4.12) has shown, from a thermodynamic description of the magnetic processes near the Curie point, that the relation

$$\sigma^2_{H,T} = \sigma^2_{0,T} + \frac{aH}{\sigma_{H,T}}$$ may be applied.

Thus, on a plot of σ^2 against $\frac{H}{\sigma}$ the isotherm whose linear extrapolation passes through the origin reveals the Curie temperature ($\sigma_{0,T} = 0$). This procedure requires the gathering of much data and in this work a considerably simpler and often used method is employed instead. As before, the magnetisation in fields of order 10^4 oe can be taken as the spontaneous magnetisation at temperatures not too near the Curie point, since up to a few degrees from this temperature the difference is about 1%. The molecular field predictions used by Weiss and Forrer (ref. 4.13) that

$\sigma^2_{0,T} \propto (T_c - T)$ may be used, in which case the extrapolation of a σ^2 vs T curve to zero yields the Curie temperature as the intercept on the temperature axis.

(d) Calibration and Accuracy.

It has already been stated that the magnetisation of the specimen is related to the current, i_c, in the dc coil, and this relationship is numerically established by using a specimen of known mass and magnetisation and measuring the required balance current. This calibration process was carried out using

samples of Iron and Cobalt, the magnetisation data being obtained from the absolute data of Weiss and Forrer (ref. 4.13). The magnetisation per unit mass (σ) of a specimen is then given by

$$\sigma = S. \frac{i_\sigma}{m} \qquad \text{.....(4.5)}$$

where m is the specimen mass and S the calibration constant. In atomic units the magnetisation is then obtained from equ. 3.1,

$$\sigma = \frac{S.\ i_\sigma.A}{m.\ 5586} \quad \mu_B \text{ per molecule(or formula unit)} \qquad \text{.....(4.6)}$$

where A is the atomic or molecular weight.

In practice the quantities i_σ and m are measured in milliamps and milligrammes respectively. For the original pick-up coil system the factor S was 43.65 units giving an ultimate sensitivity of 4.4×10^{-4} emu corresponding to 10 μA. For the series of compounds investigated in this work the atomic (molecular) weight is approximately 250, the maximum specimen size was approximately 100 mgm giving a maximum sensitivity in these compounds of 0.002 μ_B per formula unit. Considering equ. 4.6 the quantities liable to error are S, i_σ and m (and A, the molecular weight, to a much lesser extent owing to slight departures from stoichiometry of the compounds in their manufacture).

The error in i_σ is better than 0.5%, and m could be measured to better than 1%. The overall accuracy may be put at 2% since the i_σ uncertainty in the calibration factor, S, must be included. The calibration specimens were very carefully weighed to better than 0.1% so reducing as far as possible errors in S.

CHAPTER 4 - REFERENCES

4.1 Sucksmith, W., and Pearce, R.R. Proc. Roy. Soc. (London) 167A, 189 (1938)

Sucksmith, W. Proc. Roy. Soc. (London) 170A, 551 (1939)

4.2 Wolf, W. P. J. App. Phys., 28, 780, (1957)

4.3 Morrish, A.H. "Physical Principles of Magnetism" Wiley (1966)

4.4 Smith, D.O. Rev. Sci. Inst., 27, 261, (1956)

4.5 Foner, S. ibid., 27, 548, (1956)

4.6 Foner, S. ibid., 30, 548, (1959)

4.7 Ellis, D. Ph.D. Thesis, Durham

4.8 Thompson, D.R. Ph.D. Thesis, Durham

4.9 Hutchinson, F. Ph.D. Thesis, Durham

4.10 Zijlstra, H. "Experimental Methods in Magnetism, Part II", North Holland, (1967)

4.11 "Reference tables for Copper-Constantan Thermocouples", British Standard No. 1828, (1961)

4.12 Belov, K.P. "Magnetic Transitions", Consultants Bureau, New York, (1961)

4.13 Weiss, P., and Forrer, R. Ann. Phys. (Paris), 12, 297, (1929)

CHAPTER 5

EXPERIMENTAL RESULTS

5.1 Specimen Preparation and Lattice Parameters

The majority of the specimens were prepared at the department of Physical Metallurgy of the University of Birmingham by Dr. I. R. Harris using the standard arc furnace technique. Briefly, this consists of melting together stoichiometric quantities of the required metals on a water cooled copper hearth, under an atmosphere of pure argon at reduced pressure ($\sim$ 200 Torr), using a controllable electric arc. The lower face of the melted button is, of course, in contact with the cold copper so that it is necessary to turn the specimen over and remelt it several times to obtain a homogeneous mixture. The difficulty in obtaining single phase RB_2 compounds was mentioned in chapter 2 and in this work each specimen was vacuum annealed just below the peritectic temperature for about 10 days. The specimens were examined visually for excessive oxidation (severe blue discolouration of the surface, or worse) and otherwise any thin oxide film was removed by filing in an argon atmosphere glove box. Powdered samples from the button specimens were examined by X-ray diffraction using an 11 cm Debye-Scherrer powder camera. The films so obtained, were analysed in the usual way, the lattice parameter being derived from a Nelson Riley extrapolation (ref. 5.1) to eliminate systematic errors. A computer programme was written for analysing cubic powder diffraction patterns and appears in appendix II.

The lattice parameters are given in table 5.1 and are plotted as a function of composition in fig. 5.1. All the $(Nd,Gd)Co_2$ specimens were single phase to the limit of X-ray powder pattern determination ($\sim$ 1%).

TABLE 5.1

Lattice Parameters of $Nd_xGd_{1-x}Co_2$, C15 Cubic Laves Phase

Composition	Lattice Parameter a in Kx
x	(Å = Kx x 1.00202)
0	7.2425
0.17	7.2472
0.33	7.2509
0.45	7.2568
0.5	7.2601
0.55	7.2619
0.57	7.2632
0.59	7.2675
0.67	7.2682
0.70	7.2706
0.83	7.2752
1.00	7.2835

5.2 Magnetic Measurements

The saturation magnetisation ($\sigma_{S,T}$) was obtained for each specimen at 4.2K from the magnetisation versus field data using the vibrating sample magnetometer by extrapolation of the σ vs $\frac{1}{H}$ plot to $H = \infty$ (chapter 4 section 4.3.6c). The magnetisation versus temperature behaviour was examined at a variety of fields from zero to 8 kOe. The latter data was used to find the Curie temperature using a σ^2 vs T plot extrapolated to zero magnetisation (also see chapter 4 section 4.3.6c). Those specimens which were found to exhibit compensation points were examined under conditions of zero applied field to obtain the temperature at which the magnetisation reversed (T_{comp}). All the specimens were further checked for compensation points using the elegantly simple method of Gorter and Schulkes (ref. 5.2) in which the specimen is allowed to warm up (from, e.g. 77K) while suspended on a torsion free thread between the poles of a small magnet ($\sim$ 2kOe). As the compensation temperature (if any) is reached the specimen can be seen to "free" itself from the magnetic field and above this temperature it rotates through 180° as the magnetisation reverses direction. In this process the spins, which cause the magnetisation, remain fixed relative to the specimen, the inertia of the spin system as a whole exceeding that of the specimen, whereas if the specimen were fixed, as in VSM measurements, the spin system is made to rotate by any applied field (see chapter 3 section 3.2).

Table 5.2 contains the magnetic data for the $(Nd,Gd)Co_2$ series giving σ_{sat}, % saturation, T_c and T_{comp} where applicable. In fig. 5.2 is shown

TABLE 5.2

MAGNETIC DATA FOR $Nd_xGd_{1-x}Co_2$

Composition x	σ_{sat} μ_B/formula unit	% Sat. at 12kOe	T_c K ± 2 unless otherwise stated	T_{comp} K ± 2
0	5·09	96	416	-
0·17	3·54	91	362	-
0·33	2·23	91	301	-
0·45	1·12	89	275	-
0·5	0·59	80	253	-
0·55	0·18	66	240	-
0·57	0·00	0	235	90,205
0·582	-	-	235	126
0·59	0·33	74	230	146
0·615	-	-	225 ± 5	171
0·63	-	-	220 ± 5	180
0·67	1·00	85	200 ± 10	200
0·7	1·24	88	202	-
0·75	2·045	88	185	-
0·83	2·89	87	156	-
1·0	4·20	91	113	-

the variation of σ_{sat} and % saturation (percentage of σ_{sat} at maximum applied field) with composition, while in figure 5.3 is given the variation of T_c across the series, and in fig. 5.4 the compensation point versus composition is plotted. Figs. 5.5 - 5.20 show some typical behaviour of selected compounds throughout the composition range.

A few specimens of the series $(Nd,Gd)Ni_2$ were made to find the behaviour of the (Nd-Gd) sublattice magnetisation, and the saturation moment and Curie temperature versus composition are plotted in fig. 5.21.

Susceptibility measurements at elevated temperatures were made on all the compounds but these were severely affected by second phases in most cases. Fig. 5.22 shows the behaviour for the $GdCo_2$ and $Nd_{.17}Gd_{.83}Co_2$ specimens and Fig. 5.23 for $Nd_{.9}Gd_{.1}Co_2$, a typical biphase material. The results of these measurements are discussed together with the other results in the next chapter.

CHAPTER 5 - REFERENCES

5.1 Nelsen, J.B., and Riley, D.P., Proc. Phys. Soc., 57, 160, (1945)

5.2 Gorter, E.W., and Schulkes, J.A. Phys. Rev. 90, 487, (1953)

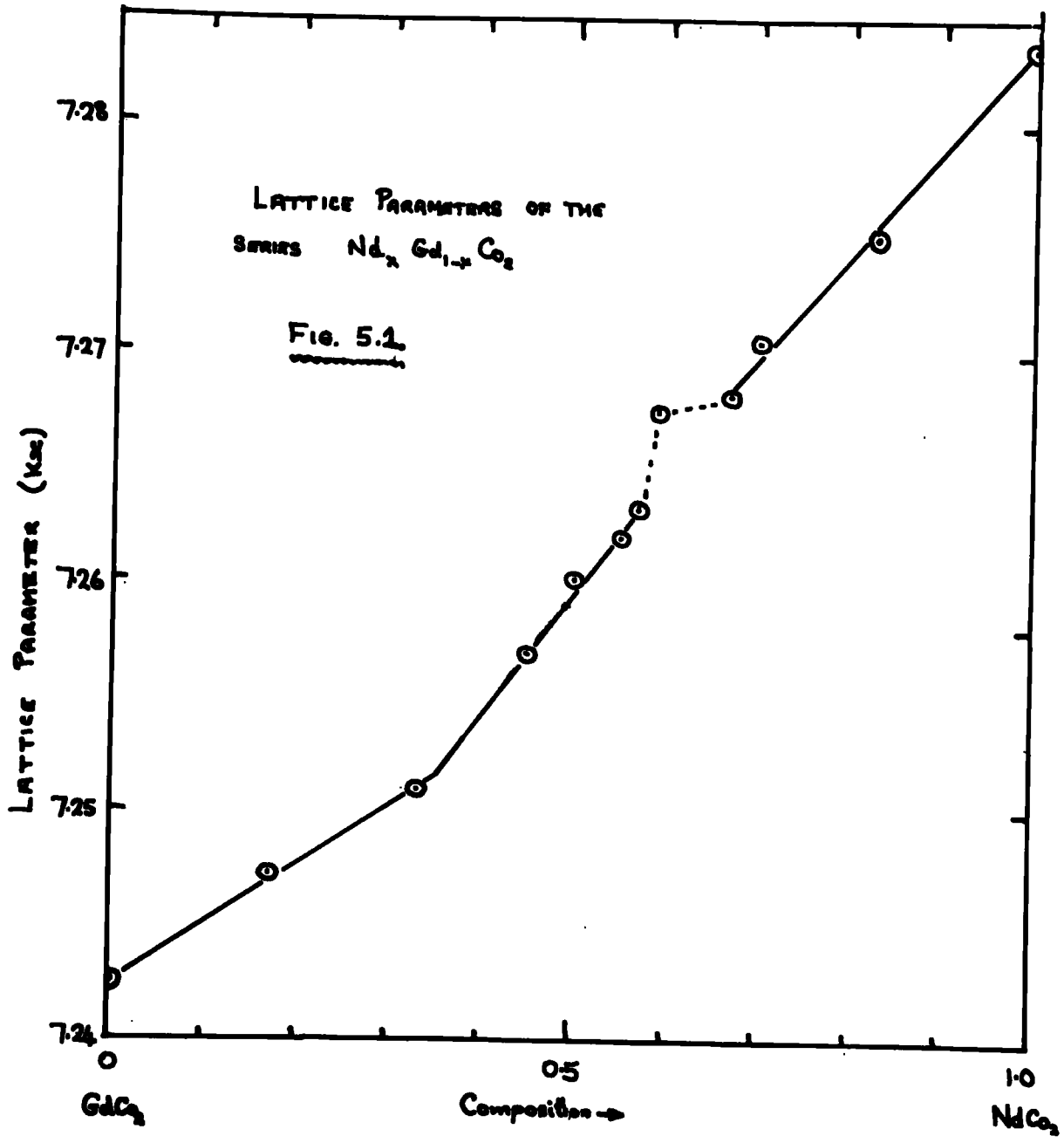

Lattice Parameters of the series $Nd_x Gd_{1-x} Co_2$

Fig. 5.1

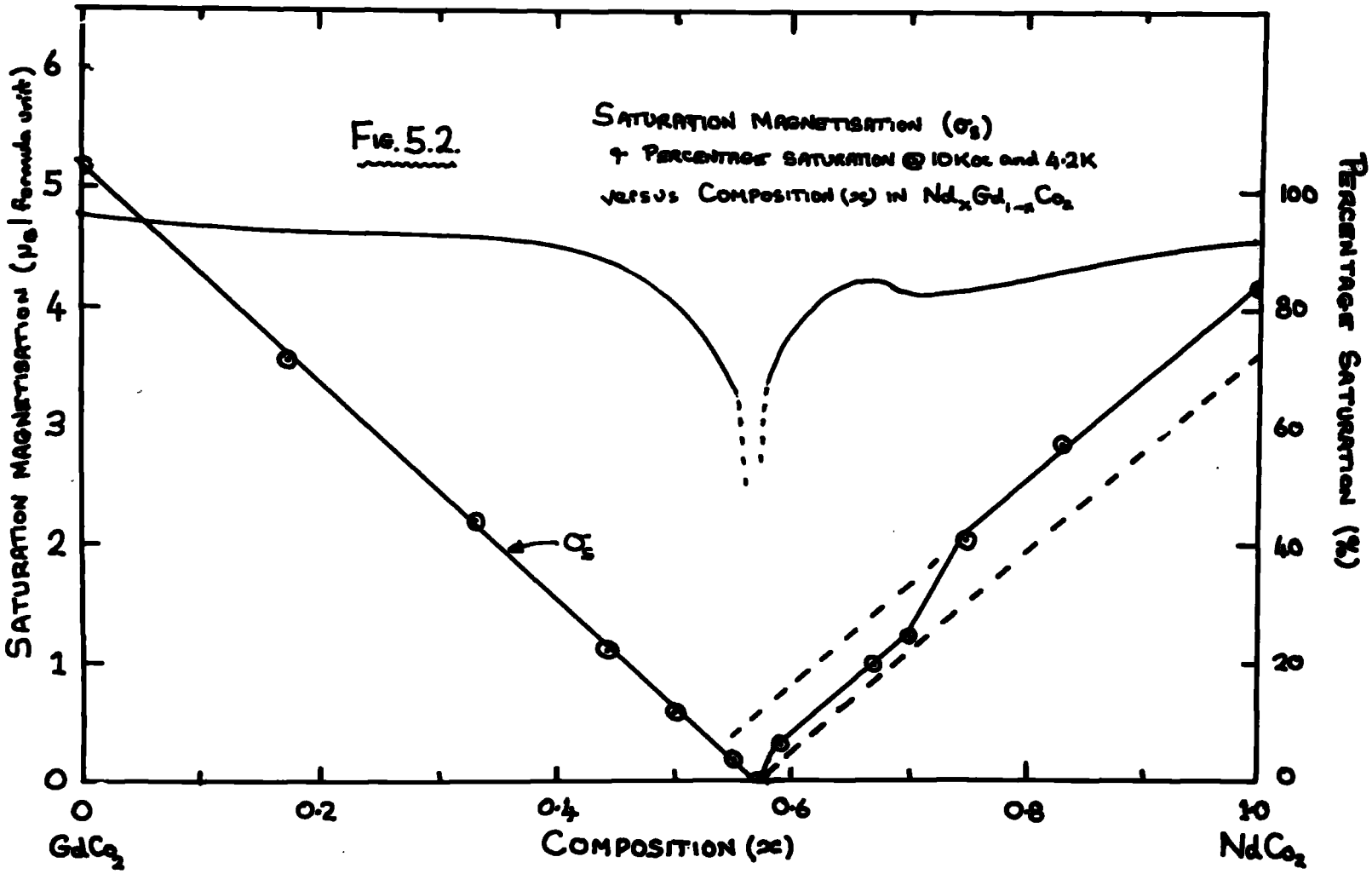
Fig. 5.2.
Saturation Magnetisation (σ_s)
& Percentage Saturation @ 10Koe and 4.2K
versus Composition (x) in $Nd_xGd_{1-x}Co_2$
Saturation Magnetisation (μ_B/Formula unit)
Percentage Saturation (%)
Composition (x)
σ_s
0
1
2
3
4
5
6
0
20
40
60
80
100
0
0.2
0.4
0.6
0.8
1.0
$GdCo_2$
$NdCo_2$

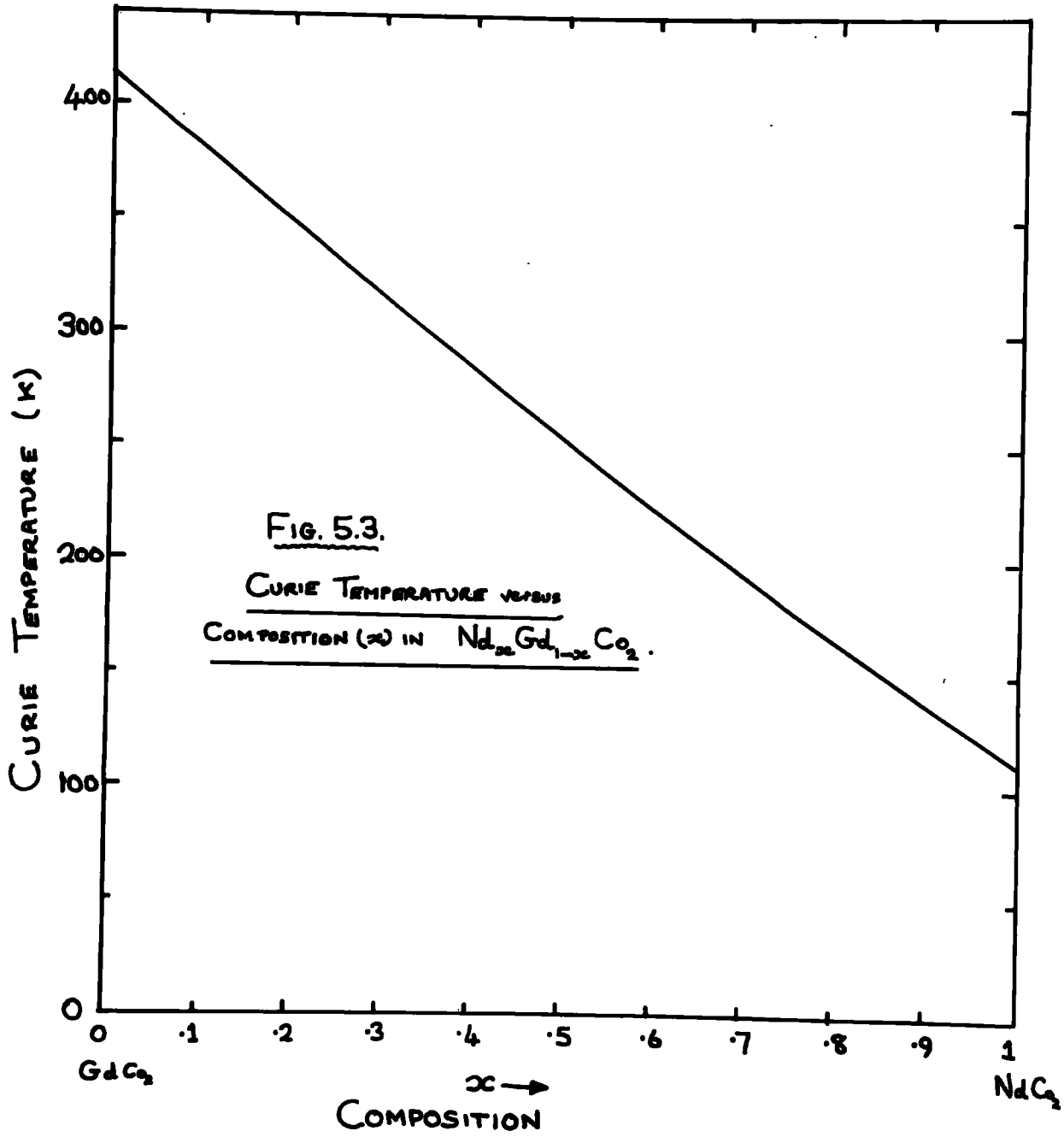

FIG. 5.3.

CURIE TEMPERATURE VERSUS COMPOSITION (x) IN $Nd_xGd_{1-x}Co_2$.

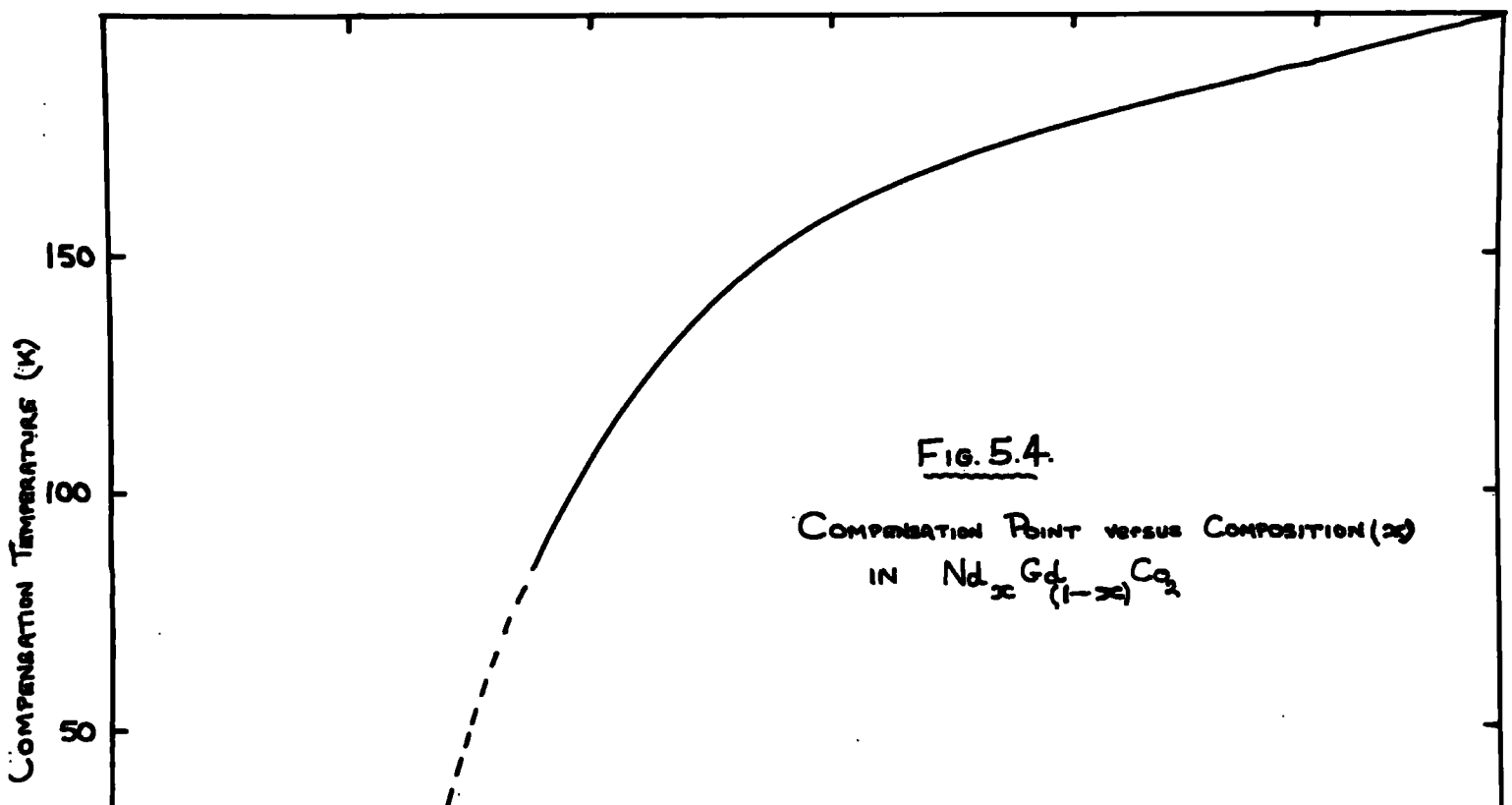

FIG. 5.4.

COMPENSATION POINT VERSUS COMPOSITION (x) IN $Nd_xGd_{(1-x)}Co_2$

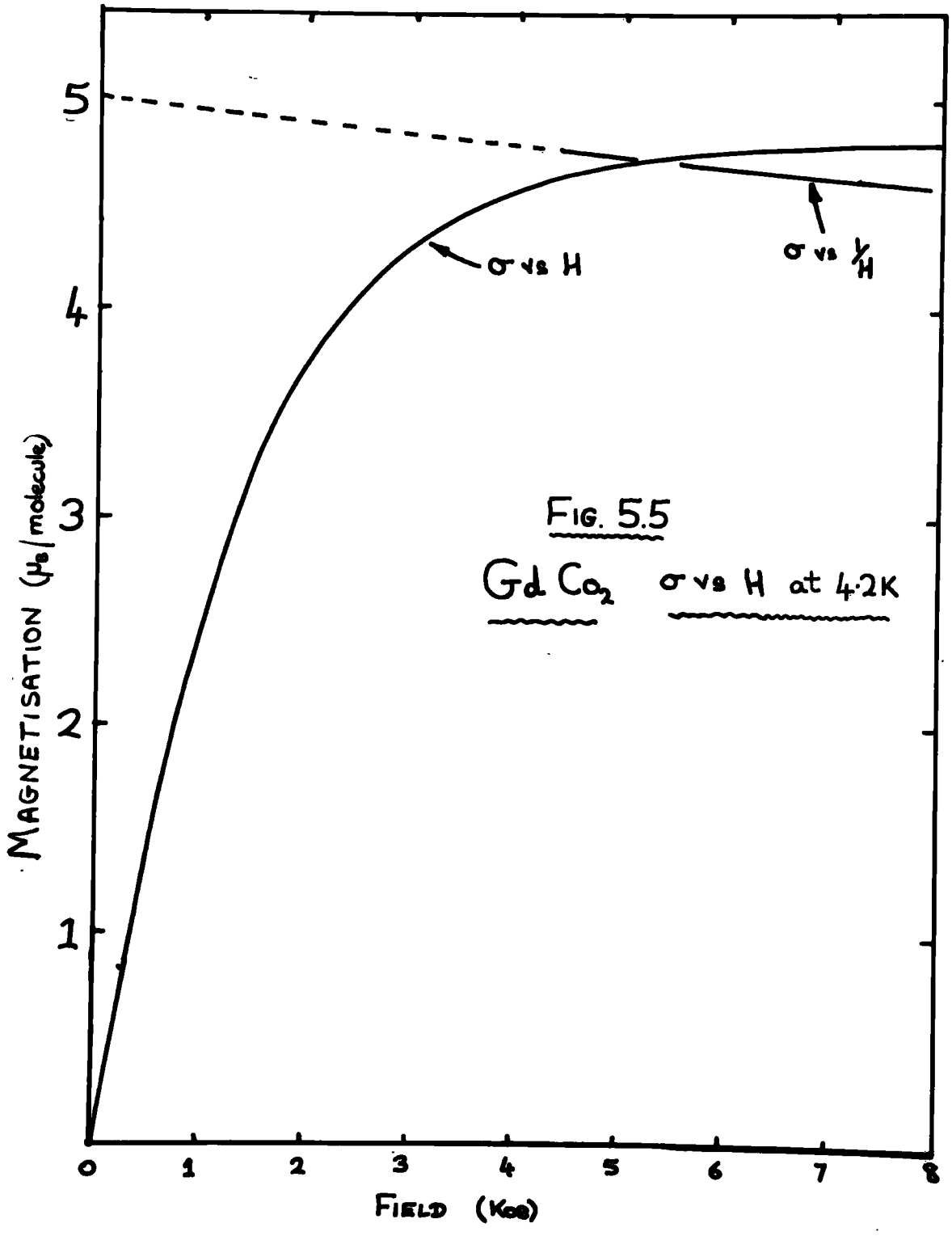

FIG. 5.5

$GdCo_2$ σ vs H at 4.2K

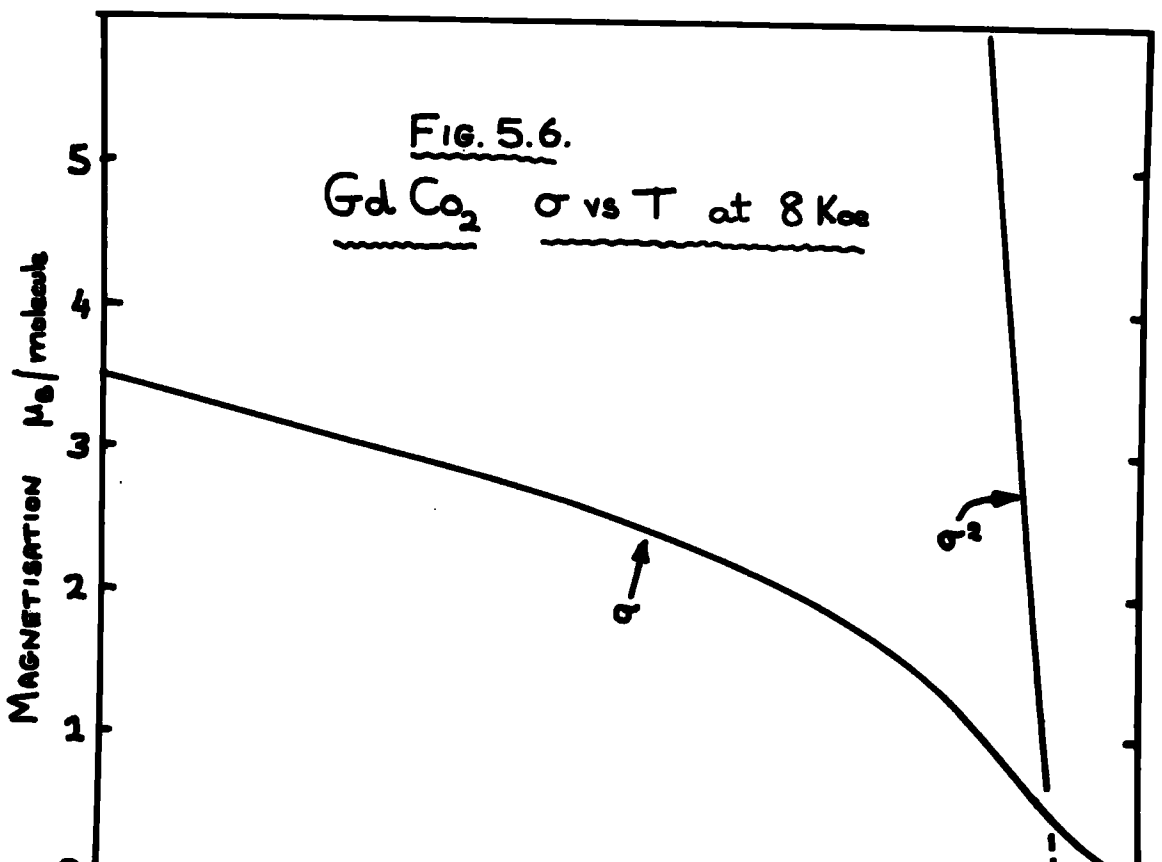
FIG. 5.6.
Gd Co2 σ vs T at 8 Koe
MAGNETISATION μB/molecule
0
1
2
3
4
5
250
300
400
400
TEMPERATURE (K)
σ
σ2

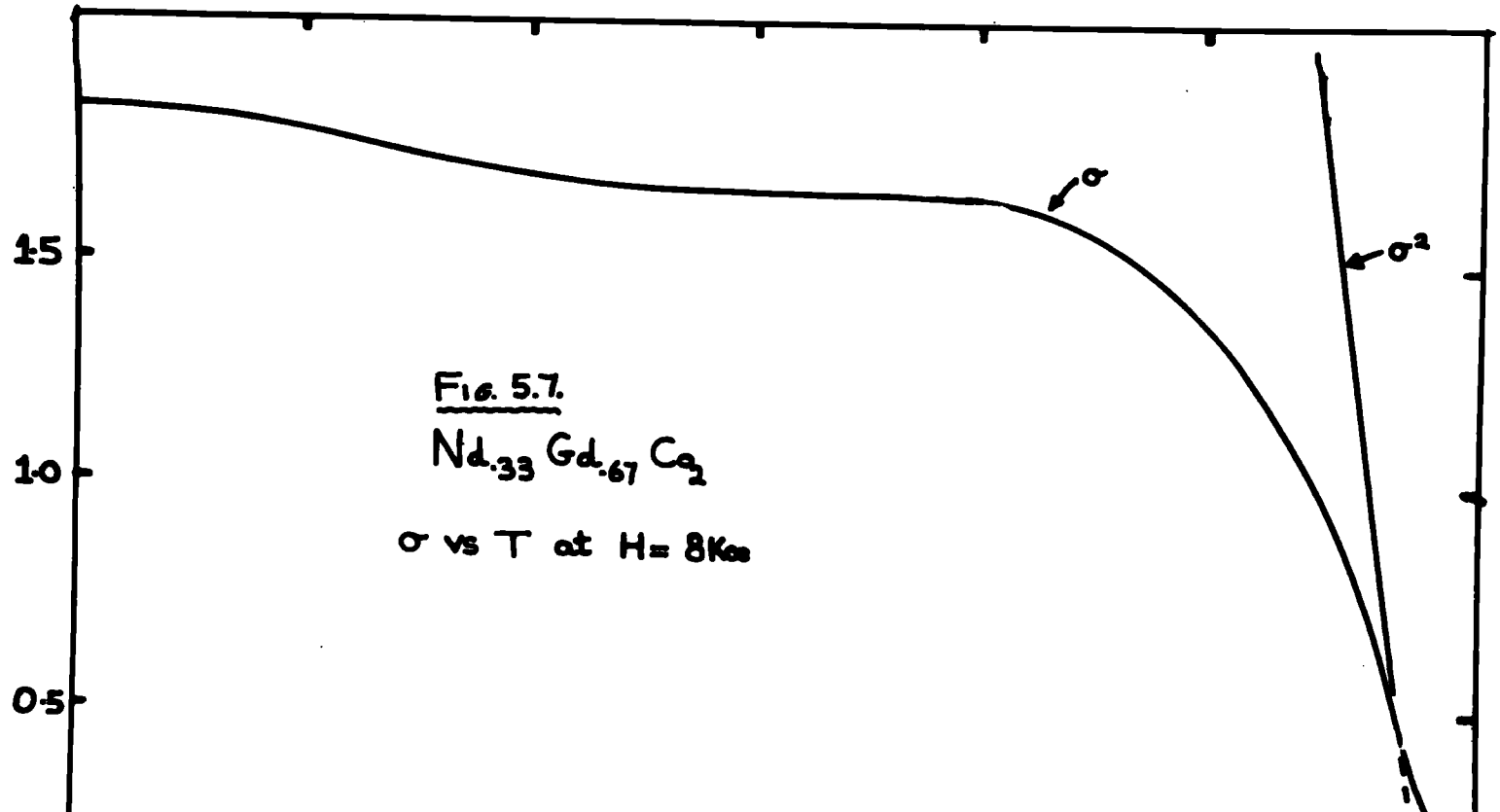

Fig. 5.7.

$Nd_{.33}Gd_{.67}Ca_2$

σ vs T at H = 8Koe

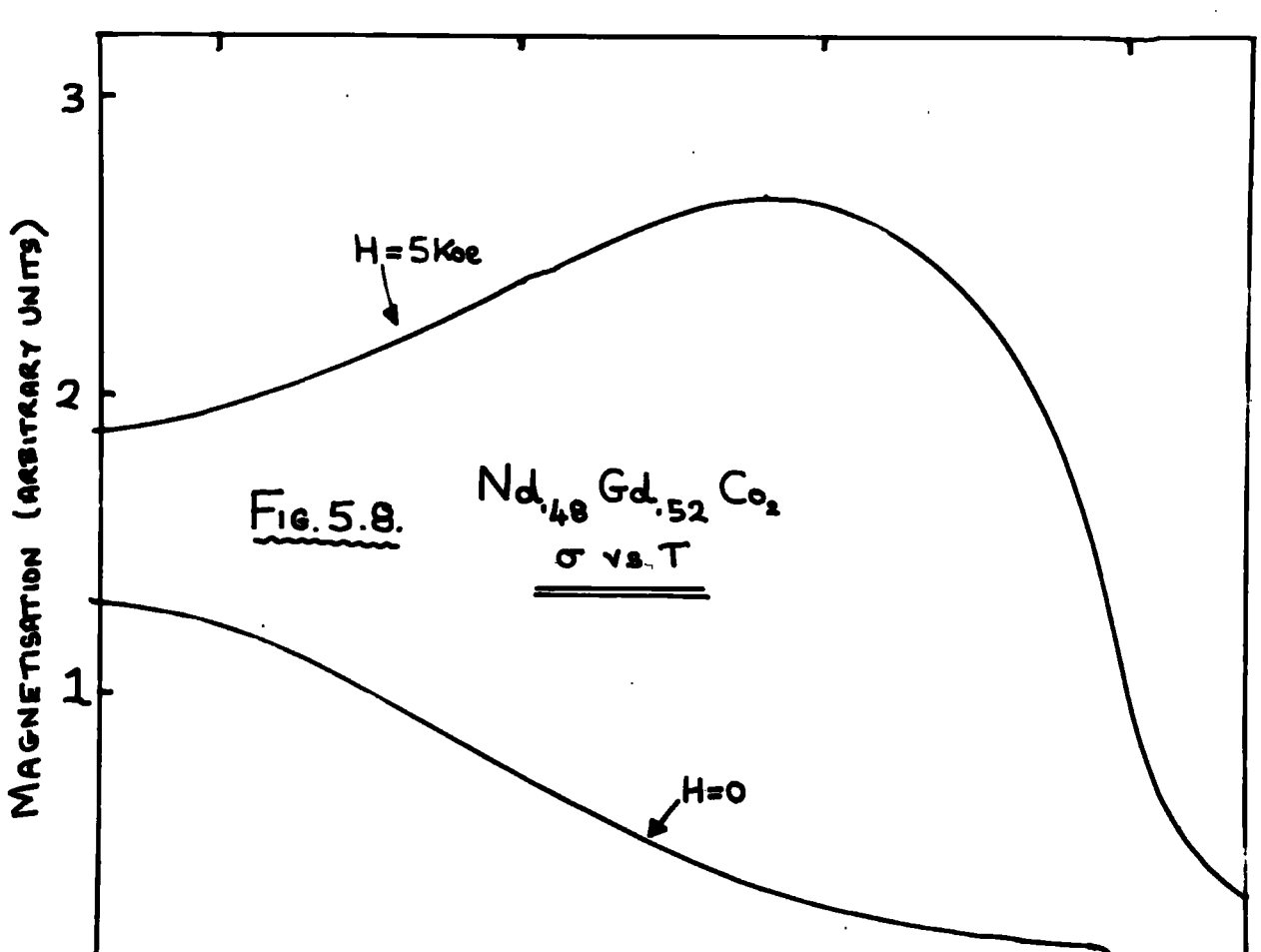

FIG. 5.8. $Nd_{.48}Gd_{.52}Co_2$ σ vs. T

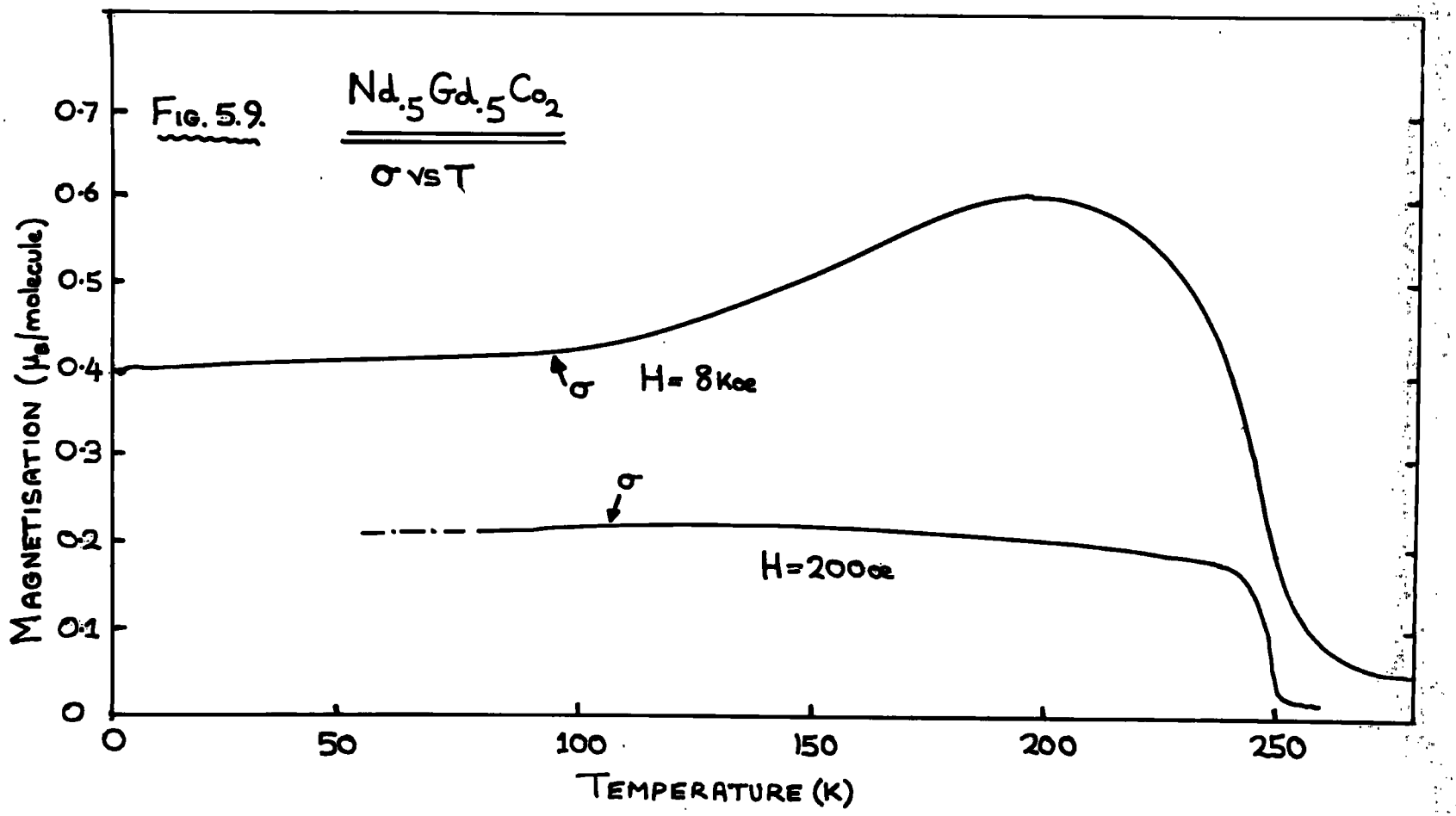
Fig. 5.9.
$Nd_{.5}Gd_{.5}Co_2$
σ vs T
Magnetisation (μ_B/molecule)
0·7
0·6
0·5
0·4
0·3
0·2
0·1
0
σ
H= 8Koe
σ
H=200oe
0
50
100
150
200
250
Temperature (K)

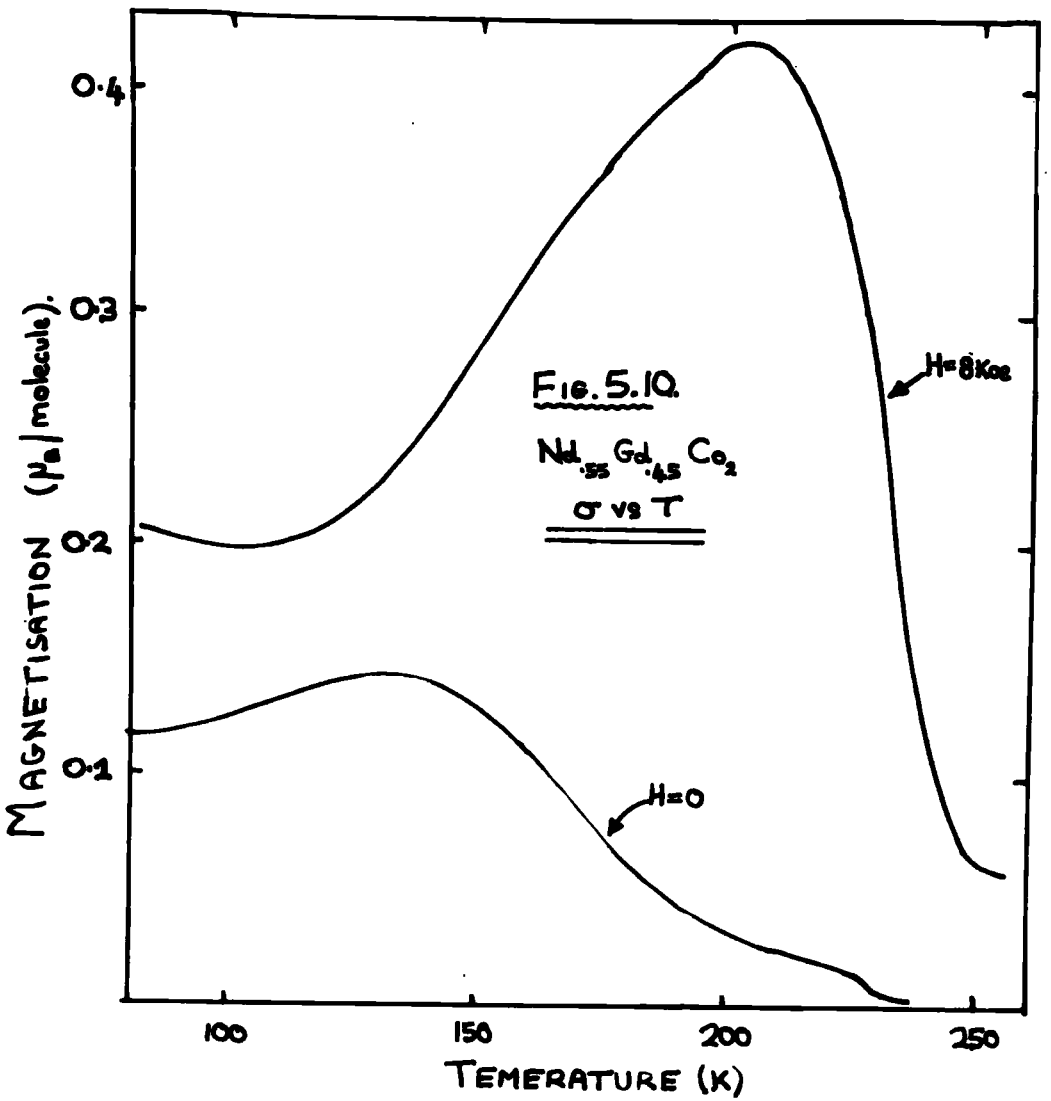

FIG. 5.10.

$Nd_{.55}Gd_{.45}Co_2$

σ vs T

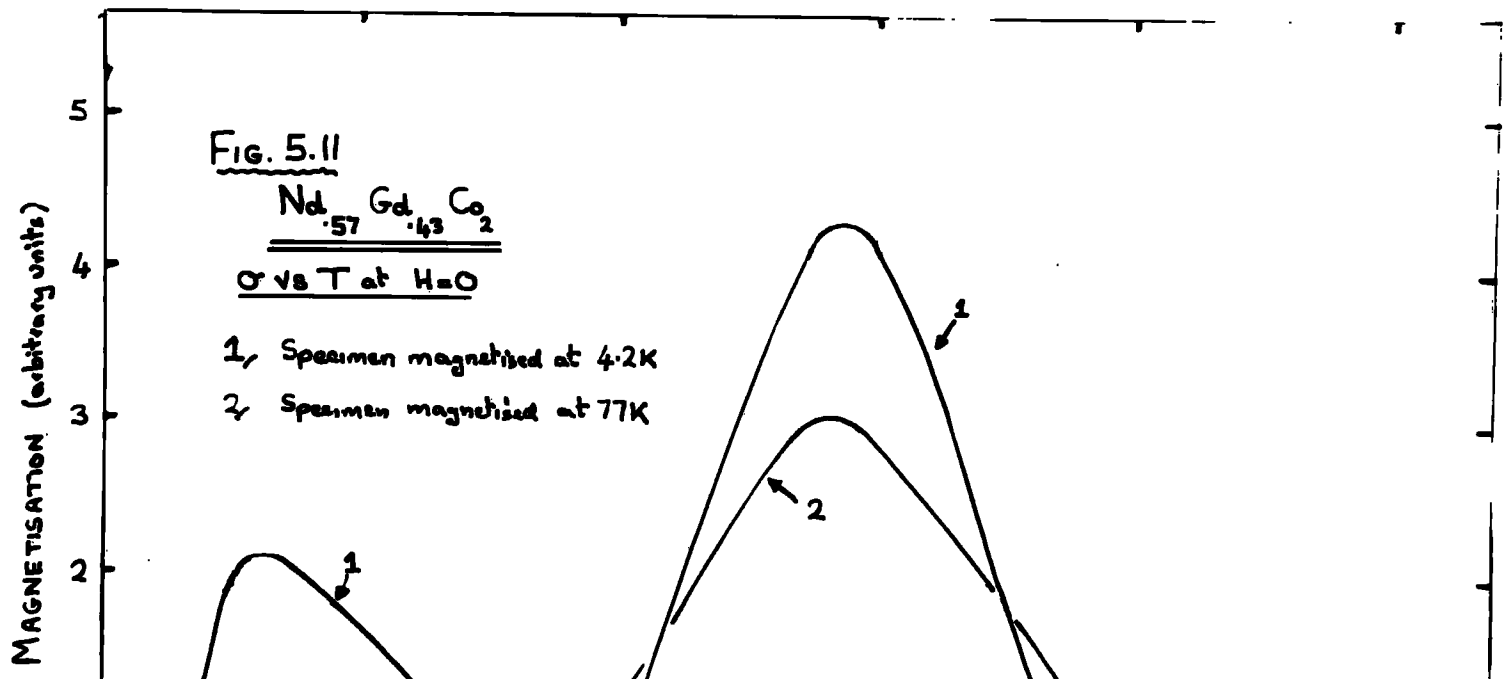
FIG. 5.11
$Nd_{.57}Gd_{.43}Co_2$
σ vs T at H=0
1, Specimen magnetised at 4·2K
2, Specimen magnetised at 77K
MAGNETISATION (arbitrary units)
TEMPERATURE (K)
1
2
1
2
1
2
3
4
5
50
100
150
200
250

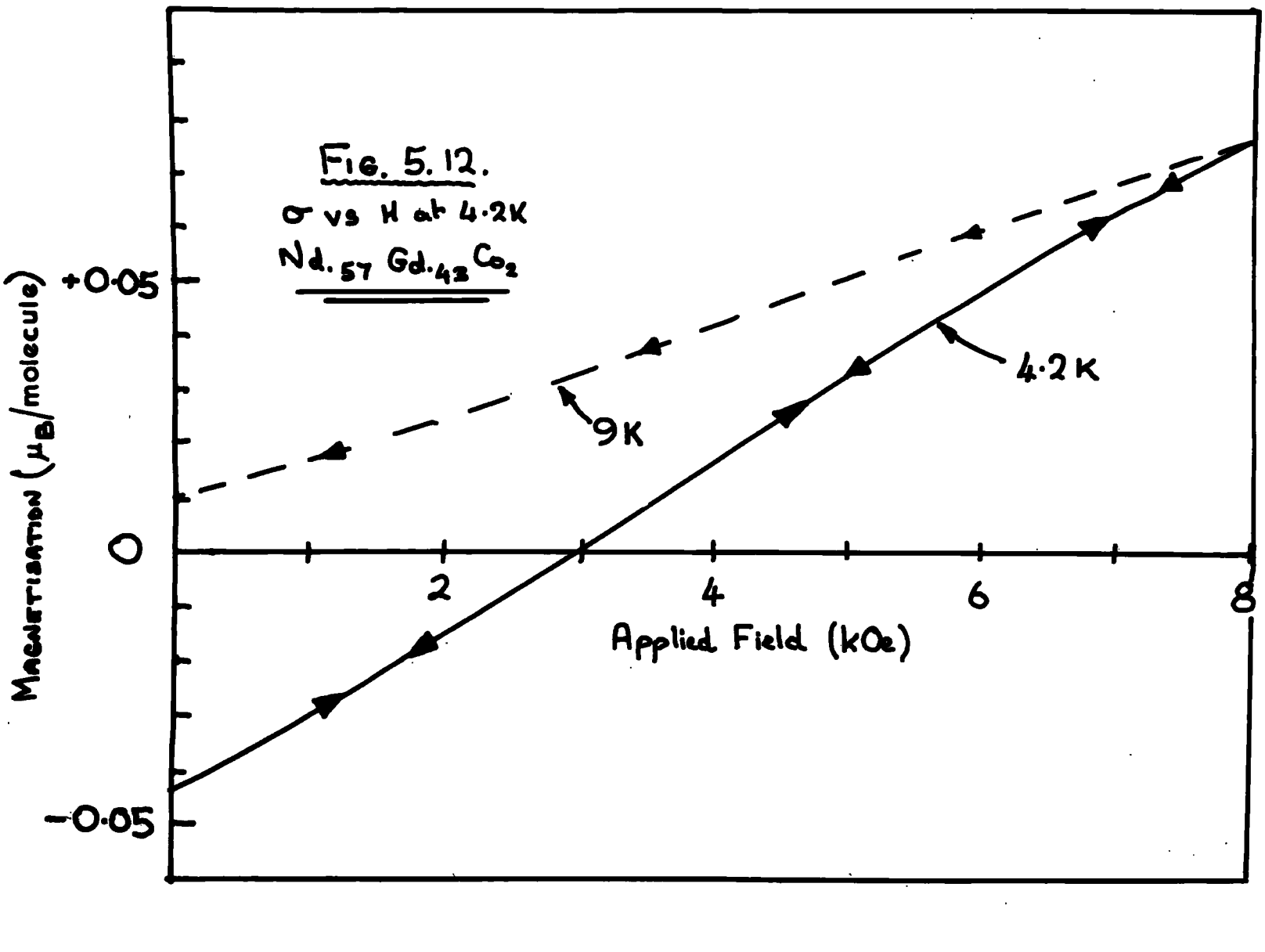
Fig. 5.12.
σ vs H at 4.2K
Nd.57 Gd.43 Co2
+0.05
0
−0.05
Magnetisation (μB/molecule)
9K
4.2K
2
4
6
8
Applied Field (kOe)

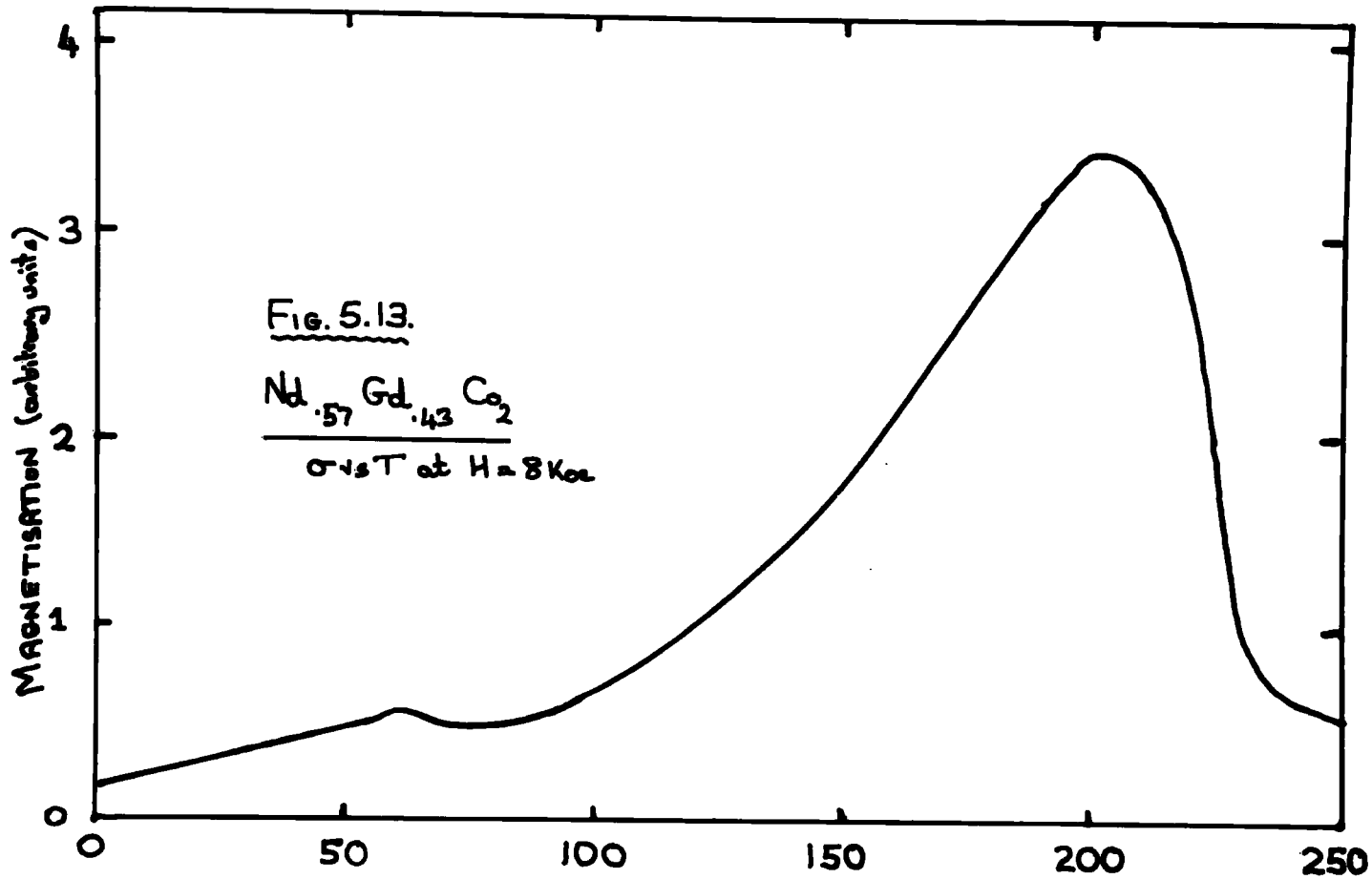

FIG. 5.13.

$Nd_{.57}Gd_{.43}Co_2$

σ vs T at H = 8 Koe

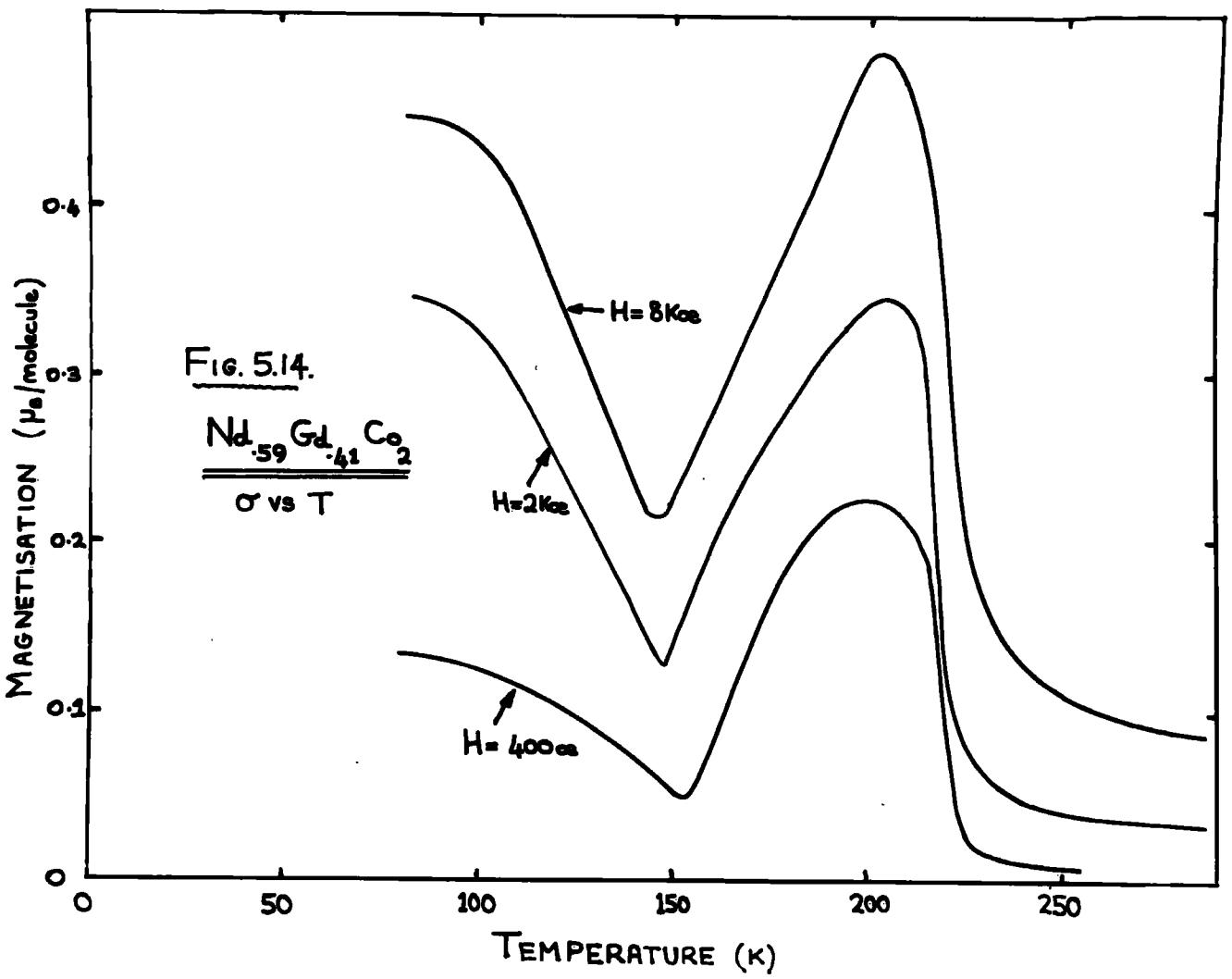

FIG. 5.14.

$Nd_{.59}Gd_{.41}Co_2$

σ vs T

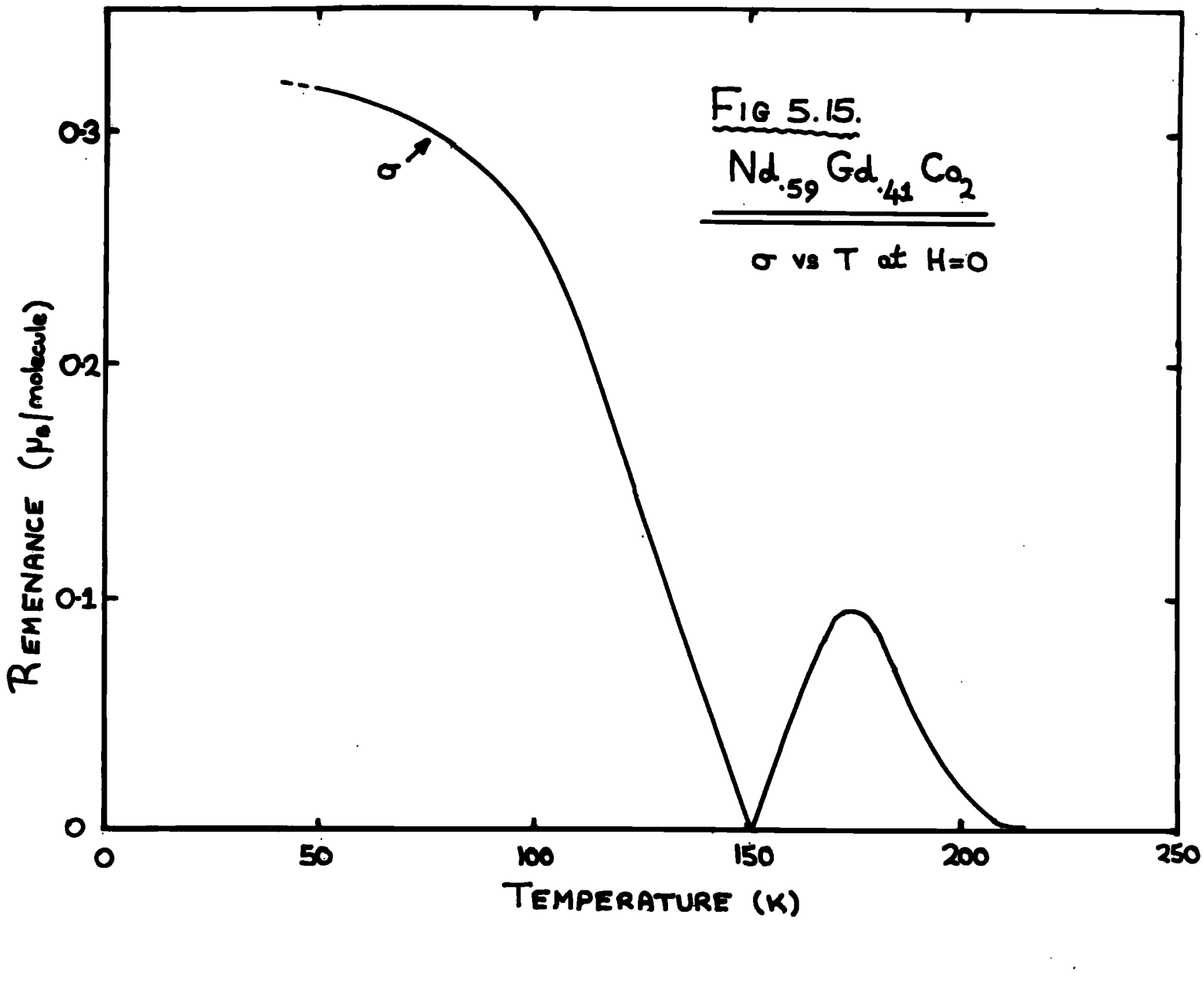
FIG 5.15.
$Nd_{.59}Gd_{.41}Co_2$
σ vs T at H=0
σ
REMENANCE (μ_B/molecule)
0.3
0.2
0.1
0
0
50
100
150
200
250
TEMPERATURE (K)

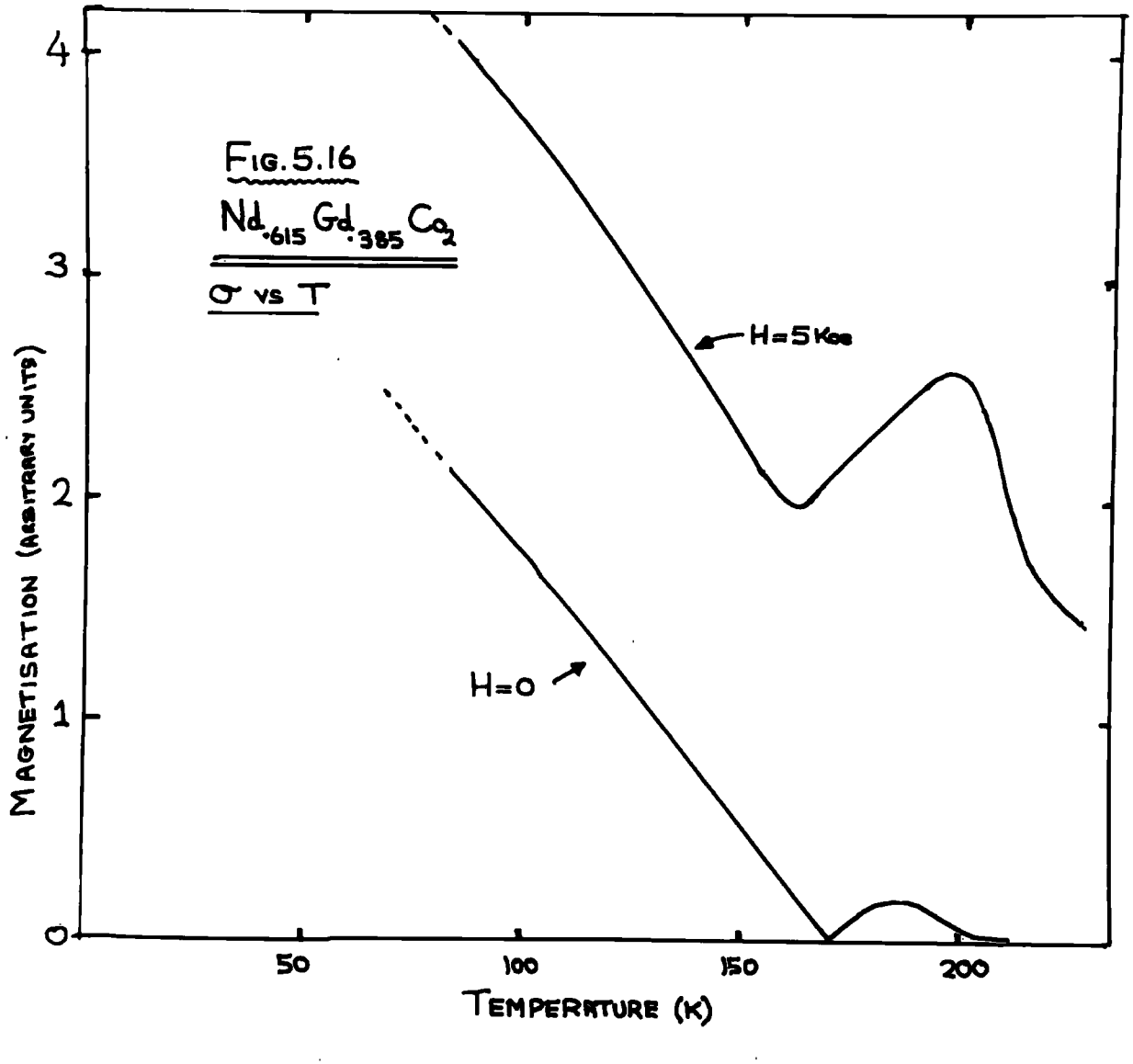
FIG. 5.16
$Nd_{.615}Gd_{.385}Co_2$
σ vs T
H=5Koe
H=0
MAGNETISATION (ARBITRARY UNITS)
TEMPERATURE (K)
0
1
2
3
4
50
100
150
200

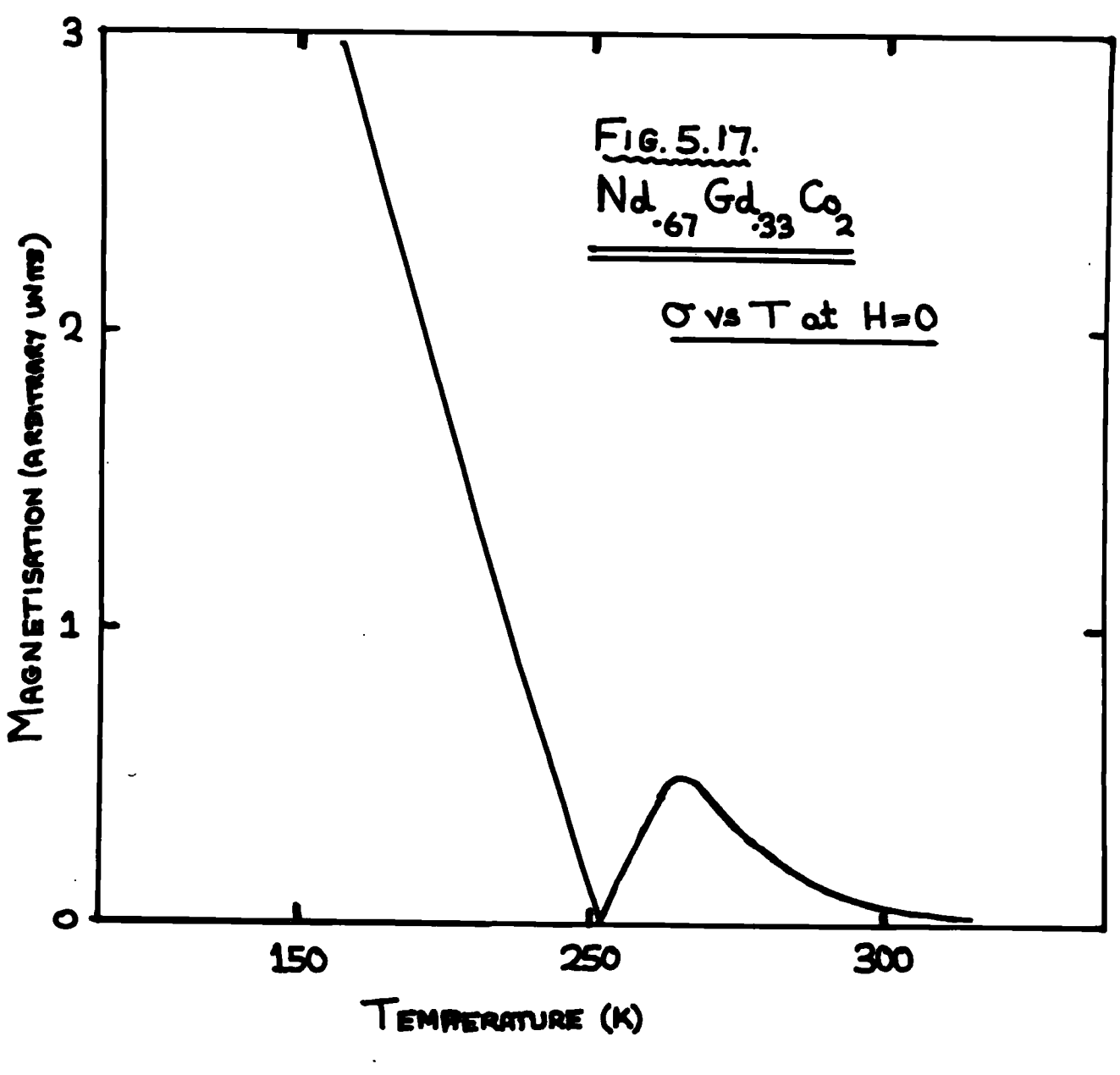

FIG. 5.17.

$Nd_{.67}Gd_{.33}Co_2$

σ vs T at H=0

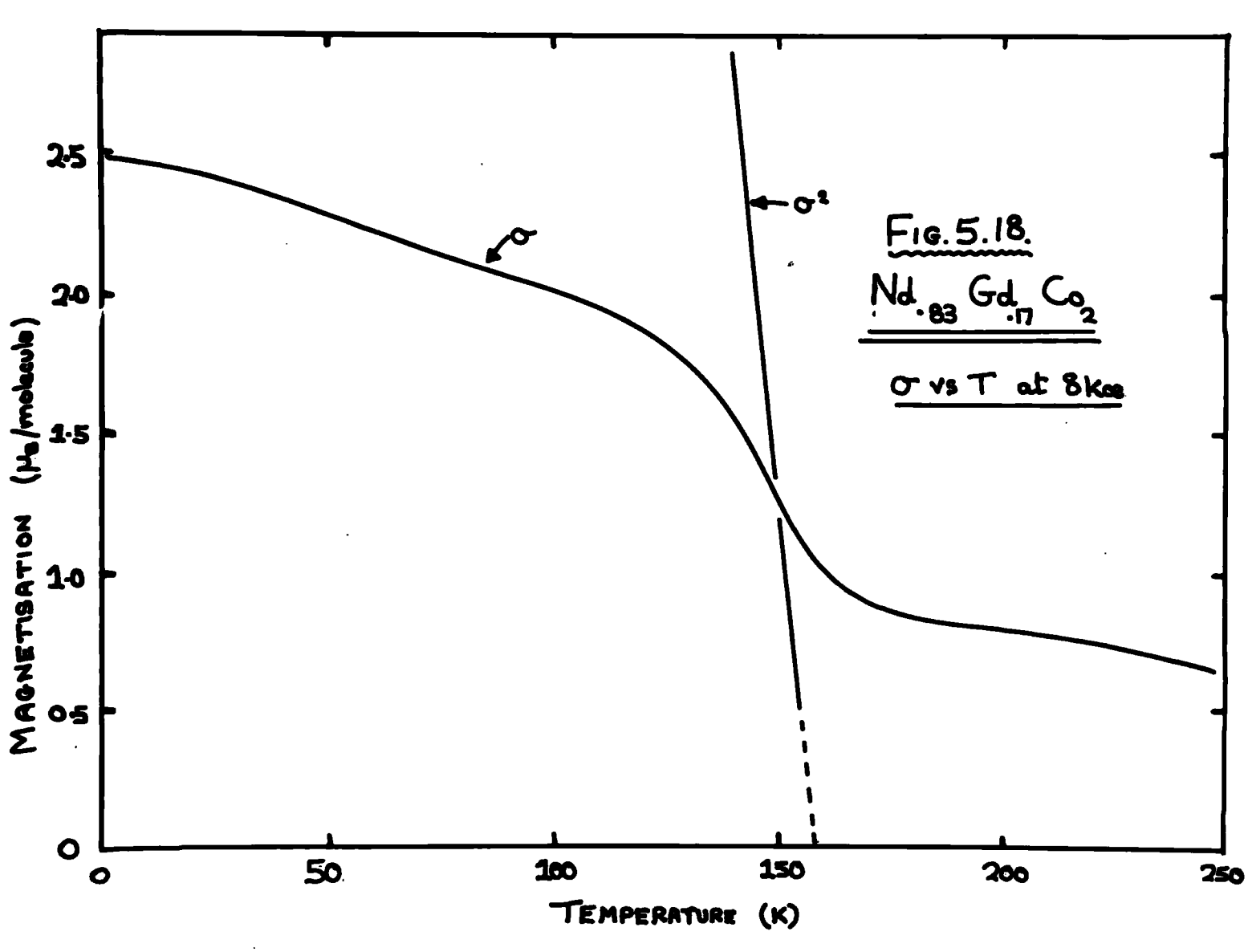

FIG. 5.18.

$Nd_{.83}Gd_{.17}Co_2$

σ vs T at 8 kOe

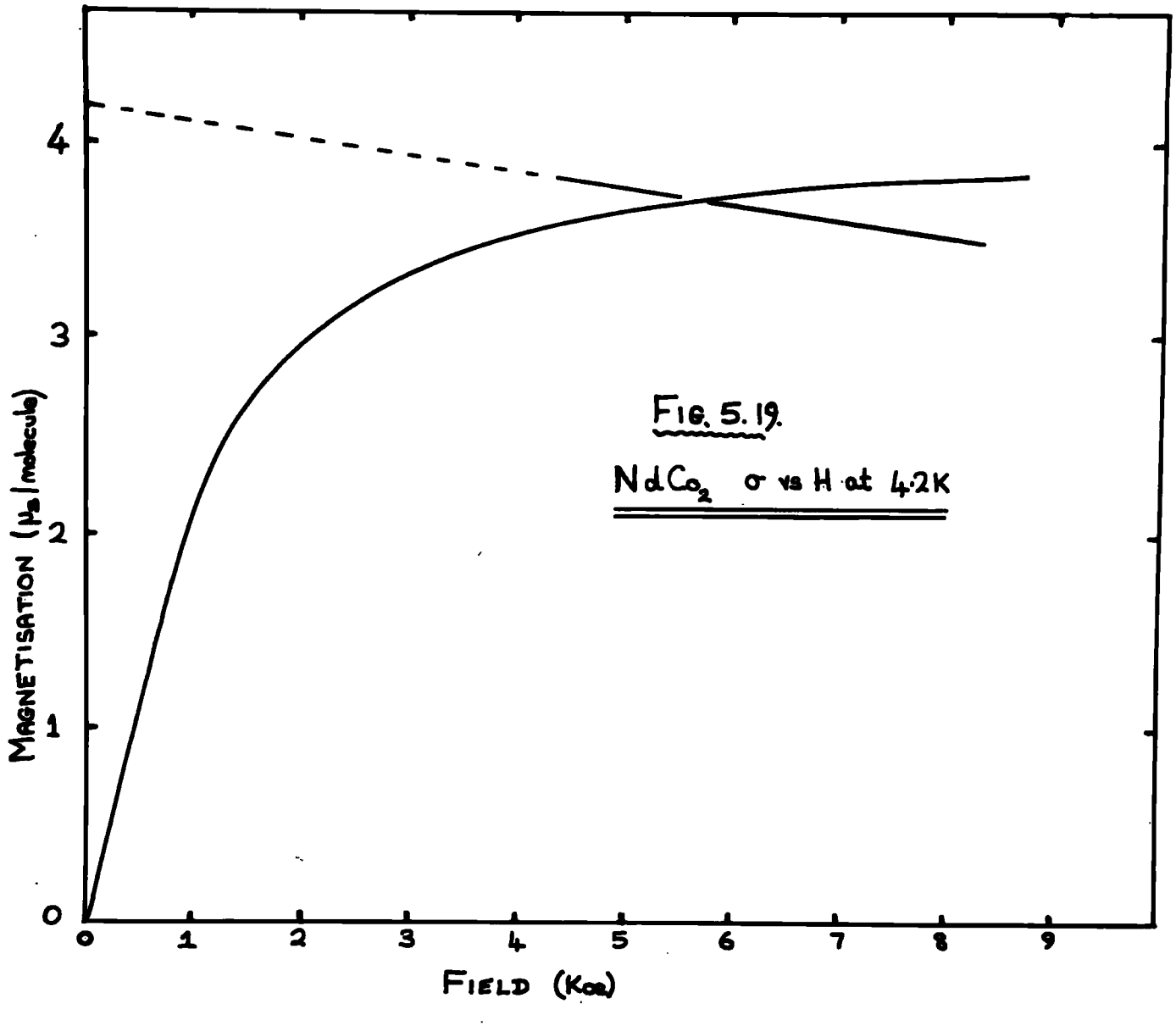

FIG. 5.19.

$NdCo_2$ σ vs H at 4.2K

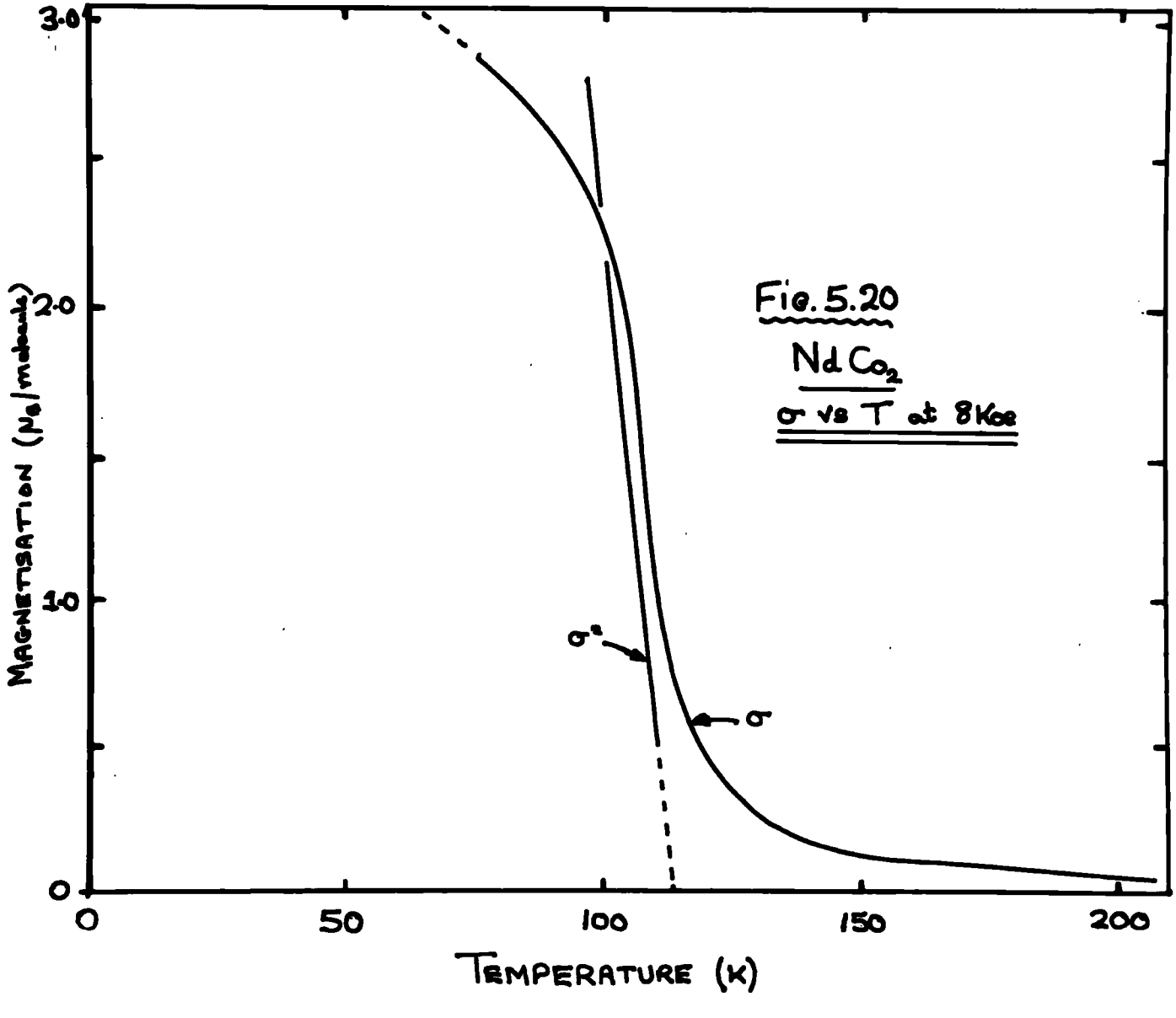

Fig. 5.20

$NdCo_2$

σ vs T at 8Koe

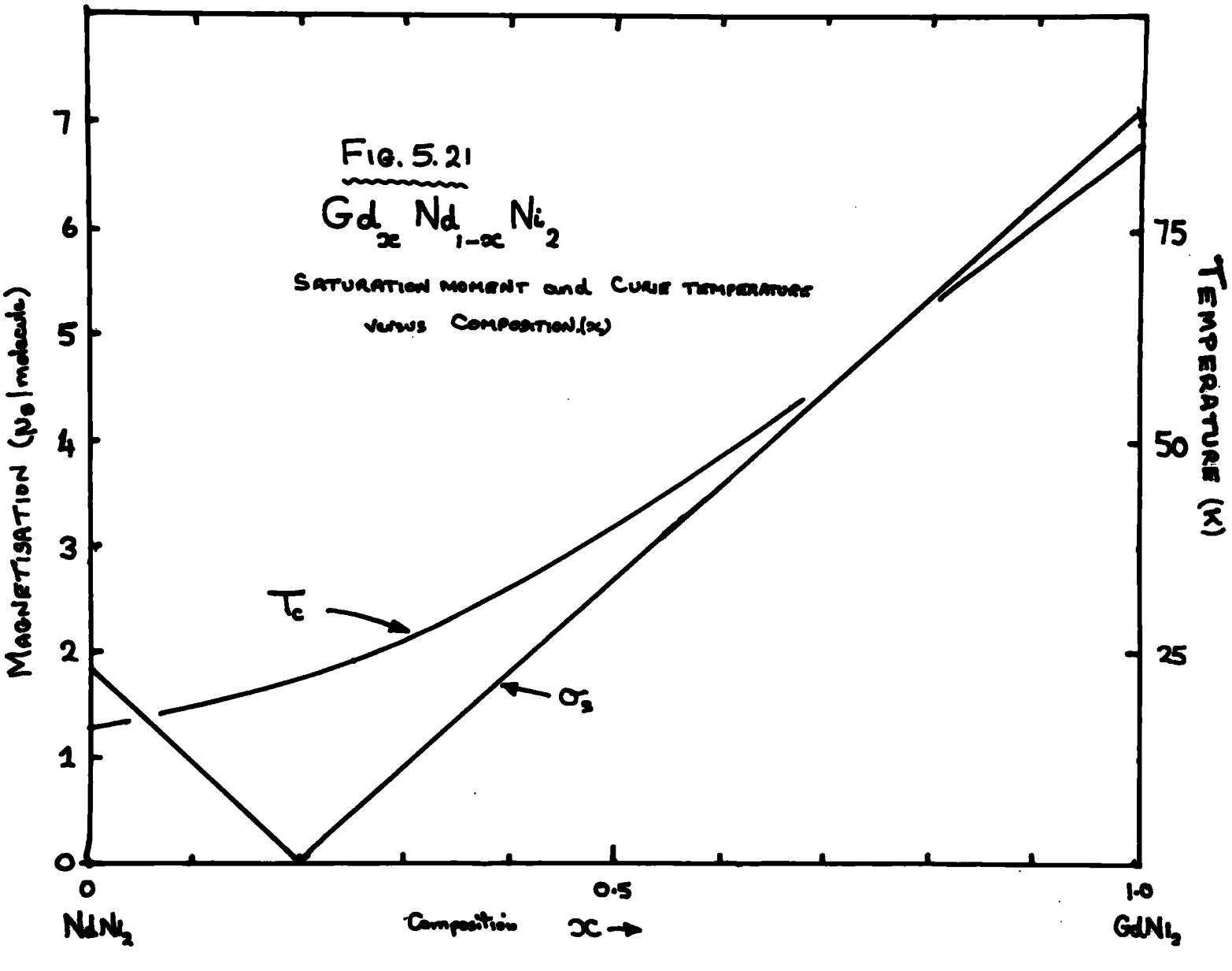
FIG. 5.21
$Gd_x Nd_{1-x} Ni_2$
SATURATION MOMENT and CURIE TEMPERATURE VERSUS COMPOSITION (x)
MAGNETISATION (μ_B/molecule)
TEMPERATURE (K)
T_c
σ_s
0
1
2
3
4
5
6
7
25
50
75
0
0.5
1.0
$NdNi_2$
Composition $x \rightarrow$
$GdNi_2$

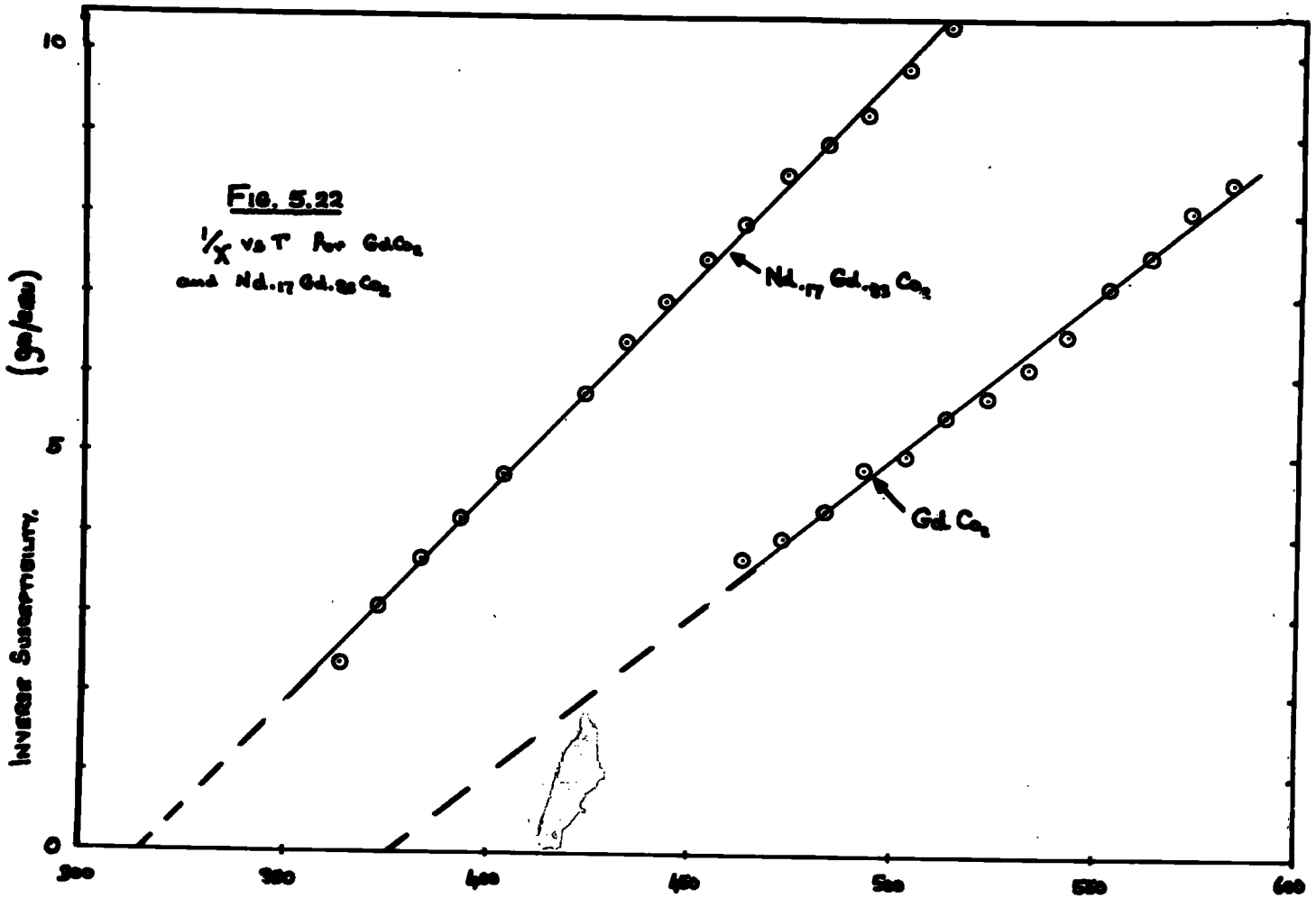
FIG. 5.22
1/χ vs T for GdCo2
and Nd.17 Gd.83 Co2
Nd.17 Gd.83 Co2
Gd Co2
INVERSE SUSCEPTIBILITY, (gm/emu)
TEMPERATURE (K)
0
5
10
300
350
400
450
500
550
600

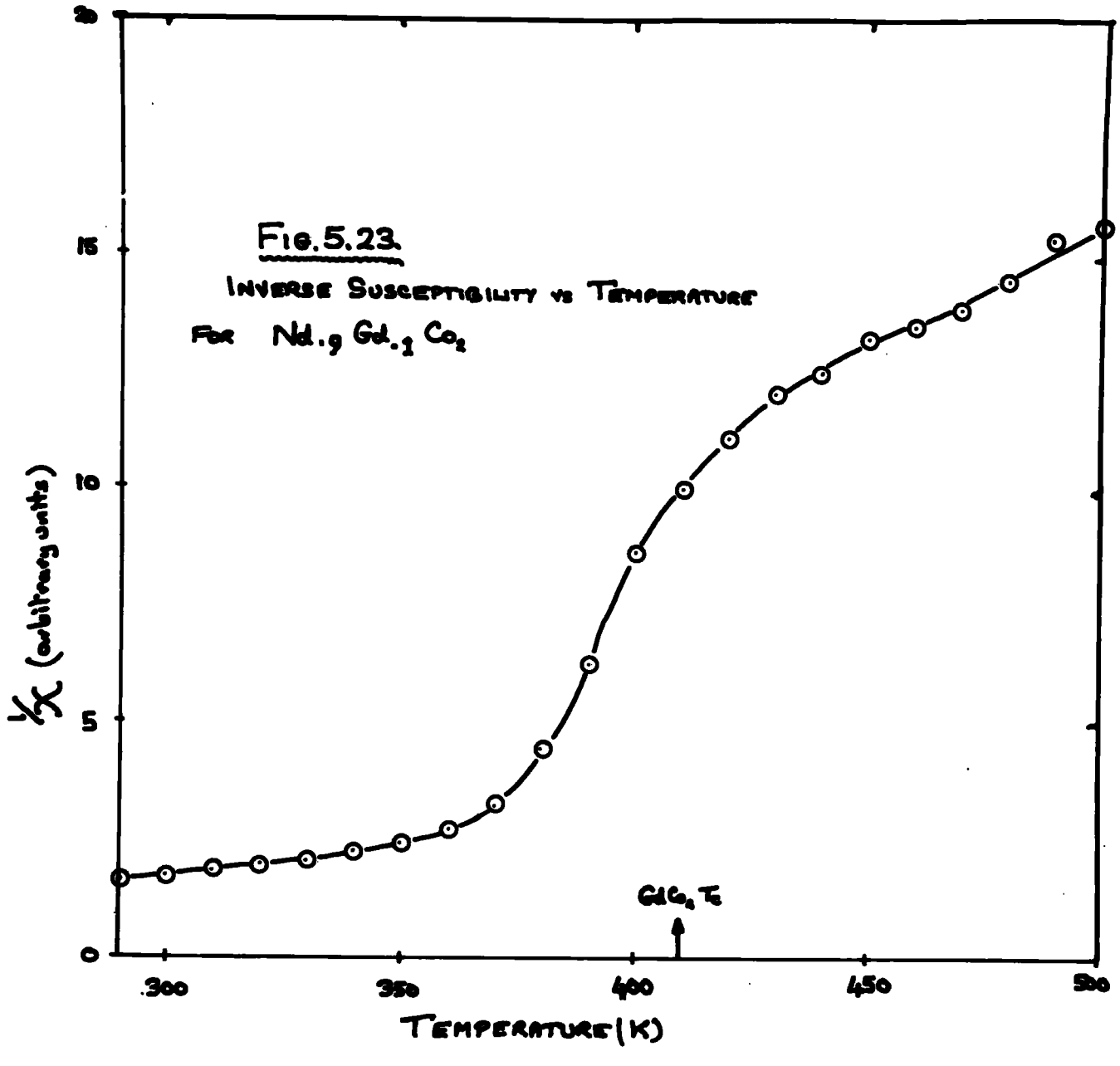
Fig. 5.23.
INVERSE SUSCEPTIBILITY VS TEMPERATURE
FOR Nd.9 Gd.1 Co2
1/χ (arbitrary units)
0
5
10
15
20
300
350
400
450
500
TEMPERATURE (K)
GdCo2 Tc

CHAPTER 6

DISCUSSION OF RESULTS

In this chapter the results given in chapter five are discussed in some detail and accounted for on the basis of the information given in chapters two and three. The lattice parameter data is considered first followed by the magnetic results.

6.1 Lattice Parameter Data

The lattice parameters of the $Nd_xGd_{1-x}Co_2$ series given in fig. 5.1 show several interesting features. Firstly, the gradient change in the vicinity of x = 0.35 is probably directly associated with the magnetostrictive effects already discussed in chapter two for $GdCo_2$ where the magnetic contribution to the binding energy is negative. The Curie point data (in fig. 5.3) show that those compounds below x = 0.35 (i.e. towards the $GdCo_2$ end) are magnetically ordered at the X-ray measuring temperature ($\sim$ 293K). Furthermore, extrapolation of the lattice parameter data for x > 0.35 yields a 'non magnetic' $GdCo_2$ lattice parameter of 7.233KX (1 Å ≡ 1.00202KX) in excellent agreement with the value of 7.2333 ± 0.0005 KX obtained by Mansey et al (ref. 2.15b) from expansion measurements on $GdCo_2$. The data above x = 0.35 is best fitted by two lines with a slight change of slope in the region of x = 0.65 apart from the anomalous point at x = 0.59. The magnetisation measurements were made upon the same specimens for which the lattice parameters are given in fig. 5.1. Further specimens were prepared at the University of Birmingham to investigate the anomaly at x = 0.59 and the further slight anomaly at x = 0.7. The results of this investigation showed rather surprisingly that the lattice

TABLE 6.1

Typical Spectrographic Analysis of Koch-Light Gadolinium Ingot (99.9%)

Element	Estimated quantity present
Samarium	50 ppm
Terbium	300 ppm
Europium	100 ppm
Yttrium	50 ppm
Iron	100 ppm
Calcium	100 ppm
Copper	100 ppm
Neodymium	300 ppm

parameters of the compounds were dependent upon the source of the Gadolinium. In this work, the gadolinium was obtained from either Koch-Light Laboratories Limited or Johnson and Matthey (Rare Earth Products) Ltd., the two sources giving very similar stated purities, and the Koch-Light analysis appears in Table 6.1. The original series of compounds was made from Johnson-Matthey gadolinium at the compositions x = 0, 0.13, 0.33, 0.5, 0.67, 0.83, 1.0; however, in the light of the magnetic results, further specimens were made at Birmingham for the compositions x = 0.55, 0.57, and 0.59. This last specimen was made from Koch-Light gadolinium and its lattice parameter is the anomalous one in fig. 5.1. When further specimens were made at different compositions more anomalies resulted, until it was realised that it was the source of the gadolinium which affected the lattice parameters. The preliminary results of these further structural measurements are given in figure 6.1 and the difference caused by the source of the gadolinium is clear. This behaviour is believed to be the result of the gadolinium containing interstitial gas which expands the gadolinium lattice, consequently the Koch-Light series shows a smaller change in the lattice parameter in going from $NdCo_2$ to $GdCo_2$. The Johnson-Matthey specimens upon which the magnetic studies reported here were carried out, now show a small anomaly in the region of x = 0.7. At the present time the exact nature of this anomaly is uncertain, insofar as it is either a slope change or a small dip, but observations on further stoichiometries should clarify this point. One further aspect worth noting is that the deviation from a Vegard's Law behaviour between 'non-magnetic' $GdCo_2$ and $NdCo_2$ is very small particularly when compared with the large deviations which are seen in, for example, the $Er(Fe-Co)_2$ and

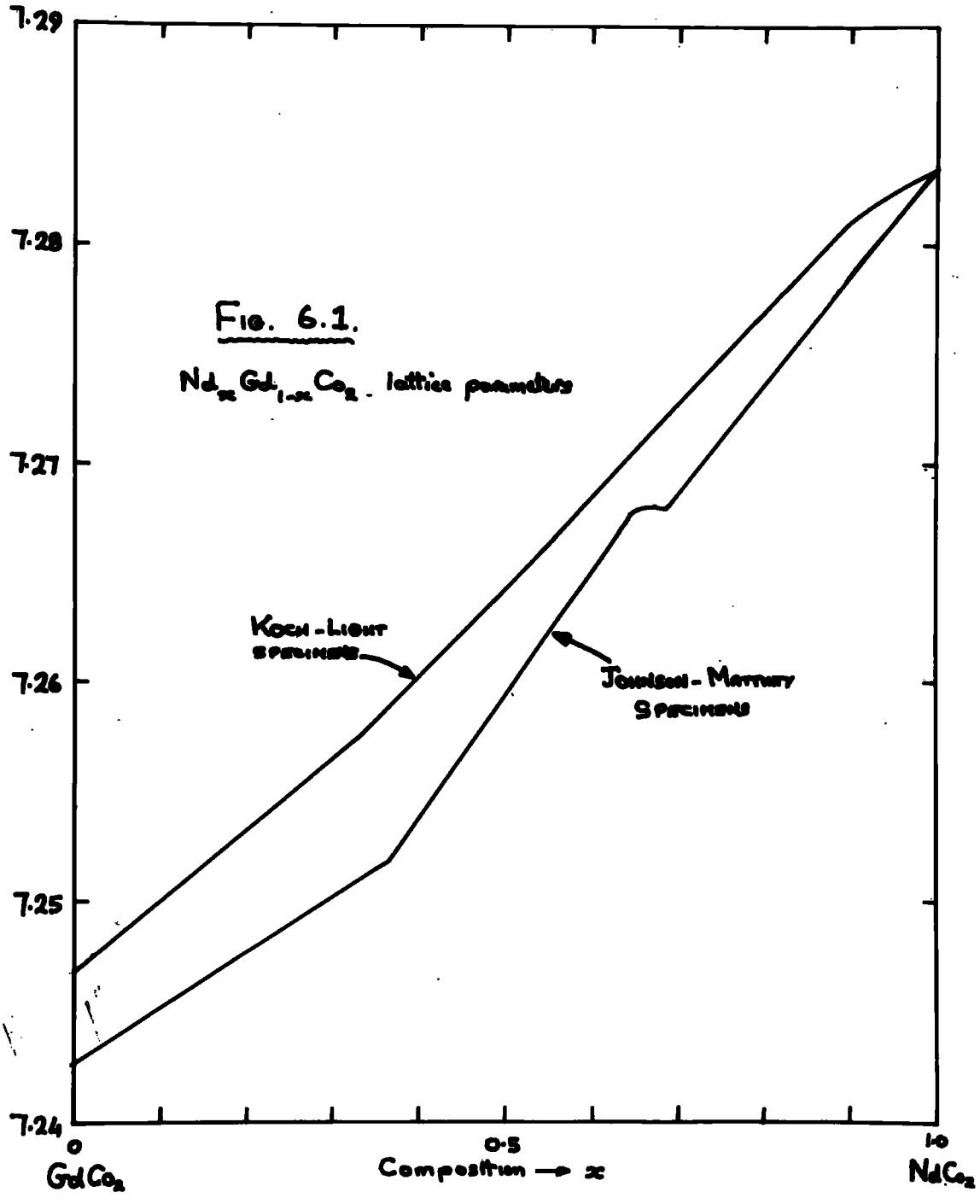
7·29
7·28
7·27
7·26
7·25
7·24
Fig. 6.1.
$Nd_xGd_{1-x}Co_2$ - lattice parameters
Koch-Light specimens
Johnson-Matthey specimens
0
0·5
1·0
$GdCo_2$
Composition → x
$NdCo_2$

$Er(Co\text{-}Ni)_2$ series (see fig. 2.6) (ref. 2.47). These deviations have been attributed to the changing magnitude of the 3d-transition metal moment and in the case of the $(Nd,Gd)Co_2$ compounds the transition metal moment may be expected to remain reasonably constant leading to the lack of any large deviation from Vegard's Law.

6.2 Susceptibility Results

It was mentioned in chapter five that the susceptibility measurements suffered from the effects of a second phase and, in general, as the results for $Nd_{.9}Gd_{.1}Co_2$ (fig. 5.23) show, this phase was $GdCo_2$. Calculation of the quantity of this second phase component, from the magnetisation magnitude, shows that the impurity phase is about 0.005% of the total specimen. This percentage is very small, revealing the effectiveness of the annealing process, but unfortunately the sensitivity of the susceptibility measurements is such that impurity levels ten times smaller than this can be detected. At the time of the measurements the apparatus was limited in its upper temperature, at least for these specimens, by slow decomposition of the sample by oxidation of the rare earth component because the susceptibility balance system was not fully adapted to high vacuum evacuated work. The view that insufficiently high temperatures were attained is supported by the results for the $GdCo_2$ and $Nd_{.17}Gd_{.83}Co_2$ compounds which showed no second phase effects (fig. 5.22). The effective moments calculated from the graphs for these two compounds ($p_{eff} = 7.34\mu_B$ for $GdCo_2$ and $p_{eff} = 6.45\mu_B$ for $Nd_{.17}Gd_{.83}Co_2$) are approximately 75% of the calculated theoretical values, furthermore, the paramagnetic Curie

points are close to the ferromagnetic Curie points, a feature that is not generally expected in ferrimagnetic materials. (In these compounds, the extrapolation of the $1/\chi$ vs T plot from high temperature gives a θp much less than T_c because $1/\chi$ falls rapidly to zero near T_c). Thus it is thought that although reasonably straight lines may be drawn through the points on these curves (fig. 5.22), the materials are not yet upon the Curie Weiss part of the $1/\chi$ vs T plot.

6.3 Magnetisation Results

The saturation magnetisation data[5] at 4.2k given in fig. 5.2 together with the percentage saturation at 10 kOe imply an equilibrium concentration (i.e. one for which the resultant magnetisation is zero) at x = 0.57. Indeed, a specimen prepared at this composition showed a linear behaviour of σ vs H (fig. 5.12) with σ very small ($< 0.01\mu_B$), this result being taken to indicate zero saturation moment. The σ vs H behaviour of this specimen is further discussed below. The saturation moments at 4.2K for $x < 0.57$ lie on an almost perfect straight line but the data above 0.57 are best fitted by two straight lines with the slight vertical shifts at x = 0.59 and x = 0.73. It is possible that the displacement at x = 0.59 is due to the fact that this specimen contains Koch-Light gadolinium and the slightly different lattice parameter (0.05%) of this specimen from that of a hypothetical Johnson-Matthey specimen may be enough to upset the precise location of the equilibrium concentration. Thus it may be more correct to ignore this point and draw the line from the x = 0.7 specimen through the zero point at 0.57. The anomaly

at x = 0.73 is larger and furthermore, is accompanied by a dip in the percentage saturation curve and also the lattice parameter anomaly (fig. 6.1) already discussed, thus it may be taken that the shift at x = 0.73 is an established phenomenon.

In order to analyse the saturation moment data it is necessary to know the result, in terms of coupling of the individual moments, of the various exchange interactions (these are given later in table 6.2). The review of chapter two has shown that the heavy rare earths in general align antiparallel to the transition metal moment, whereas the light rare earths are parallel. Further, the psuedobinary $(Nd,Gd)Al_2$ was understood in terms of a gadolinium sublattice ordered antiparallel to the neodymium sublattice. In this work this coupling was further substantiated by making specimens in the series $(Nd,Gd)Ni_2$, the magnetic results of which are shown in fig. 5.21, and indeed the equilibrium concentration was located precisely where it might be expected on these grounds. Turning to the $(Nd,Gd)Co_2$ compounds, it is known that the terminal compounds $GdCo_2$ and $NdCo_2$ are ferrimagnetic and ferromagnetic respectively so that it is reasonable to assume that these structures remain stable throughout the composition range. The neutron diffraction studies of Moon et al. (ref. 2.53) showed that, in the RCo_2 compounds, the moment associated with the cobalt ion is $1.0\mu_B$ in the heavy rare earth compounds and $0.8\mu_B$ in the light rare earth compounds. These results were taken from polycrystalline samples, of course, and the resulting accuracy is only $\pm 0.2\mu_B$ for each moment. In $NdCo_2$ the neodymium moment was measured as $2.6\mu_B$ ($\pm$ 0.2) giving a total moment of $4.2\mu_B$ for the compound, in excellent agreement with the present

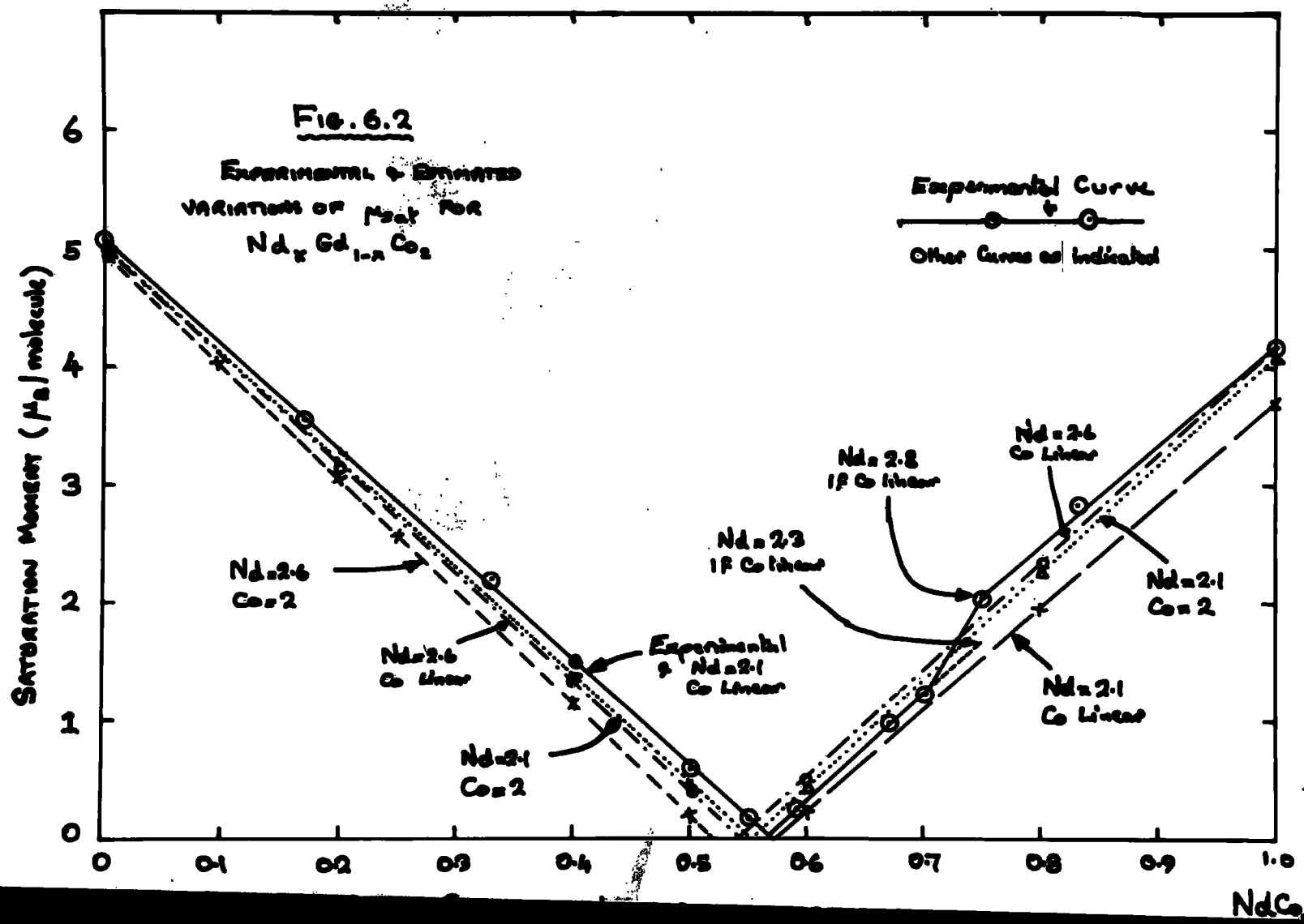
Fig. 6.2
Experimental & Estimated
variation of μ_{sat} for
$Nd_x Gd_{1-x} Co_2$
Experimental Curve
Other Curves as indicated
Saturation Moment (μ_B/molecule)
Nd=2.6
Co=2
Nd=2.6
Co Linear
Experimental
& Nd=2.1
Co Linear
Nd=2.1
Co=2
Nd=2.3
If Co linear
Nd=2.8
If Co linear
Nd=2.6
Co Linear
Nd=2.1
Co=2
Nd=2.1
Co Linear
0
1
2
3
4
5
6
0
0.1
0.2
0.3
0.4
0.5
0.6
0.7
0.8
0.9
1.0
$NdCo_2$

study. If a moment of $7.0\mu_B$ is attributed to gadolinium throughout the series, which is reasonable on the grounds that it is essentially unaffected by the crystal field, then the total moment of $GdCo_2$ is $5.0\mu_B$, also in good agreement with the present study. The saturation moment data across the composition range may be analysed in terms of these moment values. Fig. 6.2 shows the saturation moment vs composition data together with the estimated behaviours obtained by assigning various values to the individual moments. Because the cobalt moment is $1.0\mu_B$ at the $GdCo_2$ end and $0.8\mu_B$ at $NdCo_2$, it is assumed in some of the estimated curves of fig. 6.2 that the cobalt moment varies linearly between these two extremes. This process may be rather meaningless in view of the errors of $\pm 0.2\mu_B$ but it is reasonable as a starting basis to take values close to the middle of the errors. Examination of fig. 6.2 reveals that the experimental data in the range $0 < x < 0.57$ is fitted by assuming a neodymium moment of $2.1\mu_B$ and a linear variation of the cobalt moment. The other estimated curves are at least $0.2\mu_B$ lower than the experimental data and the fit of the above values to this data would seem to lend support to the idea of a slowly varying cobalt moment. The behaviour above $x = 0.57$ is more complex but if a linear variation of the cobalt moment is retained then at $x = 0.7$ a neodymium moment of $2.3\mu_B$ is required and at $x = 0.75$ this moment has risen to $2.8\mu_B$. The best fit of the estimated behaviours is given by assuming a neodymium moment of $2.6\mu_B$ at $x = 0.75$, the curve for the $2.1\mu_B$ neodymium moment lying well off the experimental data. It is thus well established that some form of rapid and non-linear moment change occurs in the region of $x = 0.73$ and a mechanism by which this may

occur is required.

Turning now to the magnetisation versus temperature behaviour, for the majority of the compounds this is typical of ferrimagnetic materials although the observation of compensation points (the magnetisation passes through zero and becomes negative) was possibly only under zero applied field. Fig. 5.14 for $Nd_{.59}Gd_{.41}Co_2$ shows typical isofield curves and in fig. 5.15 the variation of remanence with temperature for this specimen can be seen. This behaviour is best understood in terms of fanning of the antiparallel component moments under the influence of the applied field, meaning that these structures are 'soft' ferrimagnets. Indeed most of the rare earth intermetallic compounds which show compensation points do so only in the manner of fig. 5.14, unlike the true ferrites where the spin structures are unable to fan out and the magnetisation falls to zero at the compensation temperature in an applied field. The compensation temperature versus composition data are given in fig. 5.4 for the remanence results. Normally, the intercept at zero temperature for such a curve will be at the equilibrium concentration and in this case the intercept is at x = 0.555. This value is reasonably close to 0.57 but the behaviour of the x = 0.57 specimen reveals the cause of the discrepancy. Fig. 5.11 (curve 1) shows the variation of remanence with temperature for this specimen after magnetisation at T = 4.2K. For a normal ferrimagnetic material it is expected that a specimen compensated at 0K, the equilibrium concentration, will have non-compensated sublattices and show a net resultant moment at temperatures above 0K and below the Curie point (cf. curve no. 4 of fig. 3.2.2). This is because of the different variation of the magnetisation of each sublattice with temperature, so that the remanence for such a

specimen will rise from zero and return again only at the Curie point. The x = 0.57 specimen exhibits unique behaviour since it is again compensated at both 90K and 205K, showing a more complex behaviour than might be expected at first sight on theoretical grounds. It should be noted that the temperature plotted for this specimen in the remanence data of fig. 5.4 is the second, 90K, point at which the magnetisation becomes zero. The curve (2) of fig. 5.11 shows the remanence after magnetisation of the specimen at 77K, and it should be noted that this curve shows no compensation points at all.

A further unusual aspect of the equilibrium specimen (0.57) lies in its σ vs H behaviour at 4.2K, given in fig. 5.12. The magnetisation is almost linearly dependent upon applied field, but the specimen shows a negative remanence which may be removed by application of a positive field, in which case it will return when the field is removed, or, by allowing the specimen to warm up slightly with or without an applied field (dotted part of curve). The spin structure may be expected to rotate when the remanence is negative with respect to the applied field, for $0 < H < 3$kOe and that it does not lies in the fact that the remanence is only $0.045\mu_B$ so that the positive energy of this moment in the field is insufficient to overcome the barriers to spin rotation arising from the general anisotropy of the moment interaction and the specimen shape.

Thus there are three major anomalies to be explained for the compounds:

(1) the change in one of the component moment values that must accompany the sudden rise in the saturation moment at x = 0.73;

(2) the three apparent compensation points for the x = 0.57 specimen when it is magnetised at 4.2K, and the lack of compensation points when the specimen is magnetised at 77K; and

(3) the anomalous σ vs H behaviour of this composition.

The first of these requires some mechanism by which the moment of one (or all) of the three types of ion can change. It has already been pointed out that the Gd ionic moment is unchanged by the crystal field so that it will certainly remain constant at $\sim 7.0\mu_B$ throughout the composition range $0.7 < x < 0.75$. The cobalt moment is within $0.2\mu_B$ of either $1.0\mu_B$ or $0.8\mu_B$ from the neutron studies, but if the cobalt moment is to be responsible for this first anomaly then a change of $0.5\mu_B$ is required ($0.25\mu_B$ per Cobalt) over the above short composition range. Such a change is certainly unreasonable on the grounds of electron transfer effects and further if the cobalt moment did so change, this would be accompanied by a drastic change in the exchange field which would almost certainly show in the Curie temperature data. That such a correlation with the Curie temperature does not occur may therefore be taken to show that this moment anomaly is not of cobalt origin. It therefore appears that the neodymium ion must in some way be responsible, and the only manner in which this is possible is through changes in the crystal field quenching of the orbital component of the angular momentum of this ion. It is assumed that the antiparallel (Gd) sublattice does not fan at 4.2 K since this would also account for the observed moment increase. This assumption is justified by the fact that the equilibrium concentration specimen exhibits almost zero magnetisation implying that, at 4.2 K, the spin structures are stable. As was pointed out in chapter three, the structures are simplified in these compounds by virtue of the fact that all the interactions mutually assist the others, in other words the magnetic moments within the individual sublattices

tend to align parallel to one another (unlike the intrasublattice interactions of the ferrites). This fact tends to rule out the possible explanation of anomalies (2) and (3) in terms of a complex ferrimagnetic structure involving, for example, canted spins since there is no immediately obvious process whereby this canting can or should occur.

6.4 The Effect of the Crystal and Exchange Fields on the Nd^{3+} ion.

The effects of the crystal and exchange fields on the ionic neodymium moment were explored initially since this process is simpler than some complex ferrimagnetic model. The basis for crystal field calculations was laid down in chapter three and all that is necessary now is to give the estimations of the various starting parameters used in the calculation. The first objective in crystal field calculations is, of course, to know the field in terms of the operater equivalents for the axis of symmetry chosen as the easy magnetic direction, and this has been done for the 100 and 111 directions in equations 3.8 and 3.9 respectively. It is then necessary to estimate the values of the coefficients B_4 and B_6 which appear in the two equations. These coefficients are given in chapter three equation 3.18, and within the coefficients the term R_2 is related to the lattice parameter, for which the value a = 7.25 Å was used, by equation 3.17. The charge on the rare earth ion, Z_2, is, of course, three but that of the transition metal, Z_1, is uncertain and may be +1 to -1 depending upon the extent of electron transfer. In the calculation this fact is allowed for in the scaling factor SF (see below). The values of $\langle r^n \rangle$ are taken from Freeman and Watson's theoretical calculations of the radial integral (ref. 3.8). Substitution

of these values, together with the appropriate β_J, into the equation for B_4 yields a value of -0.0015 meV. In the final input to the programme for diagonalising the energy matrix (see Appendix II), B_4 is used as a multiplicative factor and the value used in the programme was-0.003 meV, the value used by Bleaney in his calculations for $NdNi_2$(ref. 3.13). (Note: Calculation of B_4 for this system gives a B_4 of-0.0018 meV). The choice of a value for B_4 is arbitrary considering the number of approximations inherent in the calculations so that an order of magnitude is all that is required. Because the Hamiltonian used in the calculations has the form given in equation 3.14, the value of B_6 need not be calculated, since the sixth degree contribution is represented by the ratio of the 4th/6th degree terms in x. However, in assessing the range of reasonable values for x, the term has to be estimated and the resultant range for x is 0.990 - 1.000. The Zeeman term in equation 3.14 is also simply calculated since the internal field is used as a variable spanning 0 - 2 MOe and all that is required is an estimate of the maximum energy that such an internal field generates at the neodymium site - this is of order 10 MeV. Consequently, in the programme, the internal field contribution was stepped in the range 0 - 10 MeV. The ratio of crystal field energy to Zeeman energy was allowed to vary further through the scaling factor, SF, which was given the range 0.3 - 1.2.

The results of the crystal field calculations were printed in the form of the eigenvalues, the matrix of eigen vectors together with the moments associated with each level, and finally the original energy matrix, for the particular H value considered. From the printer output therefore, the diagrams

FIG. 6.3

100 Axis Easy Direction

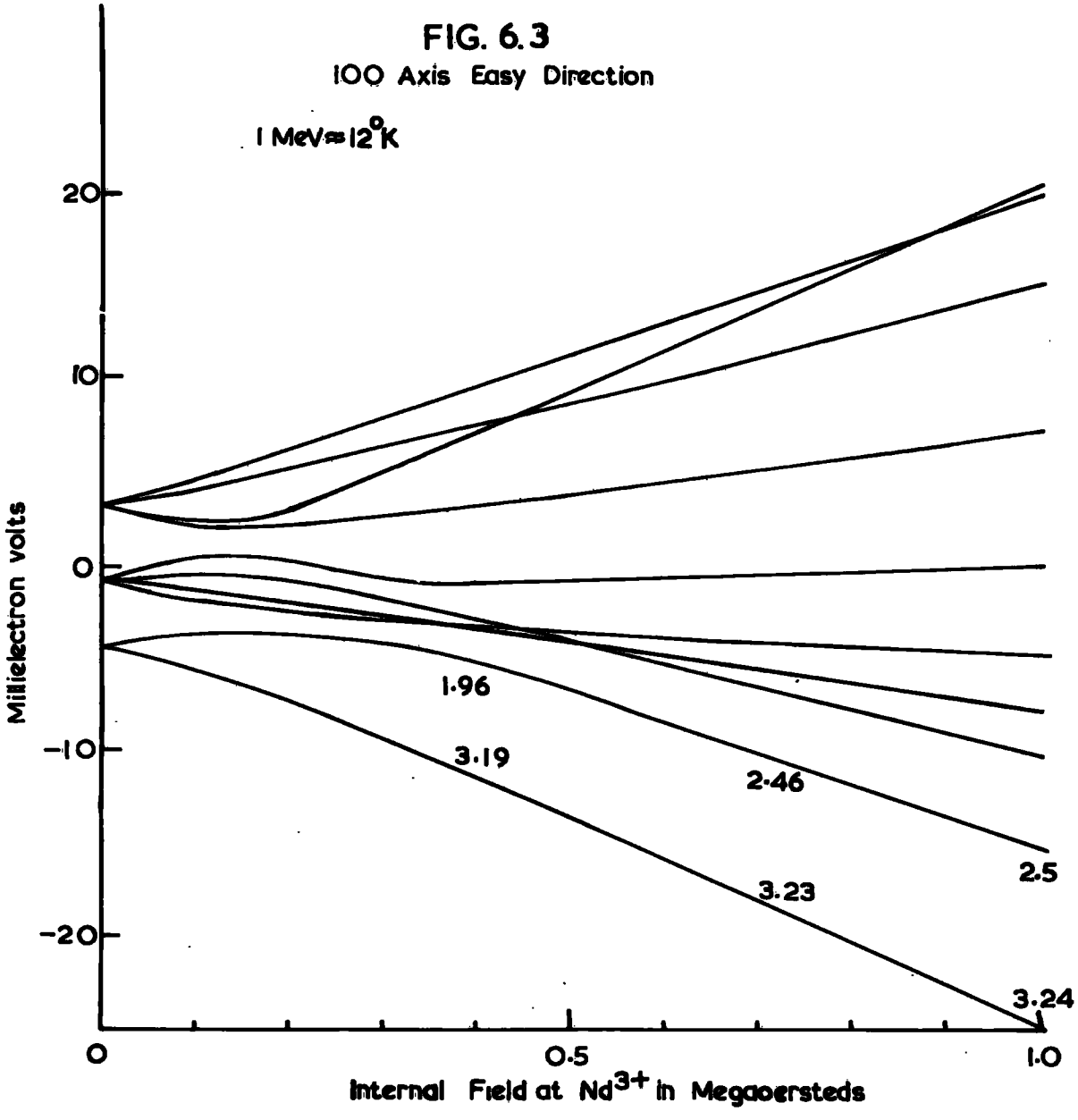

of energy versus internal field was constructed along with a list of moments associated with each level known at the various values of H_{int}. The figures 6.3 and 6.4 show two of these diagrams, the former for the (100) direction and the latter for the (111) direction. The effect of varying the ratio of the fourth to sixth degree coefficients through alteration of x is simply to adjust the initial gaps between the two quartet states and the doublet, and to a lesser extent the magnitude of the overall initial crystal field splitting. This will, in turn, affect the point at which the crossover of two levels occurs as the internal field rises, and this point is also affected by the ratio of the crystal field to Zeeman field energies through the factor SF. The overall results may be pictured in terms of figs. 6.3 and 6.4 as a set of diagrams showing varying degrees of initial splitting (H=0, and Y axis stretching), together with variable relative Zeeman contributions (X axis stretching).

The magnetic moment value shown against a level is, of course, associated with that particular level alone and the physically observed moment at a temperature T is derived from the Boltzmann distribution function for the system given in equation 3.16. Consequently the moment that is observed will depend on the relative separation of the energy levels and their moment values.

6.5 Examination of the Anomalous Magnetic Behaviour in the Light of the Crystal Field Calculations

Cursory perusal of the level scheme for a (100) easy axis (fig. 6.3) shows that the ground state of the neodymium ion has a fairly constant magnetic moment of $\sim 3.2\mu_B$ above H = 0.4MOe and further, the first excited state is

FIG. 6.4

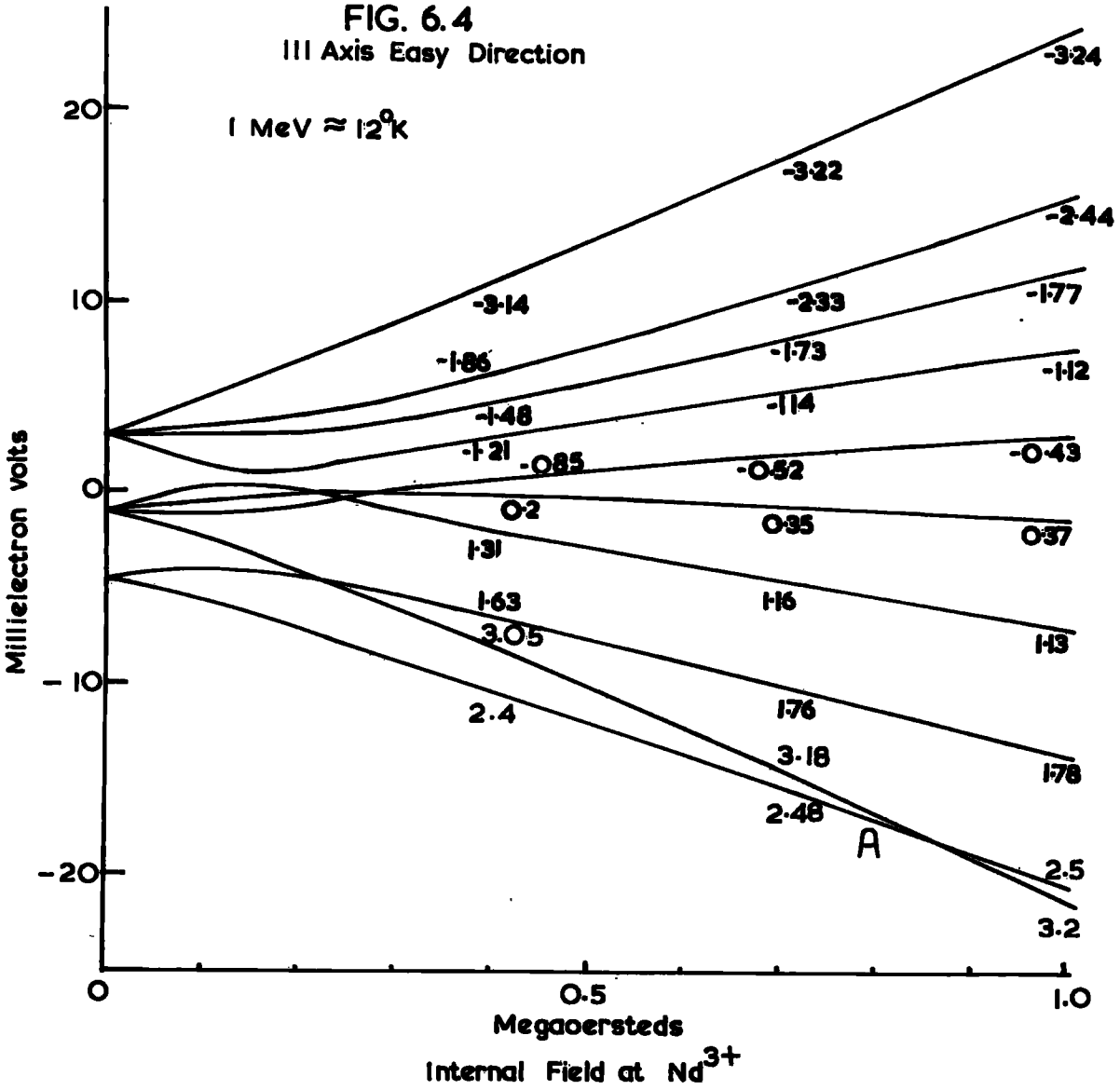
111 Axis Easy Direction
1 MeV ≈ 12°k
20
10
0
-10
-20
Millielectron volts
-3·24
-3·22
-2·44
-3·14
-2·33
-1·77
-1·86
-1·73
-1·12
-1·48
-1·14
-1·21
-0·85
-0·52
-0·43
0·2
0·35
0·37
1·31
1·63
1·16
3·05
1·13
2·4
1·76
3·18
1·78
2·48
A
2·5
3·2
0
0·5
1·0
Megaoersteds
Internal Field at Nd3+

some way above the ground state and shows also a reasonably constant moment. If the 100 axis were chosen as the easy direction then the crystal field can in no way explain through an increase in the ionic neodymium moment the anomalous magnetic phenomena observed and discussed in section 6.3. The 111 axis diagram on the other hand, shows that the ground state is crossed by a level with a higher moment value and in the particular case given in fig. 6.4 the ground state with a moment of $\sim 2.5\mu_B$ is crossed at $H_{int} \approx 0.85$ MOe by the 111 then 1st excited state with a moment of $\sim 3.2\mu_B$. The possibilities inherent in this behaviour are immediately obvious, for example, it is possible for the neodymium ionic moment at 0K to increase by as much as $0.7\mu_B$ by moving through the crossover region.

It is fruitful to examine the behaviour of the neodymium ionic moment with increasing temperature, and this is achieved using the distribution function of equation 3.16. A computer programme written for this purpose is given in Appendix II. The results of one such calculation are given in figure 6.5 and this also shows the effect of including different numbers of levels in the calculation. It is clearly best to include all ten levels in order to get the correct behaviour of the magnetic moment. Note that fig. 6.5 corresponds to calculations in the region of point A in fig. 6.4 i.e. to the left of the crossover point. The detailed shape of this temperature variation can, of course, be altered by varying the energy gap between the levels or, in other words, the position along the H axis of fig. 6.4. The next figure (6.6) shows the variation with temperature for various H values for the same SF and x as used in fig. 6.5.

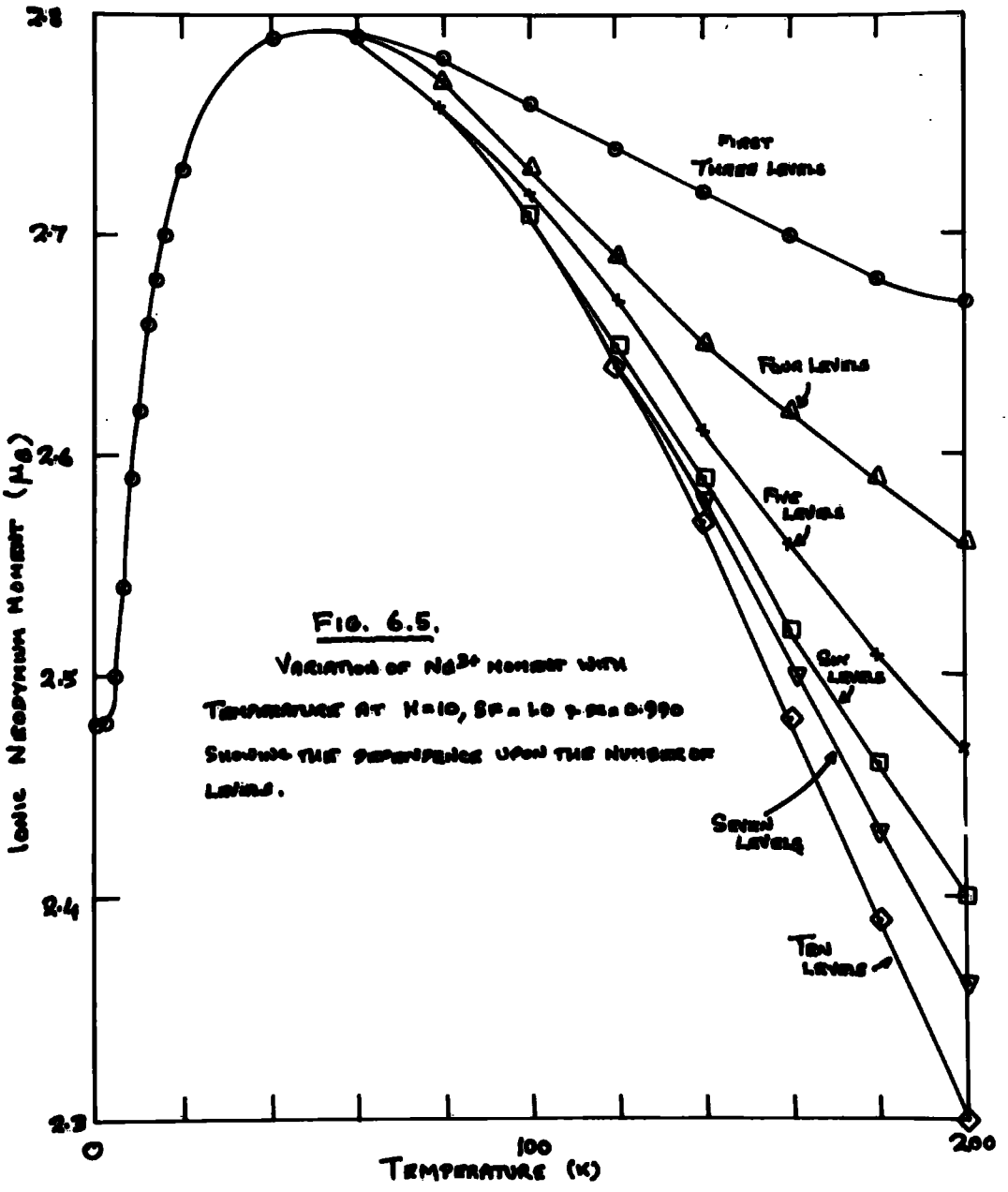

FIG. 6.5.

VARIATION OF Nd^{3+} MOMENT WITH TEMPERATURE AT H=10, SF = 1.0 p.s.u. 0.990 SHOWING THE DEPENDENCE UPON THE NUMBER OF LEVELS.

Consider now the first curve (1) of fig. 5.11 showing the remanence from 4.2 K of the 0.57 specimen. If it is supposed that the neodymium internal field is in the region A of fig. 6.4 then the form of the remanence behaviour may be understood. When the temperature rises the neodymium moment rises rapidly (as in fig. 6.6) with the result that the system is no longer compensated so that a positive net moment (in the neodymium sublattice direction) is observed in the region $0 < T < 90$ K. However, as the temperature rises still further, the excitation to the higher(low moment) states is increased causing a subsequent reduction in the ionic neodymium moment. This reduction coupled to the Brillouin function decay of the system results in the gadolinium sublattice magnetisation matching and then exceeding that of the neodymium sublattice giving the reversal at 90 K after which point the net magnetisation is in the gadolinium magnetisation direction until the second reversal at 205 K. This reversal is possibly a new compensation point resulting from the changed neodymium sublattice magnetisation but this conclusion is difficult to verify. An alternative explanation might involve an impurity which remains magnetised in the original direction (+ve) in which the magnetising field was applied (at 4.2 K) and does not demagnetise until higher temperatures are reached. Support for this view comes from the actual size of the magnetisation at 220 K which is of order $0.003\mu_B$. A crude estimate of the required change in moment to account for the remanence behaviour of curve (1) may be obtained from the ratio of the magnetisation with an applied field to the remanent magnetisation at, for example, the peak of the remanence curve at $T = 150$ K, this giving a method of assessing the moment reduction in the remanent state.

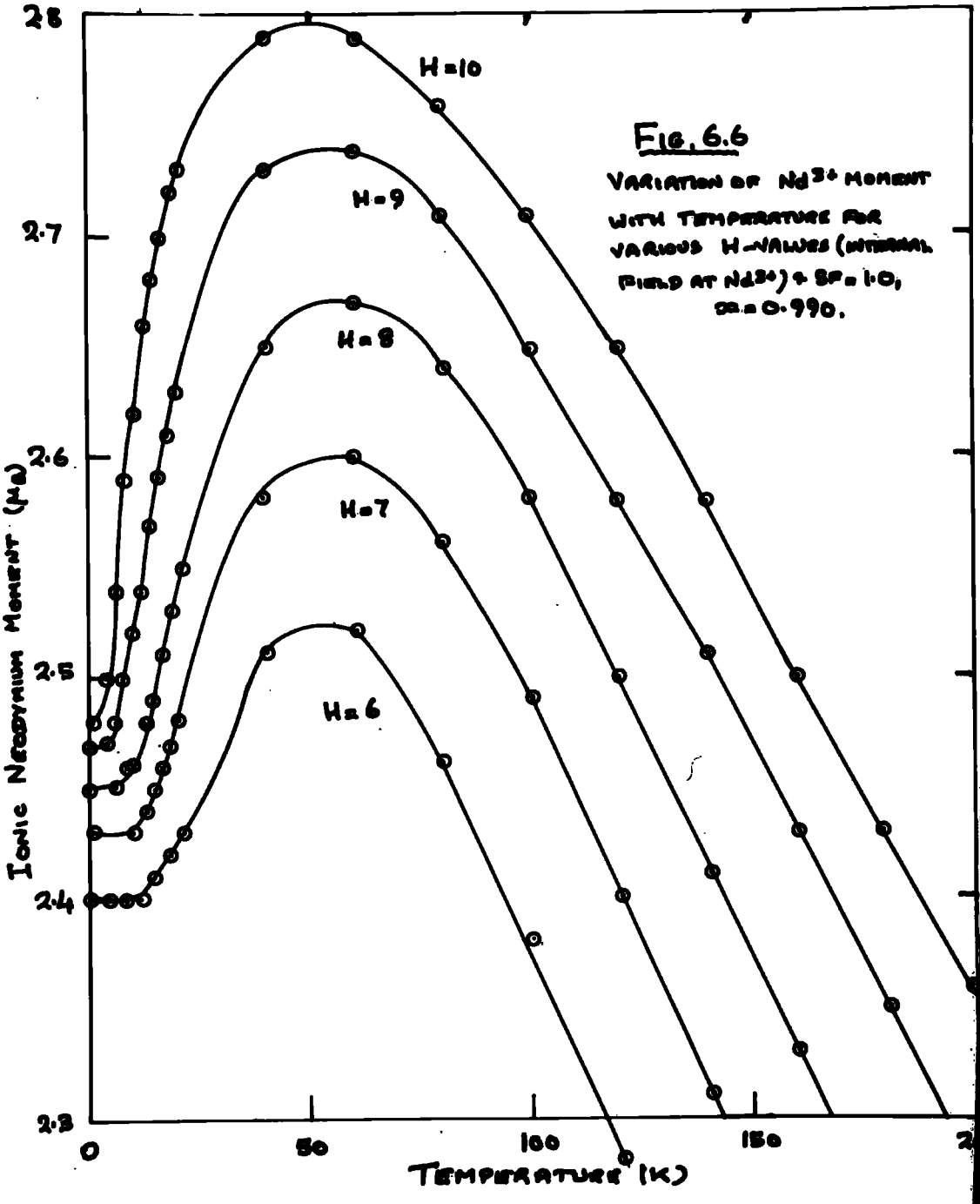

FIG. 6.6

VARIATION OF Nd^{3+} MOMENT WITH TEMPERATURE FOR VARIOUS H-VALUES (INTERNAL FIELD AT Nd^{3+}) + SF = 1·0, σ = 0·990.

On this basis, the observed change between the points A and B (remembering B is negative) on fig. 5.11 of $\sim 0.07\mu_B$ requires a neodymium moment change of $\sim 0.5\mu_B$. Alternatively, the peak, A, requires the neodymium moment to increase by $0.2\mu_B$ before decreasing to below its original value by T = 90 K (here, as mentioned before, the Brillouin function for this sublattice assists the reduction) in order that the net moment may pass through zero. Reference to fig. 6.6 shows that by a suitable choice of H value (and of course SF and x), the demanded moment changes are feasible and further, the similarity of the peak A and the curves in fig. 6.6 is plain adding weight to this interpretation.

The second curve of fig. 5.11(2) showing the remanence versus temperature after magnetising the sample at 77 K may also be accounted for on this basis. At the magnetising temperature the specimen is close to the second compensation point and it is quite probable that in this state the application of a strong magnetic field favours the gadolinium sublattice with the result that a small remanence develops in this direction. Raising the temperature then, will continue the process of neodymium moment reduction giving the rise in observed remanence above 100 K. The subsequent reduction is of course due to the proximity of the Curie temperature. The lack of a reversal in magnetisation at 205 K lends further support to the idea that this is an impurity effect since the impurity magnetisation will be in the positive (field) direction, as before. A further factor which tends to favour the above analysis of the second curve (2) is that magnetisation at 55 K followed by a remanence measurement gave a curve exactly the same as curve 1, implying that at 55 K the neodymium ionic moment is sufficiently high to give remanence in the neodymium direction.

The curious behaviour of σ vs H in fig. 5.12 may also be accounted for in terms of this changing neodymium moment. After cooling the specimen to liquid helium in a small positive field, a small negative remanence was seen to develop. This phenomenon was apparently repeatable being observed upon several occasions. If the magnetic field is applied again the magnetisation increases, passing through zero and becoming positive above 3k0e, but on reducing the field the magnetisation follows the same path giving a negative remanence again. It is this negative remanence that is anomalous and it arises from the effect of the applied field upon the neodymium moment. An increasing applied field has the effect of moving to the right in the energy level diagram of fig. 6.4, in other words, the ground state moment of the neodymium ion rises. An estimate of this change at 4.2 K, can be made and in the case of SF = 1.0, x = 0.990 in the region H = 8-10 MeV, the change is $\sim 0.03\mu_B$/10k0e applied field. This predicted change together with the increase in magnetisation expected for any compensated ferrimagnet or paramagnetic material will account for the observed behaviour of fig. 5.12. Increasing the temperature will, of course, increase the neodymium moment and cause the dotted curve to be observed. This portion of the curve was seen towards the end of a 'helium run' and the specimen was at $\sim$ 9 K when the field was reduced to zero, giving a positive remanence. This small positive remanence is in fact the starting point for the remanence vs temperature curve (1) of fig. 5.11 giving corroborative evidence for the explanation above.

Finally, it is possible to account for the saturation moment anomaly at x = 0.73, by assuming that the effect of increasing the neodymium concentration

is to increase the internal field at the neodymium site, in other words moving to the right in fig. 6.4. Thus as the concentration of neodymium is increased it is suggested that at x = 0.73 the crossover point is reached and above this concentration level the neodymium ground state moment is $\sim 3.25\mu_B$ (as opposed to $2.5\mu_B$ before the crossover). The previously mentioned moment increase of $\sim 0.7\mu_B$ at 0K occurs over an infinitesimal H variation, but at 4.2K the range is wider and the increase smaller due to thermal excitation. A change in the region of $0.5\mu_B$ is possible over a reasonably short range of H ($\sim$ 1 MeV) or, correspondingly, a short compositional change. Estimation of the expected range is very difficult and it is merely pointed out here that this proposal accounts for the observed behaviour, this point is returned to later in section 6.6. It was mentioned earlier that, assuming a gadolinium moment of $7.0\mu_B$ and a linear cobalt moment variation, then the neodymium moments at x = 0.7 and 0.75 are $2.3\mu_B$ and 2.8 respectively. These values are approximately $0.2\mu_B$ lower than those predicted by the crystal field calculations and this may arise in a number of ways. Firstly, the assumptions as to what the component moments should be are based upon Neutron diffraction studies and the errors in these alone cover the predicted values, giving some measure of agreement between the theoretical and experimental results. Secondly, the crystal field calculations are based upon a point charge model a fact which can hardly be reconciled with charged spheres in contact! The third and fourth nearest neighbours have also been ignored in the calculation. The third nearest neighbours are B ions at 0.65 ao, the fourth are A ions at 0.71 ao which gives an error in the region of $\sim$ 10% in the original calculations. This error will not affect the moment

values at the crossover point and is more than amply covered in the ranges given to SF and x. Finally, the polarisation of the conduction electrons will affect the estimated values of the component moments when these are calculated from the experimental results. As was discussed in chapter two, the electron polarisation has been observed to be both parallel to the rare earth spin (e.g. gadolinium metal with a polarisation $\sim 0.55\mu_B$, and in gadolinium doped $LaAl_2$, ref. 2.32) and antiparallel to the rare earth spin (RAl_2's ref. 2.22). It may be supposed that $(Nd,Gd)Co_2$ is similar to $(Gd)LaAl_2$ so that a positive polarisation of the conduction electrons is favoured. If such is the case then this polarisation can easily be of order $0.2\mu_B$ and is an unseen component opposite to the magnetic moments of the neodymium ions. Therefore, in analysing the experimental data in terms of moments the neodymium moment is apparently reduced so that it is necessary to add the conduction electron polarisation to the estimated neodymium moment to obtain a 'true' value of this moment. It is, of course, possible that the polarisation is negative relative to the rare earth spins in which case the neodymium moment is estimated too large, but in the absence of any evidence to the contrary, it is perhaps reasonable to invoke a positive polarisation. It may be added that if there is no polarisation at all then the experimental and calculated results still agree within the stated limits.

6.6 Some Molecular Field Considerations

In attempting to account for the saturation moment data it was tacitly assumed that the internal field at the neodymium site increased with larger

TABLE 6.2

Molecular Field Interactions in the $(Nd,Gd)Co_2$ System

Interaction	Interacting Ions	Sign	Size
λ_{11}	Nd - Nd	+ (fm)	small (20K in $NdNi_2$)
λ_{12}, λ_{21}	Nd - Gd and vice-versa	- (afm)	probably small?
λ_{13}, λ_{31}	Nd - Co and vice-versa	+ (fm)	moderate (~ 100K)
λ_{22}	Gd - Gd	+ (fm)	moderate (85K in GdNi
λ_{23}, λ_{32}	Gd - Co and vice-versa	- (afm)	large))) 400 K
λ_{33}	Co - Co	+ (fm)	large)

Neodymium concentration. It was thought that a simple molecular field treatment of the system would yield confirmatory evidence for this assumption but the following discussion shows that this is not the case.

The possible interactions within the $(Nd,Gd)Co_2$ system are given in table 6.2 together with the sign of each interaction and some estimation of its size (in K). Using this nomenclature we may thus write the internal field at the neodymium site, if the cobalt ionic moment direction is defined as positive, as

$$H_{Nd} = \lambda_{11} \underline{M}_1 - \lambda_{22} \underline{M}_2 + \lambda_{13} \underline{M}_3$$

where $\underline{M}_n$ are the magnetisation vectors. Now $\underline{M}_2$ is antiparallel to the other two vectors so that, in terms of the magnitudes of the vectors m_n, we have

$$H_{Nd} = \lambda_{11} m_1 + \lambda_{12} m_2 + \lambda_{13} m_3.$$

The reduced composition factor x must be included in this equation and it is assumed that this may be accomplished in the following manner:-

$$H_{Nd} = x\,\lambda_{11} m_1 + (1-x)\,\lambda_{12} m_2 + \lambda_{13} m_3$$

The slight compositional dependance of the cobalt moment, m_3, has been ignored in this equation. Therefore at the $GdCo_2$ end of the series (x = 0) we have for the first neodymium ion added

$$H_{Nd}(x=0) = \lambda_{12} m_2 + \lambda_{13} m_3$$

and at the $NdCo_2$ end of the series (x = 1)

$$H_{Nd}(x = 1) = \lambda_{11}m_1 + \lambda_{13}m_3.$$

Examination of these two equations shows that the condition $\lambda_{11}m_1 > \lambda_{12}m_2$ is necessary for the field at the neodymium site to increase with increasing x, and the truth of this condition relies on the size of λ_{12}. An indication of the magnitude of this interaction may be obtained from the $(Nd,Gd)Ni_2$ system since, in this series, there are but three interactions (λ_{11}, λ_{22} and λ_{12}) because the nickel ion carries zero magnetic moment. The ferrimagnetic Curie temperature for such a two sublattice system can be expressed in terms of the Weiss constants (C_n) and the molecular field constants λ_{nm} (see for example ref. 3.1, p494, equ. 9-2.13). Substitution of the values for C_n of the terminal compounds $NdNi_2$ and $GdNi_2$ with the appropriate composition factor into such an expression leads to the value of λ_{12} at the composition value in question. In the present instance it was found that $\lambda_{12} > \lambda_{11}$ by a factor of two, the discrepancy being enlarged when the magnetisation vectors are included since $m_2 > m_1$. Therefore it is clear that such a simple treatment will not yield the desired result. This fact is perhaps not surprising in view of the approximations involved, such as the estimation of λ_{12} from the nickel series instead of from the cobalt compounds themselves. Furthermore, the manner in which the composition factor, x, is included in the equations assumes that the sublattice contributions to the internal field are linearly independent upon x, which may not be the case, although the available evidence supports this view.

Among the other possible means of estimating the internal field, two methods are perhaps worth mentioning. Bloch and Lemaire (ref. 6.1) developed a phenomenological theory to account for the high temperature susceptibility data of the

RCo_2 compounds. This theory assumes that the cobalt has an exchange enhanced susceptibility with the rare earth carrying a permanent moment and the experimental data are fitted using the enhanced susceptibility and the molecular field interactions as parameters. Thus given good susceptibility data it is possible to obtain through a fitting procedure an estimation of the molecular fields. Unfortunately the lack of such data in the present case makes this calculation pointless and indeed some of the results quoted in ref. 6.1 are inconsistent with the experimentally derived parameters throwing some doubt upon the ultimate validity of this method.

The second method of estimating the molecular field interactions, due to Bowden et al. (ref.6.2), describes the inclusion of crystal field effects within the framework of the molecular field approximation. One of the results of this work is an equation relating the crystal and molecular field parameters and the paramagnetic transition temperature. To obtain an unequivocal value of the molecular field it is necessary to have accurate values for the crystal field parameters together with the paramagnetic transition temperature and use a complex fitting process. Quite apart from the lack of accurate data on the paramagnetic region, the crystal field parameters are not sufficiently defined to warrant the process.

One further aspect of Bowden's work (ref. 2.50) relates to the easy direction in the RB_2 compounds. It was mentioned earlier in chapter two that the Mössbauer technique can reveal the easy axis in polycrystalline samples and in ref.2.50 the experimentally observed easy axes are predicted by a simple theory based upon the sign of the fourth degree crystal field parameter, B_4. For S-state ions (and ions which carry zero magnetic moment) the easy axis is determined by the transition metal component which favours the 111-axis. Neodymium, however, has a negative fourth degree crystal field parameter

resulting in a predicted easy axis of 100 for $NdCo_2$. In the present work the crystal field parameters consistent with the best interpretation of the magnetic data require an appreciable sixth degree contribution and also that the easy axis be in the 111-direction. The simple theory of ref. 2.50 assumes that the sixth degree crystal field parameter is very small. It is reasonable therefore that the relatively large sixth degree parameter in the compounds, together with the influence of the $GdCo_2$ component will result in the 111-direction being the easy axis of magnetisation.

6.7 Conclusion

It may be said in conclusion that the compound series $(Nd_xGd_{1-x})Co_2$ generally shows the behaviour to be expected from a ferrimagnetic intermetallic compound and that the anomalies discovered may be attributed to the effects of the crystal and internal magnetic fields upon the neodymium ion. The good agreement between the experimental data and the theoretical predictions clearly demonstrates that this type of calculation can be successfully and usefully applied to materials of this type in spite of the fact that exact calculations are not possible.

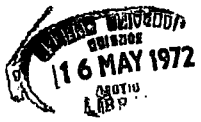

CHAPTER 6 - REFERENCES

6.1 Bloch, D., and Lemaire, R., Phys. Rev., B., 2, 2 (1970)

6.2 Bowden, G.J., Bunbury, D.St.P., and McCausland, M.A.H., To be published.

APPENDIX I

FURTHER ELECTRONIC CIRCUITS

In this appendix, the circuits of the commercial parts of the V.S.M. are given. Also included are the potentiometer power supply and Hall Probe Circuit.

CONTENTS

AMPLIFIER CIRCUIT

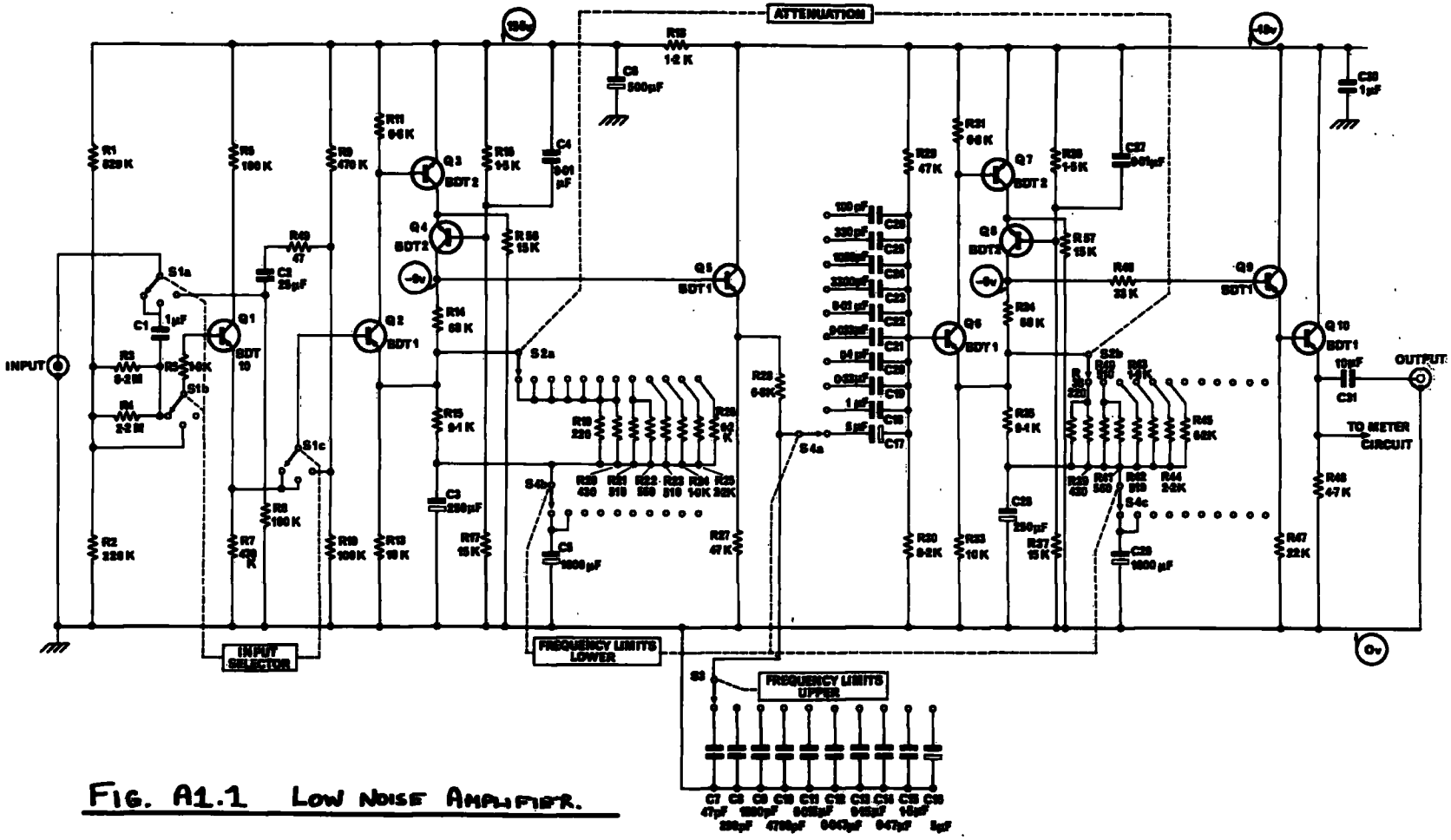

FIG. A1.1 LOW NOISE AMPLIFIER.

METER CIRCUIT

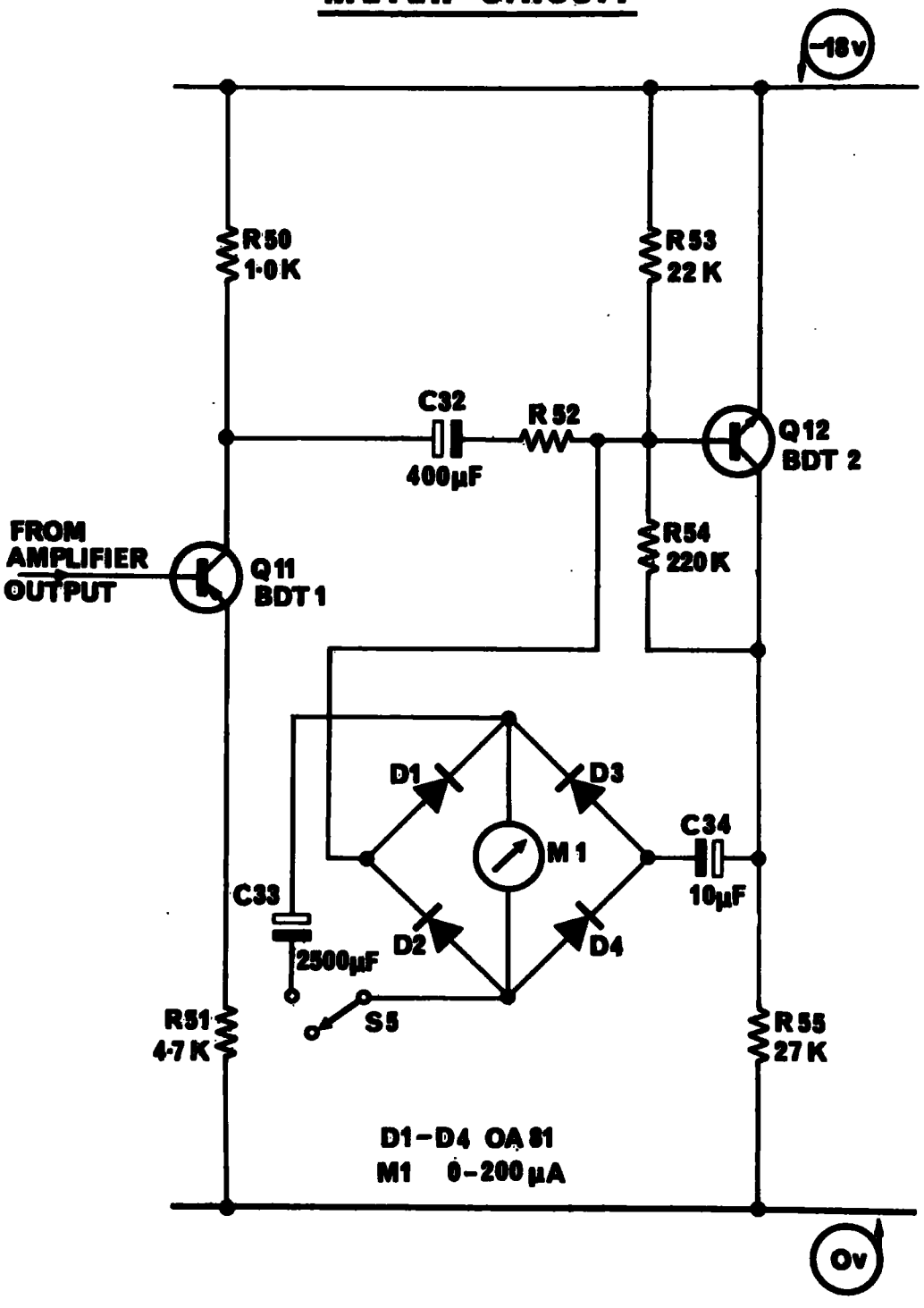

Fig A1.2 L.N.A. METER CIRCUIT.

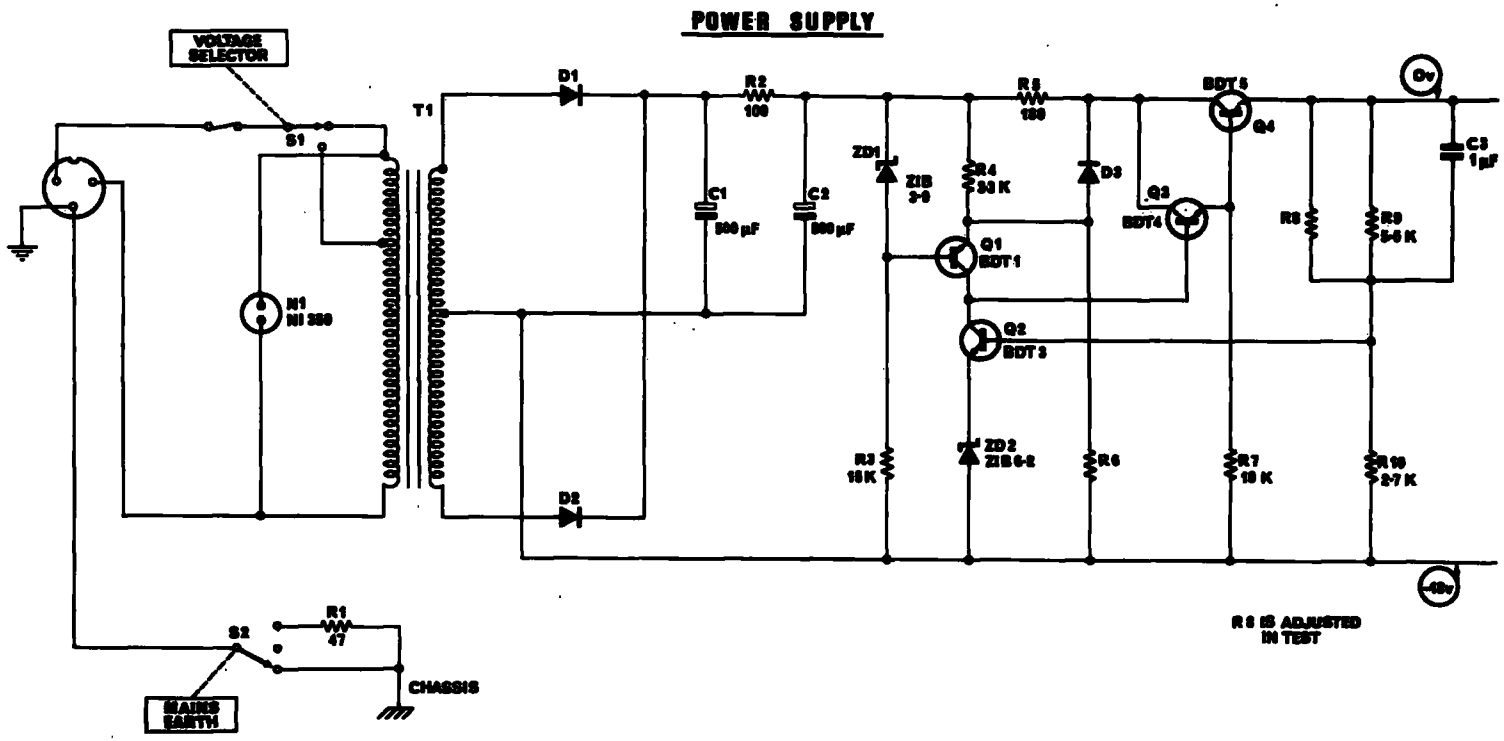

Fig. A1.3 L.N.A. Power Supply.

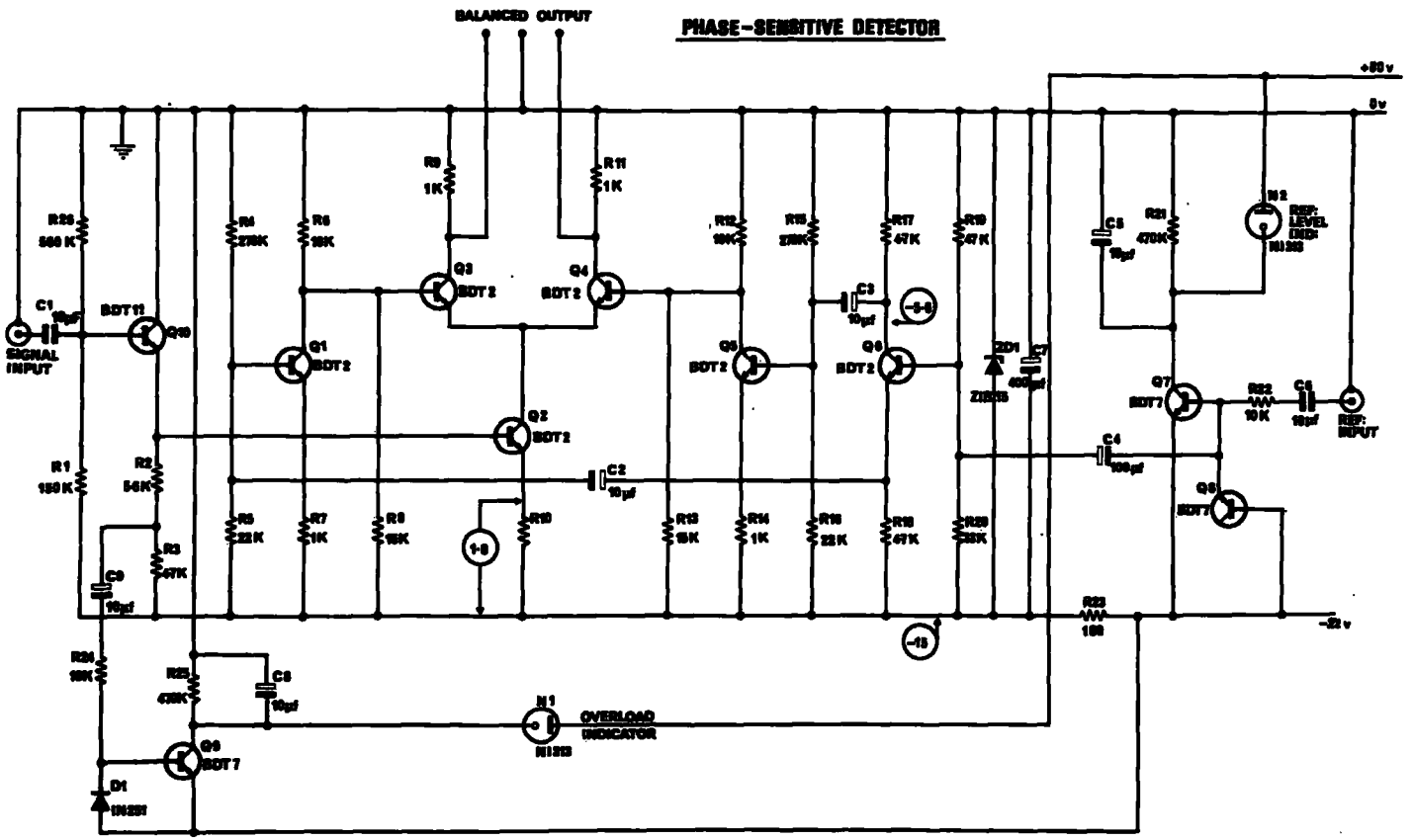

Fig. A1.4 Phase Sensitive Detector.

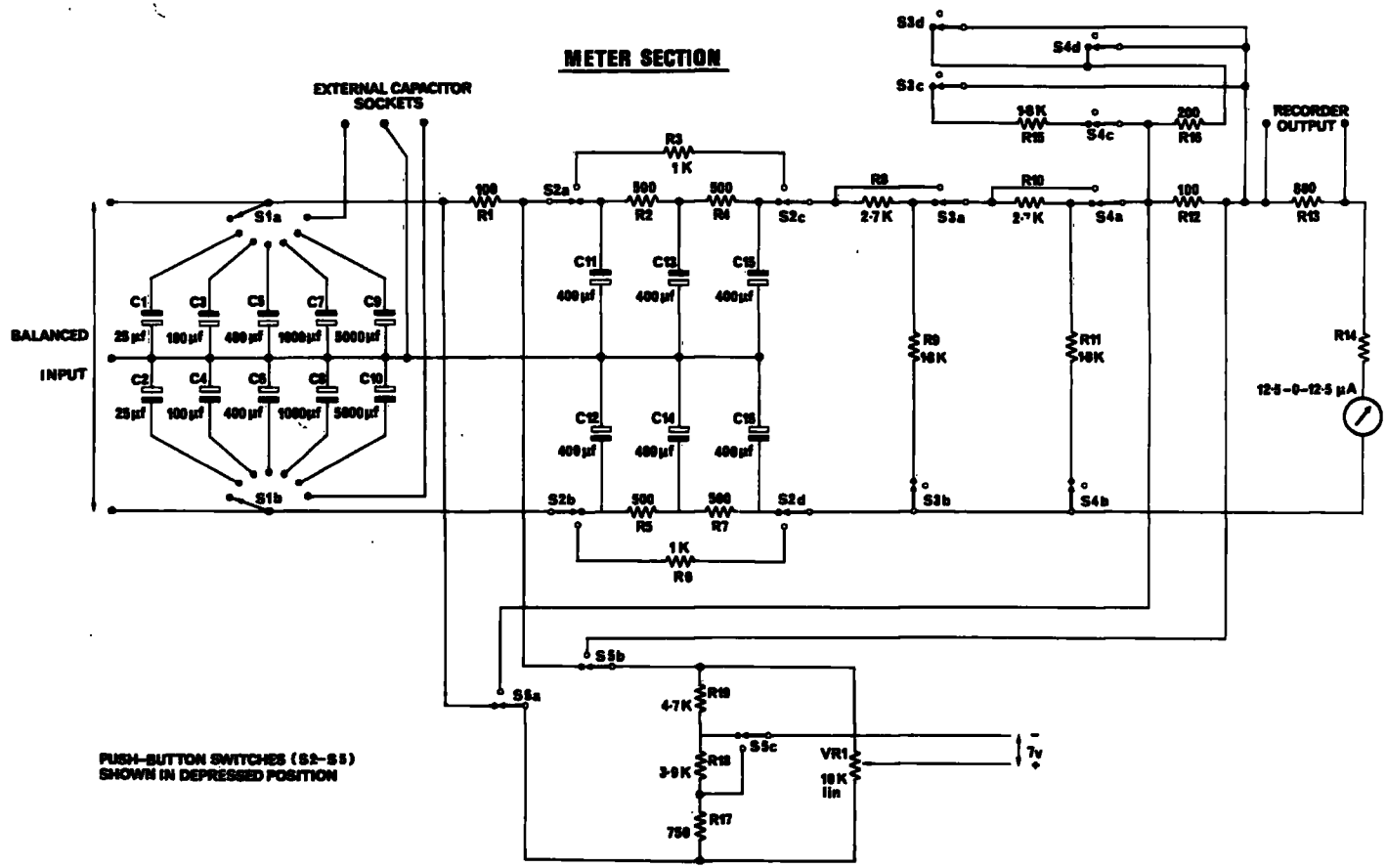

PUSH-BUTTON SWITCHES (S2–S5) SHOWN IN DEPRESSED POSITION

FIG. A1.5 P.S.D. METER SECTION.

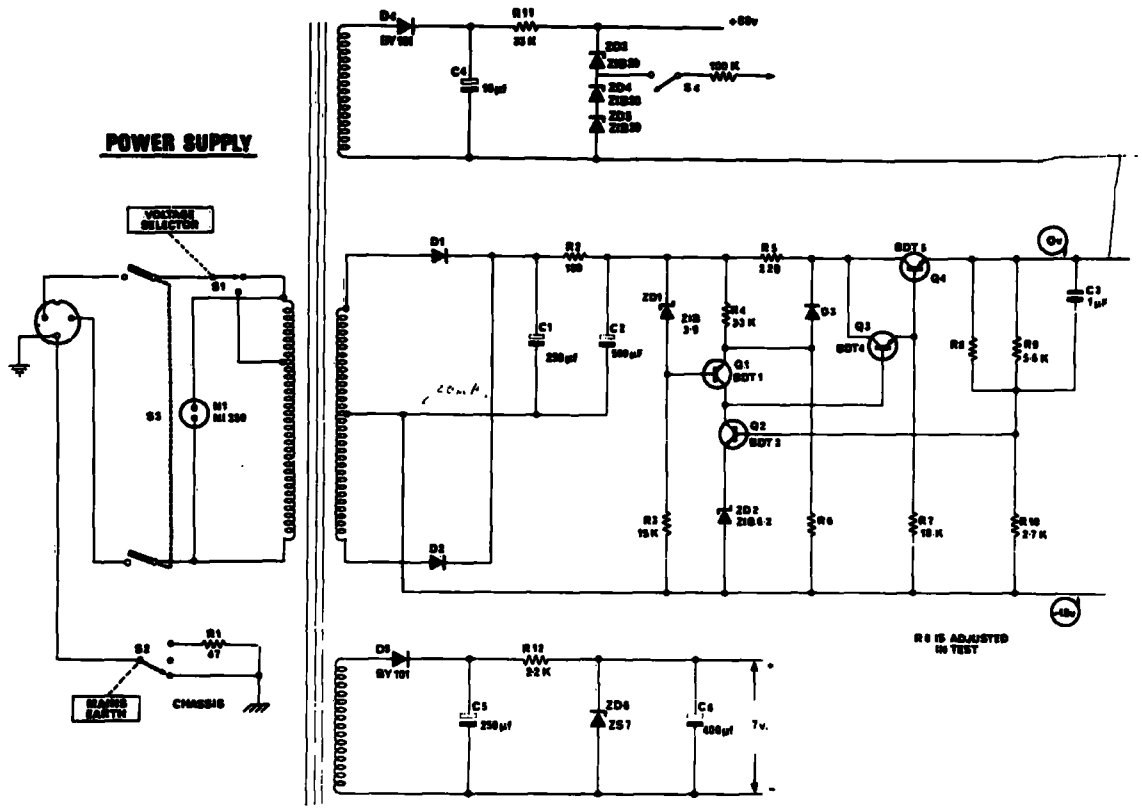

FIG. A1.6 P.S.D. POWER SUPPLY.

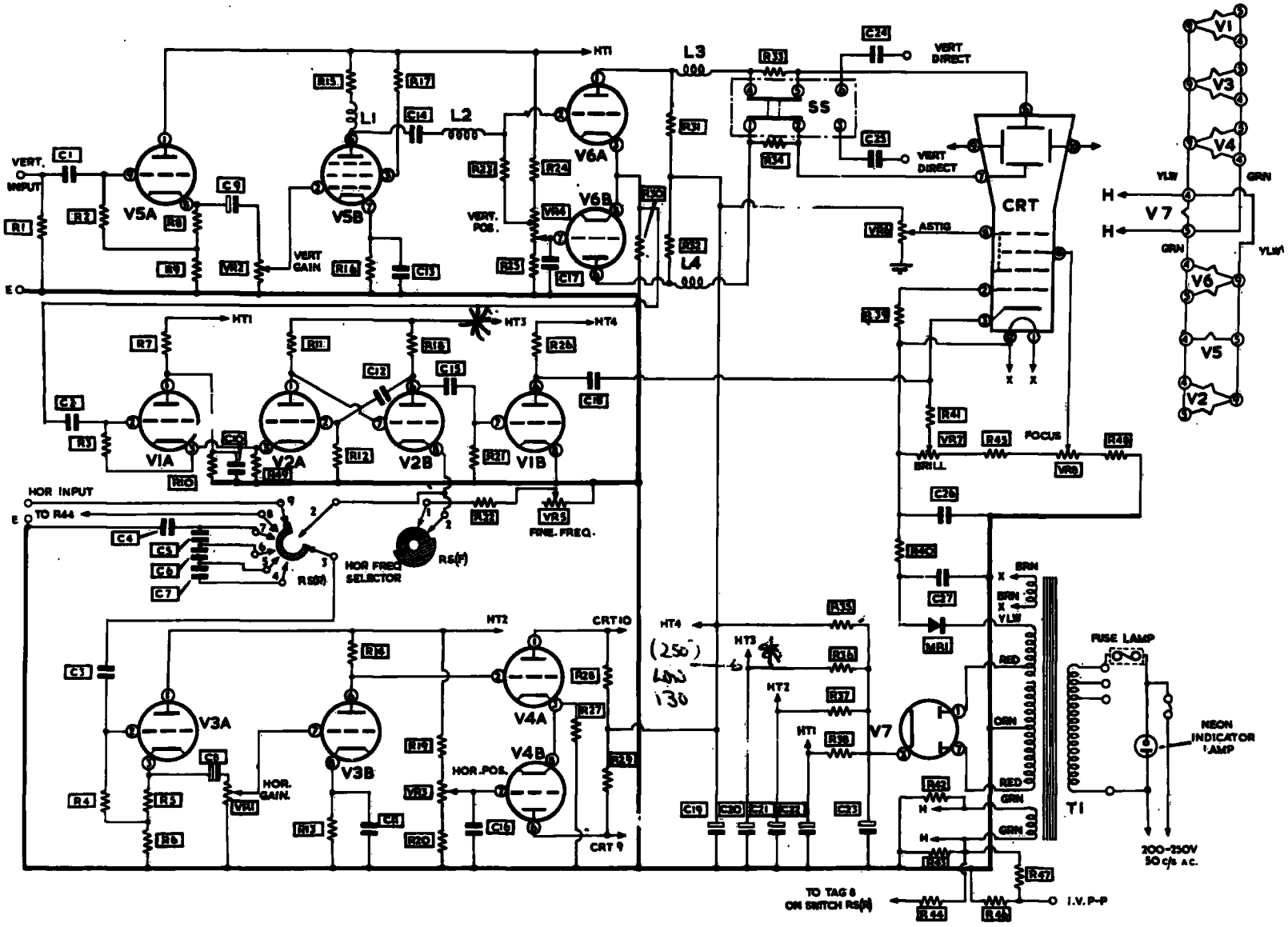

FIG. A1.7 Oscilloscope

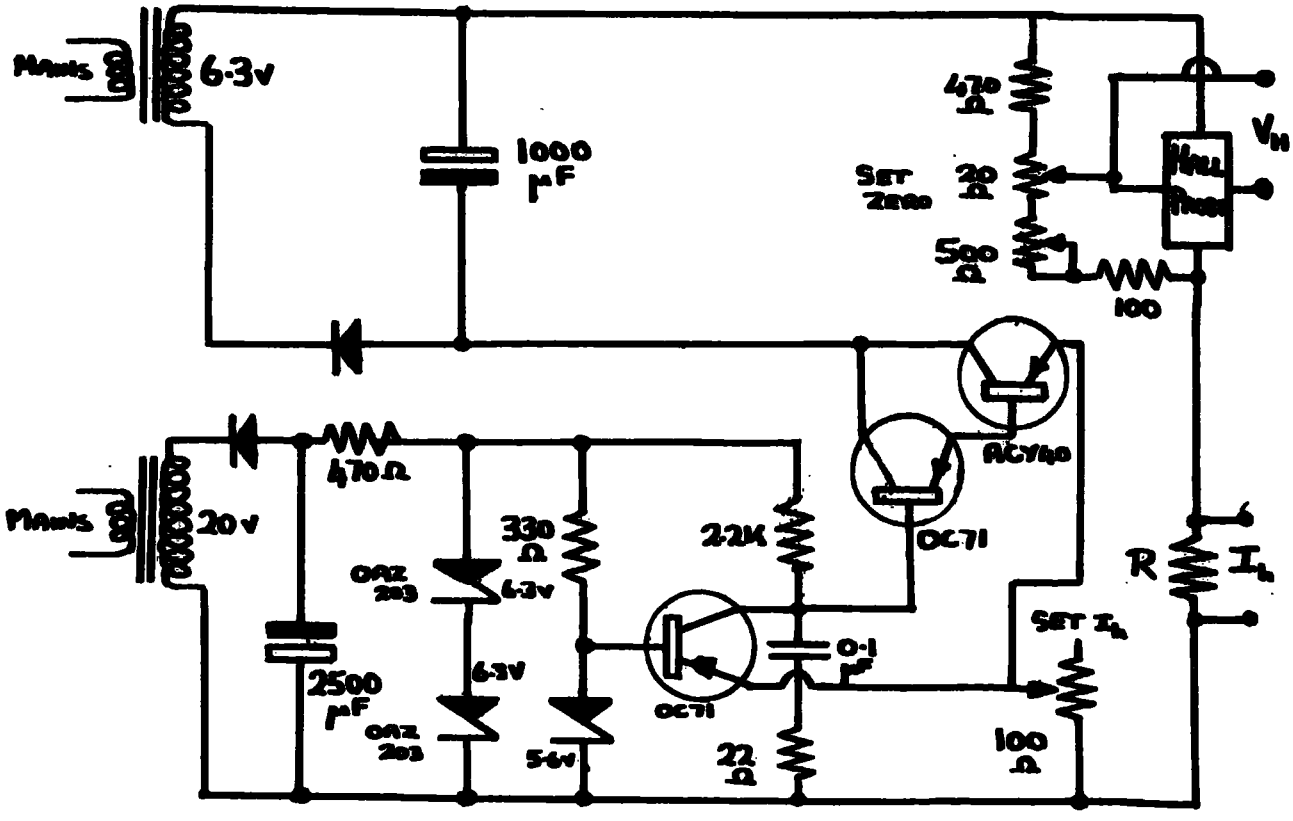

HALL PROBE CURRENT = 100mA

SENSITIVITY = 0·39 mV/mA.K_g.

HALL PROBE:- AEI type HP1A2 no 2158.

FIG. A1.8 HALL PROBE CIRCUIT.

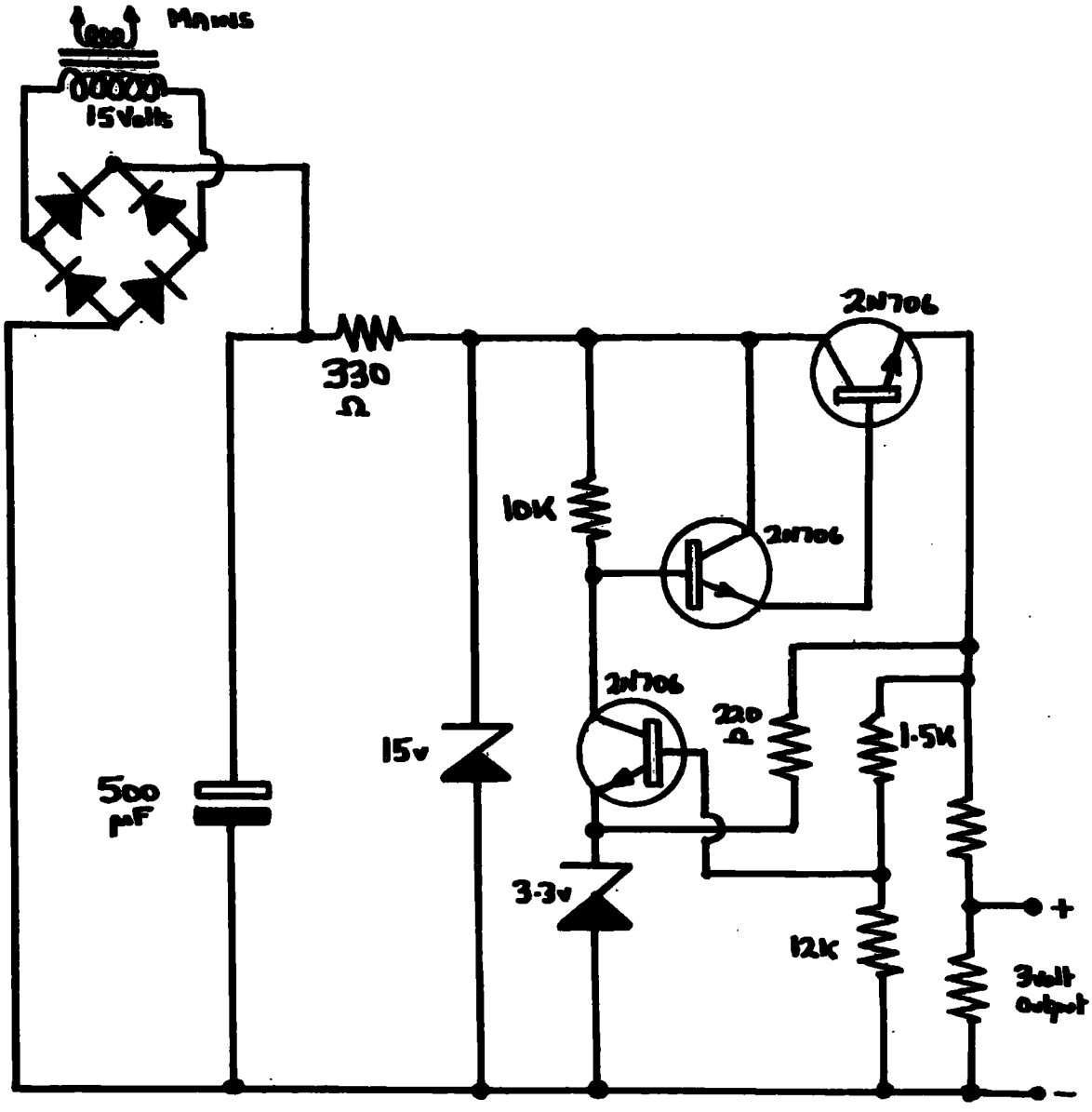

FIG. A1.9. POTENTIOMETER POWER SUPPLY.

APPENDIX II

COMPUTER PROGRAMMES

The programmes given in this appendix were written in the language PL/1 for use on the IBM 360/67 computer of the Universities of Durham and Newcastle. The programmes were primarily developed for use on the time sharing terminal system (M.T.S.) available at the Durham Physics Department.

CONTENTS

CUBSOLV

```
1       CUBSOLV: PROC OPTIONS(MAIN);
2       DCL(AB(50)) FLOAT;
3       DCL(H(50),B(50),C(50),Q(50),D(50),R(50),HH(50))FLOAT;
4      DCL(N,NF,NM,U)FIXED BIN,DATA FILE INPUT;
5      DCL(WW(0:1),F(50),G(50))FLOAT,DATA FILE INPUT;
6       DCL (ZOO) FIXED INITIAL (0);
7      DCL(NN(50),DD(50),MM(50),V)FLOAT;
8      DCL(ZZ,AA,II,P,I,T,NI,K,L,M,J,BA,XX) FIXED BIN;
9      DCL NAME CHAR(50) VARYING,DATA FILE INPUT;
10      /* DATA FORM: U, NO. OF FILMS; NAME, NAME OF COMPOUND;
11      W, WEIGHTED MEAN VALUE OF WAVELENGTH; WW, PAIR OF WAVELENGTH VALUES;
12      N,NO OF LINES;NF,NO OF FORWARD REFS;NM,LAST LINE BEFORE DOUBLETS;
13      F(I),G(I), PAIRS OF NOS READ OFF DEVICE SMALLER NO, FIRST.*/
14      LESQ: PROCEDURE (AB,MM,N);
15      DCL (XX,L,M,K) FIXED BIN;
16      DCL(Y(2,2),S(1,2),X(50,2),Z(2,2),AB(*),MM(*),B,SSR,RSQ,A,E)FLOAT;
17       DO K = 1 TO N;
18          X(K,1)=AB(K);
19      END;
20      DO K = 1 TO N;
21       X(K,2)= MM(K);
22      END;
23      PUT LIST('NO.OF POINTS TO BE USED IN EXTRAPOLATION')SKIP;
24      PUT SKIP;
25      GET LIST (XX);
26      Y= 0;
27      DO L= 1 TO 2;
28      DO M= 1 TO 2;
29      DO K= XX TO N;
30      Y(L,M)=Y(L,M)+(X(K,L)*X(K,M));
31     END;
32      END;
33      END;
34      S=0;
35      DO L= 1 TO 2;
36      DO K= XX TO N;
37        S(1,L)=S(1,L)+X(K,L);
38      END;
39      END;
40      Z=0;
41      DO L= 1 TO 2;
42       DO M = 1 TO 2;
43       Z(L,M)= Y(L,M)-(S(1,L)*S(1,M)/(N-XX+1));
44        END;
45        END;
46       B=Z(1,2)/Z(2,2);
47       SSR= Z(1,2)*B;
48       RSQ=SSR/Z(1,1);
```

CUBSOLV (Continued)

```
49        A=(S(1,1)-(B*S(1,2)))/(N-XX+1);
50        IF (Z(1,1)-SSR)<0 THEN GO TO L4;
51        E=SQRT((1/Z(2,2))*((Z(1,1)-SSR)/(N-XX-1)));
52        GO TO L5;
53        L4: E=0;
54        L5: PUT SKIP EDIT ('INTERCEPT ON Y AXIS = ',A,'A')(A(22),F(10,6),A)
55        PUT SKIP EDIT ('SLOPE = ',B)(A(8),F(8,4));
56        PUT SKIP EDIT ('ERROR = ',E)(A(8),F(6,5));
57      END LESQ;
58      GRAPH: PROC (AB,MM,N);
59      DCL (AB(*),MM(*),Z(50),M(50),XX(50)) FLOAT;
60      DCL(Y(50),X(50)) FLOAT;
61      DCL (I,N) FIXED BIN;
62      Y=AB;
63      X=MM;
64      DO I=1 TO N;
65      M(I)= TRUNC (Y(I)*10);
66      Y(I)=      (Y(I)*10)-M(I);
67      Y(I)=Y(I)*70;
68      Z(I)= TRUNC(Y(I));
69      IF((Y(I)-Z(I)))>0.49 THEN Z(I)=Z(I)+1;
70      X(I)=25*X(I);
71      XX(I)= TRUNC(X(I));
72      IF (X(I)  -XX(I))>0.49 THEN XX(I)=XX(I)+1;
73      END;
74      PUT PAGE;
75      PUT LIST('GRAPH BEGINS');
76      PUT EDIT('********************')(A(20));
77      DO I=5 TO N;
78      PUT EDIT ('*')( SKIP(XX(I)),X(Z(I)),A);
79      END;
80      PUT SKIP EDIT('********************')(A(20));
81      PUT EDIT('END OF GRAPH')(A(12));
82      PUT SKIP;
83      END GRAPH;
84      GET FILE (DATA) LIST(U);
85      DO I=1 TO U;
86      Q=0;
87      GET FILE (DATA) LIST(NAME);
88      GET FILE(DATA) LIST(W);
89      GET FILE(DATA) LIST(WW);
90      GET FILE(DATA) LIST(N,NF,NM);
91      NI=0;
92      DO I=1 TO NM;
93      NI=NI + 1;
94      GET FILE(DATA) LIST(F(I),G(I));
95      HH(I)=(G(I)-F(I))/4;
96      IF NI>NF THEN DO;
```

CUBSOLV (Continued)

```
 97       HH(I)=90-HH(I);
 98       END;
 99       H(I)=HH(I)/57.296;
100       C(I)=SIN(H(I));
101       Q(I)=C(I)*C(I);
102       D(I)=W/(2*C(I));
103      END;
104       DO I=(NM+2) BY 2 TO N;
105       DO T=0 TO 1;
106       IF T=0 THEN I=I-1;
107       GET FILE(DATA) LIST(F(I),G(I));
108       H(I)=(90-((G(I)-F(I))/4))/57.296;
109       C(I)=SIN(H(I));
110       Q(I)=C(I)*C(I);
111       D(I)=WW(T)/(2*C(I));
112       IF T=0 THEN I=I+1;
113       END;
114       END;
115       PUT SKIP(3);
116       PUT SKIP LIST (NAME);
117       PUT SKIP EDIT ('WAVELENGTH = ',W,'A')(A(13),F(7,5),A);
118       PUT LIST ('D VALUES') SKIP;
119       PUT SKIP;
120       DO I=1 TO N;
121       PUT EDIT ('D(',I,') = ',D(I))(X(5),A(2),F(2,0),A(4),F(5,3));
122       IF I/4=1 THEN PUT SKIP;
123       IF I/4=2 THEN PUT SKIP;
124       IF I/4=3 THEN PUT SKIP;
125       IF I/4=4 THEN PUT SKIP;
126       IF I/4=5 THEN PUT SKIP;
127       END;
128       PUT SKIP EDIT ('SINE SQUARED VALUES')(A(19));
129       PUT SKIP;
130       DO I=1 TO N;
131       PUT EDIT(Q(I))(X(2),F(6,4));
132       END;
133       PUT SKIP LIST('FIRST TRIAL S-VALUE');
134       PUT SKIP;
135       LOOO: GET LIST(ZZ);
136       ZOO=0;
137         DO I=1 TO N;
138       IF ZOO=0 THEN GO TO LOO;
139       ELSE DO;
140       DD(I)=Q(I)/Q(BA);
141       ZZ=20;
142       GO TO LO;
143       END;
144       LOO: DD(I)=Q(I)/Q(1);
```

CUBSOLV (Continued)

```
145       L0: NN(I)=ZZ*DD(I);
146       AA=TRUNC(NN(I));
147       V=ABS(AA-NN(I));
148       IF V<0.49 THEN GO TO L2;
149       ELSE DO;
150       AA=AA+1;
151       L2: R(I)=AA;
152       IF R(I)=20 THEN DO;
153       BA=I;
154       ZOO=1;
155       END;
156       END;
157       END;
158       PUT SKIP EDIT ('CORRESPONDING S VALUES')(A(22));
159       PUT SKIP;
160       DO I=1 TO N;
161       PUT EDIT(R(I))(X(5),F(3,0));
162       END;
163       PUT SKIP LIST('LATTICE PARAMETER ASSOCIATED WITH
164       TRIAL S-VALUE IS-');
165       PUT SKIP EDIT(SQRT((R(1)*W*W)/(4*Q(1))))(F(5,3));
166      PUT SKIP LIST ('TYPE 1 IF ANOTHER TRIAL S-VALUE IS
167       REQUIRED OTHERWISE TYPE ANY OTHER NUMBER');
168       PUT SKIP;
169       GET LIST(II);
170       IF II=1 THEN GO TO LOOO;
171       PUT LIST('TYPE FINAL SERIES OF S-VALUES WITH
172       ANY NECESSARY HUMAN ADJUSTMENT');
173       PUT SKIP;
174      R=0;
175      DO I=1 TO N;
176      GET LIST (R(I));
177      END;
178      PUT LIST ('LATTICE PARAMETER')SKIP;
179       DO T=1 TO NM;
180       AB(T)=SQRT((R(T)*W*W)/(4*Q(T)));
181       END;
182       DO I=(NM+2) TO N BY 2;
183       DO T=0 TO 1;
184       IF T=0 THEN I=I-1;
185       AB(I)=SQRT((R(I)*(WW(T)**2))/(4*Q(I)));
186       IF T=0 THEN I=I+1;
187       END;
188       END;
189       DO T=1 TO N;
190       PUT SKIP;
191       PUT EDIT('A(',T,') = ',AB(T),'A')(A(2),F(2,0),A(4),F(7,4),A);
192       MM(T)=0.5*((COS(H(T))**2)/SIN(H(T))+(COS(H(T))**2)/H(T));
```

CUBSOLV (Continued)

```
>    193        PUT EDIT ('NR = ',MM(T))(X(3),A(5),F(6,4));
>    194        PUT EDIT ((H(T)*57.296),'DEGREES')(X(3),F(5,2),X(2),A(7));
>    195        END;
>    196        CALL GRAPH(AB,MM,N);
>    197        CALL LESQ(AB,MM,N);
>    198        END;
>    199        END CUBSOLV;
#END OF FILE
#
```

DIAG

```
1       (SUBRG):
2       DIAG:PROC OPTIONS(MAIN);
3       DCL(A(N,N),R(N,N))BIN FLOAT CONTROLLED;
4       DCL(N,MV) FIXED BIN,DATA FILE STREAM INPUT;
5       DCL(B(N,N),E(N,N))FLOAT CONTROLLED,DATA FILE STREAM INPUT;
6       DCL(IND) FIXED BIN;
7       DCL YY FIXED BIN INITIAL(0);
8       DCL(Y,G,SUM)FLOAT;
9       DCL(P,M) FLOAT;
10      DCL(SF,X,INCX,INCS,MAXS)FLOAT;
11      DCL(C(N,N),D(N,N))BIN FLOAT CONTROLLED;
12      DCL(INDD)FIXED BIN;
13      DCL(MAXH,B4,B6)FLOAT;
14     DCL(H,I,J,K,L,S)FIXED BIN;
15      PUT LIST('DATA FORM: SF,X,INCS,INCX,MAXS,P(INIH),MAXH,IND(=1(0))');
16      PUT LIST('G-VALUE.....B4.....B6');
17      PUT SKIP;
18      GET LIST(SF,X,INCS,INCX,MAXS);
19      PUT DATA(SF,X,INCS,INCX,MAXS);
20      PUT SKIP;
21      Y=X;
22      GET LIST (P);
23      GET LIST (MAXH);
24      PUT DATA(MAXH);
25      GET LIST(INDD);
26      GET LIST(G);
27      PUT DATA(INDD,G);
28     GET LIST(B4,B6);
29     PUT DATA(B4,B6);
30      PUT SKIP;
31      GET FILE(DATA) LIST (N,MV);
32     ALLOCATE A;
33     ALLOCATE B;
34      ALLOCATE C;
35      ALLOCATE D;
36      ALLOCATE E;
37     ALLOCATE R;
38      M=P;
39      DO I=1 TO N;
40       DO J=1 TO N;
41      GET FILE (DATA)LIST(B(I,J));
42       END;
43      END;
44      B=B*B4;
45      DO I=1 TO N;
46      DO J=1 TO N;
47     GET FILE (DATA) LIST (E(I,J));
48     END;
```

DIAG (Continued)

```
49        END;
50       E=E*B6;
51        L1:SF=SF+YY*INCS;
52        L2:P=M;
53        AGAIN: A=SF*(X*B+(1-ABS(X))*E);
54        PUT EDIT('SCALE FACTOR = ',SF)(A(15),F(5,2));
55        PUT EDIT('4/6 RATIO = ',X)(X(5),A(12),F(6,3));
56        PUT SKIP;
57        PUT LIST('H VALUE');
58        PUT SKIP;
59        PUT EDIT(P)(F(5,2));
60        PUT SKIP;
61        PUT SKIP;
62        C=0;
63        DO J=1 TO N;
64        C(J,J)=P*(5.5-J);
65         END;
66        A=A-C;
67        D=A;
68       CALL MSDU(A,R,N,MV);
69        PUT LIST ('EIGEN VALUES ARE');
70        PUT SKIP;
71       DO K=1 TO N;
72        PUT EDIT(A(K,K))(X(2),F(9,2));
73        END;
74        PUT SKIP;
75        DO K=1 TO N;
76        PUT EDIT (A(K,K))(X(2),F(9,6));
77        END;
78       PUT SKIP;
79        PUT LIST('EIGEN VECTORS ARE');
80        PUT SKIP;
81        DO L=1 TO N;
82        SUM=0;
83        DO S=1 TO N;
84        PUT EDIT(R(S,L))(X(3),F(7,4));
85         SUM=SUM+(R(S,L)**2)*((0.5*(N+1))-S)*G
86        ;
87        END;
88         PUT EDIT('MOMENT=',SUM)(X(3),A(7),F(6,2));
89        PUT SKIP;
90        END;
91       PUT SKIP;
92        IF INDD=1 THEN DO;
93        PUT LIST('ORIGINAL MATRIX');
94        PUT SKIP;
95        DO I=1 TO N;
96        DO J=1 TO N;
```

DIAG (Continued)

```
 97        PUT EDIT(D(I,J))(X(2),F(9,5));
 98        END;
 99        PUT SKIP;
100        END;
101        END;
102       PUT SKIP;
103        IF P>MAXH THEN GO TO L4;
104        IF P>9.9 THEN GO TO L4;
105        IF P<1.9 THEN DO;
106        P=P+0.2;
107        GO TO AGAIN;
108        END;
109        IF P<3.9 THEN DO;
110        P=P+0.4;
111        GO TO AGAIN;
112        END;
113        P=P+1;
114        GO TO AGAIN;
115        L4: IF ABS(X)>0.99999 THEN GO TO L3;
116        X=X+INCX;
117        GO TO L2;
118        L3:X=Y;
119        IF SF<MAXS THEN DO;
120         YY=YY+1;
121         GO TO L1;
122        END;
123        END DIAG;
#END OF FILE
#
```

FIT

```
1     FIT:PROC OPTIONS(MAIN);
2     DCL NAME CHAR(50) VARYING;
3     DCL (VC(M)) FLOAT CONTROLLED;
4     DCL(HC(M)) FLOAT CONTROLLED;
5     DCL(A(4))FLOAT;
6     DCL(I,J,K,M) FIXED BIN;
7      DCL Y FLOAT;
8      GJM : PROCEDURE(A,B,X,NA)FLOAT;
9        /* SOLVES A SET OF NA SIMULTANEOUS EQ. FOR X AX=B SEE
10       HAWGOOD NUMERICAL ANALYSIS FOR ALGOL VERSION.GAUSS JORDAN METHOD.*/
11     DECLARE(A(*,*),B(*),X(*),PIVOT,PIVPROD,MULT,COMP)FLOAT,
12     (PIVROW(NA),PIVCOL(NA),I,JC,IA,JA,IC,IO,JO,N)FIXED BINARY;
13       DCL (J)FIXED BINARY ;
14     PIVPROD=1;
15     DO I=1 TO NA;
16     PIVROW(I), PIVCOL(I) = I ;
17     END;
18     DO N=1 TO NA;
19     PIVOT=A(PIVROW(N),PIVCOL(N));
20     IO,JO=N;
21     IA=PIVROW(N); JA=PIVCOL(N);
22     DO I = N TO NA ;
23     DO J=N TO NA;
24      IC=PIVROW(I);  JC=PIVCOL(J);
25     COMP=A(IC,JC);
26     IF ABS(COMP)>ABS(PIVOT) THEN DO;
27     PIVOT=COMP;
28     IA=IC; IO=I;
29     JA=JC; JO=J;
30     END;
31     END;
32     END;
33     PIVROW(IO)=PIVROW(N);
34     PIVCOL(JO)=PIVCOL(N);
35     PIVROW(N)=IA; PIVCOL(N)=JA;
36     B(IA)=B(IA)/(PIVOT);
37     PIVPROD=PIVPROD*PIVOT;
38     DO J=N+1 TO NA;
39     JC=PIVCOL(J);
40     A(IA,JC)=A(IA,JC)/PIVOT;
41      END;
42     DO I=1 TO NA ;
43     IF I^= IA THEN DO ;
44     MULT=A(I,JA);
45     B(I)=B(I)-B(IA)*MULT;
46     DO J=(N+1) TO NA;
47     JC=PIVCOL(J);
48     A(I,JC)=A(I,JC)-A(IA,JC)*MULT;
```

FIT (Continued)

```
 97       PUT LIST(NAME);
 98       PUT SKIP;
 99       PUT LIST('   DEGREES K   MICROVOLTS');
100       PUT SKIP;
101       DO J=0 TO 80 BY 1;
102        Y=A(1)+A(2)*J+A(3)*(J**2)+A(4)*(J**3);
103       PUT EDIT(J,' K',Y)(X(6),F(2,0),A(2),X(9),F(3,0));
104       PUT SKIP;
105       END;
106       END FIT;
END OF FILE
```

FIT (Continued)

```
      END;
      END;
      END;
    END;
    DO I=1 TO NA;
    X(PIVCOL(I))=B(PIVROW(I));
    END;
    RETURN(PIVPROD);
    END GJM;
    POLYFIT: PROC(V,H,M,X);
     DCL((V,H)(M),A(4,4),     X(4),B(4),G1) FLOAT,I FIXED BIN;
      DCL(W) FIXED BINARY;
      A=0; B=0; X=0;
    DO I=1 TO M BY 1; A(1,1)=A(1,1) +1;A(1,2),A(2,1)=A(1,2)+V(I);
    A(1,3),A(2,2),A(3,1)=A(1,3)+V(I)*V(I);
    A(1,4),A(2,3),A(3,2),A(4,1)=A(1,4)+V(I)**3;
    A(2,4),A(3,3),A(4,2)    = A(2,4) + V(I)**4;
    A(3,4),A(4,3)=A(3,4)+V(I)**5; A(4,4) = A(4,4)+ V(I)**6;
       B(1)=B(1)+H(I);
     B(2)=B(2)+H(I)*V(I);
     B(3)=B(3)+H(I)*V(I)**2;
     B(4)=B(4)+H(I)*V(I)**3;
     END;
      W=4;
      G1=GJM(A,B,X,W);
    END POLYFIT;
   PUT LIST('TITLE OF OPERATION');
   PUT SKIP;
   GET LIST(NAME);
   PUT LIST('NO OF DATA POINTS');
   PUT SKIP;
   GET LIST(M);
    ALLOCATE HC;
    ALLOCATE VC;
   PUT LIST ('DATA POINTS: X,Y')
   ;
   PUT SKIP;
   DO I=1 TO M;
   GET LIST(VC(I),HC(I));
   END;
   CALL POLYFIT(VC,HC,M,A);
   DO K=1 TO 4;
   PUT DATA(A(K));
   END;
   PUT SKIP;
   PUT SKIP(2);
   PUT LIST('OUTPUT DATA');
   PUT SKIP;
```

FIT : OUTPUT

OUTPUT DATA
GOLD(0.2% IRON)/COPPER THERMOCOUPLE CALIBRATION

DEGREES K	MICROVOLTS	DEGREES K	MICROVOLTS
0 K	684	40 K	223
1 K	668	41 K	216
2 K	652	42 K	209
3 K	636	43 K	201
4 K	620	44 K	194
5 K	605	45 K	187
6 K	590	46 K	180
7 K	575	47 K	174
8 K	561	48 K	167
9 K	546	49 K	160
10 K	533	50 K	154
11 K	519	51 K	148
12 K	506	52 K	141
13 K	493	53 K	135
14 K	480	54 K	129
15 K	467	55 K	123
16 K	455	56 K	117
17 K	443	57 K	111
18 K	431	58 K	105
19 K	420	59 K	100
20 K	408	60 K	94
21 K	397	61 K	88
22 K	386	62 K	82
23 K	376	63 K	77
24 K	365	64 K	71
25 K	355	65 K	66
26 K	345	66 K	60
27 K	335	67 K	55
28 K	325	68 K	49
29 K	316	69 K	44
30 K	307	70 K	38
31 K	298	71 K	33
32 K	289	72 K	27
33 K	280	73 K	22
34 K	271	74 K	17
35 K	263	75 K	11
36 K	255	76 K	6
37 K	247	77 K	0
38 K	239	78 K	-6
39 K	231	79 K	-11
40 K	223	80 K	-17

#EXECUTION TERMINATED
#

MOMENT

```
1       MOMENT:PROC OPTIONS(MAIN);
2        DCL(T,EX,SUM1,SUM2,K)FLOAT;
3        DCL MM FLOAT;
4        DCL (I,J,L,N) FIXED BIN;
5       DCL(E(N),M(N)) FLOAT CONTROLLED,DATA FILE STREAM INPUT;
6        DCL A CHAR(100) VARYING;
7        PUT LIST('NUMBER OF CALCULATIONS TO DO,PLEASE?');
8       PUT SKIP;
9        GET LIST(L);
10       J=0;
11       AGAIN: GET FILE(DATA) LIST(A);
12       GET FILE(DATA) LIST (N);
13       ALLOCATE E;
14       ALLOCATE M;
15      DO I=1 TO N;
16       GET FILE(DATA) LIST(E(I));
17       END;
18       DO I=1 TO N;
19       GET FILE(DATA) LIST(M(I));
20       END;
21       PUT SKIP(3);
22       PUT LIST (A);
23       PUT SKIP(2);
24       PUT LIST('INPUT DATA');
25       PUT SKIP;
26       PUT LIST('EIGEN VALUE       MOMENT');
27       PUT SKIP(2);
28       DO I=1 TO N;
29       PUT EDIT(E(I),M(I))(X(3),F(6,2),X(11),F(5,2));
30       PUT SKIP;
31       END;
32       PUT SKIP(2);
33       PUT LIST('OUTPUT DATA');
34       PUT SKIP;
35       K=0.0862;
36       PUT EDIT('MOMENT','TEMPERATURE(K)')(X(3),A(6),X(6),A(14));
37       PUT SKIP;
38       PUT EDIT(M(1),'0')(X(3),F(6,2),X(13),A);
39       PUT SKIP;
40       DO T=20 TO 200 BY 20;
41       SUM1=0;
42       SUM2=0;
43        DO I=1 TO N;
44       IF N=1 THEN DO;
45         EX=1;
46         GO TO L1;
47         END;
48         EX=EXP(-(E(I)-E(1))/(K*T));
```

MOMENT (Continued)

```
 49        L1: SUM1 =SUM1+M(I)*EX;
 50          SUM2=SUM2+EX;
 51         END;
 52        MM=SUM1/SUM2;
 53        PUT EDIT(MM,T)(X(3),F(6,2),X(10),F(4,0));
 54        PUT SKIP;
 55       END;
 56        J=J+1;
 57        IF J<L THEN GO TO AGAIN;
 58       END MOMENT;
END OF FILE
```

MSDU

```
1       MSDU:PROCEDURE (A,R,N,MV);
2       DECLARE
3            (I,IND,J,L,M,MV,N)
4            FIXED BINARY,
5            ERROR EXTERNAL CHARACTER(1),
6            (A(*,*),R(*,*),ANORM,ANRMX,THR,U,Y,SINX,
7            SINX2,COSX,COSX2,SINCS,FN)
8            BINARY FLOAT;
9       ERROR='0';
10       IF N <= 1
11      THEN DO;
12           ERROR='1';
13           GO TO FIN;
14           END;
15      FN=N;
16      IF MV=0
17      THEN DO;
18             DO I=1 TO N;
19               DO J=1 TO N;
20               R(I,J)=0;
21               END;
22             R(I,I)=1;
23             END;
24           END;
25      ANORM=0;
26           DO I=1 TO(N-1);
27             DO J=(I+1) TO N;
28             ANORM=ANORM+A(I,J)*A(I,J);
29             END;
30           END;
31       IF ANORM <= 0.0
32      THEN GO TO SORT;
33      ANORM=1.414*SQRT(ANORM);
34      ANRMX=ANORM*1.0E-6/FN;
35      IND=0;
36      THR=ANORM;
37      S10:
38         THR=THR/FN;
39      S20:
40         L=1;
41      S30:
42        M=L+1;
43      S40:
44         IF ABS(A(L,M))>=THR
45         THEN DO;
46            IND=1;
47            U=0.5*(A(L,L)-A(M,M));
48            Y=-A(L,M)/SQRT(A(L,M)*A(L,M)+U*U);
```

MSDU (Continued)

```
49            IF U<0.0
50            THEN Y=-Y;
51            SINX=Y/SQRT(2.0*(1.0+(SQRT(1.0-Y*Y))));
52            SINX2=SINX*SINX;
53            COSX=SQRT(1.0-SINX2);
54            COSX2=COSX*COSX;
55            SINCS=SINX*COSX;
56              DO I=1 TO N;
57              IF I<L
58              THEN DO;
59                IF I<M
60                THEN DO;
61                  U=A(I,L)*COSX-A(I,M)*SINX;
62                  A(I,M)=A(I,L)*SINX+A(I,M)*COSX;
63                  A(I,L)=U;
64                  END;
65                END;
66            ELSE IF I>L
67            THEN DO;
68              IF I<M
69              THEN DO;
70                U=A(L,I)*COSX-A(I,M)*SINX;
71                A(I,M)=A(L,I)*SINX+A(I,M)*COSX;
72                END;
73              ELSE IF I>M
74              THEN DO;
75                U=A(L,I)*COSX-A(M,I)*SINX;
76                A(M,I)=A(L,I)*SINX+A(M,I)*COSX;
77                END;
78              IF I¬=M
79              THEN A(L,I)=U;
80              END;
81            IF MV=0
82            THEN DO;
83              U=R(I,L)*COSX-R(I,M)*SINX;
84               R(I,M)=R(I,L)*SINX+R(I,M)*COSX;
85              R(I,L)=U;
86              END;
87            END;
88          U=2.0*A(L,M)*SINCS;
89          Y=A(L,L)*COSX2+A(M,M)*SINX2-U;
90          U=A(L,L)*SINX2+A(M,M)*COSX2+U;
91          A(L,M)=(A(L,L)-A(M,M))*SINCS+A(L,M)*(COSX2-SINX2);
92          A(L,L)=Y;
93          A(M,M)=U;
94          END;
95        IF M ¬= N
96       THEN DO;
```

MSDU (Continued)

```
 97          M=M+1;
 98          GO TO S40;
 99          END;
100      IF L¬=(N-1)
101      THEN DO;
102          L=L+1;
103          GO TO S30;
104          END;
105      IF IND=1
106      THEN DO;
107          IND=0;
108          GO TO S20;
109          END;
110       IF THR > ANRMX
111      THEN GO TO S10;
112      SORT:
113          DO I=1 TO N;
114            DO J=1 TO N;
115            IF A(I,I)<A(J,J)
116            THEN DO;
117              U=A(I,I);
118              A(I,I)=A(J,J);
119              A(J,J)=U;
120              IF MV=0
121              THEN DO;
122                DO L= 1 TO N;
123                U=R(L,I);
124                R(L,I)=R(L,J);
125                R(L,J)=U;
126                END;
127              END;
128            END;
129          END;
130      END;
131      FIN:
132      RETURN;
133      END;
END OF FILE
```